

DTIC FILE NUMBER

AFOSR-TR- 89-0845

(2)

DETERMINISTIC AND STOCHASTIC WAVEFIELDS IN  
THE NEAR-FIELD FROM EXPLOSIVE SOURCES

AD-A210 057

Annual and Final Report

Grant AFOSR-84-0016

15 Oct 87 - 14 Apr 89

SDTICD  
ELECTED  
JUL 05 1989

(1b) H

PI: Brian W Stump

Department of Geological Sciences

Southern Methodist University

Dallas, Texas 75275

DISTRIBUTION STATEMENT A	
Approved for public release; Distribution Unlimited	

89 6 29 018

UNCLASSIFIED

SECURITY CLASSIFICATION OF THIS PAGE

Form Approved  
OMB No. 0704-0188

## REPORT DOCUMENTATION PAGE

1a. REPORT SECURITY CLASSIFICATION <b>UNCLASSIFIED</b>		1b. RESTRICTIVE MARKINGS										
2a. SECURITY CLASSIFICATION AUTHORITY		3. DISTRIBUTION/AVAILABILITY OF REPORT Approved to public release; distribution unlimited.										
2b. DECLASSIFICATION/DOWNGRADING SCHEDULE												
4. PERFORMING ORGANIZATION REPORT NUMBER(S)  SMU G-5		5. MONITORING ORGANIZATION REPORT NUMBER(S) <b>AFOSR - TR - 89 - 0845</b>										
6a. NAME OF PERFORMING ORGANIZATION Southern Methodist Univ. Dept. of Geological Sciences	6b. OFFICE SYMBOL (If applicable)  NP	7a. NAME OF MONITORING ORGANIZATION <b>AFOSR</b>										
6c. ADDRESS (City, State, and ZIP Code) Southern Methodist University Dept. of Geological Sciences Dallas, Texas 75275	7b. ADDRESS (City, State, and ZIP Code) Bldg 410 Bolling AFB DC 20332-6448											
8a. NAME OF FUNDING/SPONSORING ORGANIZATION AFOSR/NP	8b. OFFICE SYMBOL (If applicable)  NP	9. PROCUREMENT INSTRUMENT IDENTIFICATION NUMBER <b>AFOSR-84-0016</b>										
8c. ADDRESS (City, State, and ZIP Code)  Building 401 Bolling AFB, DC 20332	10. SOURCE OF FUNDING NUMBERS  PROGRAM ELEMENT NO. 61102F PROJECT NO. 2309 TASK NO. A2 WORK UNIT ACCESSION NO.											
11. TITLE (Include Security Classification) Deterministic and Stochastic Wavefield in the Near-Field from Explosive Sources												
12. PERSONAL AUTHOR(S) B. W. Stump, L. Grant, M. Bogaards, E. Flynn, R. Reinke												
13a. TYPE OF REPORT Final Technical	13b. TIME COVERED FROM 15 Oct 87 TO 14 Apr 89	14. DATE OF REPORT (Year, Month, Day) 89 05 24	15. PAGE COUNT 316									
16. SUPPLEMENTARY NOTATION Seismology, explosion source; moment tensors, inversion, seismic modeling.												
17. COSATI CODES <table border="1"><tr><th>FIELD</th><th>GROUP</th><th>SUB-GROUP</th></tr><tr><td></td><td>UG-11</td><td></td></tr><tr><td></td><td></td><td></td></tr></table>		FIELD	GROUP	SUB-GROUP		UG-11					18. SUBJECT TERMS (Continue on reverse if necessary and identify by block number)  <i>See Item 16</i>	
FIELD	GROUP	SUB-GROUP										
	UG-11											
19. ABSTRACT (Continue on reverse if necessary and identify by block number)  An experimental technique for characterizing the seismic source from chemical explosions in different geological material is presented. The specific example of an explosion in alluvium is given. The importance of a complete seismic site characterization prior to the experiment is emphasized. This characterization must include determination of both compressional and shear properties at the test site.												
20. DISTRIBUTION/AVAILABILITY OF ABSTRACT <input checked="" type="checkbox"/> UNCLASSIFIED/UNLIMITED <input type="checkbox"/> SAME AS RPT <input type="checkbox"/> DTIC USERS		21. ABSTRACT SECURITY CLASSIFICATION <b>UNCLASSIFIED</b>										
22a. NAME OF RESPONSIBLE INDIVIDUAL <i>Bruce L. Smith</i>		22b. TELEPHONE (Include Area Code) <i>202-767-4908</i>	22c. OFFICE SYMBOL <b>NP</b>									

**DETERMINISTIC AND STOCHASTIC WAVEFIELDS IN  
THE NEAR-FIELD FROM EXPLOSIVE SOURCES**

**Annual and Final Report**

**Grant AFOSR-84-0016**

**15 Oct 87 - 14 Apr 89**

**PI: Brian W Stump**

**Department of Geological Sciences**

**Southern Methodist University**

**Dallas, Texas 75275**

## INTRODUCTION

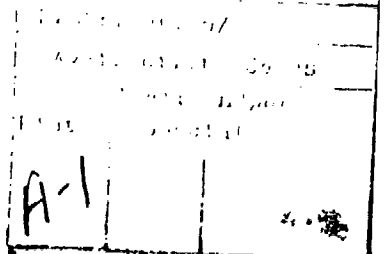
The work performed over the past year of this contract is summarized in three sections. The first is comprised of the final report documenting the work of Lori Grant on characterizing small explosion seismic source functions. Section two summarizes talks and papers given in the past year under this contract. The final section contains reprints of three papers published under this contract in the last year.

**Experimental Determination of Seismic Source Characteristics for Small Explosions** by Lori Grant describes a set of experiments and analysis designed to characterize the equivalent elastic source functions of explosions in different media. The particular tests studied were in alluvium and a set of site characterization procedures were developed to support the source study. The techniques and format developed in this study could be applied to other geological media. Bounds are placed upon the explosive source function constrained with only the site characterization data and then compared to the model developed from the actual explosion data. This comparison quantifies the predictive capability for the explosive source function in a new media. In the inversion of the observational data for the equivalent seismic source function a strong trade-off is identified between the shear wave velocity of the medium and the symmetry of the equivalent source function. This last result emphasizes the need to include a good characterization of the P and S wave properties of a test site. Unfortunately S or shear wave characterization tools are not as well developed as those for P or compressional waves.

Two papers were presented at a variety of technical meetings in the last year. The abstracts from these talks are included in section 3.

Three papers were published in the past year. Two appeared in the **Bulletin of the Seismological Society of America**, Stochastic Geologic Effects on Near-Field Ground Motions in Alluvium and Experimental Confirmation of Superposition from Small Scale Explosions. The third paper published in **Journal of Geophysical Research** is entitled Effects of Source Depth on Near-Source Seismograms.

This year of research has focused on a transition from our previous source studies to an increased emphasis on the geophysical characterization of the shallow near-surface environment. This characterization is needed to improve our ability to quantify the seismic source function as well as estimate the explosive ground motion loading one might expect in a particular geological material. The papers in the Bulletin summarize our early attempts to separate the *stochastic and deterministic parts of the wavefield*.



EXPERIMENTAL DETERMINATION OF SEISMIC SOURCE  
CHARACTERISTICS FOR SMALL CHEMICAL EXPLOSIONS

A Thesis Presented to the Graduate Faculty of  
Dedman College  
of  
Southern Methodist University  
in  
Partial Fulfillment of the Requirements  
for the Degree of  
Master of Science  
with a  
Major in Geophysics  
by

Lori T. Grant  
(B.S., University of Texas at Dallas, 1985)

December 17, 1988

Grant, Lori Teresa

B.S., University of  
Texas at Dallas, 1985

Experimental Determination of  
Seismic Source Characteristics  
for Small Chemical Explosions

Advisor: Dr. Brian W. Stump

Master of Science degree conferred December 17, 1988

Thesis completed December 10, 1988

A deterministic source model is defined using three-component acceleration data from seven 5 lb. test shots recorded with identical instrumentation all within the same test bed. Observational ranges are between 5 and 60 meters with good azimuthal coverage.

Inversions are done utilizing the moment tensor representation ( $M = G^{-1}U$ ), where  $M$  is the second order moment tensor containing source information,  $G$  is the matrix of Green's functions and  $U$  are the observed seismograms. The Green's functions are based on a velocity model derived for the test site. Moment tensor inversions with observational data result in source strengths of between .6 and  $4 \times 10^{15}$  dyne-cm for the layered half-space and between 2 and  $8 \times 10^{15}$  dyne-cm when the half-space path functions are used.

Forward models are calculated for a range of site models. The moment calculated from forward models is between 1.1 and  $2.5 \times 10^{15}$  dyne-cm. Sensitivity studies with the synthetic data set emphasize the importance of shear velocity in separating source-path trade-offs.

## CONTENTS

LIST OF FIGURES .....	viii
LIST OF TABLES .....	x
LIST OF SYMBOLS .....	xi
LIST OF ABBREVIATIONS .....	xii
ACKNOWLEDGEMENTS .....	xiii
CHAPTER	Page
1. INTRODUCTION.....	1
A. Explosion Seismic Source Function.....	2
1. The Isotropic Source .....	5
2. The Non-isotropic Source .....	12
B. Source Scaling.....	14
C. Examples of Experimental Seismology.....	15
D. Specifics of This Study.....	17
2. OBSERVATIONAL DATA.....	20
A. Explosion Data.....	20
1. Experimental Layout .....	20
2. Data Corrections .....	23
3. Data Characteristics .....	25
B. Site Characterization Data.....	41
1. Refraction Surveys .....	41
2. First Arrivals .....	48
3. Shear Velocities .....	49
4. Q in Dry Alluvium .....	50

3. FORWARD SYNTHETIC MODELS.....	53
A. Introduction .....	53
B. Theoretical Source Function: RDP .....	55
1. BASIC Model .....	60
a) Long period level: LPL.....	64
b) Source Overshoot.....	66
c) Corner frequency.....	67
2. Source Depth of Burial .....	68
3. CART Reduced Displacement Potentials .....	70
C. Path Calculations .....	74
1. Half-space Greens Functions .....	74
2. Layered Half-space Greens Functions .....	83
4. MOMENT TENSOR INVERSIONS.....	91
A. Moment Tensor Representation of the Source .....	92
B. Solution of the Inverse Problem .....	95
C. Source Inversions with Synthetic Data .....	98
1. Synthetic Inversions Input: $Us=MG$ .....	99
2. Noise Tests .....	102
3. Example of Source-Path Trade-offs .....	115
4. Station Distribution Tests .....	120
5. Condition Numbers .....	121
6. Time Domain Fits .....	123
D. Source Inversions with Observational Data .....	129
1. Half-space Inversions .....	129
2. Layered Half-space Inversions .....	137
3. Condition Numbers .....	148
4. Time Domain Fits .....	150

5. SUMMARY AND CONCLUSIONS.....	145
A. McCormick Ranch Geological Model .....	115
B. Forward Modeling .....	146
C. Source Physics .....	146
1. Repeatability .....	146
2. Source Symmetry .....	147
3. Source Coupling .....	147
D. Source Scaling .....	147
E. Recommendations .....	148
APPENDICES	
A. DATA CORRECTIONS.....	149
B. COMPLETE EXPLOSION DATA SET.....	183
C. CART PEAK TIME DOMAIN AMPLITUDES.....	240
D. ART PEAK TIME DOMAIN AMPLITUDES.....	242
REFERENCE LIST .....	245

## LIST OF FIGURES

Figure	Page
1.1 Magnitude Versus Yield for Explosions at NTS .....	3
1.2 Peak Scaled Acceleration Versus Scaled Range .....	4
1.3 Reduced Displacement Potentials in Four Media .....	9
2.1 ART Array Configuration .....	22
2.2 CART Array Configuration .....	24
2.3 Particle Motion Diagrams 5 - 13.5 Meters .....	26
2.4 Particle Motion Diagrams 20.3 - 40.6 Meters .....	28
2.5 ART Observed Velocity at 30 Meters .....	30
2.6 CART/ART Peak Velocity Versus Range .....	37
2.7 CART/ART Peak Acceleration Versus Range .....	38
2.8 CART/ART Peak Displacement Versus Range .....	39
2.9 CART/ART Peak Transverse Amplitudes Versus Range ....	40
2.10 Map View of CART/ART Refraction Surveys .....	43
2.11 ART/CART Refraction Profiles: Long and Short Line ..	45
2.12 ART/CART Refraction Profile: Short Line .....	46
2.13 Amplitude Ratio Versus Shear Velocity Ratio .....	51
3.1 Pressure Function .....	57
3.2 RDP Sensitivity Analysis .....	63
3.3 Effect of Source Burial Depth on RDP .....	69
3.4 Range of CART Reduced Displacement Potentials .....	72
3.5 Half-space Synthetics: HS115 Path, Basic Source ....	77

3.6 Half-space Synthetics at 9 Meters: Source Study .....	79
3.7 Half-space Synthetics at 27 Meters: Source Study .....	82
3.8 Layered Half-space Synthetics: Path N, Basic Source .	86
3.9 Layered Half-space Synthetics: Source Study .....	88
4.1 Moment Tensor Representation of the Basic Source ....	101
4.2 Green's Functions at 27 Meters (a)HS115 (b)HS366 ....	103
4.3 Synthetic Inversion 115BIC1N00 .....	106
4.4 Synthetic Inversion 115BIC1N1 .....	108
4.5 Synthetic Inversion 115BIC1N10 .....	109
4.6 Green's Functions and Synthetics at 27 Meters .....	112
4.7 Synthetic Inversion 366BIC1X .....	114
4.8 Condition Numbers for Synthetic Inversions .....	117
4.9 Fits for Synthetic Inversion 115BIC1N10 .....	121
4.10 Fits for Synthetic Inversion 366BIC1X .....	122
4.11 Fits for Synthetic Inversion OMEGAN1 .....	123
4.12 Observational Inversion 115C1 .....	127
4.13 Observational Inversion 366C1 .....	129
4.14 Observational Inversion C1F .....	133
4.15 Observational Inversion C1H .....	134
4.16 Observational Inversion C1N .....	136
4.17 Observational Inversion C1O .....	137
4.18 Condition Numbers for Observational Inversions .....	138
4.19 Fits for Observational Inversion 115C1 .....	141
4.20 Fits for Observational Inversion 366C1 .....	142
4.21 Fits for Observational Inversion C1N .....	143

## LIST OF TABLES

Table	Page
1. Summary of Observational Data	21
2. Amplitude Decay Exponents	36
3. McCormick Ranch Site Model	42
4. Source Parameters: in Figure 3.2	62
5. CART Source Parameters	71
6. Half-space Velocity Models	76
7. Layered half-space Velocity Models	84
8. Source Inversion with Synthetic Data	100
9. Peak Time Domain Amplitudes of Synthetic Source Inversions	105
10. Correlation Coefficients of Synthetic Source Inversions	120
11. Peak Time Domain Amplitudes of CART 1 Observational Inversions	125
12. Correlation Coefficients of Synthetic Source Inversions	140
13. Types of Observed Slopes with Percentages	152

LIST OF SYMBOLS

Symbol	Units	Notes
W	kt	yield in equivalent kt of TNT
h	m	(source) depth of burial below surface
r	m	range; source-receiver offset
r <sub>el</sub>	m	elastic radius
r <sub>c</sub>	m	cavity radius
ψ(τ)	m <sup>3</sup>	reduced displacement potential
α	1/s	decay constant (of pressure function)
c	m/s	compressional velocity
β	m/s	shear velocity
λ	dyne-cm/s <sup>2</sup>	Lame's constant
μ	dyne-cm/s <sup>2</sup>	shear modulus
ρ	gm/cm <sup>3</sup>	density
P <sub>cc</sub>	dyne-cm/s <sup>2</sup>	steady-state pressure
P <sub>os</sub>	dyne-cm/s <sup>2</sup>	peak shock pressure
P <sub>o</sub>	dyne-cm/s <sup>2</sup>	pressure amplitude; P <sub>o</sub> = P <sub>os</sub> - P <sub>cc</sub>
ω <sub>o</sub>	1/s	characteristic frequency
σ		Poisson's ratio
U <sub>o</sub>	m/s	observational velocity
U <sub>s</sub>	m/s	synthetic velocity
G		Green's function
M <sub>ij</sub>	dynes-cm	seismic moment tensor

#### LIST OF ABBREVIATIONS

ART	Array Test Series
CART	Contained Array Test Series
CHEAT	Contained High Explosive Alluvium Test
CRY	Cube-Root-Yield
ESSF	Explcsion Seismic Source Function
GLI	Generalized Linear Inversion
HFRO	High frequency roll off (of spectrum)
kt	Kilotons
LPL	Long period level (of spectrum)
NTS	Nevada Test Site
RDP	Reduced Displacement Potential
RVP	Reduced Velocity Potential
SD	Scaled depth (of burial)
SNR	Signal to Noise Ratio
UNE	Underground Nuclear Explosion

## ACKNOWLEDGEMENTS

Many thanks to my advisor Professor Brian Stump. He provided the project, the funding, the technical support and an enormous amount of patience. I feel fortunate to have been one of his graduate students. I would also like to thank the other members of my committee, Gene Herrin, Bob Reinke and David Blackwell for their guidance.

This project was funded by Air Force Contract No. AFOSR-84-0016. The field data for this thesis was collected by Bob Reinke and Al Leverette, both at the Air Force Weapons Laboratory. I appreciate their efforts and Bob Reinke's technical advice throughout the project.

Many thanks to my friends among the students, faculty and staff at SMU for making the research environment both stimulating and enjoyable.

And most important of all, I dedicate this thesis to my parents, Pat and John Grant. I thank them for their continual support, their guidance and their love.

## CHAPTER 1

### INTRODUCTION

The objective of this research is to improve our understanding of explosion source functions. Carefully controlled small scale tests are utilized in a two-step approach to define a deterministic source model. The first step is to produce forward models of near-field waveforms using analytic source functions and numerical Green's functions. These synthetic seismograms are then compared to the observed seismograms to quantify the path effects. The second step utilizes the Green's functions obtained in Step 1 in an inversion of the observed seismograms for the six time functions of the second order moment tensor representing the source. The inversion scheme was developed by Stump and Johnson (1984 (see also Stump and Johnson (1977) and Stump (1979)).

The main application of results from this study is to aid in the refinement of yield-scaled source models with the goal of better estimating explosion yield from seismic observations. Interest in this subject has recently increased as requirements of a verifiable test ban treaty are becoming more severe.

A large body of observational data exists and has been used to empirically constrain source parameter scaling rela-

tions for the explosion seismic source function (ESSF). However, despite the advances in modeling the ESSF the relationship of seismic amplitude to event yield is still not clear. The problem is illustrated in Figure 1.1 taken from OTA report of May 1988. Seismic magnitude is plotted against event yield from UNE tests at NTS. Magnitude is related to the log of the amplitude of teleseismic body waves. The scatter in the data points represents a variation in seismic magnitude for a given yield. Assuming the appropriate magnitude-yield curve has been calculated, the ability to predict event yield from magnitude is at least limited by the scatter of the data.

As another example, peak acceleration versus distance from the source is plotted in Figure 1.2 for several UNEs at Pahute Mesa, NTS. The Kearsarge test is the most recent event at a yield approaching the 1974 Test Ban Treaty threshold of 150 kt. Kearsarge observations exhibit a factor of 7 scatter in peak acceleration at a single range. (B. Stump personal communication, August, 1988).

The scatter illustrated in Figures 1.1 and 1.2 makes it difficult to develop a simple magnitude-yield scaling relation even when the tests have the same source medium as in Figure 1.2.

#### A. Explosion Seismic Source Function

The fundamental goal in source studies is to obtain a specific time history of the explosion seismic source

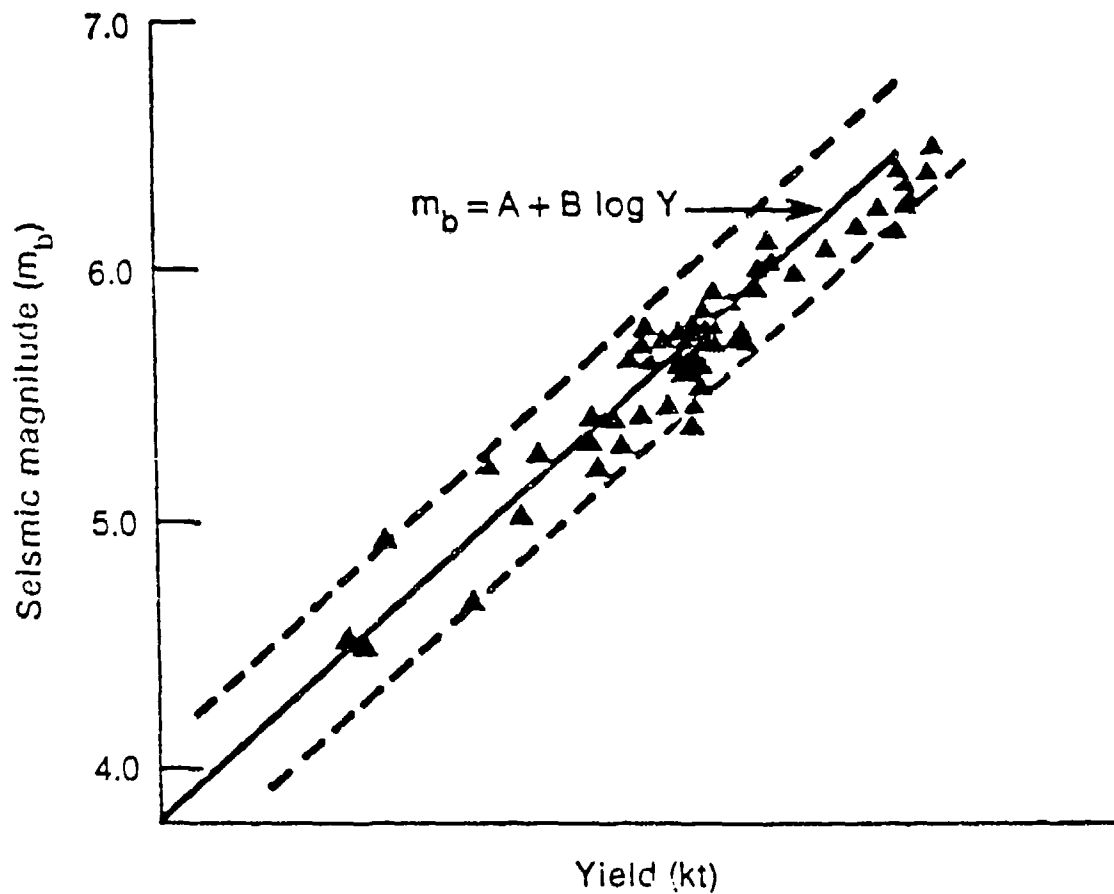


Figure 1.1. Magnitude versus yield for explosions at the Nevada Test Site. (Modified from Office of Technology and Assessment Report, May 1988)

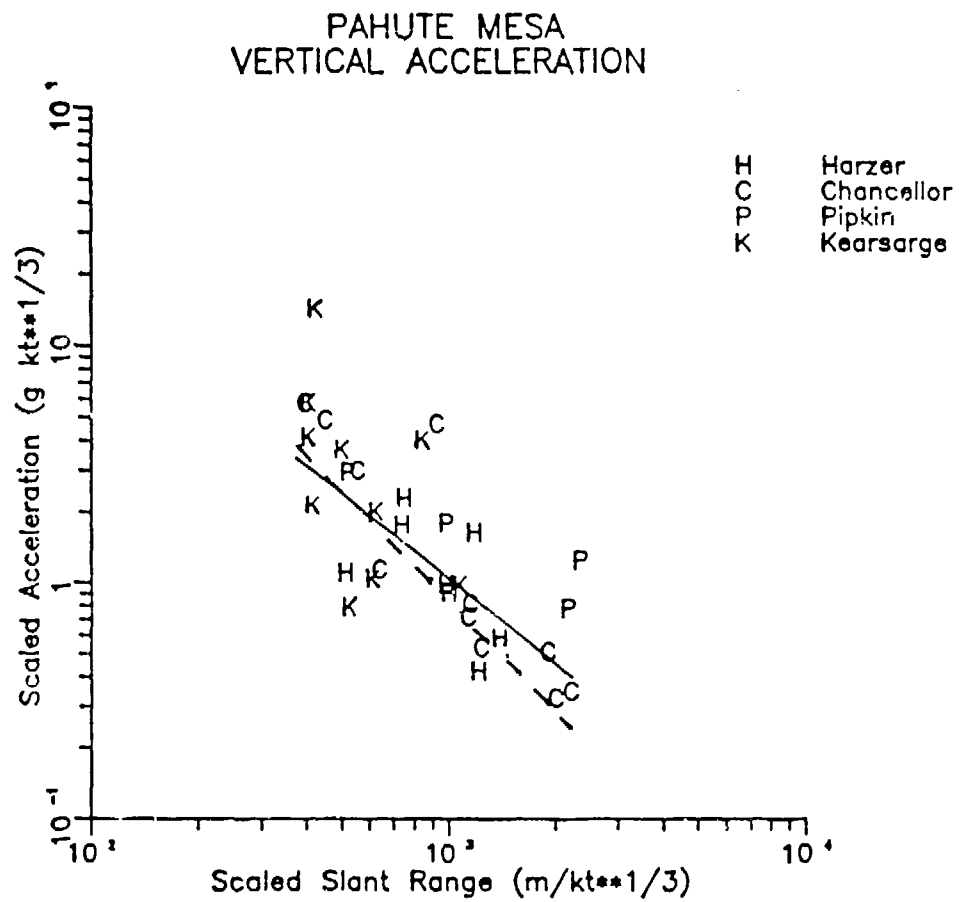


Figure 1.2. Peak scaled acceleration versus scaled range for nuclear explosions at Pahute Mesa, Nevada Test Site. This plot illustrates the factor of 2 scatter that is observed in the peak accelerations from nuclear explosions. (From B. Stump, personnal communication)

function (ESSF). Masse (1981), in his review of underground nuclear explosion source models, suggests that an adequate source model may combine several different mechanisms in sequence to explain observed seismic signals. Stump (1985), for example, has successfully modelled near-field explosion waveforms as a combination of the spherically symmetric explosion followed by cylindrically symmetric spallation of the near surface layers. It is convenient to branch into two categories of source studies at this point. The first describes that part of the source which is spherically symmetric or isotropic and concerned with the transfer of chemical (or nuclear) energy into seismic disturbance; the second includes all non-isotropic source contributions.

### 1. The Isotropic Source

Rather than beginning at the exact point of detonation, the task of describing the isotropic source function is simplified by assuming an "equivalent" source acting at the "elastic" radius. The elastic radius defines a volume inside which pressures are too large to apply infinitesimal strain theory. At radial distances beyond the elastic radius pressures are sufficiently reduced so that Hooke's law can be applied relating pressure to displacement.

For this approximation to be valid, the data should be dominated by wavelengths that are longer than the elastic radius. The reasoning is that when the seismic wavelengths of the data are longer than the elastic radius, the details

cf the source inside the elastic radius cannot be resolved by the data. In other words, the data are not contaminated by source details which are not included in the physical description.

The smallest expected wavelength for this data set is 4.5 m. This value is the ratio of the slowest expected P velocity in the test site (270 m/s, Section 2.B.1) with the highest frequency in the data ( 60 Hz, Section 2.A.2). The dominant frequency in the velocity spectra (shown in Appendix B), 10 Hz, corresponds to a wavelength of 27 m.

This method of assuming an equivalent elastic radiator was first discussed by Sharpe (1942) who formulated the response of an elastic whole space to an arbitrary pressure pulse on the inside of a spherical cavity. In the idealized statement of the problem the perfectly spherical cavity exists in an isotropic homogeneous elastic wholespace. Under these conditions an explosion produces displacements only in the radial direction; spherical compressional waves emanate from the center of the equivalent radiator.

The wave equation for this problem reduces to one dimension in spherical coordinates

$$(1.1) \quad \frac{\partial^2 \psi}{\partial r^2} = \frac{1}{c^2} \frac{\partial^2 \psi}{\partial t^2}$$

where solutions are in terms of the potential,  $\psi$ . Displacements are related to the potential by

$$(1.2) \quad u(r, t) = \frac{\partial}{\partial r} (\psi(\tau)/r)$$

where  $\tau = t - (r - r_{el})/c$  is the arrival time at  $r$  as a function of the compressional velocity,  $c$ .

Sharpe found solutions to Equation 1.1 satisfying the boundary condition that the pressure applied to the interior cavity must equal the radial stress in the medium at the cavity radius ( $r = r_{el}$ )

$$(1.3) \quad - \left[ (\lambda + 2\mu) \frac{\partial u}{\partial r} + 2\lambda \frac{u}{r} \right]_{r=r_{el}} = p(t)$$

Solving Equation 1.3 for displacement and substituting into Equation 1.2 gives the relation between potential  $\Psi(\tau)$  and pressure,  $p(t)$ .

$$(1.4) \quad - \left[ \frac{(\lambda + 2\mu)}{r_{el}^2 c} \ddot{\Psi}(\tau) + \frac{4\mu}{r_{el}^2 c} \dot{\Psi}(\tau) + \frac{4\mu}{r_{el}^3 c} \Psi(\tau) \right]_{r=r_{el}} = p(t)$$

Frequency domain solutions have been published by Latter (1959) and Blake (1952).

Dimensional analysis of Equation 1.2 shows that the potential has units of volume. Because the potential is independent of distance from the source it is often called "reduced" displacement potential abbreviated RDP.

Carrying out the partial derivative Equation 1.2 becomes

$$(1.5) \quad u(r,t) = r^{-2} (\psi(\tau)) + \frac{1}{cr} \left( \frac{d\psi}{d\tau} \right)$$

At large distances from the source, the first term in Equation 1.5 is much smaller than the second. Thus the far-field ( $r \gg r_{el}$ ) displacement is approximated by

$$(1.6) \quad u(r,t) = \frac{1}{cr} \left( \frac{d\psi}{d\tau} \right)$$

Equations 1.4 and 1.6 are the foundation for calculating the seismic source function. Specific pressure functions in Equation 1.4 lead to a predicted shape of the reduced displacement potential (RDP) independent of travel path and distance from the source. When the potential is inserted into equation 1.6, ground motion is predicted.

Once scaling relationships of the RDP are known, equations 1.6 can be used to predict the ground motion of an unknown explosion source. What is necessary in developing scaling relations is to determine how the RDP changes as each of the variables in Equation 1.4 change.

Werth and Herbst (1963) used Equation 1.6 in a different approach. They obtained potentials from measurements of ground motion near the elastic radius of nuclear explosions detonated in four media types. Their far-field RDPs for tuff, salt, granite and alluvium are shown in Figure 1.3a.

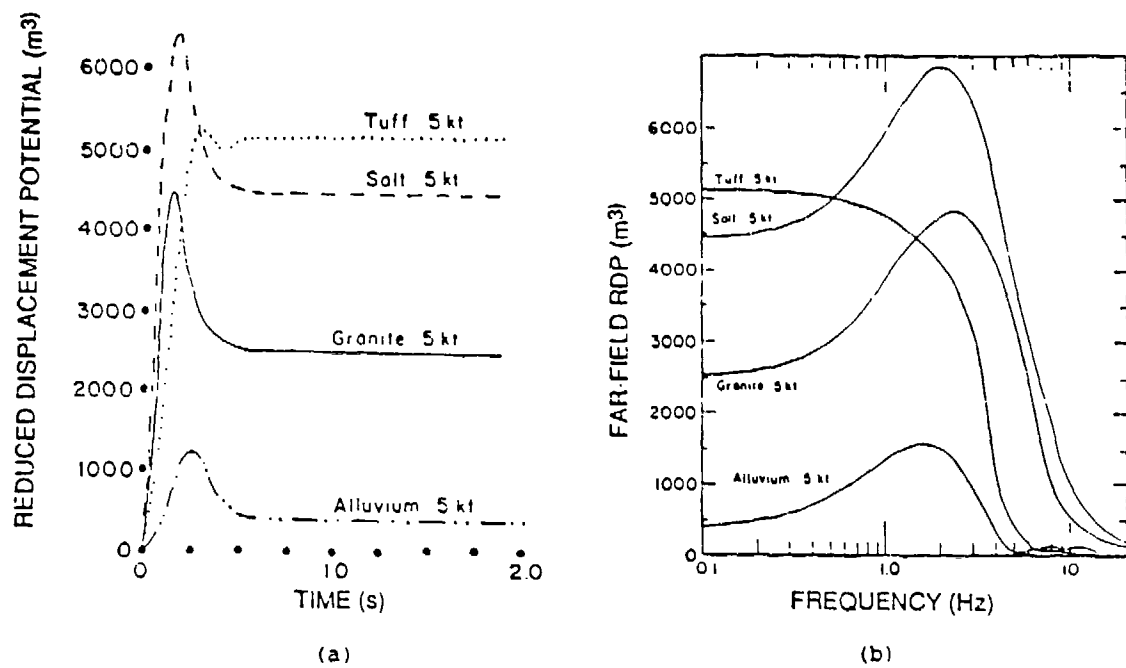


Figure 1.3. Reduced Displacement Potentials. Curves are for explosions in tuff, salt, granite and alluvium. (a) Time domain (b) Frequency domain. (From Wirth and Herbst, 1963)

The Fourier transforms of the far-field RDPs are shown in Figure 1.3b. The data used by Werth and Herbst were free field measurements. The instruments were at depth in a horizontal plane with the device. Thus the free surface effect which may increase the amplitude by a factor of two does not contaminate the data.

Near-source free-field data of the type used by Werth and Herbst are not often available. The standard approach is to correct observed seismograms for features not related to the detonation (e.g. attenuation, and then fit an analytic function to the remaining data which is interpreted as the equivalent source.

Haskell (1967) fit the curves in Figure 3b with simple analytic functions describing the characteristics in terms of three parameters: steady state or DC level of potential,  $\Psi(0)$ , which is related to the residual displacement produced by the explosion; source overshoot, the ratio of the peak potential to the steady state potential; and a time constant specifying the characteristic time of the source function (i.e. corner frequency).

Mueller and Murphy (1971) followed Latter's (1959) steps to express the RDP in the frequency domain in terms of the pressure function. From forward models of close-in observations of UNEs they incorporated the effects of device burial depth and medium characteristics in defining the pressure function. The Mueller-Murphy model is one of the most extensively used source models. It is the primary model

used in this study because of the ability to incorporate depth effects and other physical measurements affecting the source function. Section B in Chapter 3 is devoted to the description of the Mueller-Murphy source model.

Several additional models have been developed over the past 30 years which fit near-field and teleseismic observations: von Seggern and Blanford (1972) modified Haskell's model based on teleseismic observations of three UNEs; Helmberger and Hadley (1981) utilized both local and teleseismic observations of two NTS events to propose yet another modification of Haskell's model. Burger et.al. (1987) made comparisons between the Helmberger-Hadley model and the Mueller-Murphy model to determine Q.

Physical phenomena which may vary with explosive type, emplacement media, depth of burial, shape and size of cavity among other parameters complicate the problem of RDP yield scaling. Problems arise when the RDP obtained for a source detonated in one medium is used to predict the RDP of a source of different yield detonated in a different medium at a different depth because scaling relations are not adequately known. Recent review articles which outline current understanding in this area include: Minster (1985), Bache (1982), and Masse (1981).

Many of the unresolved questions center around the dependency of source coupling on shot parameters. Basically, coupling efficiency decreases as material strength increases (increasing depth) because the amplitude of the pressure

function depends on the residual displacement which is smaller for more competent rock. Coupling efficiency also decreases as air-filled porosity increases (decreasing depth) because more energy is spent in collapsing the pore spaces. Trade-offs must be understood before observations can be adequately modeled to develop yield-scaling relations that are good over a large range of event magnitudes.

## 2. The Non-isotropic Source

The above methods of determining the ESSF assume spherical symmetry. This assumption may not be strictly valid. Thus non-isotropic components of the explosion may lead to biased estimates of the RDP. In other words, the source function is model dependent. Departures from spherical symmetry have long been observed for large underground explosions (Minster, 1985,. To develop seismic magnitude-yield relations it would be best to use the isotropic source only. In order to separate the isotropic from the non-isotropic source contributions a more thorough understanding of the non-isotropic source is necessary.

Lay (1984) proposed two methods to explain the generation of non-isotropic source contributions by explosions: driven motion on pre-existing planes of weakness, and stress relaxation around the fracture zone. Both of these sources have earthquake-like radiation patterns and both contribute shear waves to the radiated seismic energy. The generation of surface waves and shear waves by explosions

is not very well understood. More effective discrimination between earthquakes and small explosions is one of the areas that will benefit from the study of the generation of surface waves and shear waves from small explosions.

Another non-isotropic contribution is spall, failure of near surface layers produced upon conversion of compressional waves to tensile waves at the free surface. When the spalled layers fall back to the surface the downward impulse produces P, S<sub>v</sub> and Rayleigh waves which are delayed in time relative to the initial explosion (Viecelli 1973). The first order symmetry of this delayed source is cylindrical and, because of its proximity to the free surface, the spall source is a very efficient generator of surface waves. Stump (1984) has shown that spall may explain the late Rayleigh wave arrivals on near-field seismograms following explosions. Day (1982), however, showed that there is no spall contribution to surface waves at 20 seconds and therefore spall will not complicate the magnitude-yield relations calculated from surface waves at the 20 second period. Stump (1985) modeled the time function of the spall source which is controlled by the shape of the isotropic pulse and the tensile strength of the medium and found that the contribution from spall dominates in the period range of 0.5 to 2.0 seconds. His findings suggest that magnitude-yield estimates from near-source body waves should take into account the spall contribution to the seismic energy. More work is necessary to develop scaling relations for the spall source.

### B. Source Scaling

We wish to make yield determinations based on the scaling of the isotropic source (RDP). Assuming that non-isotropic radiation has been accounted for, comparisons are made between source spectra based on changes in long-period level, corner frequency and high-frequency roll-off with increasing yield.

Haskell's model utilizes cube-root-yield (CRY) scaling based on the assumption that the scale lengths change as the radius of the explosive device. The inclusion of depth effects by Mueller and Murphy (1971) causes a change in the scaling characteristics of the RDP resulting in a modified scaling model.

Haskell's model predicts a long-period level (LPL) proportional to yield ( $W^{1.0}$ ) while Mueller-Murphy's LPL is proportional to  $W^{.76}$ . The implication is that for a given LPL, classical CRY scaling results in a smaller yield interpretation than the modified source model.

If CRY scaling applies then the corner frequency scales as  $W^{-1/3}$  compared to  $W^{-.19}$  for the Mueller-Murphy model. Beyond the corner frequency the CRY spectrum is proportional to  $W^{1/3}$  and the Mueller-Murphy spectrum is proportional to  $W^{.53}$ . High-frequency decay for these two models is asymptotic to frequency raised to the -4 and -2 power respectively. Another widely used model was proposed by von Seggern and Blanford (1972). The frequency spectrum of the RDP is expressed in a much simpler form than the Mueller-Murphy

model yet the spectra exhibit the  $\omega^{-2}$  roll-off at high frequencies.

It is difficult to compare the utility of one model over another because scaling relations are derived from different data sets. The Mueller-Murphy model is often more desirable because of the ability to include measurements of the elastic radius and other parameters. On the other hand, use of the Mueller-Murphy model requires estimation of a large number of variables and introduces considerable capacity for error.

### C. Examples of Experimental Seismology

In an alternative approach to the problem of quantifying the explosion source function, experimental seismology is explicated. Small scale chemical tests are conducted which reduce complexities by isolating certain variables (depth of burial for example) while reproducing important features of the underground nuclear explosion. Insights into physics of near-source phenomena gained from small scale chemical tests may then be used to model the large body of available observational data and to develop yield-scaled source models that are site specific. The following paragraphs describe two experiments conducted by the SMU research group.

Depth of burial effects in alluvium were quantified by Flynn (1986). The data set included observations of a series of detonations of 253 lbs. of TNT ranging from underburied excavation events (1.85 m) to overburied, fully contained events (11.5 m). As overburden increases, there is suf-

ficient vertical coupling to form an initially spherical explosion. Uncontained events release energy through the free surface resulting in initially cylindrical symmetry. Flynn related the shift to higher frequencies with increasing depth to a shift from cylindrical Sv-Kayleigh energy to spherical P-wave energy. Her energy calculations estimate P-wave source coupling efficiency to be 40% of the total seismic energy for the shallow event. The deeper, fully contained event partitioned 80% of the total seismic energy into the P-wave.

Reinke and Stump (1988) quantified the azimuthal coherence of near-source waveforms from 5 pound explosions in alluvium. Waveforms are coherent to 35 Hz. Variations above 35 Hz are attributed to scattered energy from waves that interact with test bed inhomogeneities. They ruled out, through small tests, the possibility of instrument variation. They also confirmed the repeatability of the source in this test series through a series of detonations in a controlled pit in which every shot variable remained constant.

Small scale tests such as these are relatively inexpensive and instrumentation of a significant part of the wavefield is possible. An additional advantage is that test results are directly applicable to other studies in the same test environment.

#### D. Specifics of This Study

The current study is unique to the standard yield scaling approach in two ways. First, the observed seismograms result from tests designed specifically to isolate the effects of containment and to quantify source symmetry. Secondly, the moment tensor representation is used to allow for non-isotropic source contributions.

The inversion scheme used in this study is that of Stump and Johnson (1984) wherein they represent the explosion source in terms of the seismic moment tensor. A point source is assumed and observed seismograms are inverted for the temporal details of the source function.

This procedure requires careful modeling of the path contributions in order to minimize source-path trade-offs. It is really another way of correcting observed seismograms to obtain an estimate of the source time history just outside the non-linear region.

The isotropic moment tensor represents the volume change due to the spherically symmetric explosion source. It has the same shape and time dependence as the reduced displacement potential (RDP):

$$(1.7) \quad M(\tau)_{ISO} = 4\pi\rho\alpha^2 \Psi(\tau)$$

where  $\Psi(\tau)$  is the potential function introduced in Equation 1.1. Thus the isotropic moment and reduced displacement potential are similar analytical forms of the seismic source

function. The units of seismic moment are force by distance. The development of the moment tensor source representation is found in Chapter 4.

The isotropic component of the source is represented by the trace of the moment tensor. The deviatoric source is that which remains after the isotropic component is removed (Stump, 1984).

$$(1.8) \quad M_{ISO} = \frac{1}{3} M_{ij} \delta_{ij}$$

$$(1.9) \quad D_{ij} = M_{ij} - M_{ISO} \delta_{ij}$$

Similar analyses to the one contained in this thesis have been completed for a 253 pound chemical explosion (Stump 1987) and three nuclear explosions (Stump and Johnson (1984)). The depth and observational ranges of the test reported in this study are a scaled version of the 253 lb test.

This work is presented in four primary sections: (1) Observational Data: Description of the data includes general observations of amplitude decay with range, development of surface waves with range and a summary of the velocity and attenuation model of the test site. (2) Synthetic Data: The propagation contribution is modeled with theoretical Green's functions and checked by convolution with a Mueller-Murphy source to produce synthetic seismograms in a series of forward models. (3) Inversions: Generalized linear

inversions are first done with synthetic seismograms to verify the inversion code and replicate experimental conditions. The observed seismograms are then inverted for the moment tensor representing isotropic and deviatoric components of the source. Several different inversions were completed to investigate the effects of station distribution and dependency on the Green's functions. (4) The conclusions are presented in terms of the physical models for contained sources. The analysis and comparisons focus on the isotropic peak time amplitude and the long-period level of the frequency spectrum.

## CHAPTER 2

### OBSERVED DATA SET

The data consist of near-source observations recorded on triaxial accelerometers for seven 5 lb ( $2.5 \times 10^{-6}$  kt) chemical shots in dry alluvium. Explosive yield, explosive type and test medium are held constant, the only variations being source burial depth and station distribution. In addition to the explosive tests, refraction surveys have been completed to constrain the velocity structure of the test site. Experimental data are summarized in table 1.

#### A. Explosion Data

##### 1. Experimental Layout

Two series of tests were designed specifically to constrain source symmetry and to quantify containment. The Array Test Series (ART) with a source burial depth of 1 meter resulted in uncontained shots. Three of the ART arrays were in a circular pattern with 6 stations distributed at a single range (10, 20 and 30 meters) for each test. The ART Line Test consisted of 11 stations distributed at 5 meter intervals a single azimuth between 10 and 60 meters. ART test configurations are illustrated in Figure 2.1. Data in the Contained Array Test Series (CART) were generated by

TABLE 1  
SUMMARY OF OBSERVATIONAL DATA

Components Recorded at each station	Range (meters)	Array Type	Number Stations
-------------------------------------	----------------	------------	-----------------

ART: 5 lbs. TNT at 1 meter depth

ART 1:	3	10	circular	6
ART 2:	3	20	circular	6
ART 3:	3	30	circular	6
ART LINE TEST:	3	10-60	linear	11

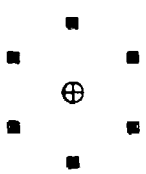
CART: 5 lbs. TNT at 3 meters depth

CART 1:	3	13.5-40.6	azimuthal	7
CART 2:	3	5-13.5	azimuthal	7
CART 3:	3	5-40.6	linear	6

Refraction Surveys: Betsy Seisqun™ source at 1 meter

1-m spacing EW	vertical	1.0-72.0	linear	24
1.5-m spacing NS	vertical	1.5-36.5	linear	24
7.6-m spacing EW	vertical	5.0-183.0	linear	24

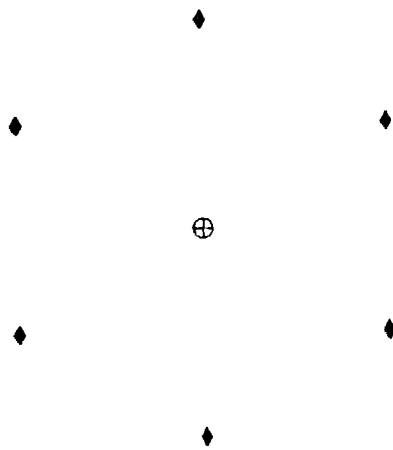
ART1



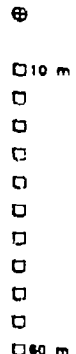
ART2



ART3



ART LINE



⊕ SHOT LOCATION  
■ RECEIVER AT 10 m  
★ RECEIVER AT 20 m  
◆ RECEIVER AT 30 m

↑ e' NORTH

Figure 2.1. Array configuration of the four tests in the ART series. Shot depth is 1 meter below the surface.

three fully contained explosions with a source burial depth of 3 meters below the surface. CART arrays are shown in Figure 2.2. CART data includes two arrays in which 7 stations were distributed at various azimuths and one linear array of 6 stations along a single azimuth. CART observational ranges are between 5 and 40.6 meters.

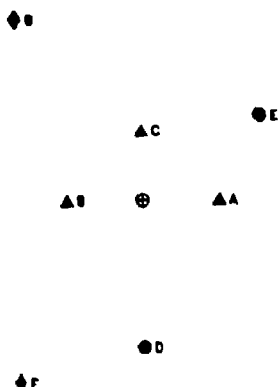
Instrumentation for all tests is identical. Force balance accelerometers were buried below the surface and digital data were recorded in the field with a sample rate of 200 samples/second. A 5 pole anti-alias filter with cutoff at 70 Hz was applied before recording. A total of 147 channels of explosion data were recorded.

## 2. Data Corrections: Acceleration to Velocity

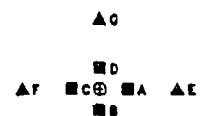
Inversions of the ART/CART data set utilize velocity records. In obtaining velocity from the raw field data, several steps were necessary. First the data were deglitched and rescaled. Next each channel was integrated to yield velocity waveforms. After integration two corrections were applied; slope removal and a high-pass filter. Additionally, all corrected velocity records have been integrated a second time to displacement so time domain displacement amplitudes could be estimated. No further corrections were necessary after integration to displacement because the displacement waveforms did not exhibit a step or ramp.

The data corrections are explained and illustrated in Appendix A. Additionally Appendix A documents different

CART1



CART2



CART3

⊕  
■ A  
+ B  
▲ C  
× D  
● E  
◆ F

⊕ SHOT LOCATION  
■ 5.0 m  
+ 9.7 m  
▲ 13.5 m  
× 20.3 m  
● 27.0 m  
◆ 40.6 m

10° NORTH

Figure 2.2. Array configuration of the three tests in the CART series. Shot depth is 3.0 meters below the surface.

types of slope corrections that have been applied to the CART data and justifies the design of the high-pass filter.

As a result of tests outlined in Appendix A, the frequency band of usable data has been quantified as 5 - 60 Hz. The long period cut off is determined by the 2-pole high pass Butterworth filter with corner 3 dB down at 3.5 Hz. At the short periods, the cut-off is determined by the anti-alias filter; 5-pole at 70 Hz applied before recording. Thus interpretation of results outside this frequency band will be pursued with caution. Details about this bandwidth are given in Appendix A.

### 3. Data Characteristics

The complete explosion data set is presented in Appendix B. The data are, by design, simple in character; the explosion is the simplest source; the test bed is not complex; and travel paths are short and therefore simplified. The following sections list important characteristics of the data.

#### a) Simple Waveforms at Close Ranges

As an example of the simple waveforms at close ranges, the vertical and radial components of velocity at the 5, 9.7 and 13.5 meter ranges of CART 3 are illustrated in Figure 2.3. The particle motion diagrams shown at the right of the figure are the plot of radial versus vertical amplitude. At these close ranges radial and vertical waveforms are dominated by

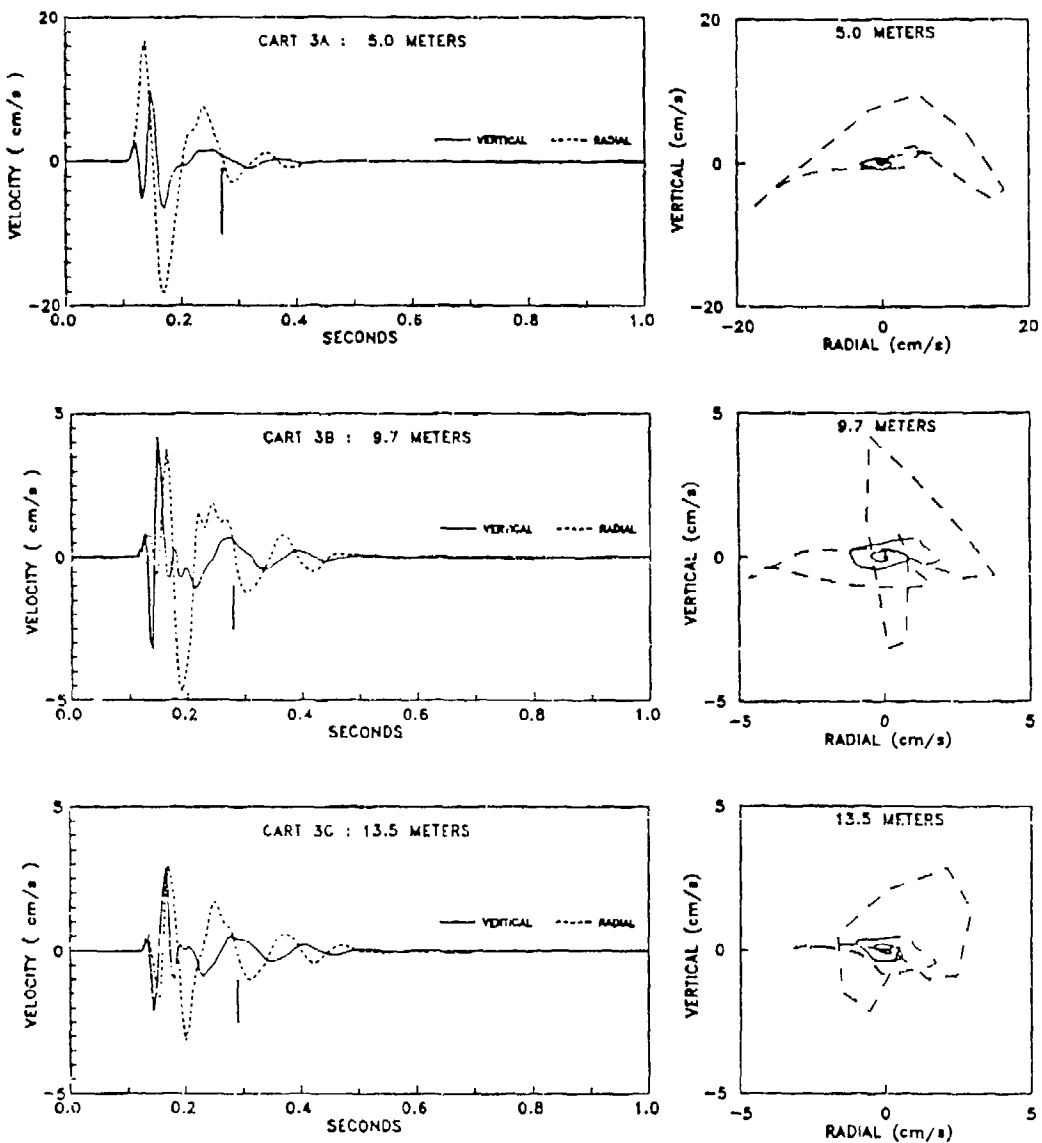


Figure 2.3. Particle motion plots from CART 3 linear array. On the left are the radial and vertical time series and on the right are the particle motion in the vertical-radial plane. The vertical line between .2 and .4 seconds indicates the picks for Rayleigh wave arrival.

one cycle. This arrival is the P-wave energy package identifiable by linear particle motions. The surface waves, associated with elliptical retrograde particle motion have only 20 - 30 % of the amplitude of the body wave at these close ranges. At 5 meters the signal duration is typically .25 - .4 seconds increasing to .4-.65 seconds at 13.5 meters with little development of surface waves.

b) Development of Surface Waves with Range

The signals recorded at 20.3, 27 and 40.6 meters are shown in Figure 2.4. The waveforms become more complex with increasing range as shear and surface wave energy arrives. Two particle motion windows separate the early P-wave energy (dashed line) from the later SV-Rayleigh energy (solid line). The Sv and Rayleigh energy packages are difficult to separate because there is not sufficient dispersion at these ranges. At the onset of the Sv-Rayleigh package the radial and vertical components are about 90 degrees phase shifted from each other resulting in the elliptical particle motion. There is an increase in signal duration associated with the longer travel paths. At the 20 - 27 meter range signal duration has increased to 1 second. Beyond 30 meters the surface wave amplitudes are relatively equal to or greater than the body wave amplitudes.

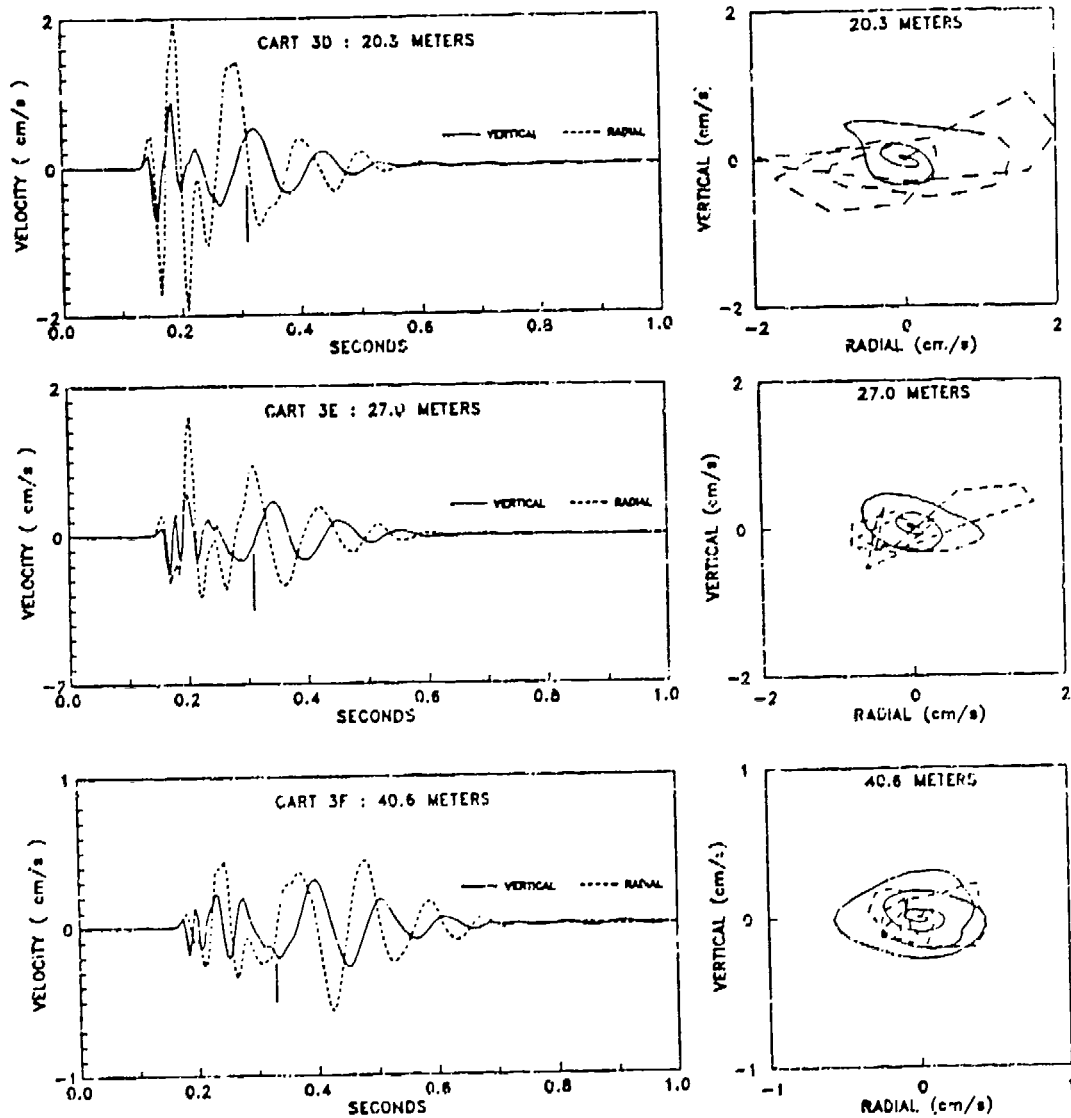


Figure 2.4. Particle motion plots from CART 3 linear array. On the left are the radial and vertical time series and on the right are the particle motion in the vertical-radial plane. The vertical line between .2 and .4 seconds indicates the picks for Rayleigh wave arrival.

### c) Azimuthal Symmetry of Waveforms

As observations are compared azimuthally, radials and verticals appear very similar in shape while the transverse do not show such similarities. As an illustration, the ART 3 observed velocities are shown in Figures 2.5a-c. The surface wave at about .2 seconds can be seen on the radials and verticals at this range. ART 3 peak radial amplitudes average 1 cm/s with a maximum of 30% variation. The ART 3 peak vertical amplitudes average 0.5 cm/s with only 17% variation. The amplitude of the radial component is twice the vertical at this range. ART 3 peak transverse amplitudes average .22 cm/s and vary as much as 81%. The transverse components appear dissimilar especially in terms of when the energy arrives in time.

It is worth noting that the above similarities in radial and vertical components apply to the lower frequencies which dominate the time series. Reinke and Stump (1988) have studied similar waveforms from the same test site and report incoherence in the data above 35 Hz.

### d) Amplitudes with Range

This section will quantify the ART/CART amplitude decay with distance. For competent rock at distances where the medium is responding elastically, the body wave amplitude is expected to decay due to geometrical spreading at a rate inversely proportional to distance. When attenuation is taken into account the decay rate is higher.

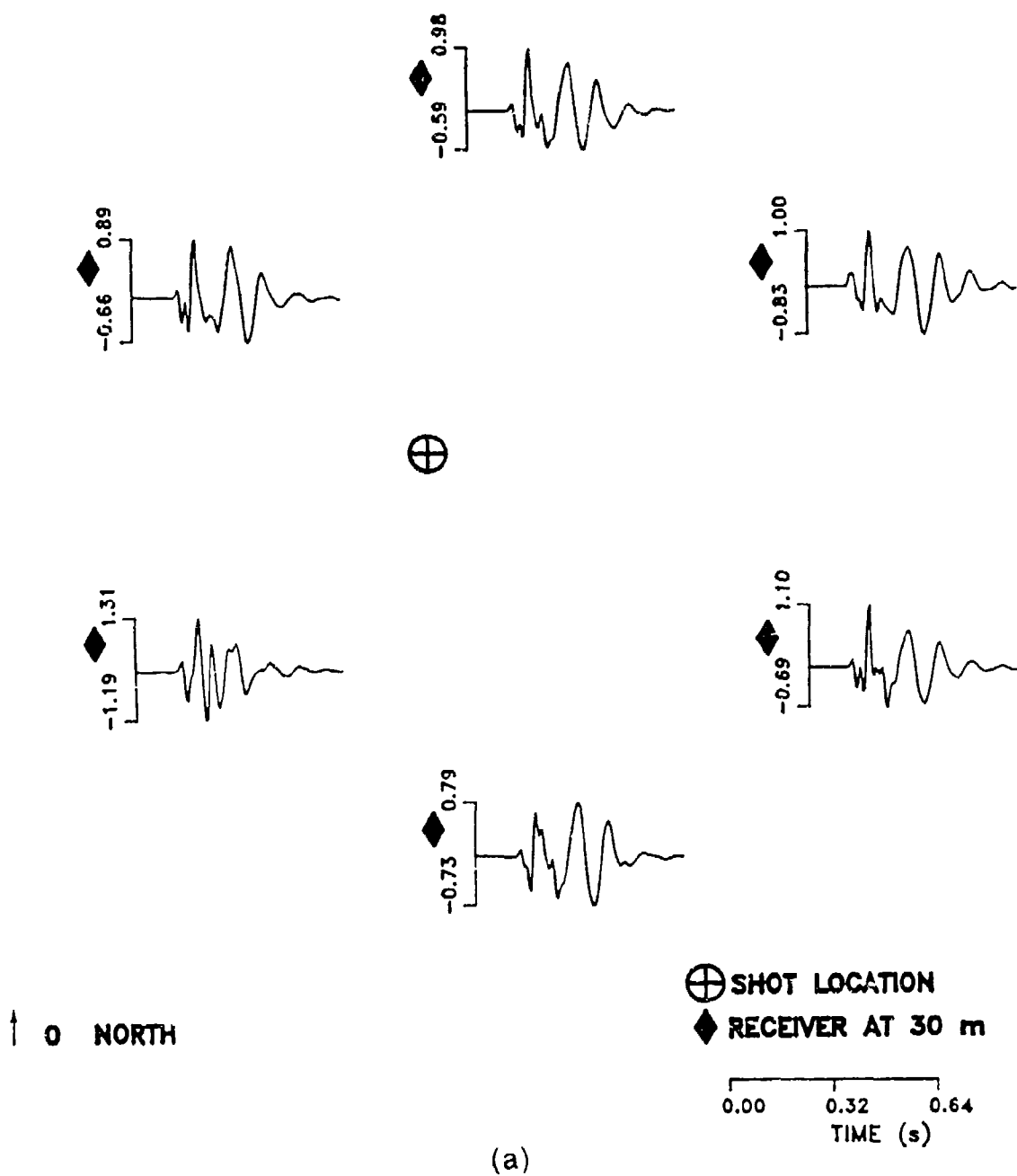


Figure 2.5. ART velocity records at 30 meters. (a) radial  
(b) transverse (c) vertical

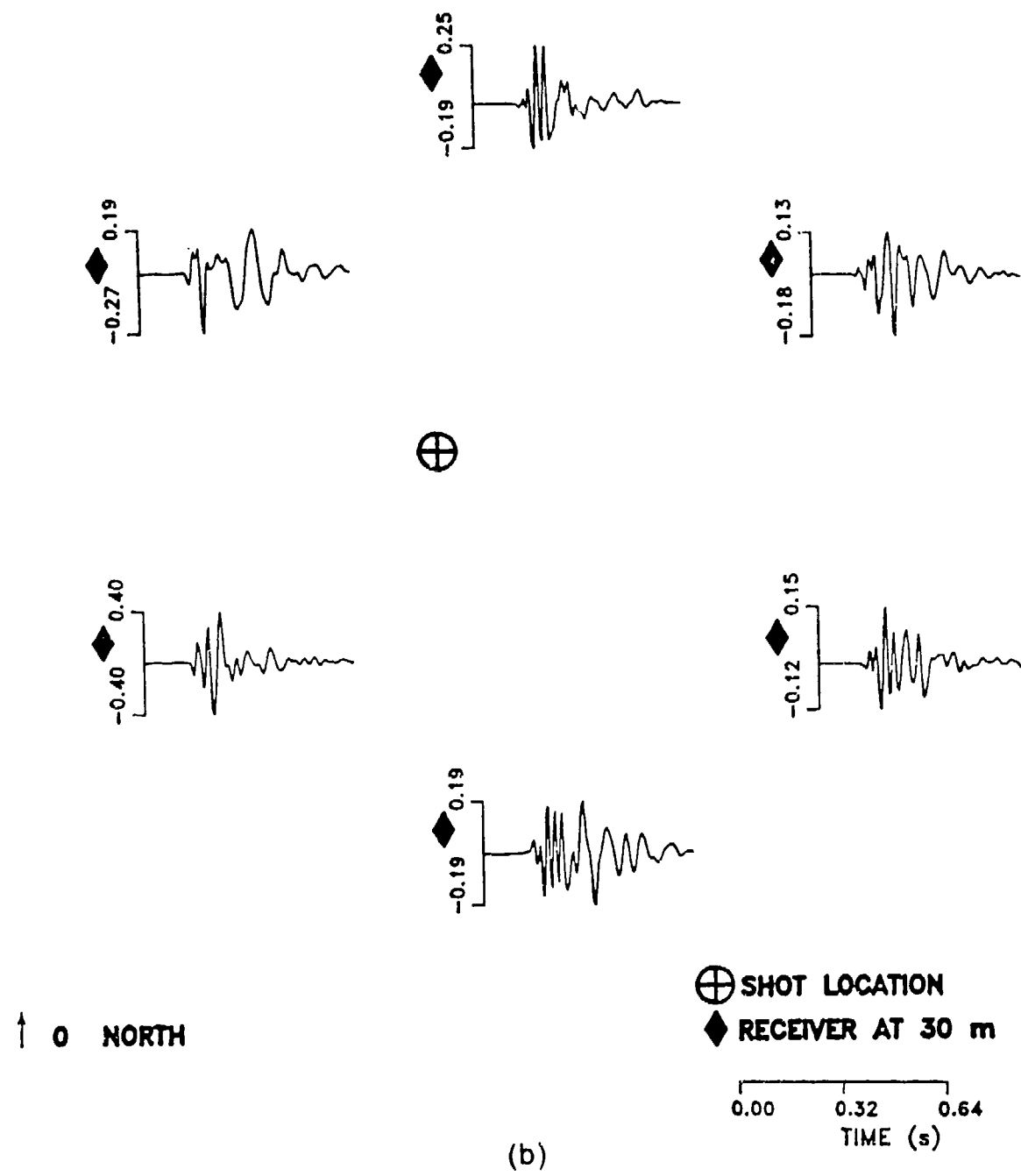


Figure 2.5 Continued.

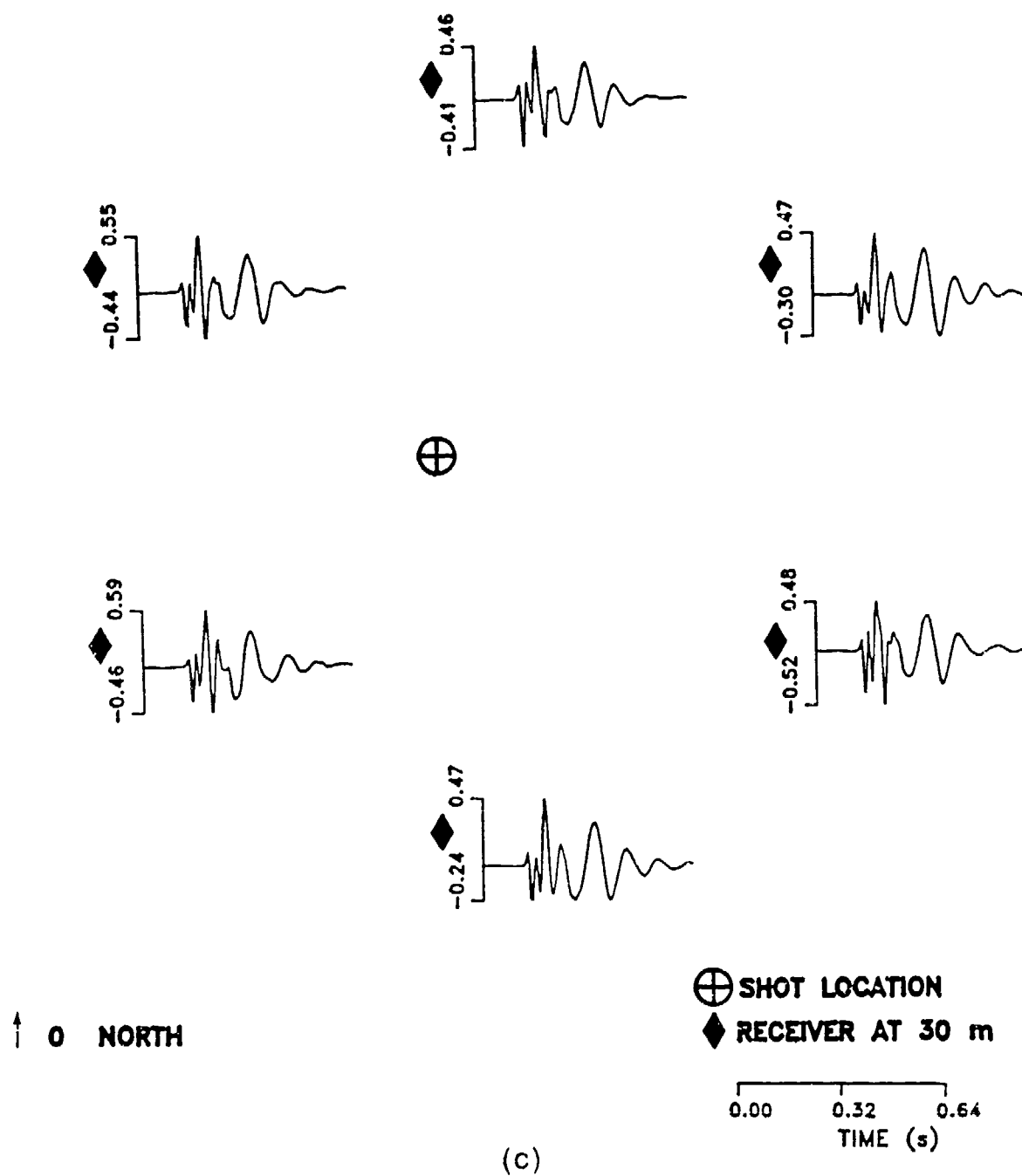


Figure 2.5 Continued.

Perret and Bass (1975) studied amplitude decay rates of measurements from 60 underground nuclear explosions ranging in yield from 67 kt to 2.5 kt (compared with  $2.5 \times 10^{-6}$  kt for ART/CART). Instruments were typically fielded along a horizontal radius at shot depth. The data were compiled from published reports and include all known tests up until the time of the report. Eight of these explosions were detonated in dry alluvium at burial depths between 300 and 500 meters (compared with 1 and 3 meters for ART and CART). One of the eight alluvial events was under-buried for partial containment.

Perret et.al. compiled plots of peak vertical particle velocity versus scaled range and fit linear trends of the form

$$(2.1) \quad U = U_0 \left( \frac{r}{W^{1/3}} \right)^{-n}$$

where  $U_0$  is the amplitude,  $r$  is the distance between source and receiver in meters (scaled by  $kt^{1/3}$ ),  $W$  is the energy yield in equivalent kilotons of TNT and  $n$  is the power exponent describing the decay rate.

Data corresponding to measurements in dry alluvium showed much faster decay rates than those for dry tuff, wet tuff or hard rock. Two distinct trends were identified for dry alluvium. Between 30 and  $150 \text{ m}/kt^{1/3}$ , the best fit line

$$(2.2) \quad U_1 = 1.52 \times 10^6 \left( \frac{r}{W^{1/3}} \right)^{-3.27}$$

was found. Between 100 and 350 m/kt<sup>1/3</sup> the amplitudes were observed to decay slower according to the best fit line

$$(2.3) \quad U_2 = 3.68 \times 10^1 \left( \frac{r}{W^{1/3}} \right)^{-1.16}$$

Perret and Bass attribute the two different attenuation rates to regions of non-linear and linear material response. Because dry alluvium has stronger attenuation properties than other media the crossover to a decay rate close to the inverse first power (Equation 2.3) is observed within the span of observational ranges. This crossover was not observed for the other media types studied by Perret and Bass. Thus at scaled ranges greater than 150 m/kt<sup>1/3</sup> the alluvium response is classified as linear.

ART/CART peak vertical and radial velocity as a function of scaled range is plotted in Figure 2.6. The closest observation, 5 m, corresponds to a scaled range of 368.4 m/kt<sup>1/3</sup> and the most distant observation, 60 m, to a scaled range of 4420.8 m/kt<sup>1/3</sup>.

The line fitting the ART/CART vertical trend in Figure 2.6a is given as

$$(2.4) \quad U_v = 1 \times 10^{5.17} \left( \frac{r}{W^{1/3}} \right)^{-1.67}$$

Similar analysis of the radial component in Figure 2.6b gives,

$$(2.5) \quad U_r = 1 \times 10^{4.94} \left( \frac{r}{W^{1/3}} \right)^{-1.48}$$

The exponent, -1.48, falls within the range reported by Perret et. al.

The transverse peak amplitudes are plotted in Figure 2.9. Here the amplitudes are smaller and the scatter in the amplitude is much greater.

Considering the differences in yield and depth of burial of the ART/CART data compared to the Perret and Bass data, the amplitude decay trends for alluvium compare favorably (Equation 2.3). The ART/CART trend has a larger amplitude and a faster decay rate. The larger amplitudes occur because the material, being much closer to the surface, has slower velocities and the faster decay rate because the material, being much closer to the surface is less consolidated and thus more attenuative. These comparisons have not accounted for the factor of 2 amplitude often introduced between chemical and nuclear explosions. Nor have these comparisons accounted for the amplitude effects of the free surface.

Perret and Bass also fit linear trends to acceleration and displacement records. Figures 2.7 and 2.8 illustrate the amplitude decay of the ART/CART acceleration and displacement observations. The ART/CART trends are summarized in table 2.

TABLE 2  
APMLITUDE DECAY EXPONENTS

	Vertical	Radial
<u>Acceleration</u>		
ART	-1.79	-1.37
CART	-1.89	-1.29
ALL	-1.88	-1.32
<u>Velocity</u>		
ART	-1.54	-1.63
CART	-1.87	-1.56
All	-1.75	-1.56
<u>Displacement</u>		
ART	-1.12	-1.70
CART	-1.70	-1.85
ALL	-1.57	-1.81

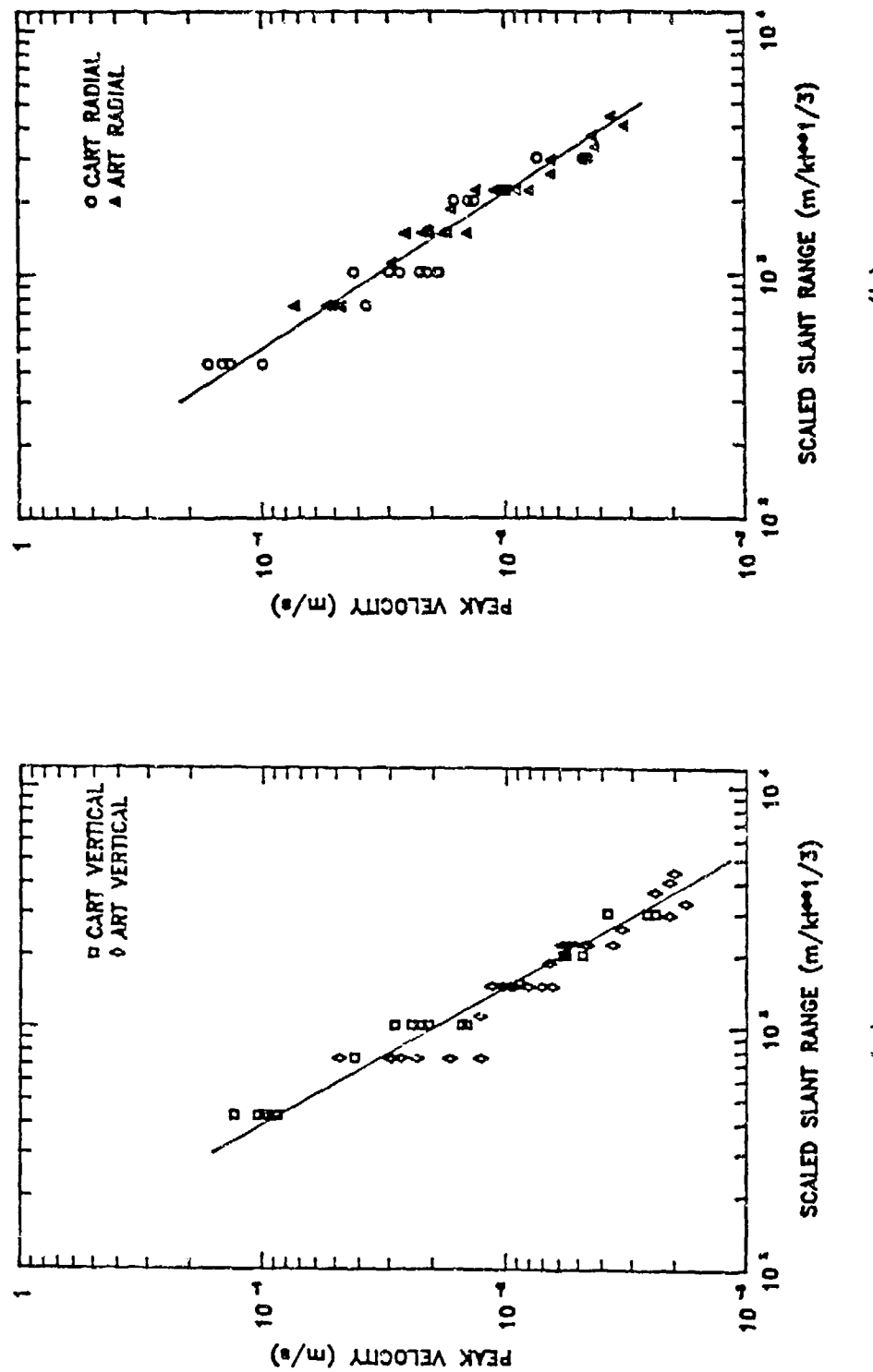


Figure 2.6. Peak velocity versus scaled slant range. (a) vertical (b) radial

(b)

(a)

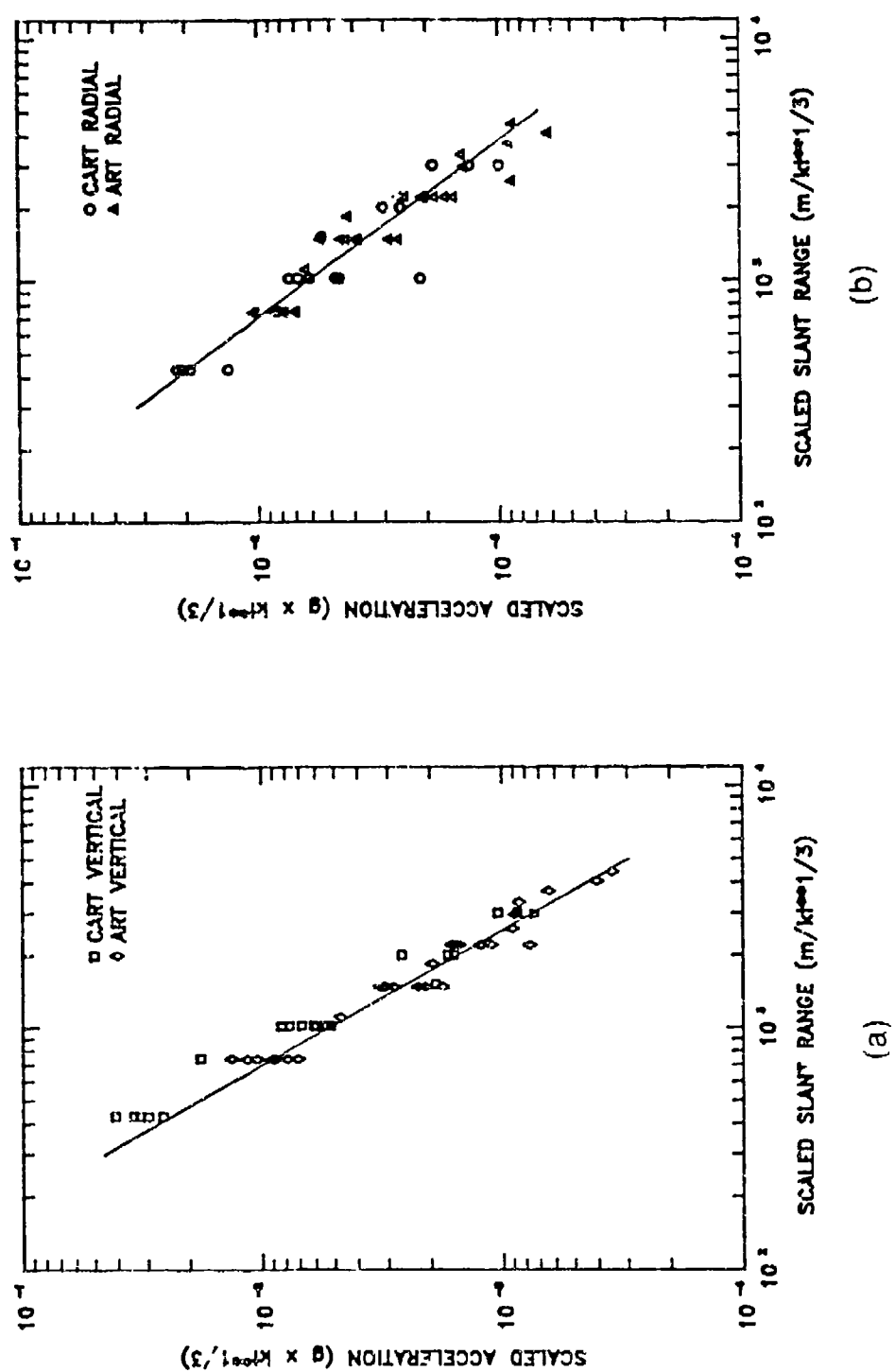


Figure 2.7. Scaled acceleration versus scaled slant range. (a) vertical (b) radial

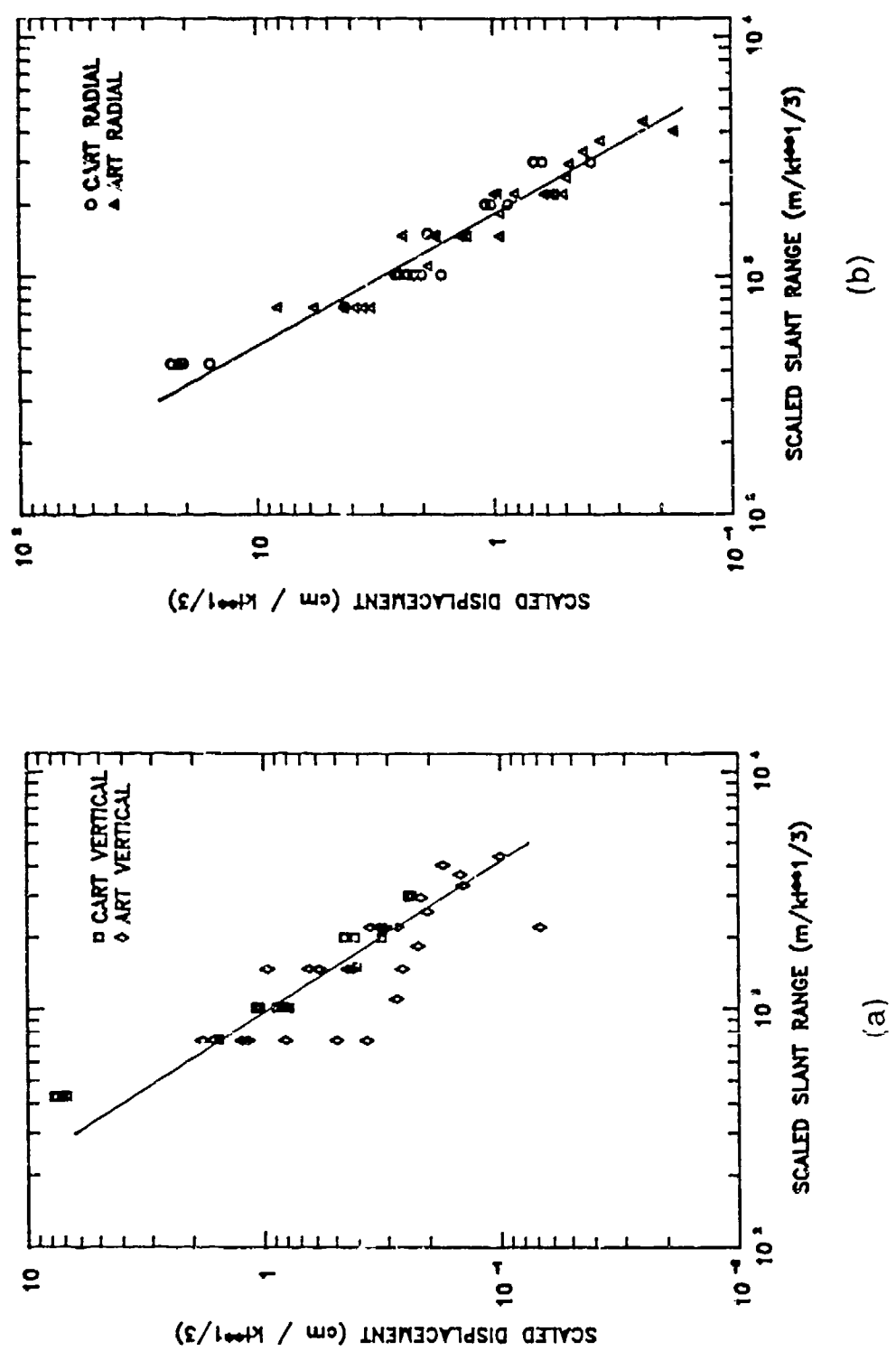


Figure 2.8. Scaled peak displacement versus scaled slant range. (a) vertical (b) radial

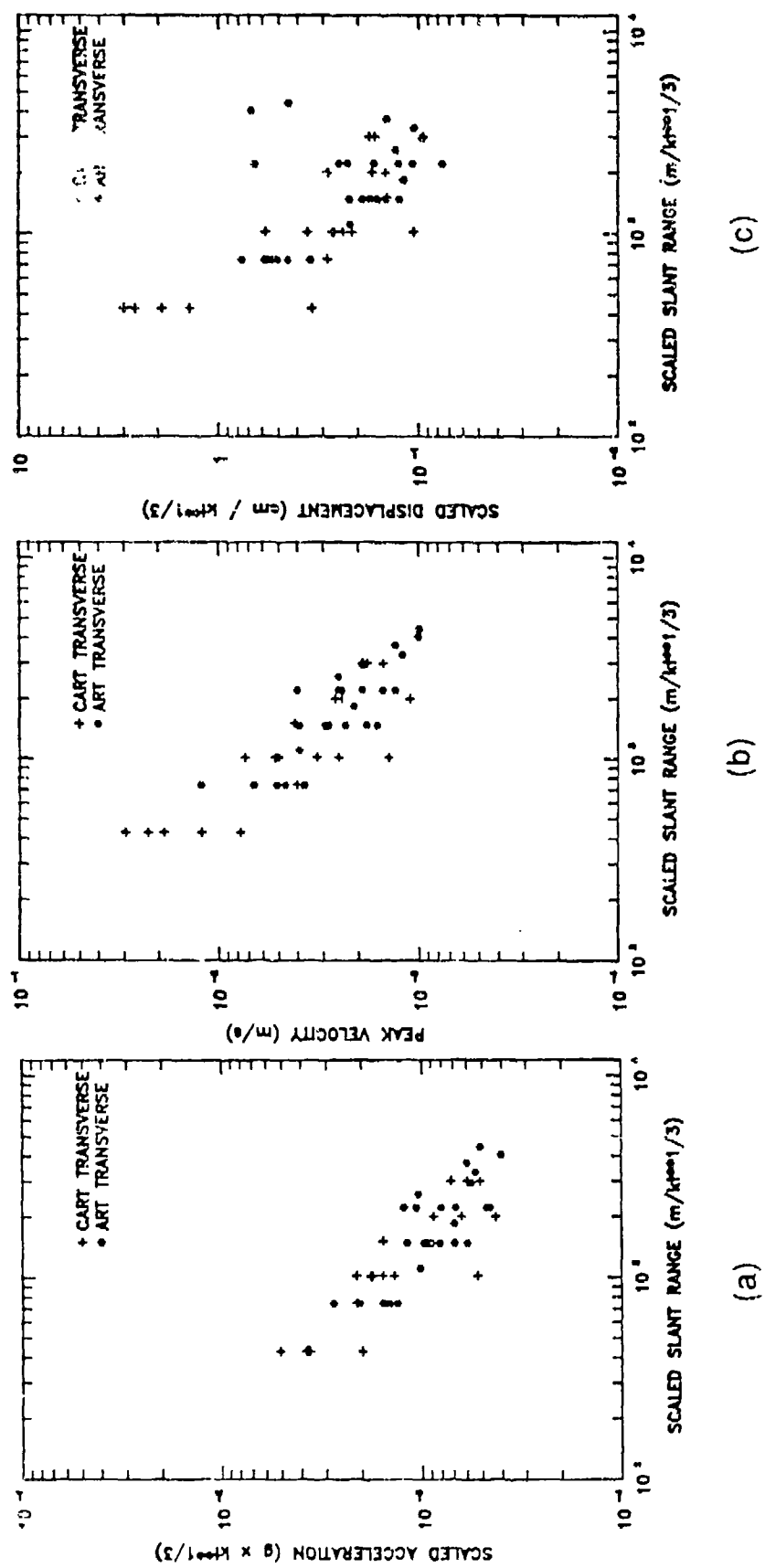


Figure 2.9. Peak transverse amplitudes versus scaled slant range. (a) acceleration  
(b) velocity (c) displacement

### B. Site Characterization Data

The ART/CART experimental test site is part of McCormick Ranch near Albuquerque, N.M., chosen in part because of the available site characterization data. The site is on an old playa composed of plane layered dry alluvium with the water table at a depth of 75 meters. Caliche is present on the test site and has been exposed by several of the test shots. Trenching at the site confirms geometry of the caliche to be discontinuous stringers within the upper few meters of the test bed. The significance of these inhomogeneities is in their ability to scatter waves.

The velocity model for the ART test site is based on previous models by Stump and Reinke (1982) with modifications resulting from additional refraction surveys and analysis of three-component waveforms recorded in the ART Line Test. The current model is two layers over a half-space as shown in table 3. For comparison, the velocity model used by Stump and Reinke (1982) is also given in table 3. The following sections discuss the model components and their derivation.

#### 1. Refraction Surveys

Three refraction surveys were completed on the ART/CART test site on McCormick Ranch using a Betsy<sup>TM</sup> seisgun source. Figure 2.10 shows the acquisition geometry. Two East-West lines run through the ART test area; one with 7.6 meter

TABLE 3  
MCCORMICK RANCH SITE MODEL

	$\alpha$ (m/s)	$\beta$ (m/s)	$\rho$ (gm/cm <sup>3</sup> )	$Q\alpha$	$Q\beta$	Depth (m)	$\sigma$
<u>Grant Model 1988</u>							
Layer 1:	270	120	1.8	10	4	0.0	.38
Layer 2:	670	230	1.9	50	22	3.0	.43
Half Space:	930	360	2.0	100	44	19.0	.41
<u>Stump-Reinke 1982 Model</u>							
Layer 1:	366	244	1.8			0.0	.10
Layer 2:	671	366	1.9			3.4	.29
Layer 3:	823	366	2.0			13.4	.38
Half Space:	1128	610	2.1			24.0	.29

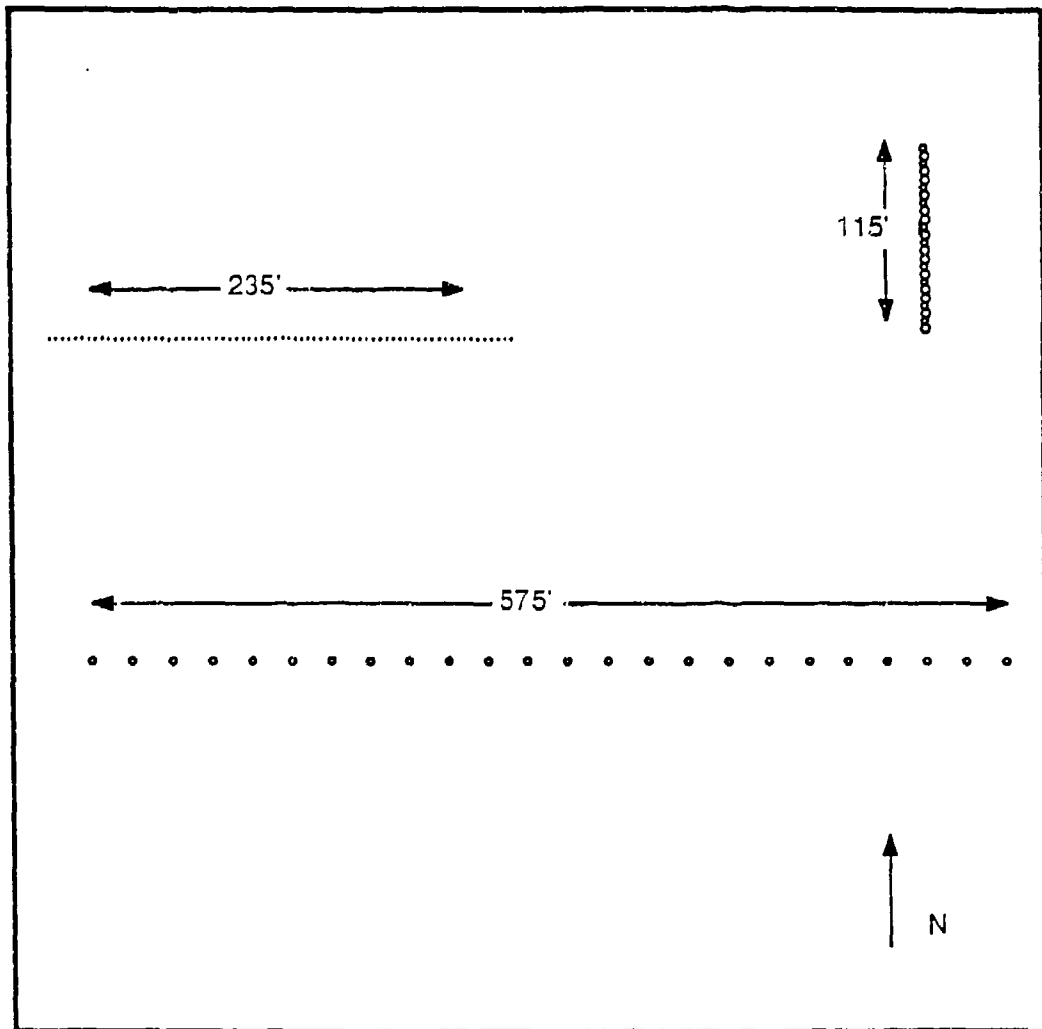


Figure 2.10. Three refraction surveys over the ART/CART test site. The line illustrated at upper left contains 72 receivers at 1 meter spacing for a total length of 235'; upper right: 24 receivers at 5' spacing for a total length of 115'; bottom: 24 receivers at 25' spacing for a total length of 575'.

geophone spacing for a total length of 575' (187 meters) and the other with a 1 meter geophone interval for a total length of 235' (72 meters). The third line runs North-South over the CART test area which is about 50 meters to the northwest of the ART test area. This line is 115' (36.5 meters) in length with a 1.5 meter geophone spacing.

Travel time curves for the long and short East-West lines are plotted together in Figure 2.11. The large symbols represent the travel times of the long line and the smaller symbols represent the travel times of the short line. While the short line with closer receiver spacing affords more detailed interpretation than is possible for the long line, the slopes of the two profiles closely agree. The long line is thus used for a gross model and the short line for details of the upper few meters.

Interpretation of the long line is as follows: two distinct branches on the travel time curves correspond to a slow velocity between 650 and 659 m/s and a fast velocity of 931-958 m/s. The crossover distance at 99 meters suggests the velocity increase is at a depth of 19-20 meters. The symmetry of the forward and reverse profiles confirms a plane layered model. In summary, the interpretation of the long line is a layer over a half-space.

Interpretation of the short line is facilitated by Figure 2.12. The forward and reverse profiles are plotted in the same direction to emphasize the similarities and differences. The travel time curves agree well except at

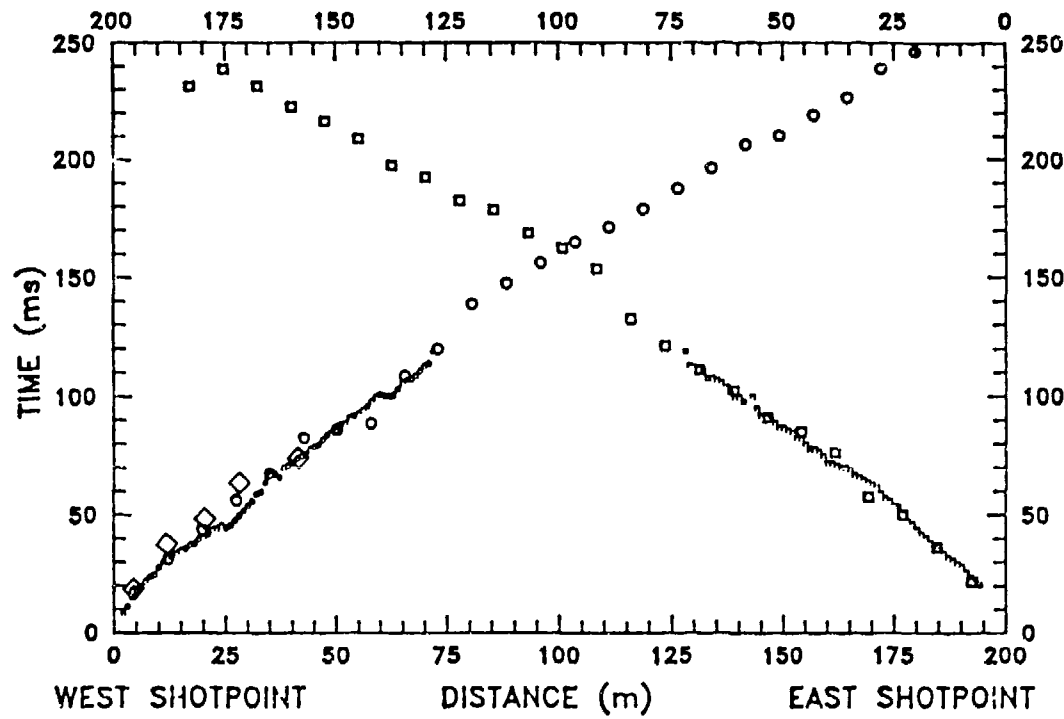


Figure 2.11 ART/CART refraction profiles. The forward and reverse times for both the long and short lines are plotted. Detail of the short line is shown in Figure 2.12. Large symbols denote first arrival times picked from CART explosion data at 5, 13.5, 20.3, 27.0 and 40.6 meters.

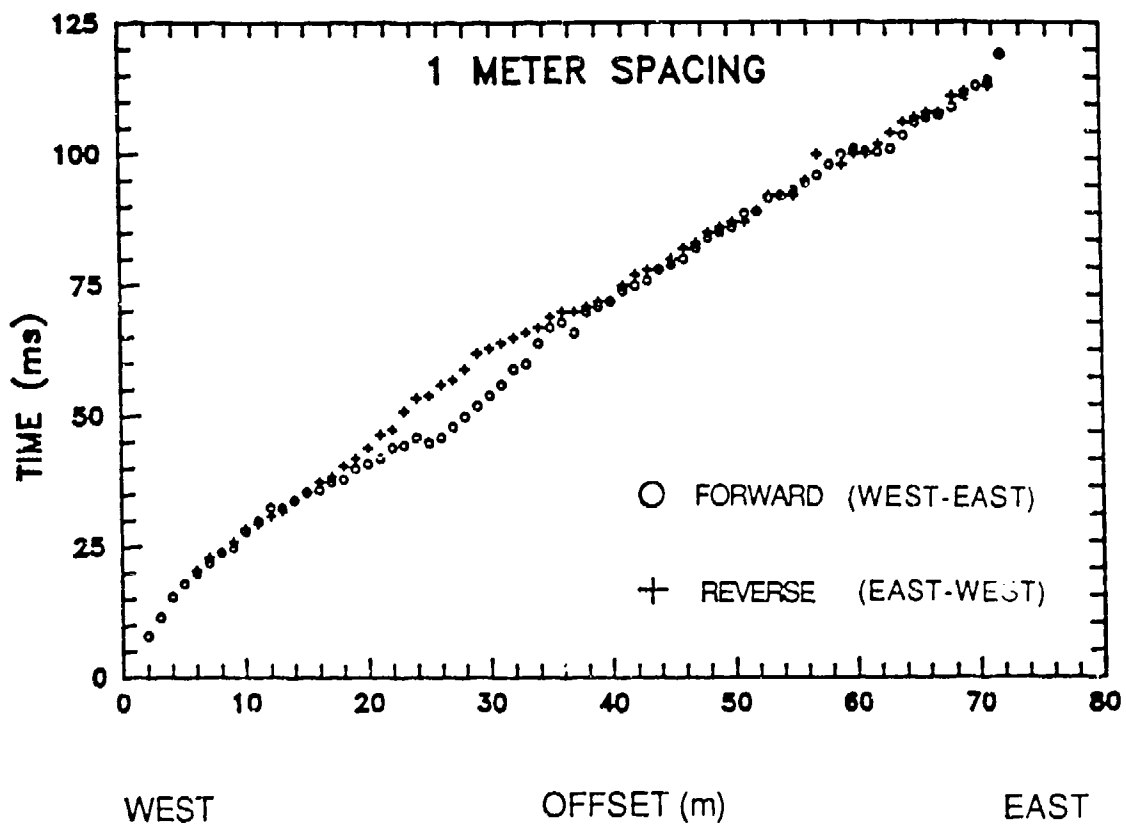


Figure 2.12 ART/CART refraction profiles. The forward and reverse times from 1-meter spacing line are plotted in the same direction. Travel times match between 0-20 meters and between 40-65 meters.

offsets from 18 to 38 meters. Two possibilities exist: either the times on the forward line are early in the 18-38 meter range or the reverse times are late. Referring back to Figure 2.11, the former assumption is made. The receivers at offset distances between 18 and 38 meters from the forward shot are affected by a subsurface structure that results in anomalously early travel times on the forward travel time curve. Following this reasoning three branches were drawn on the reverse travel time curve for the initial interpretation. Layer one velocity is 277 m/s with a thickness of 2.0 meters. Layer two velocity is 544 m/s with a thickness of 2.8 meters. The third layer begins at 4.8 meters and has a velocity of 782 m/s. The short line interpretation consists of velocity increases at 2.0 meters and 4.8 meters while the long line interpretation shows a velocity increase of 1. at 19-20 meters depth.

To merge the information from the long and short lines, the slowest velocity of 277 m/s is assigned to the uppermost layer. The velocity increase from 544 to 782 m/s at 4.8 meters is taken as an average velocity to match the 671 m/s value of the 20 meter thick layer in the long line interpretation.

The north-south line through the CART test area indicates velocities and depths consistent with the above interpretations. The exception is that the top layer appears to be more shallow and slower than indicated by the short east-west line.

To summarize, the current velocity model is 2 layers over a half-space and is compared to the 1982 Stump-Reinke model in table 3. The velocities of the layers have been rounded down and the thickness of the upper layer has been increased to 3.0 meters. Derivation of the shear velocities is discussed in Section 2.B.3. The high Poisson's ratios are consistent with measurements of P and S travel time as shown in table 6 and discussed in Section 3.C.1.

## 2. First Arrivals

Of the 20 CART observations, the precise shot times were recorded on the seismograms for only 8 stations. These stations do cover the range of CART observations (5.0 - 40.6 meters) and there are multiple observations because of the overlap of station locations. The arrival times of the first breaks on the vertical component of the CART data have been plotted on the refraction profile to confirm the velocity interpretations in Figure 2.11. The agreement between CART arrival times and the refraction arrival times on the 1-m line is poorest at 27 meters within the range of the anomalous arrival times discussed above. The time difference between CART and the forward travel time is 16 ms and only 7 ms between CART and the reverse travel time. This is further confirmation that the 1 m forward line is anomalous and may be affected by an inhomogeneity. This inhomogeneity could be in the form of a caliche stringer.

### 3. Shear Velocities

While the P-velocities and layer thicknesses are straightforward calculations from the refraction surveys and first arrival data, the S-velocities are more difficult to constrain. One reason is that the close-in observations do not allow time for good separation between P and S energy. Previous studies on the test site by Stump and Reinke (1982) used cross-hole shear surveys to get a shear velocity of 366 m/s between 13.5 and 24 meters which will be used for the ART/CART half space shear velocity. Their surveys were less reliable above 13 meters due to scatter in the data. Section C.2 in Chapter 3 discusses the more realistic multi-layered model with the 366 m/s velocity in the halfspace.

Particle motion plots have been completed for the ART Line Test and used to estimate the layer shear velocities listed in table 3. The time of the change from rectilinear to retrograde motion was noted for each station from 10 to 60 meters. Also recorded was the ellipticity or the ratio between the radial and vertical axes of the particle motion of the Rayleigh wave as well as the period of the first full Rayleigh cycle.

Mooney and Bolt (1966) produced by numerical analysis curves detailing the relationship between Rayleigh wave dispersion and the medium parameters for a layer over a half space. They emphasized that the most important parameter is the ratio between shear velocities. One of their curves, reproduced in Figure 2.13 was used to constrain the shear

velocity in the most shallow layer. The ratio  $\beta_1 T/h$  is plotted along the x-axis and the ratio of horizontal to vertical amplitudes (ellipticity) is plotted along the y-axis. With a layer thickness (h) of 3 meters from the refraction profiles, Rayleigh period (T) of .105 seconds at 55 meters, ellipticity of 2.05 from the particle motion plots and half-space shear velocity of 360 m/s the Mooney and Bolt curve suggests the shear velocity ratio is 3. Thus with a reliable measurement of the half space shear velocity of 360 m/s, the upper layer velocity is estimated at 120 m/s. Layer 2 shear velocity is estimated at 230 m/s. This value was chosen because it is intermediate between 120 m/s and 360m/s and because it was used by Stump and Reinke (1982) for their most shallow layer. This estimation of the shear velocities is only a first approximation. Further analysis would include a complete dispersion analysis and possibly structure inversion.

#### 4. Q in Dry Alluvium

Q estimates are included in the site model to account for seismic attenuation due to absorption and scattering. The ART/CART test medium is low velocity, low density and low Q resulting in rapid absorption of seismic energy with wave propagation. As quantified by the amplitude decay plots in Figures 2.6-2.8, the observed exponent describing decay rate for spherical waves was larger than expected based on the results of Perret and Bass (1975). No corrections have been

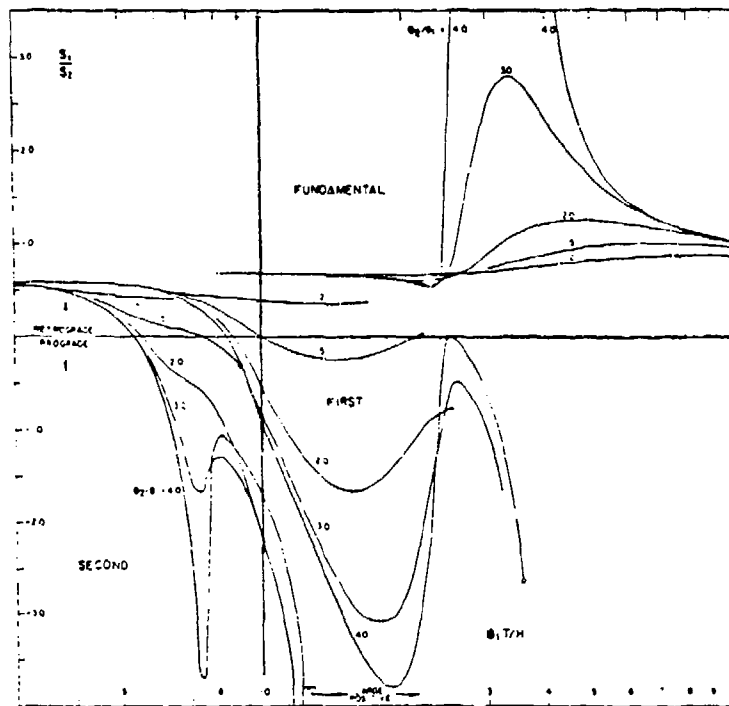


Figure 2.13. Amplitude ratio versus shear velocity ratio.  
(From Mooney and Bolt, 1966).

made for differences between chemical and nuclear explosives or for free surface effects.

Standard measurements of Q are impractical in low-Q environments. Anderson (1988) has addressed this problem in measuring Q for unconsolidated backfills. Using standard refraction equipment, he made base measurements taken close to the (sledge hammer) source to quantify the change in pulse shape with distance. Anderson focused on the first cycle of the P-waves for which propagation distances are between 3 and 10 meters. He reports average Q values between 7.5 and 10.

A value of  $Q_a$  for the first layer of ART/CART site model is appropriately low at 10. Based on synthetic tests of modeling observational waveforms, Q increases with depth. Modeling exercises also showed that the estimates of Q for Layer 2 and the half space do not strongly affect the synthetics.  $Q_a$  in the second and third layers is 50 and 100 respectively.  $Q_b$  for the ART/CART site model is assigned a value of 40%  $Q_a$  in Layer 1 and 44%  $Q_a$  layer 2 and the Half-space.

## CHAPTER 3

### FORWARD SYNTHETIC CALCULATIONS

#### A. Introduction

In the previous chapter observational refraction and explosion velocity data were analyzed for geophysical parameters of the test site. Velocities, layer thicknesses and attenuation factors define the McCormick Ranch site model listed in table 3. In the current chapter these parameters are used to predict the velocity response of the test site to a 5 lb. charge representing the combined CART source.

The general approach to building the synthetic velocity,  $U_S$ , is the representation theorem abbreviated

$$(3.1) \quad U_S(\omega) = S(\omega)G(\omega)$$

where seismograms are calculated in the frequency domain as a product of the source function  $S(\omega)$  and the Green's functions  $G(\omega)$  representing the path effects. Both  $S(\omega)$  and  $G(\omega)$  will be tested. Equations 4.4 and 4.5 which are discussed in the next chapter are a more precise representation of the way the synthetics are calculated.

The Mueller-Murphy (1971) characterization of the synthetic source was chosen because it provides a physical basis for incorporating depth effects and variations in

material constants. Their model predicts the far-field reduced displacement potential (RDP) for yield,  $w$ , at a depth,  $h$ , in a test medium with specified density and velocities. A range of  $S(\omega)$  are possible given the uncertainty of the McCormick Ranch site model specifically the shear velocity at the source burial depth of 3 meters.

Path models are calculated first for a simple half space and then for a layered half space structure. Results are presented as a suite of forward models derived by combining the range of source functions with the range of path functions. Comparisons are then possible between synthetic and observed waveforms and any differences are attributed to a deficiency in the theoretical source or path model.

This forward modeling exercise serves several purposes. First, a preliminary investigation of a range of source functions provides a basis for comparison of the isotropic moment to be calculated in the next chapter. A catalog of Mueller-Murphy theoretical source function changes with material constants will allow better interpretation of the inverted source function and quantify the resolvability of the model with this data set.

Secondly the trade-offs between  $S(\omega)$  and  $G(\omega)$  are addressed.  $G(\omega)$  are not known exactly but are approximated and any errors in  $G(f)$  map into the inverted source functions,  $S_i(\omega)$ ,

$$(3.2) \quad S_i(\omega) = G(\omega)^{-1} U_C(\omega)$$

where  $G(\omega)^{-1}$  is the inverse of the Green's functions and  $U_o(\omega)$  are the observed seismograms. This equation will be discussed in the next chapter. The set of path models are utilized in a series of inversions in the next chapter to proceed with the quantification of how  $S_i(\omega)$  is affected by errors in  $G(\omega)$ .

A third application of the synthetic seismograms calculated in this section is to use them in trial inversions. Several synthetic trials were designed to show the effects of noise in the waveforms and the effects of station distribution : the calculation of the inverted source.

#### D. Theoretical Source Function: RDP

The historical basis of the reduced displacement potential (RDP) as a suitable description of the isotropic component of the explosion seismic source function (ESSF) was reviewed in Chapter 1. Now the exact form of the Mueller-Murphy (1971) RDP is given in order to study the effect various parameters have on theoretical predictions. The Mueller-Murphy RDP is singled out here because it is the only source model that directly incorporates depth of burial effects and other physical parameters.

At distances much greater than the elastic radius,  $r_e$ , the far-field RDP is described in the frequency domain for an arbitrary pressure pulse acting at the elastic radius in an

isotropic homogeneous wholespace

$$(3.3) \quad \Psi(\omega) = \frac{r_{el}c^2}{4\mu} \frac{p(\omega)}{(\omega_0^2 - \beta'\omega^2 + i\omega_0\omega)}$$

where  $p(\omega)$  is the Fourier transform of the pressure pulse,  $p(t)$ ;  $c$  is compressional velocity;  $\omega_0 = c/r_{el}$  is characteristic frequency; and  $\beta' = (\lambda + 2\mu)/4\mu$  for Lame's constant,  $\lambda$ , and shear modulus,  $\mu$  (Equation 10, Mueller and Murphy, 1971).

Mueller and Murphy analyzed free-field observations at close ranges to several VNE's to propose the analytical description of the pressure time function

$$(3.4) \quad p(t) = (P_0 e^{-\alpha t} + P_{oc}) H(t)$$

illustrated in Figure 3.1.  $P_{oc}$  is the steady state pressure;  $P_o = P_{os} - P_{oc}$  is the magnitude of the pressure difference between peak pressure,  $P_o$  and steady state pressure,  $P_{oc}$ ;  $\alpha$  is the decay constant; and  $H(t)$  is the unit step function. Source overshoot is the ratio of the peak pressure to the step pressure

$$(3.5) \quad R = P_{os}/P_{oc}$$

and is greater for hard rock than for soft or porous rock. Source overshoot controls the peak in the source spectrum.

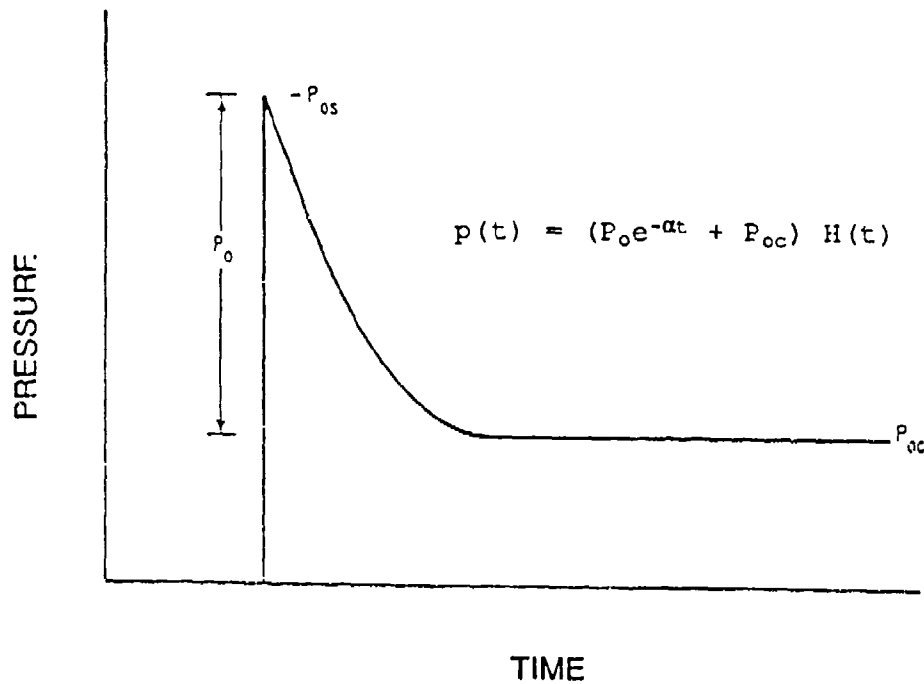


Figure 3.1. Pressure function used to calculate the reduced displacement potential.  $P_{oc}$  is steady state pressure,  $P_{os}$  is peak shock pressure and  $P_s = P_{os} - P_{oc}$ . (From Mueller and Murphy, 1971)

Note that von Seggern and Blanford (1972) defined source overshoot as the ratio of pressure amplitude to steady-state pressure ( $B = P_0/P_{oc}$ ).

Calculation of the theoretical RDP using Equation 3.3 requires an estimate of the pressure function in Equation 3.4. Mueller-Murphy developed the following scaling relations for parameters in Equation 3.4 in terms of the basic shot variables: yield,  $W$ , depth of burial,  $h$ , P-wave velocity, S-wave velocity and density.

Peak shock pressure,  $P_{os}$ , measured from close-in free-field data is in general slightly larger than the overburden pressure

$$(3.6) \quad P_{os} = 1.5\rho gh$$

for density,  $\rho$ , gravitational acceleration,  $g$ , and depth,  $h$ .

The relation for steady state pressure,  $P_{oc}$ , was derived by considering permanent displacement at the elastic radius. In an incompressible solid

$$(3.7) \quad P_{oc} = k_1 \frac{4}{3} \mu \left( \frac{r_e}{r_{el}} \right)^3$$

where a compaction factor,  $k_1$  ( $< 1.0$ ), is necessary to lower the step pressures to match observations of steady state pressures in porous (compressible) rocks (Equation 18, Mueller and Murphy, 1971).

The step pressure in Equation 3.7 depends on elastic radius and cavity radius which scale with yield and burial depth as follows:

$$(3.8) \quad r_{el} = k_2 \frac{W^{1/3}}{h^{.42}}$$

$$(3.9) \quad r_c = k_3 \frac{W^{.29}}{h^{.11}}$$

Cavity radius is smaller for competent rock in which there is little pore space to collapse as the cavity grows and is larger for porous material.

The decay constant,  $\alpha$ , of the pressure function is proportional to the theoretical corner frequency,  $\omega_o$ :

$$(3.10) \quad \alpha = k_4 \omega_o$$

The proportionality constants,  $k_i$ , in Equations 3.7 - 3.10 are medium dependent. Mueller-Murphy constants for the tuff-rhyolite of Pahute Mesa at NTS, the most intensely studied and modeled source medium, are  $k_1 = .4$ ,  $k_2 = 1490$ ,  $k_3 = 31.4$  and  $k_4 = 1.5$ . Mueller-Murphy also list some of the constants for granite, salt, shale and alluvium.

The CART yield and depth of burial are

$$(3.11) \quad W = 2.5 \times 10^{-6} \text{ kt}$$

(3.12)

$$h = 3.0 \text{ meters}$$

The UNEs studied by Mueller-Murphy were all buried at depths large enough to ensure containment. The normal scaled depth for containment,

(3.13)

$$SD = h / W^{1/3} \text{ m}$$

is  $122W^{1/3}$  m for  $h$  in meters and  $W$  in kilotons. The CART explosion is overburied at  $221W^{1/3}$  m while the ART explosion is underburied at  $74W^{1/3}$  m.

The above scaling relations (Equations 3.7 - 3.10) predict the shape of the RDP from basic shot parameters and medium parameters. Many realizations of Equation 3.3 were calculated to study the change in the RDP with changing parameters.

### 1. BASIC Model

In this section (3.B.1) the characteristics of the BASIC source model are discussed followed in Section 3.B.2 by a summary of depth effects on the BASIC model. Section 3.B.3 gives physical evidence for the parameters of the BASIC model along with two other models summarizing a realistic range of possible parameters for the ART/CART source.

The BASIC model used for the CART test site was first calculated for a scaled depth of  $122W^{1/3}$  m assuming a cavity radius of 0.64 m, elastic radius of 7.0 m, compressional

velocity of 366 m/s, shear velocity of 244 m/s and density of 1.9 gm/cm<sup>3</sup>. These parameters result in a source spectrum with a long period level of 0.035 m<sup>3</sup>, no overshoot ( $B=1.0$ ), and a theoretical corner frequency of 8.3 Hz.

Figure 3.2a-d illustrates the result of varying the following four parameters with respect to the BASIC RDP; (a) cavity radius, (b) elastic radius, (c) velocities (compressional and shear) and (d) Poisson's ratio (changing shear velocity only). The BASIC RDP is the dashed curve in Figure 3.2. The parameters for these trials are listed in table 4. Because the RDP is only slightly affected by changing density the effect of density is not illustrated.

The three characteristics that change in Figure 3.2 are: long period level (LPL), source overshoot ( $B$ ), and corner frequency ( $f_0$ ). These are notably the three parameters that Haskell and others have used to fit analytical functions to observed RDPs (Haskell (1967), von Seggern and Blanford (1972), Helmberger and Hadley (1984)).

The following sections relate the parameters in table 4 to the trial RDPs in Figure 3.2. The discussion is grouped into aspects of the RDP concerning the long-period level (LPL), source overshoot and corner frequency. Following the discussion of the characteristics of the RDP, a range of RDPs for the CANT explosion are presented along with the reasoning for assignment of each parameter. Since high-frequency level is proportional to  $\omega^{.53}$  and has a slope of  $\omega^{-2}$  for all

TABLE 4  
SOURCE PARAMETERS IN FIGURE 3.2

	Cavity	Elastic	Velocity	Poisson
$h$	1.6	1.6	1.6	1.6
$r_c$ (.64) (.53) (.43)		.64	.64	.64
$r_{el}$	7.0	(10.0) (8.8) (7.0)	7.0	7.0
$\rho$	1.9	1.9	1.9	1.9
$B$	(1) (1.8) (3.3)	(1) (2) (3)	(1) (2) (2.9)	(1) (2) (2.9)
$c$	366	366	(366) (258) (216)	366
$\beta$	244	244	(244) (172) (144)	(244) (172) (144)
$\sigma$	.1	.1	.1	(.1) (.35) (.4)
$k_1$	.4	.4	.4	.4
$k_2$	417	(597) (525) (417)	417	417
$k_3$	(28) (24) (19)	28.5	28.5	28.5
$k_4$	1.5	1.5	1.5	1.5

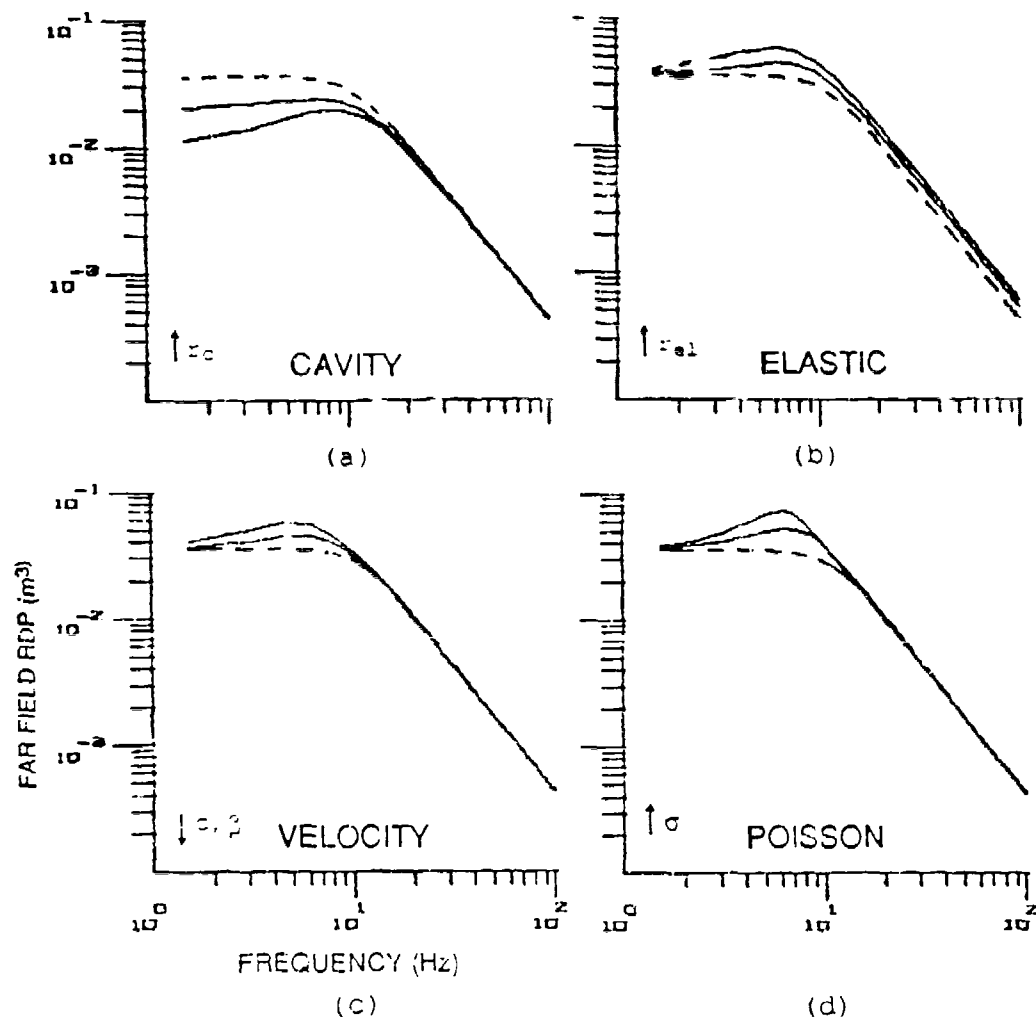


Figure 3.2. Sensitivity of reduced displacement potential to (a) cavity radius (b) elastic radius (c) compressional and shear velocity (d) Poisson's ratio.

realizations of Equation 3.3, no comparisons of high-frequency level or high-frequency roll-off are necessary.

a) Long period level: LPL

The long period level (LPL) of the source spectrum is obtained by taking the limit of Equation 3.3 as  $\omega$  approaches zero and substituting Equation 3.7 for  $P_{oc}$ ,

$$(3.14) \quad \Psi(\omega)|_{\omega=0} = \frac{r_{el}^3 P_{oc}}{4\mu} = \frac{1}{3} k_1 r_c^3$$

The LPL of the source spectrum is related to final cavity volume which increases as the cube of the cavity radius for increasing yield.

In classical cube-root-yield (CRY) scaling the cavity radius is assumed proportional to the cube root of yield so LPL is directly proportional to yield

$$\Psi(\omega)|_{\omega=0} \sim (r_c)^3 \sim W^{1.0}$$

In contrast Mueller-Murphy allow cavity radius to get larger as overburden pressure decreases or yield increases. Substituting Equations 3.13 and 3.9 into 3.14 relates Mueller-Murphy LPL to yield:

$$(3.15) \quad \Psi(\omega)|_{\omega=0} \sim (r_c)^3 \sim W^{.76}$$

This step allows a quantification of the yield ratio error associated with cavity radius error. In other words, if the true cavity radius is  $r_{c1}$  and the parameter is estimated at  $r_{c2}$  then the true yield,  $W_1$ , would be different from the predicted yield,  $W_2$ . The difference between true and expected yield can be measured as a ratio of true and predicted cavity radius.

$$(3.16) \quad \left( \frac{r_{c1}}{r_{c2}} \right)^{3/76} \sim \frac{W_1}{W_2}$$

Figure 3.2a illustrates the RDP for cavity radii of 0.43, 0.53 and 0.64 m with all other parameters held constant according to the BASIC model. The  $k_3$  proportionality factors which determine the estimated cavity radii are 28.5, 38.0 and 43.7 respectively. For a cavity radius increase from .43 to .64 meters the expected yield ratio is 5.0. The predicted yield ratio increases approximately as the ratio of predicted cavity radius ( $r_{c1}$ ) to true radius ( $r_{c2}$ ) raised to the fourth power. The implication is that estimation of relative yield from forward models is strongly dependent on the estimation of cavity radius. This weakness could be avoided with empirical measurements of  $r_c$ .

In this example, the LPL increases by a factor of 3.3 for a factor of 1.5 increase in cavity radius. This large variation in LPL could have a significant impact on calibration tests using small explosions in an inhomogeneous

test bed. Equation 3.9 predicts a cavity radius of 28 meters for 10 kt explosion in tuff-rhyolite at a scaled depth of  $122W^{1/3}$  m. The actual cavity radius may vary around the sphere but the result seen at one station is an average. For small explosions, the entire cavity radius could be contained by an inhomogeneity with a scale length of two meters so that the proportionality constant,  $k_4$ , derived for a test site would be in error.

Because cavity radius depends on pore fluids, it is also notable that small explosions can easily be placed above or below the water table. A saturated rock is less compressible leading to a smaller cavity radius for a given yield.

#### b) Source Overshoot

Source overshoot is sensitive to all parameters tested as shown in Figure 3.2a-d. The peak pressure according to Equation 3.6 for the BASIC model at a scaled depth of  $122W^{1/3}$  m (1.65 m) is  $46.1 \times 10^4$  dyne/cm<sup>2</sup>. The maximum step pressure calculated by Equation 3.7 should be less than the peak pressure. Rewriting Equation 3.7 with  $\mu = \rho\beta^2$

$$(3.17) \quad P_{oc} = k_1 \frac{4}{3} \rho\beta^2 \left( \frac{r_c}{r_{el}} \right)^3$$

shows that step pressure is decreased and overshoot is increased for decreasing  $r_c$  (Figure 3.2a); increasing  $r_{el}$  (Figure 3.2b); decreasing shear velocity (Figure 3.2c); and increasing Poisson's ratio (Figure 3.2d).

The effect of increasing the overshoot in Figures 3.2b-d is to shift the apparent corner toward the low frequencies. The LPL is not changed by overshoot in Figures 3.2b - 3.2d.

c) Corner frequency

The corner frequency dependence on elastic radius and compressional velocity is given by

$$(3.18) \quad \omega_0 = \frac{C}{r_{el}}$$

If the elastic radius is proportional to cube root of yield then the corner frequency is inversely proportional to the cube root of yield.

$$(3.19) \quad \omega_0 \sim \frac{C}{W^{1/3}}$$

The Mueller-Murphy corner scales inversely as yield raised to the .19 power as shown by substituting Equation 3.13 and 3.8 into 3.17

$$(3.20) \quad \omega_0 \sim \frac{C}{W^{.19}}$$

The inverse relationship of corner frequency and elastic radius is illustrated in Figure 3.2b (arrow is in direction of increasing elastic radius) As elastic radius increases from 7.0 to 10.0 meters the corner frequency decreases from 8.3 Hz to 5.8 Hz.

Figure 3.2c illustrates the corner frequency shift with increasing P-velocity for a constant Poisson's ratio of .1. The theoretical corner shift is from 8.3 Hz to 4.9 Hz for a decrease in P-velocity from 366 m/s to 216 m/s. The change in apparent corner frequency is also related to overshoot.

Figure 3.2d shows the effect of changing only the shear velocity and allowing Poisson's ratio to change. As Poisson's ratio increases the overshoot increases and the "apparent" corner shifts from 8.3 Hz to 7.0 Hz while the theoretical corner frequency does not change.

## 2. Source Depth of Burial

The BASIC model was calculated for normal SD of  $122W^{1/3}$  m ( $= 1.65$  m). Depth of burial effects associated with CART (SD =  $221W^{1/3}$ ) and APT (SD =  $74W^{1/3}$  m) are illustrated in Figure 3.3.

For a  $k_3$  proportionality constant of 28.5 in Equation 3.9, the predicted CART cavity radius is .68 m compared to .60 for APT. The effect of decreasing the depth of burial from CART to APT is to increase the cavity radius. As a result of increased cavity radius, the LIL of the underburied APT KIP is 1.5 times larger than that of the overburied CART KIP. The theoretical corner frequency of the predicted CART KIP is 1.6 times larger than the predicted APT corner. At frequencies below 9 Hz APT should produce greater amplitude and at frequencies > 9 Hz, CART should produce greater amplitude. Although this difference is not

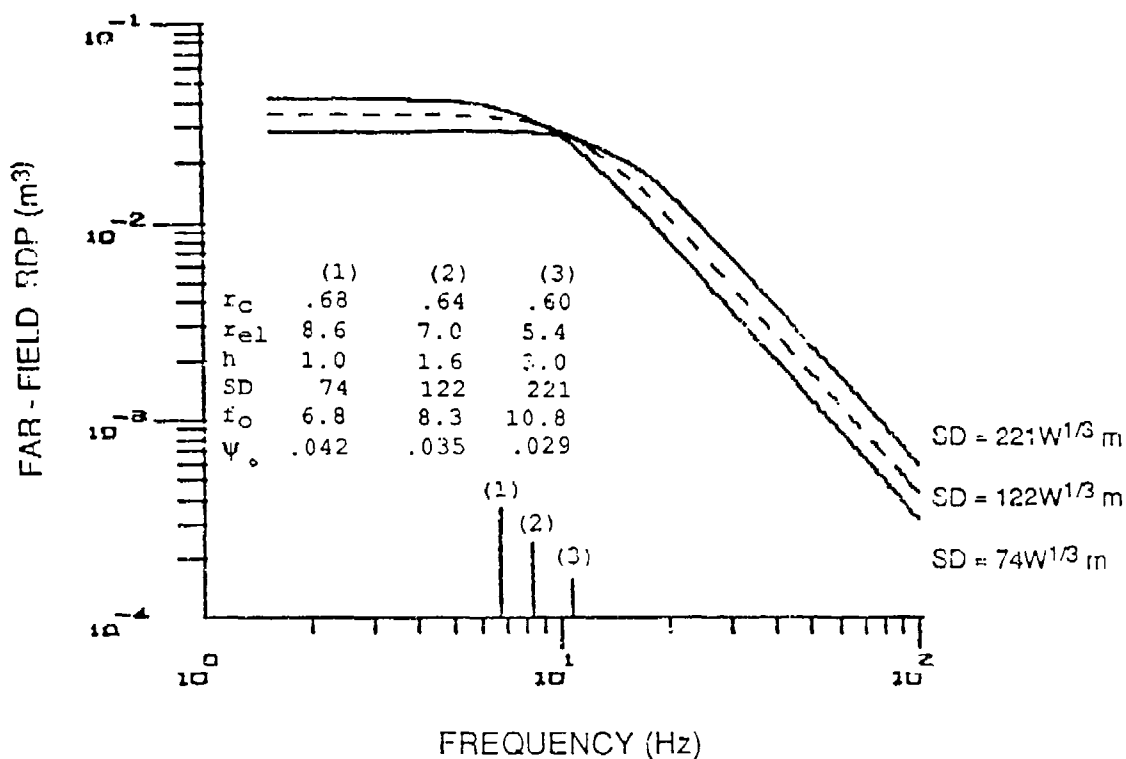


Figure 3.3. Sensitivity of the reduced displacement potential to depth of burial. Curves for normal ( $SD=122W^{1/3}$ ), overburied ( $SD=221W^{1/3}$ ) and undurburied ( $SD=74W^{1/3}$ ) scaled depths are shown. The dashed curve is the Basic source corresponding to the dashed curve in Figure 3.2.

apparent in the peak velocity versus range plots in Figure 2.7, the result is not conclusive because Figure 2.7 doesn't separate frequencies. (Perret and Bass filtered their data to get correct time domain amplitude comparisons).

### 3. CART Reduced Displacement Potentials

Table 5 lists the parameters of two additional models: SLOW92 and FAST60. These models were chosen to illustrate the extremes in LPL and corner frequency that are possible for the McCormick Ranch test site. The RDPs are plotted in Figure 3.4. Between the two extreme models, SLOW92 and FAST60, there is a factor of 3.6 increase in LPL and the corner frequency shifts by a factor of 3.5. It is believed that the RDP for the CART explosion is somewhere in between these two extreme models. Derivation of the appropriate cavity radius, elastic radius, P-velocity and S-velocity are given below.

Equation 3.9 predicts a cavity radius of 0.66 meters for the CART source in tuff-rhyolite ( $k_3=31.4$ ). Stump (1984) used  $k_3=28.7$  for dry alluvium suggesting a cavity radius of 0.60 meters. Since the CART tests are very near the surface the source medium should be less consolidated and more compressible. A lower limit of .60 to 0.66 meters is taken for cavity radius. The upper limit of the cavity radius is taken from photographs of the AMT craters which are 2.6 meters in diameter. Thus the CART cavity radius is less than 1.0 meter.

TABLE 5  
CART SOURCE PARAMETERS IN FIGURE 3.4

	BASIC	SLOW92	FAST60
$h$ (m)	1.6	3.0	3.0
$r_c$ (m)	.64	.92	.60
$r_{el}$ (m)	7.0	7.5	5.2
$\rho$ (gm/cm <sup>3</sup> )	1.9	1.9	1.9
$B$	1.0	3.1	1.0
$c$ (m/s)	366	270	600
$\beta$ (m/s)	244	120	230
$\sigma$	.1	.38	.41
$k_1$	.4	.4	.4
$k_2(r_{el})$	417	1490	876
$k_3(r_c)$	28.5	43.7	28.5
$k_4$	1.5	1.5	1.5
$i_o$	8.3	5.7	18.4

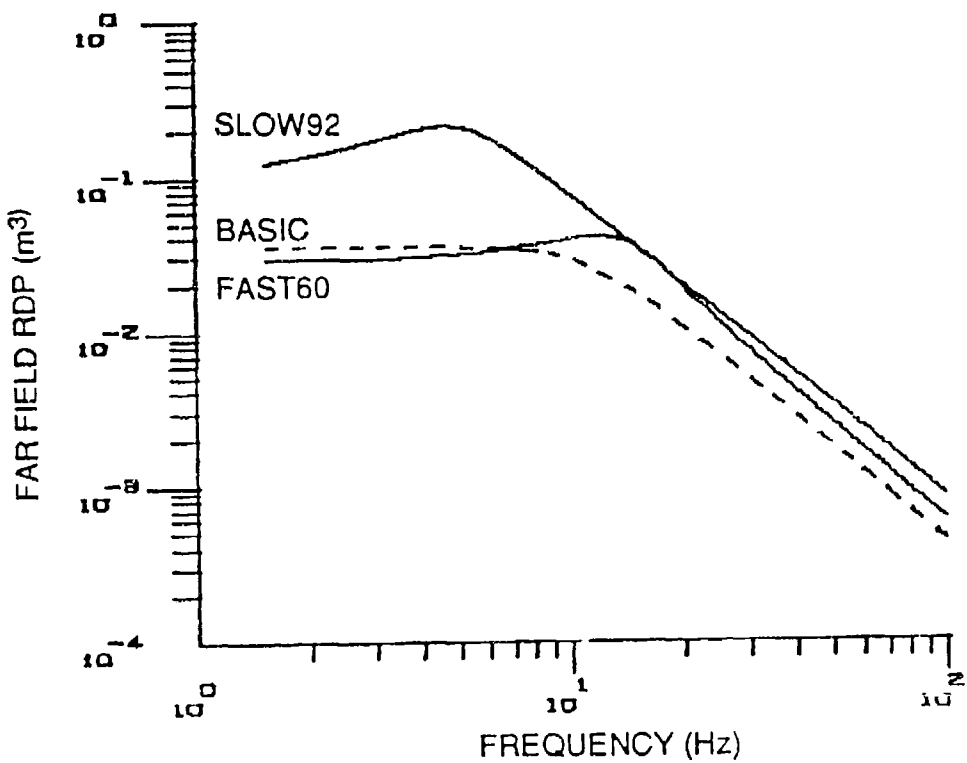


Figure 3.4 Range of possible CART reduced displacement potentials. Curves are computed from parameters listed in table 5.

Mueller-Murphy set  $k_2$  in Equation 3.8 equal to 1490 for tuff-rhyolite. This constant predicts a CART  $r_{el}$  of 12.74 m. Based on the study of amplitude versus range presented earlier (see Fig. 2.6 - 2.8), the CART elastic radius appears to be smaller than 12.74 m hence the  $k_2$  constant was assigned a lower value and 12.74 m is taken as the upper limit for the CART elastic radius. Since the linear trend fit through all peak radial velocities has a slope of -1.56, linear motion is most likely observed as close to the source as 5.0 - 10.0 meters. The BASIC model incorporates an elastic radius of 7.0 meters with a  $k_2$  value of 417.

SLOW92 combines the maximum cavity and elastic radii with the minimum wave velocities. The velocity pair,  $c = 270$  and  $\beta = 120$ , for SLOW92 is representative of the top layer in the McCormick Ranch site model given in table 3. The low shear velocity and high Poisson's ratio of .38 results in a large overshoot;  $B = 3.1$ . The low shear velocity with the large elastic radius results in the minimum theoretical corner frequency of 5.7. The analytic (or apparent) corner frequency, roughly equal to the peak in the spectrum, is at 5 Hz.

FAST60 combines the minimum radii with the maximum wave velocities. The velocity pair,  $c = 600$  and  $\beta = 230$ , corresponds to layer 2 in the McCormick Ranch site model given in table 3. The P-velocity was lowered from 670 m/s in the site model in order reduce Poisson's ratio to .41. While source overshoot for the FAST60 RDP is 1.0 there is a peak in

the spectrum due to the high Poisson's ratio. The theoretical corner frequency is 18.4 Hz and the spectrum is peaked at about 15 Hz.

### C. Path Calculations

This section documents the path models that were tested in an attempt to forward model the CART observed seismograms. These calculations begin with simple half-space (HS) models of the test site and conclude with the more complex and realistic layered half-space models (LHS). A series of models are included in each group to explore the effects of different model parameters on the synthetic seismograms.

The results of this section are displays of the various possible source models combined with the various path models. Figures 3.5, 3.6 and 3.7 are representative of the half-space models and Figures 3.8, 3.9 and 3.10 illustrate the layered half space models. Trade-offs associated with the forward modeling procedure are summarized in Section D following this section.

### I. Half-space Greens Functions

Seismograms are first synthesized for the simplest path model; an elastic half-space. The purpose is to test how much of the characteristics of the observed waveforms can be matched by the simplest model.

Green's functions are calculated for spherical waves emanating from a point source 1 meter below the free

surface in an isotropic, homogeneous, elastic half-space. The Cagniard de Hoop transform technique of Johnson (1974) calculates the total wavefield.

Two half-space models are discussed here. Model HS366 assumes the parameters of the second layer in the CART site characterization listed in table 3. P-wave velocity is 670 m/s, S-wave velocity is 366 m/s and density is 1.9 gm/cc. Poisson's ratio for this model is 0.29.

The second HS model was derived directly from CART first arrival times. The CART observations were used to calculate a P-wave velocity at each range. Sv-P times were then used to get S travel time and S-velocity at each range. The velocities of this range varying half-space model are listed in the upper part of table 6. The velocity pairs resulted in a constant Poisson's ratio of 0.43-0.45 for the six ranges. The average velocities chosen for the HS115 model are 400 m/s and 115 m/s for P and S velocities.

In summary there is a fast HS model, HS366 with a shear velocity of 366 m/s and a slow HS model with a shear velocity of 115 m/s. Green's functions were computed for each HS model at each CART range and convolved with the Mueller-Murphy source function, BASIC, discussed in the previous section. The result is a set of radial and vertical velocity synthetics for the two half-space models.

Figure 3.5 illustrates the HS115 path model with the BASIC source model. Radial and vertical synthetic

TABLE 6  
THREE HALF-SPACE VELOCITY MODELS

m	$\alpha$	$\beta$	$\rho$	$\sigma$
<u>1. Range varying half-space</u>				
5.0	227		1.9	
9.7	303	100	1.9	.44
13.5	355	115	1.9	.44
20.3	425	125	1.9	.45
27.0	465	150	1.9	.44
40.6	527	180	1.9	.43
<u>Average Half-space</u>				
2. HS366	670	366	1.9	.29
3. HS115	400	115	1.9	.45

## HALF SPACE VELOCITY SYNTHETICS

PATH: HS115 , SOURCE: BASIC

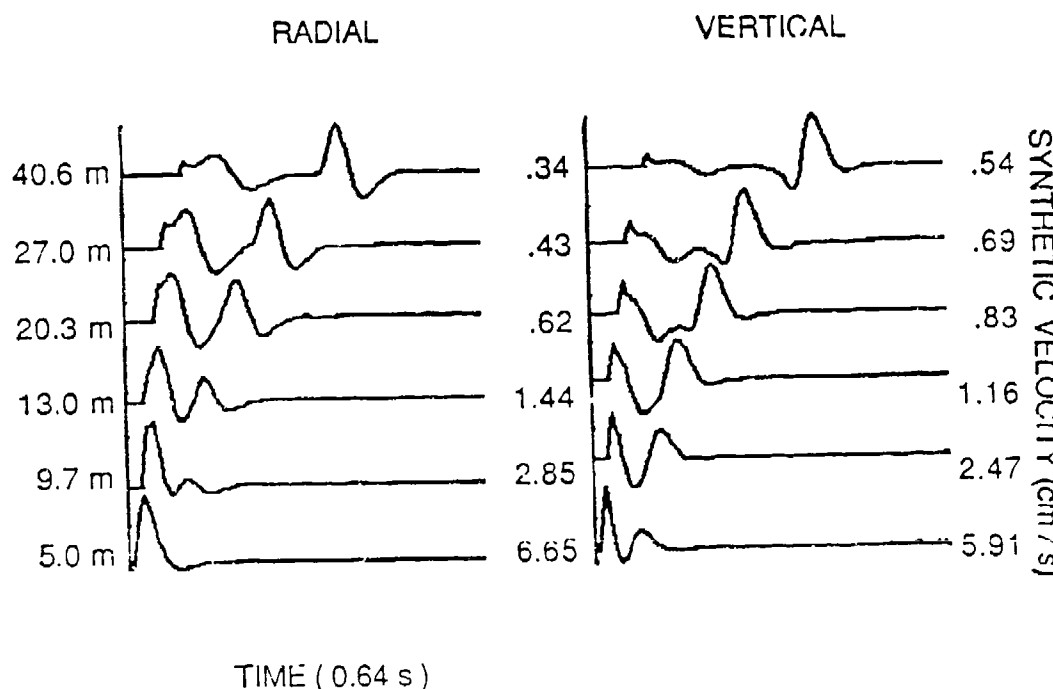


Figure 3.5. Velocity synthetics resulting from the half-space velocity model, HS115, and the Basic source model. Offset distance of calculation is shown on the left. At the right of each trace is the peak velocity.

seismograms are plotted for each CART range. Synthetic (predicted) amplitudes are given at the right of each trace.

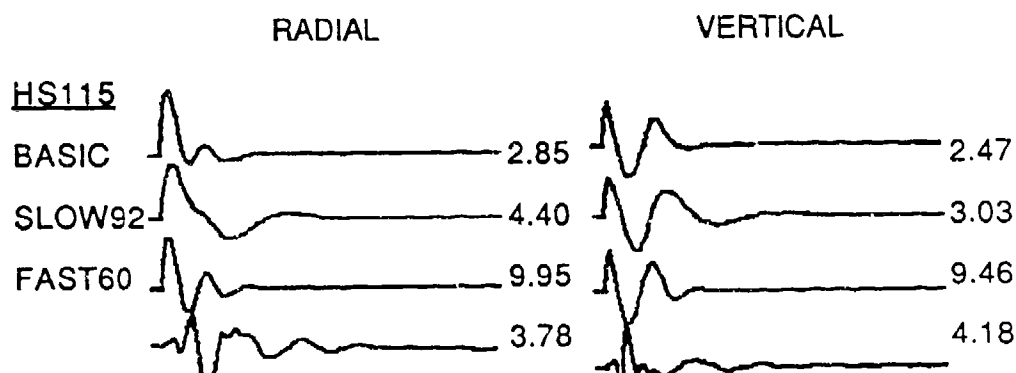
These synthetics reproduce some important aspects of the observational data that were outlined in Section 2.A.3. Specifically, the development of surface waves with range matches the observational data. The body waves dominate the signal between 5 and 13.5 meters and the surface waves dominate between 20.3 and 40.6 meters.

Another measure of the fit of synthetics to observations is the ratio of the peak radial velocity to the peak vertical velocity. The radial and vertical peaks for CART data are listed in Appendix C. At close ranges (5-13.5 m) the observed R/Z ratio is around 1.5. At more distant ranges the ratio increases to 2 or more. The half-space synthetic peak ratios show the opposite trend; at near ranges, the ratio is around 1.2 and at far ranges the ratio is .65. This suggests the peak radial component at large offsets is too small relative to the peak vertical component for the HS115 model.

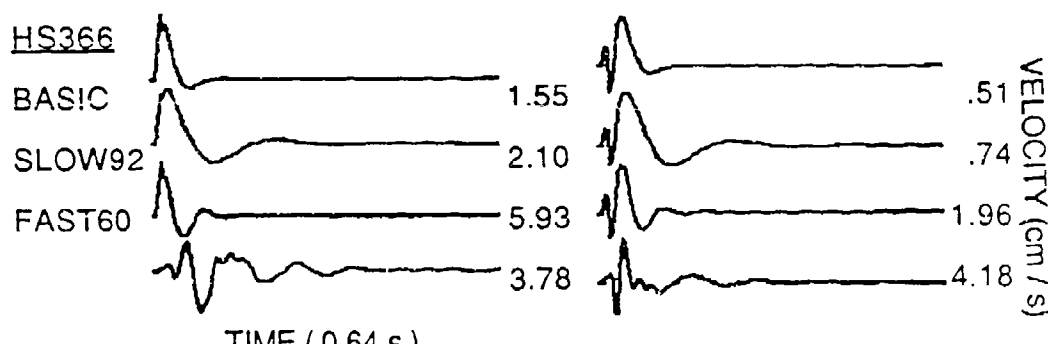
Figure 3.6 shows the effect of sources on the synthetic calculations at the 9.7 meter range. In Figure 3.6a the HS115 path model is convolved with the 3 RDPs in Figure 3.4 (after converting the RDPs to moment according to Equation 1.7 as required by Equation 4.4.) Synthetics are compared to the CART3B observation at 9.7 meters.

The factor of 3.5 -3.8 variation in amplitude is related to the relative amplitude of the source moment functions. When compressional velocity is used in Equation 1.7 to

## HALF SPACE VELOCITY SYNTHETICS 9 METERS



(a)



(b)

Figure 3.6. Radial and vertical velocity synthetics at 9 meters (a) Slow half-space model, HS115, with three sources. (b) Fast half-space velocity with three sources. The peak amplitudes are plotted at right. The bottom trace in each figure is the observed velocity from station B (at 9.7 meters) of CANT 3.

convert from reduced displacement potential to seismic moment, the order of the largest to smallest source functions changes from SLOW92 having the highest long period level followed by BASIC and FAST60 to the order in which FAST60 is largest followed by SLOW92 and BASIC. The peak observed amplitude falls within the range of synthetic amplitudes for both the radial and vertical components in Figure 3.6a.

The R/Z ratio is 1 - 1.4 for the synthetics compared to 0.9 for the CART3B observation. The relative contributions of radial and vertical components are well modeled by the HS115 synthetics at this range.

While the BASIC and FAST60 source models produce synthetics of similar shape, the SLOW92 model results in a synthetic richer in long period. This is a result of the low corner frequency of 5.7 Hz in the SLOW92 source model.

Figure 3.6b is the same as 3.6a except this time the faster HS366 path model was convolved with the 3 RDPs. Amplitudes vary by a factor of 3.8. The observed peak radial velocity falls within the range of calculated amplitudes but the calculated vertical peaks are smaller than the observed peaks.

The R/Z ratios are around 3.0 for the synthetics as compared to 0.9 for the observed seismograms. This synthetic R/Z ratio is larger for the HS366 path than for the HS115 path models because the faster shear velocities in HS366 produce lower radial peaks than for the HS115 model. The

faster model shows a smaller contribution of surface waves and in general a higher frequency content.

Figure 3.7 is the same as Figure 3.6 but synthetics are now calculated at the 27 meter range and compared to the CART1D observation at 27.0 meters. Figure 3.7a is the slow HS115 path model convolved with the 3 source models and Figure 3.7b is the fast HS366 model with the same source models.

Comparing Figure 3.7 to 3.6 it is obvious that as offset increases, the surface waves become more pronounced on both the synthetic and observed signals. The most notable difference between Figures 3.7a and 3.7b is the time of the surface wave arrival. HS115 results in a surface wave arrival that is consistent with the observation. HS366 results in a surface wave arrival that is very close in time to the body wave arrivals. This argues for a slow shear velocity as in the HS115 model. Another explanation could be a secondary source which is richer in long periods. This trade-off is discussed in Section 4.C.3.

The F/Z ratio of the surface wave peaks of CART1D is 2.4. The same F/Z ratio of the HS115 synthetics is around 0.6 and around 0.8 for the HS366 model.

The most prominent defect in the HS115 synthetics is that the vertical surface wave peak is too large relative to the radial surface wave peak. The main defect in the HS366

HALF SPACE VELOCITY SYNTHETICS 27 METERS

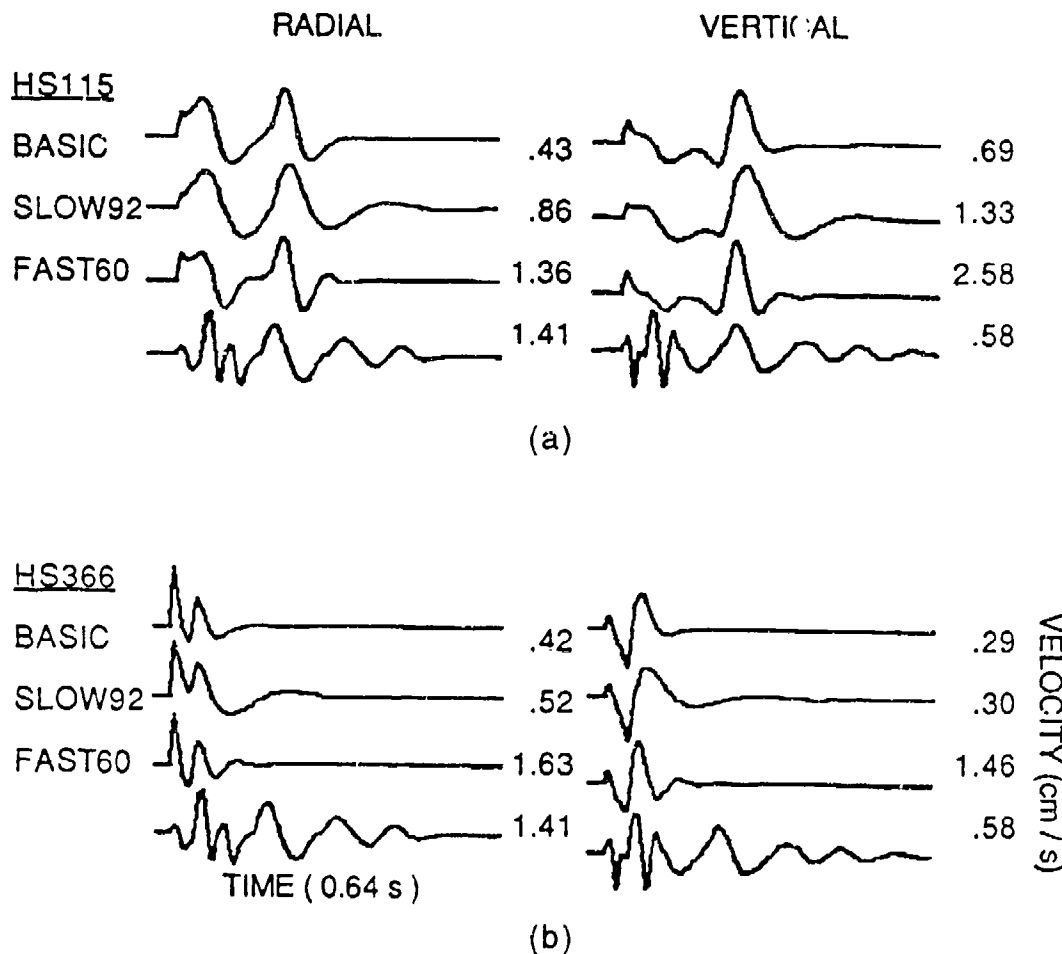


Figure 3.7. Radial and vertical velocity synthetics at 27 meters (a)Slow half-space model, HS115, with three sources. (b)Fast half-space velocity with three sources. The peak amplitudes are plotted at right. The bottom trace in each figure is the observed velocity from station D (at 27 meters) of CART 1.

synthetics is that the arrival time of the surface wave is early.

## 2. Layered Half-space Greens Functions

Half-space synthetics calculated in the previous section provided no way to return down-going energy to the receiver. In this section LHS Green's functions are convolved with the 3 RDPs to investigate the more realistic situation of a velocity structure that increases with depth and thus includes turning rays in the synthetics. Green's functions are calculated for models consisting of 2 layers over a half-space. In addition to P and S velocities, the reflectivity solution used in this section allows the specification of Q (intrinsitic attenuation) for each layer. The code follows a generalized method suggested by Fuchs and Mueller (1971).

The number of variables to be specified in the LHS models has increased 6-fold over the number of variables required for the HS models. To reflect this, the number of models necessary for comparison has also increased. Four combinations of S velocities, three combinations of Q structure and location of the source above or below the three-meter interface have been studied in 12 different models. Six of the 12 models are presented in table 7. In these particular models labeled F,H,I,K,N and O, P velocity is constant for all three layers. The effect of changing P velocities was not addressed because P-velocity was assumed the most reliable of all the estimates. Q structure does not

TABLE 7  
LAYERED HALF-SPACE VELOCITY MODELS

	F	H	I	K	N	O	
$\beta_1$	120	80	80	80	120	120	$(\alpha_1 = 270)$
$\beta_2$	360	360	360	230	230	230	$(\alpha_2 = 670)$
$\beta_3$	500	500	500	360	360	360	$(\alpha_3 = 930)$
Above			A			A	
Below	B	B		B	B		
$Q_1$	10	10	10	10	10	10	
$Q_2$	50	50	50	50	50	50	
$Q_3$	100	100	100	100	100	100	

change between these models because preliminary calculations showed that a change of Q over the range of estimates for the ART/CART test site does not severely effect the resulting synthetic.

The most important parameter and the least well constrained is the shear velocities structure. Related to this is the location of the shot relative to the most shallow interface. The 3.0 meter interface in the velocity structure in table 3 is the same as the CART shot depth. Path calculations were made with the source just above and just below the 3-meter interface. To study this parameter models H and I were completed with exactly the same parameters except the source in H was placed just below the 3-meter interface and the source in I was place just above the interface. This comparison is repeated with the pair of models N and O.

The product of this section will be a series of models with different shear structures. Inversions in the next chapter will utilize the series to address the question of how uncertainty in shear structure maps into the inverted source function.

To illustrate the general form of the LHS synthetics Figure 3.8 shows the seismograms resulting from the convolution of the path model, N, with the BASIC source. Radial and vertical synthetic velocities are plotted for each CART range with peak amplitudes listed to the right of each trace. Comparison of the this figure to Figure 3.5 shows the

LAYERED HALF SPACE VELOCITY SYNTHETICS  
PATH: N, SOURCE: BASIC

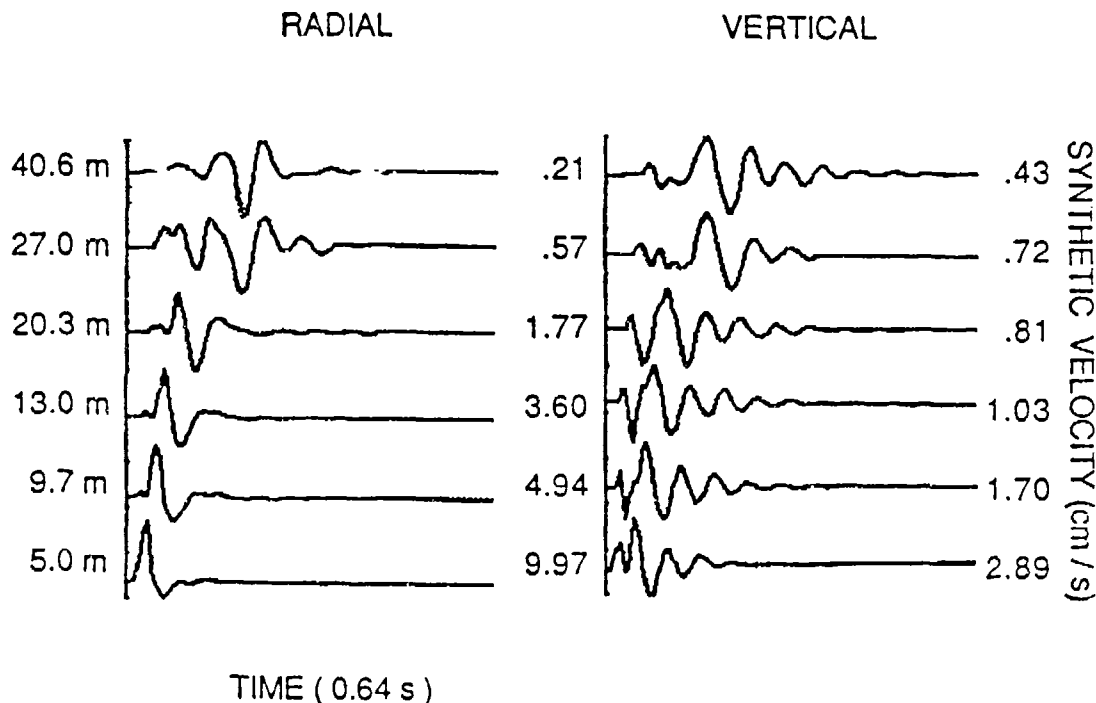


Figure 3.8. Velocity synthetics resulting from the LHS path model N, and the Basic source model. Offset distance of calculation is shown at left. At the right of each trace is the peak velocity. Compare to HS models in Figure 3.5.

difference between the HS and LHS models. The LHS synthetics are more complex and show a more oscillatory character as energy is trapped in the upper layers.

The R/Z ratio decreases with increasing offset. Radial (body wave) peaks are larger than vertical peaks at close ranges and vertical (surface wave) peaks are larger than radial peaks at 27.0 and 40.6 meters.

Figure 3.9 is the LHS source study. The 3 RDPS were each convolved with the path model, N. Calculations made at 9.7 meters are compared with the CART3B observation in Figure 3.9a. This figure is comparable to Figure 3.6 of the HS study. The observed peak amplitude falls within the range of peak synthetic amplitudes for both the radial and vertical calculations. Calculations made at 27.0 meters are compared with the CART1D observation in Figure 3.9b. This figure is comparable to Figure 3.7 of the HS study. Here the peak amplitudes of the radial synthetics underestimate the observation and the peak amplitudes of the vertical component overestimate the observation.

Synthetic R/Z ratios at 9.7 meters vary from 1.2 to 3.4 between source models. These ratios are high compared to the value of .9 for the observation. At the 27.0 meter range the surface waves are predominantly the peak amplitudes. The R/Z ratios at 27.0 meters which vary from .3 to .4 are low compared to the observed ratio of 2.43 at 27.0 meters.

Figure 3.10 is the LHS path study. The six path models (F,H,I,K,N,O) were convolved with the BASIC source. Figure

## LAYERED HALF SPACE VELOCITY SYNTHETICS

## PATH : N, SOURCE STUDY

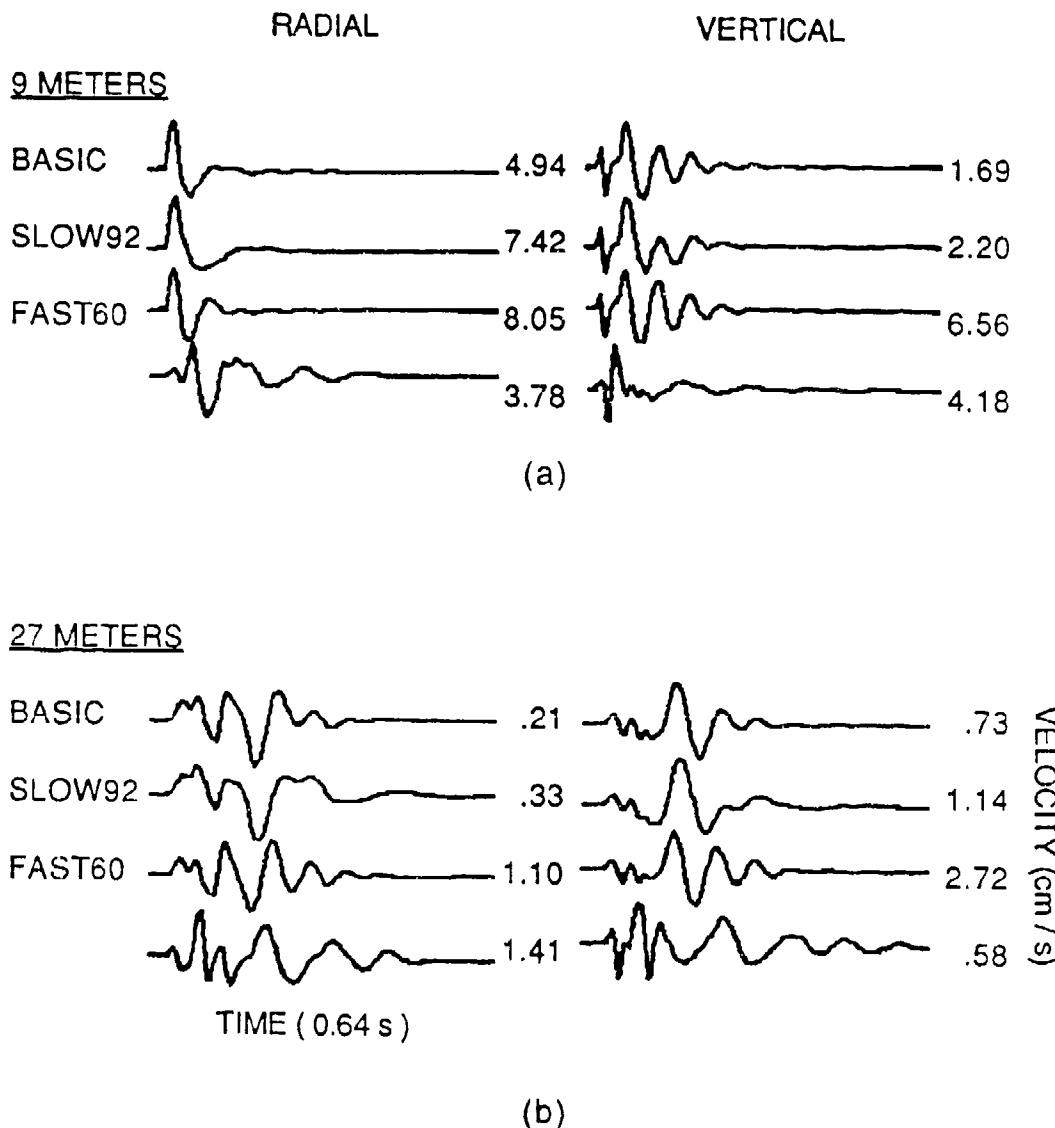


Figure 3.9. Velocity synthetics at (a) 9.7 meters and (b) 27.0 meters resulting from the LHS path model N with three sources. Peak amplitudes are plotted at the right of each trace. The bottom trace in (a) is the observed velocity from station B of CART 3. The bottom trace in (b) is from station D of CART 1. Compare to HS models in Figures 3.6 and 3.7.

SOURCE: BASIC, PATH STUDY

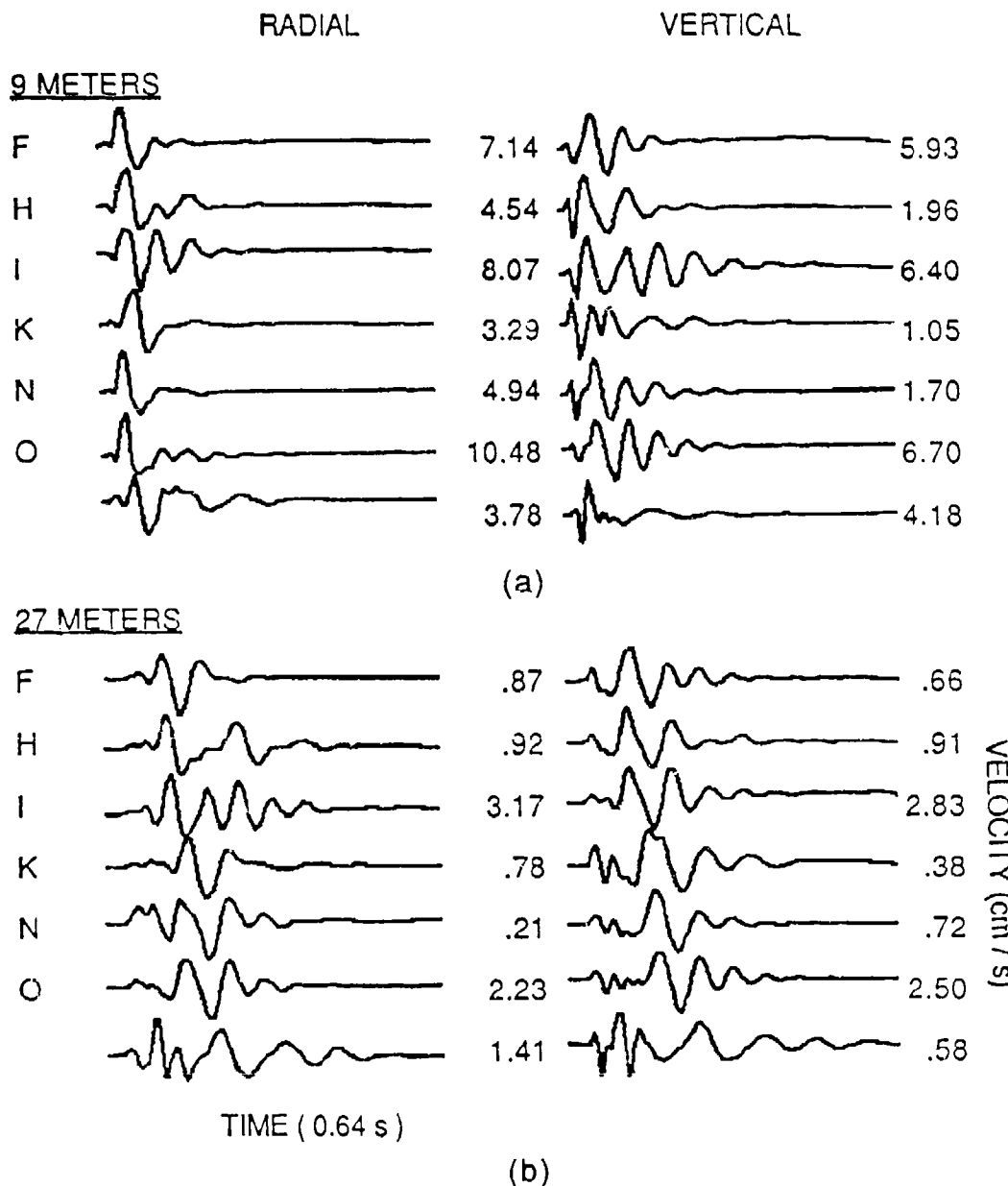


Figure 3.10. Velocity synthetics path study. Synthetics were calculated at (a) 9.7 meters and (b) 27.0 meters for the Basic source with 6 different LHS path models. The lower trace in each figure is the observed seismogram. LHS path models are summarized in table 7.

3.10a makes the comparisons at the 9.7 meter range with the CART3B observation. The synthetic radial amplitudes vary by a factor of 3.2 and the synthetic vertical amplitudes vary by a factor of 6.4 over the range of path models. Both the observed radial and vertical peak amplitudes fall within the ranges of peak synthetic amplitudes.

Models H and I have the same shear structure but the source is above the 3-meter interface in I and below the 3-meter interface in H. This difference results in a factor of 1.8 difference in amplitudes at 9.7 meters and a factor of 3.4 at 27 meters. The larger amplitudes are associated with the slower shear velocity of the upper layer. Similarly model O and N have the same shear structure but the source in O was above the 3-meter interface and the source in model N was below the 3-meter interface. Notice that the observed amplitude is more closely matched by the synthetics that were calculated with the source in the lower layer. This suggests the shear velocity of the layer that contained the explosives is closer to the shear velocities in the second layer of the two models. In particular this is between 230 m/s and 360 m/s.

## CHAPTER 4

### MOMENT TENSOR INVERSIONS

The work presented in this chapter follows the method developed by Stump and Johnson (1977) who inverted radiated seismic waves to determine the seismic source in terms of a moment tensor. A detailed derivation of the theory is given in Stump (1979). Stump showed that when the source is represented in terms of a moment tensor the relationship between data, source and propagation can be posed as a linear problem. Once the problem is linearized, the wealth of techniques for linear inversion can be utilized. The method of calculating the generalized linear inverse used in this study follows Lanczos (1961). Stump (1984) demonstrated that this method is well suited for explosion seismograms especially when the depth of the explosion is known or can be estimated.

Formulation of the inverse problem is outlined in Section 4.A and the generalized linear inverse solution is given in Section 4.B. In Section 4.C, inversions are completed with the synthetic seismograms discussed in Chapter 3. This step provides a check of the inversion code and a resolution study of the source matrix,  $M$ . In Section 4.D, inversions are completed with observational data.

### A. Moment Tensor Representation of the Source

The moment tensor representation of the source begins with the solution of the elastodynamic equations of motion written in terms of a Green's function integral with sources in terms of boundary conditions, initial conditions and body forces. The initial and boundary conditions are rewritten in their equivalent form of body forces through the application of the representation theorem.

The moment tensor representation of the source was derived from the general representation

$$(4.1) \quad U_k(\vec{x}', t') = \int_{-\infty}^{\infty} \int_{V_0} G_{ki}(\vec{x}', t'; \vec{x}, t) f_i(\vec{x}, t) d\vec{x}^3 dt$$

where  $U_k$  is the displacement in the  $k$  direction at  $(\vec{x}', t')$ ;  $G_{ki}$  are the Green's functions for the point source in the  $i$  direction observed in the  $k$  direction at  $(\vec{x}', t')$ ;  $f_i$  are body forces in the  $i$  direction at  $(\vec{x}, t)$ ; and  $V_0$  is the source volume.

Stump and Johnson (1979) expanded the Green's functions in equation 4.1 in a Taylor series about the center of the source volume,  $\vec{x} = \vec{o}$

$$(4.2) \quad G_{ki}(\vec{x}', t'; \vec{o}, t) = \sum_{n=0}^{\infty} \frac{1}{n!} x_j, \dots x_{j_n} G_{k i, j_1 \dots j_n}(\vec{x}', t'; \vec{o}, t)$$

and defined the volume integral over force by distance as the force moment tensor,  $M_{ij\dots j_n}$ ,

$$(4.3) \quad M_{ij\dots j_n}(\vec{o}, t) = \int_{V_0} x_j \dots x_{j_n} f_j(\vec{x}, t) dx^3$$

Substituting Equations 4.2 and 4.3 into 4.1 the displacement solution can be written:

$$(4.4) \quad U_k(\vec{x}', t') = \sum_{n=0}^{\infty} \frac{1}{n!} G_{ki,j\dots j_n}(\vec{x}', t'; \vec{o}, o) \otimes M_{j\dots j_n}(\vec{o}, t')$$

where  $\otimes$  is the symbol for temporal convolution.

For an explosion, the forces act at the elastic radius of the source region. Since the elastic radius of small explosions is smaller than the seismic wavelength of interest, it is realistic to simplify Equation 4.4 by localizing the force in space: a point source is assumed and only the first term in equation 4.4 is necessary.

$$(4.4) \quad U_k(\vec{x}', t') = G_{ki,j}(\vec{x}', t'; \vec{o}, o) \otimes M_{j}(\vec{o}, t')$$

The equation is further simplified by writing it in the frequency domain:

$$(4.5) \quad U_k(\vec{x}', \omega) = G_{ki,j}(\vec{x}', \omega; \vec{o}, o) \cdot M_j(\vec{o}, \omega)$$

where the temporal convolution is replaced by multiplication.

Equation 4.5 is the frequency domain solution to the elastodynamic equations of motion utilizing the moment tensor representation of the equivalent body forces. This equation is linear involving ground displacement,  $U$ , propagation path effects,  $G$ , and source effects,  $M$ . The equation is most conveniently written in matrix form

$$(4.5 \text{ abbreviated}) \quad U = GM$$

The moment tensor,  $M$ , represents the force moments and their directions as a function of time. Conservation of angular momentum requires the moment tensor be symmetric so there are 6 unique time functions:

$$\begin{bmatrix} M_{11} & M_{12} & M_{13} \\ M_{21} & M_{22} & M_{23} \\ M_{31} & M_{32} & M_{33} \end{bmatrix}$$

A purely explosion source contains identical diagonal elements,  $M_{11}$ ,  $M_{22}$ ,  $M_{33}$  and off-diagonal elements equal to zero.

$$M_{ij} = \begin{bmatrix} 1 & 0 & 0 \\ 0 & 1 & 0 \\ 0 & 0 & 1 \end{bmatrix}$$

The diagonal components of the explosion source are equal in

three orthogonal directions. This theoretical explosion source is purely volumetric: it has spherical symmetry with zero deviatoric component.

A pure earthquake source has diagonal elements that sum to zero making the volumetric source equal zero. An example is the moment tensor for a strike-slip fault:

$$M_{ij} = \begin{bmatrix} 0 & 1 & 0 \\ 0 & 0 & 0 \\ 0 & 0 & 0 \end{bmatrix}$$

Equation 4.5 was utilized in the forward models in Chapter 3 to predict ground motion,  $U$ , as a result of a 5 lb. explosion ( $M$ ) in various velocity structures ( $G$ ). In this Chapter, Equation 4.5 is utilized in the inverse modeling of the source,  $M$ .

#### B. Solution of the Inverse Problem

The method used in this study is to solve Equation 4.5 in the frequency domain and convert the moment tensor estimates to the source time functions. The equation is written for each frequency. In matrix notation the left side of Equation 4.5 is a vector containing the velocity values of each channel at a particular frequency. The right side of the equation contains the Fourier transform of the Green's functions multiplied by the Fourier transform of the moment tensor at a particular frequency.

To obtain the estimate of  $M$ , one must calculate the inverse of the  $G$  matrix. The task of inverting the matrix,  $G$ , is accomplished by the method of singular value decomposition following the work of Lanczos (1961)

$$(4.6) \quad G = WQV^T$$

$$(4.7) \quad G^{-1} = VQ^{-1}W^T$$

Equation 4.7 is the generalized inverse of  $G$ . The matrices  $W$  consists of the eigenvectors associated with eigenvalues of  $GG^T$ .  $V$  similarly consists of the eigenvectors associated with the eigenvalues of  $G^TG$  and  $Q$  is a matrix whose diagonal elements are the positive square roots of the eigenvalues of  $G^TG$ .

Both sides of Equation 4.5 are multiplied by  $G^{-1}$  and the moment tensor estimation is complete.

$$(4.8) \quad G^{-1}U = G^{-1}GM$$

$$G^{-1}U = M$$

The eigenvalues obtained in Equation 4.6 are important in defining the resolution of the inverse problem. The solution is ill-defined in directions associated with small eigenvalues. Likewise the solution has poor resolution in the directions in which there are very small eigenvalues.

The condition numbers, the ratio of largest to smallest eigenvalue, when calculated at each frequency give an indication of the frequency band of resolvable solutions. When the eigenvalues are approximately equal in magnitude the condition numbers are small and the problem has good resolution.

The degree of fit is quantified by substituting the inverted moment tensor,  $M$ , obtained from Equation 4.8 and the input Green's functions,  $G$ , back into Equation 4.5 to produce calculated seismograms.

$$4.9 \quad U_C = G (G^{-1} U_o)$$

These calculated seismograms,  $U_C$ , are then compared to the input seismograms,  $U_o$ , by measuring the correlation coefficient. A correlation coefficient equal to 1.0 is a perfect fit.

The accuracy of the moment tensor calculation is measured as a function of the variance of the data,  $U_j$ , as follows

$$(4.10) \quad \text{var } (M_{jk}) = \sum_{k=1}^l (G_{jk}^{-1})^2 \text{ var } (U_j)$$

(Stump 1979, equation 4.5).

The above three tools of error analysis: condition numbers, time domain fit and frequency domain variance, will be discussed as they apply to inversions in Section 4.C. and

4.D. Condition numbers and variances quantify the resolution of the moment tensors. Correlation coefficients quantify the degree of fit in the time domain.

### C. Source Inversions with Synthetic Data

Eight trials with synthetic data were completed to demonstrate the feasibility of source inversions with the CART observational data described in Chapter 2. This has been accomplished by simulating the ranges, azimuths and noise conditions of the observational data. The trials were designed to test the effects of signal to noise ratio (SNR), station distribution and the Green's functions on the inversions. Trial inversions suggest the CART data set meets conditions necessary to invert real data for source characteristics when the interpretations are limited to the frequency band between 1.5 and 60 Hz. Analysis of the data in Section 2.A.2 suggests a frequency band between of useable data between 3.0 and 60 Hz. The combination of these limitations results in a frequency band of 3 - 50 Hz for interpretation.

The data qualities include good SNR, good station distribution and a thorough site characterization which improves accuracy of the Green's functions. Additionally the synthetic tests emphasize the importance in calculating the correct Green's functions for reducing trade-offs between source and path functions.

The eight synthetic trials are listed in table 8. The first 3 trials investigate noise effects, the next illustrates the effects of using the incorrect Green's function and the last 4 investigate the influence of station distribution.

### 1. Synthetic Inversions Input: $U_s = MG$

The synthetic seismograms were calculated according to Equation 4.5 using the Mueller-Murphy source for a 5 lb. explosion at a normal scaled depth of  $122 \text{ m}/\text{kt}^{1/3}$ . The Basic source model was discussed in Section 3.B.1, listed in table 5 and plotted in Figure 3.4. The plot in Figure 3.4 is the time derivative of the reduced displacement potential, also called reduced velocity potential (RVP), with units of  $\text{m}^3/\text{s}$ . Equation 1.6 was used to convert the RVP in Figure 3.4 to seismic moment rate.

The moment rate tensor of the Basic source is plotted in Figure 4.1a. Since this is a purely explosion source,  $M'_{11} = M'_{22} = M'_{33} = M'_{\text{ISO}}$ . The off-diagonal components are zero ( $M'_{12} = M'_{13} = M'_{23} = 0$ ) and the deviatoric moment is zero. The moment rate peak of the diagonal components is equal to  $3.485 \times 10^{16} \text{ dyne-cm/s}$ . The integral of the moment rate is the moment tensor plotted in Figure 4.1b.

The spectrum in Figure 4.1c is the  $M'_{11}$  component which is the RVP of Figure 3.4 with a different scale. The zero-frequency or long-period level (LPL) of the isotropic moment is equal to  $1.119 \times 10^{15} \text{ dyne-cm}$  as shown in 4.1c.

TABLE 8  
SOURCE INVERSIONS WITH SYNTHETIC DATA

TRIAL NAME	Stations	Ranges	Channels	%Noise
1. 115BIC1N00	A-G	13.5-40.6	21	0
2. 115BIC1N1	A-G	13.5-40.6	21	1
3. 115BIC1N10	A-G	13.5-40.6	21	10
4. 366BIC1X	A-G	13.5-40.6	21	1
5. GAMMAN1	A-E	13.5, 27.0	15	1
6. ALPHAN1	A,B,C	13.5	9	1
7. OMEGAN1	A,D	13.5, 27.0	6	1
8. C3N1	J,D,M	13.5-40.6	9	1

● SHOT LOCATION

▲ 13.5 m

● 27.0 m

◆ 40.6 m

↑ 8° NORTH

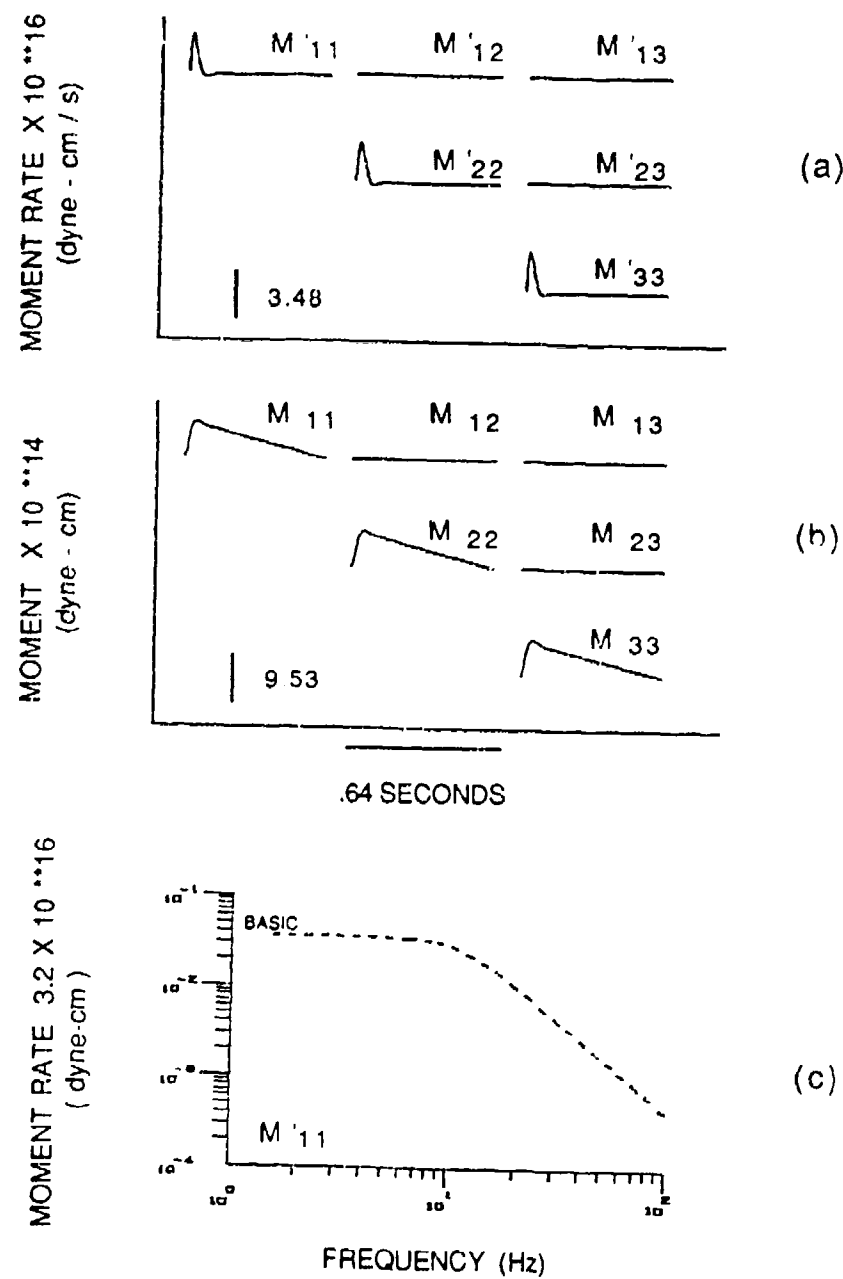


Figure 4.1 Basic source. (a) moment rate (b) moment (c) amplitude spectrum of  $M'_{11}$ . Time domain plots are scaled to the maximum shown by vertical bar. LPL of  $M'_{11} = 1.119 \times 10^{15}$  dyne-cm.

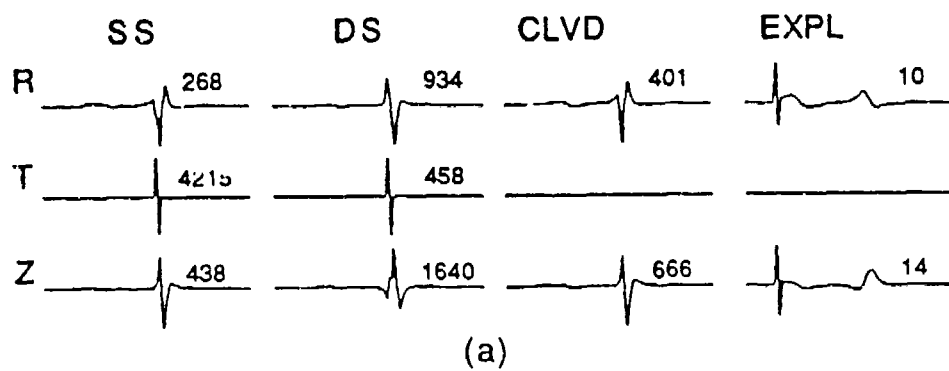
A sample of the path functions utilized in the trial inversions are represented by the 10 canonical Green's functions illustrated in Figure 4.2a. These functions are the responses at the 27.0 m range of an elastic half-space to four source types: Strike-Slip fault observed across a vertical plane ( $R, T, Z$ ); Dip-slip fault observed across a vertical plane ( $R, T, Z$ ); Compensated Linear vector dipole (CLVD) observed in a horizontal plane ( $R, Z$ ); and the explosion ( $R, Z$ ) (Stump 1979).

The synthetic velocity seismograms used in this section result from the convolution of the moment tensor in Figure 4.1a with the explosion Green's functions for the slow half-space model (HS115) in Figure 4.2a according to Equation 4.5. These synthetics were presented in Figure 3.5 and compared to the fast half-space synthetics, HS366, and to the Layered half-space synthetics in Section 3.C.2.

## 2. Noise Tests

Three noise tests were designed to study the sensitivity of the inversions to noise in the input velocity seismograms. The CART 1 configuration, shown in Figure 2.2, consists of seven stations with good azimuthal coverage (seven different azimuths) and good range coverage (3 ranges: 13.5, 27.0, and 40.6 m) for a total of 21 components. Noise tests were completed with 0%, 1% and 10% noise. As an example of the naming convention used for these trials, 115BIC1N00 indicates the HS115 path functions with the Basic source including the

## CANONICAL GREEN'S FUNCTIONS: HS115 27.0 METERS



## CANONICAL GREEN'S FUNCTIONS: HS366 27.0 METERS

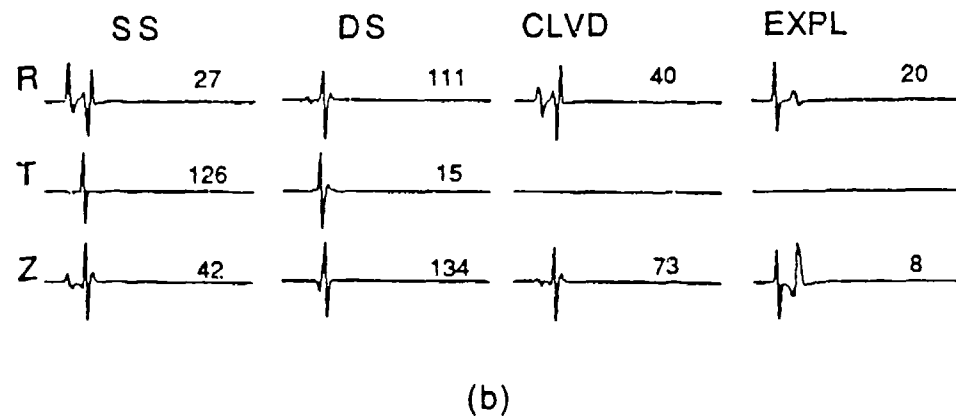


Figure 4.2. The ten canonical Green's functions for strike slip (SS), dip slip (DS), compensated linear vector dipole (CLVD) and explosion (EXPL) sources calculated for the 27.0 meter range in (a) slow half-space model and (b) the fast half-space model. Model parameters are listed in table 6.

instrument in a CART 1 configuration with 0 % noise. The time domain peaks of the source time functions resulting from synthetic noise trials are listed in table 9.

The results of trial inversion 115BIC1N00 are given in Figure 4.3. The moment rate tensor and its integral, the moment tensor, are shown in 4.3a and 4.3b. The moduli of the  $M'_{11}$  and  $M'_{12}$  elements are plotted in Figure 4.3c.

The moment rate tensor has been separated into its isotropic and deviatoric components below according to Equations 1.8 and 1.9

$$4.11 \quad M_{ISO} = 3.32 \times 10^{16} \begin{bmatrix} 1.0 & 0 & 0 \\ 0 & 1.0 & 0 \\ 0 & 0 & 1.0 \end{bmatrix} \text{ dyne-cm/s}$$

$$4.12 \quad D_{ij} = 5.4 \times 10^{13} \begin{bmatrix} 1.0 & .17 & .83 \\ .17 & 1.37 & .10 \\ .83 & .10 & -2.37 \end{bmatrix} \text{ dyne-cm/s}$$

The isotropic moment rate peak is 4.6% smaller than the input source amplitude of  $3.485 \times 10^{16}$  dyne-cm/s. The inversion results exhibit spherical symmetry. The diagonal components vary from the isotropic estimate at most by 0.4%. The isotropic moment rate is much larger than the deviatoric moment rate ( $3.32 \times 10^{16} / 5.4 \times 10^{13} = 615$ ). The LPL of the  $M'_{11}$  amplitude spectrum of  $1.0 \times 10^{15}$  dyne-cm matches closely the LPL of the input,  $1.119 \times 10^{15}$  dyne-cm.

The second trial, 115BIC1N1, includes white noise that is 1 % of the peak vertical amplitude at the 27.0 m range in

TABLE 9

 PEAK TIME DOMAIN AMPLITUDES FROM  
 SYNTHETIC SOURCE INVERSIONS
MOMENT RATE ( dyne-cm/s  $\times 10^{16}$  )

TRIAL NAME	M'11	M'12	M'13	M'22	M'23	M'33	M'ISO
115BIC1N00	3.328	.0007076	.003394	3.330	.0004466	3.310	3.324
115BIC1N1	3.338	.0005518	.003412	3.342	.001598	3.322	3.334
115BIC1N10	3.582	.006268	.009900	3.578	.008172	3.618	3.592
366BIC1X	4.326	.2402	1.035	4.192	.7170	9.958	6.158
GAMMAN1	3.330	.002126	.003842	3.330	.001140	3.306	3.322
ALPHAN1	3.428	.0006358	.002084	3.428	.001011	3.426	3.426
OMEGAN1	3.294	.002242	.01482	3.292	.02564	3.276	3.288
C3N1	3.206	.002006	.02060	3.224	.04842	3.148	3.192

MOMENT ( dyne-cm  $\times 10^{14}$  )

TRIAL NAME	M <sub>11</sub>	M <sub>12</sub>	M <sub>13</sub>	M <sub>22</sub>	M <sub>23</sub>	M <sub>33</sub>	M <sub>ISO</sub>
115BIC1N00	9.552	.012206	.06058	9.564	.007174	9.428	9.514
115BIC1N1	9.620	.007530	.05728	9.634	.015060	9.500	9.584
115BIC1N10	11.480	.074400	.09686	11.450	.074560	11.720	11.550
366BIC1X	23.300	.865000	4.50000	21.920	2.202000	36.740	27.240
GAMMAN1	9.592	.037040	.06796	9.602	.018420	9.432	9.542
ALPHAN1	10.120	.011040	.03306	10.130	.009996	10.070	10.110
OMEGAN1	8.984	.016290	.12860	8.954	.255400	8.896	8.948
C3N1	8.841	.032560	.24120	8.928	.932400	8.478	8.750

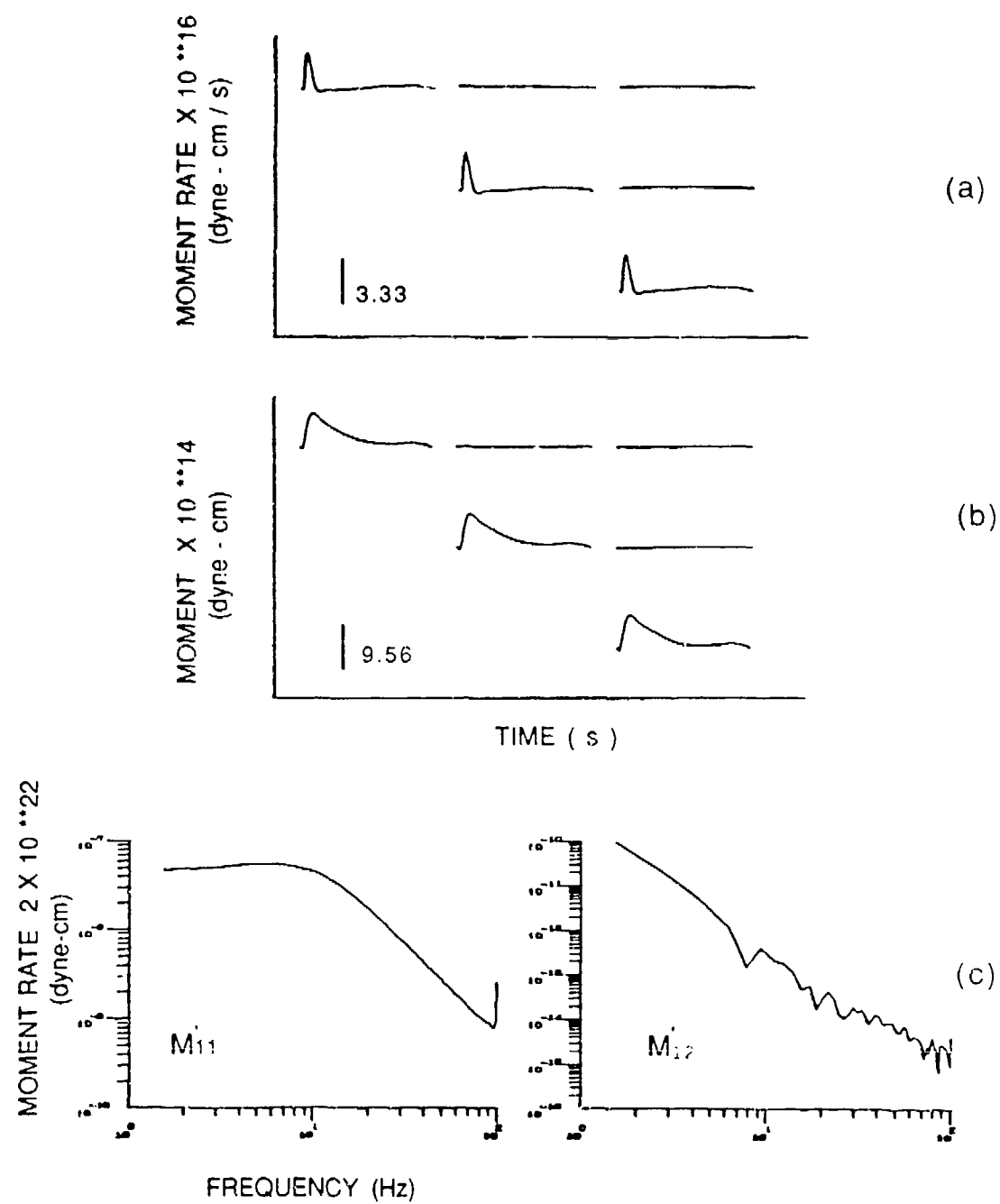


Figure 4.3. Synthetic inversion 115B1C1N00. (a) moment rate (b) moment (c) amplitude spectra. Refer to Figure 4.1 for labels. LPL of  $M'_{11} = 1.04 \times 10^{15}$  dyne-cm.

the synthetic seismograms. The results are shown in Figure 4.4. A comparison of Figure 4.4 with 4.3 shows that the inversion was not greatly affected by the addition of this noise. The peak time domain amplitude of the  $M'_{ISO}$  element is  $3.334 \times 10^{16}$  dyne-cm/s. This peak value is 4.3% smaller than the input source peak. The moment rate tensor exhibits spherical symmetry;  $M'_{11}$  and  $M'_{22}$  are within 1% of  $M'_{33}$  and the isotropic amplitude is 833 times larger than the deviatoric amplitude when the moment rate tensor is separated into its respective components.

The dashed curves in Figure 4.4c are the variances of the moment components as a function of frequency computed from the level of the white noise added to the synthetic seismograms (Stump, 1979). The standard deviation is 200 times smaller than the modulus of  $M'_{11}$  at 8 Hz and at least 5 times smaller between 1.5 and 50 Hz. LPL measured from  $M'_{11}$  is  $1.0 \times 10^{15}$  dyne-cm. Compare this to the input LPL of  $1.119 \times 10^{15}$  dyne-cm.

In the third noise test, 115BIC1N10, a similar trial inversion was completed with a noise level equal to 10% of the peak vertical amplitude at 27.0 m. As shown in Figure 4.5, the source was successfully modeled with the exception of long-period and short-period noise in the inverted source time function. The peak time domain amplitude of the  $M'_{ISO}$  element is  $3.592 \times 10^{16}$  dyne-cm/s. This value represents a 3% increase over the input value.

Again the moment rate tensor exhibits spherical symmetry. The peaks of  $M'_{11}$  and  $M'_{22}$  are within 1% of  $M'_{33}$ . The isotropic moment rate is 336 times larger than the deviatoric moment rate when separated into its respective components.

The variance curves in Figure 4.5c suggest the frequency band of the interpretable source function is more limited than the case of 1 % noise. The calculated  $M'_{11}$  modulus is 20 times larger than the variance at 8 Hz and is at least 5 times larger only between 4 and 15 Hz. However, as demonstrated in Section 3.B.1 one of the salient characteristics of the source is long-period level of the isotropic source function. Even with this limited frequency band, one would still be able to quantify the source function in terms of LPL by projecting the LPL between 4-15 Hz to the vertical axis. The LPL of  $M'_{11}$  in Figure 4.5c is  $1.1 \times 10^{15}$  dyne-cm/s.

Table 9 lists peak time domain moment estimates of the six moment rate and the six moment components. The conclusion drawn from the noise tests is that although noise as little as 1 % limits the frequency band of the interpretable source function to 1.5 - 50 Hz, the LPL of the inverted source function can still be quantified. Even for the case of 10 % noise this characteristic of the source is stable. The addition of noise does decrease the spherical symmetry of the inversions slightly by increasing the deviatoric relative to the isotropic component. With 0%

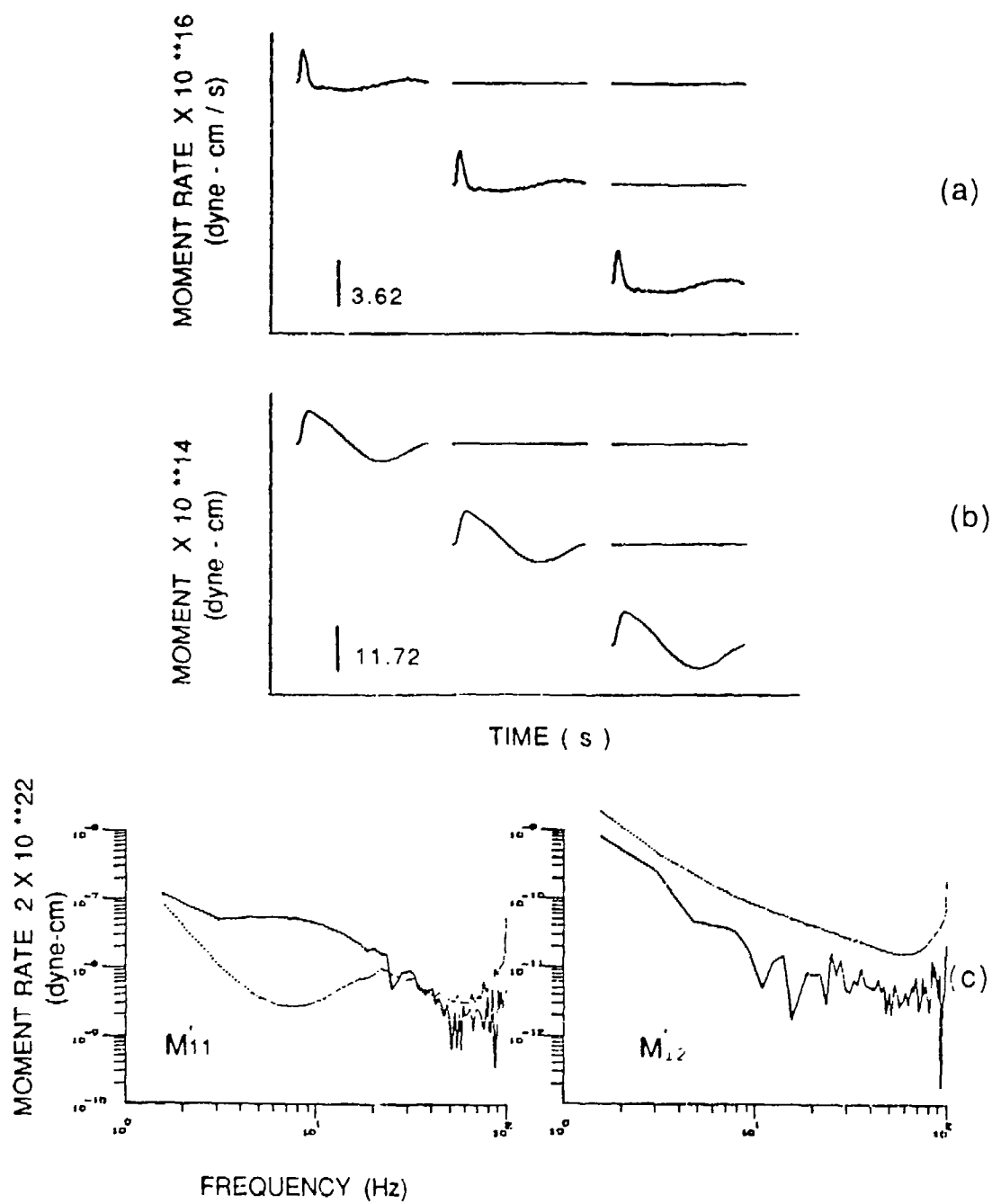


Figure 4.5. Synthetic inversion 115BIC1N10. White noise equal to 10% of the peak velocity at 27 meters was added to the synthetics before inverting for (a) moment rate (b) moment (c) amplitude spectra. Refer to Figure 4.1 for labels.

Again the moment rate tensor exhibits spherical symmetry. The peaks of  $M'_{11}$  and  $M'_{22}$  are within 1% of  $M'_{33}$ . The isotropic moment rate is 336 times larger than the deviatoric moment rate when separated into its respective components.

The variance curves in Figure 4.5c suggest the frequency band of the interpretable source function is more limited than the case of 1 % noise. The calculated  $M'_{11}$  modulus is 20 times larger than the variance at 8 Hz and is at least 5 times larger only between 4 and 15 Hz. However, as demonstrated in Section 3.B.1 one of the salient characteristics of the source is long-period level of the isotropic source function. Even with this limited frequency band, one would still be able to quantify the source function in terms of LPL by projecting the LPL between 4-15 Hz to the vertical axis. The LPL of  $M'_{11}$  in Figure 4.5c is  $1.1 \times 10^{15}$  dyne-cm/s.

Table 9 lists peak time domain moment estimates of the six moment rate and the six moment components. The conclusion drawn from the noise tests is that although noise as little as 1 % limits the frequency band of the interpretable source function to 1.5 - 50 Hz, the LPL of the inverted source function can still be quantified. Even for the case of 10 % noise this characteristic of the source is stable. The addition of noise does decrease the spherical symmetry of the inversions slightly by increasing the deviatoric relative to the isotropic component. With 6%

added noise, the ratio was 615. The ratio decreases to 336 for 10 % noise.

As reported in Chapter 2, the noise level of the observational data is below 1% so that successful source inversions using the CART data set are possible. Through synthetic testing the sensitivity of the inversion method to noise in the input seismograms was demonstrated. However, these tests were completed only for random white noise. If the actual noise is polarized or otherwise non random then the same reliability in the data may not be assumable.

### 3. Example of Source-Path Trade-offs

One synthetic trial was run as an example of source-path trade-offs. The same synthetic seismograms were input as for the 1% noise tests but this time the wrong Green's functions were input. The Green's functions used in this test are those of the fast half-space model, HS366 (table 6). Figure 4.2 illustrates the differences between the two sets of Green's functions at the 27 meter range.

Figure 4.6 compares HS115 synthetic velocity at 27 meters with the two different sets of explosion Green's functions. Radial synthetics and Green's functions are plotted on the left and vertical on the right of the figure. On the left in Figure 4.6a the radial HS115 Green's function is plotted below the radial HS115 synthetic. On the left on Figure 4.6b the radial HS366 Green's function is plotted below the radial HS115 synthetic. Similar comparisons with

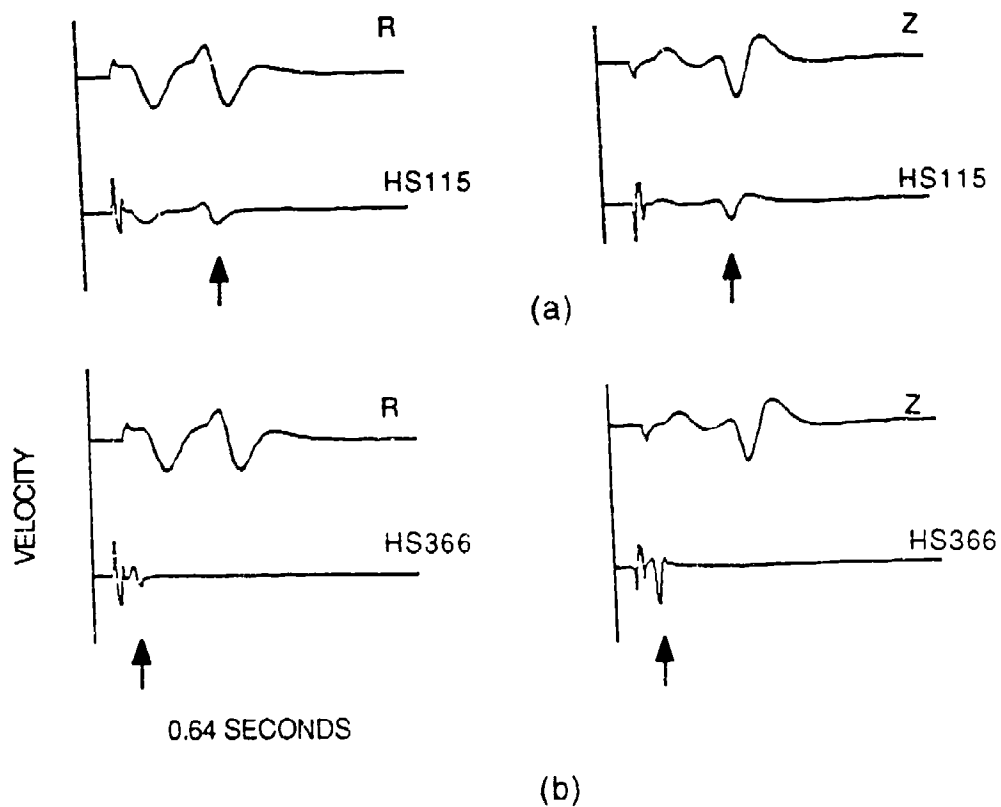


Figure 4.6 The HS115 radial and vertical velocity synthetics at the 27.0 meter range compared to the 27.0 meter Green's functions of the two HS models. Arrows point to the surface wave arrivals.

vertical synthetic and Green's functions are made on the right of the figure. The surface waves in the Green's functions are indicated by the arrows. Figure 4.6b illustrates how Green's functions with too fast a shear velocity fail to match the synthetic velocity. The separation between the body and surface waves in the Green's functions does not match that of the velocity records.

The results of the 366BIC1X inversions are given in Figure 4.7. The source and path have traded off to compensate for the lack of late surface wave arrival in the Green's function as shown in Figure 4.6. The result is a delayed time pulse in the diagonal moment tensor that is largest on the  $M'_{33}$  component.  $M'_{33}$  is 56% larger than the  $M'_{11}$  and the  $M'_{22}$  components.

The moment rate tensor is separated into its isotropic and deviatoric components below.

$$4.13 \quad M_{iso} = 6.16 \times 10^{16} \begin{bmatrix} 1.0 & 0 & 0 \\ & 1.0 & 0 \\ & & 1.0 \end{bmatrix} \text{ dyne-cm/s}$$

$$4.14 \quad D_{ij} = 1.8 \times 10^{16} \begin{bmatrix} -1.0 & .13 & .56 \\ & -1.1 & .39 \\ & & 2.1 \end{bmatrix} \text{ dyne-cm/s}$$

The moment tensor is no longer spherically symmetric; The isotropic amplitude is only 3.42 times larger than the deviatoric moment rate amplitude. Recall that this ratio was 833 when the correct Green's functions were used in inversion

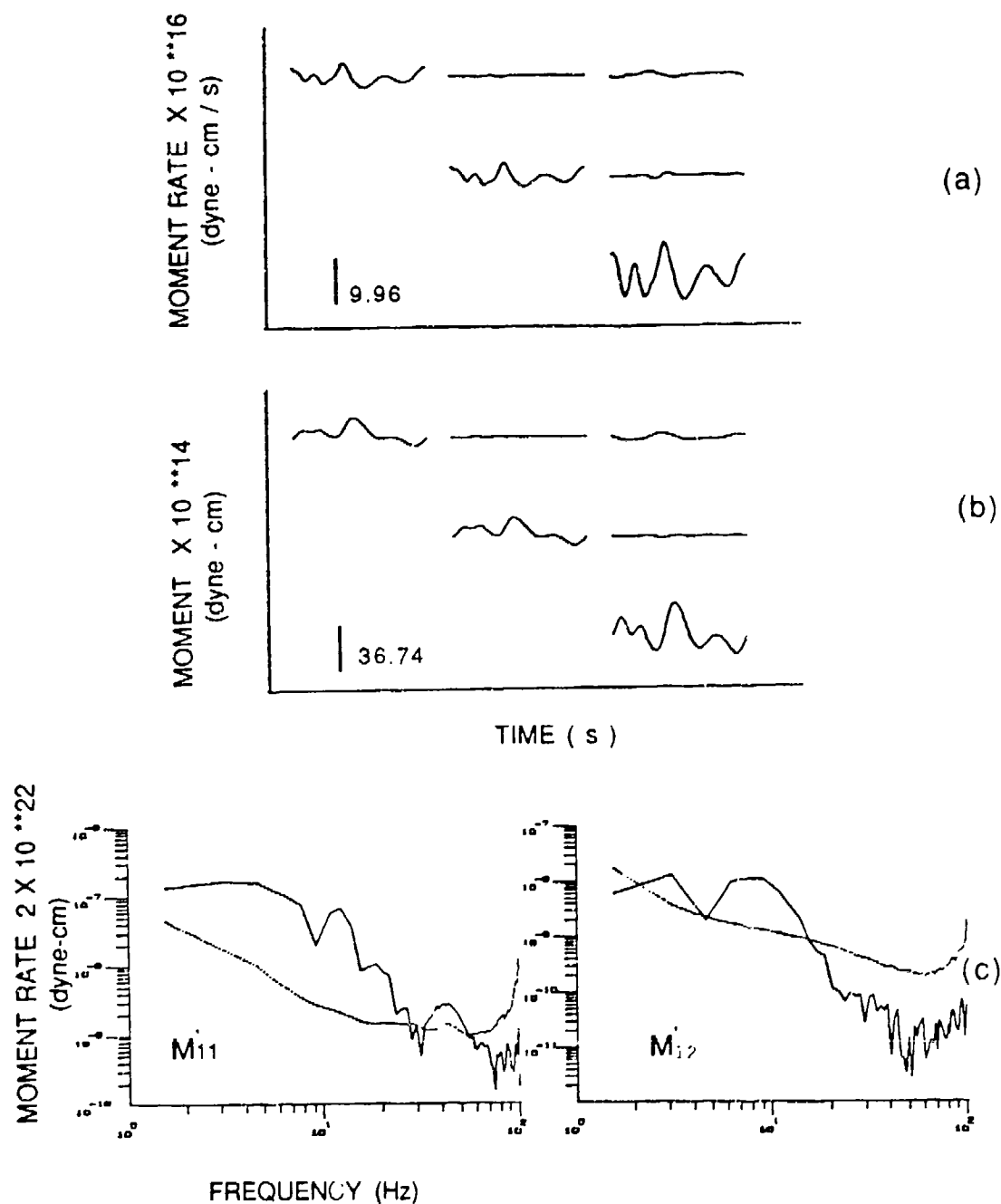


Figure 4.7. Synthetic inversion 366BIC1X. Same synthetic velocities went into the inversion but the HS366 Green's functions were substituted for the HS115 Green's functions. (a) moment rate (b) moment (c) amplitude spectra. Refer to Figure 4.1 for labels.

HS115BIC1N1. The deviatoric elements have increased in strength relative to the isotropic element.

The frequency spectra of  $M'_{11}$  and  $M'_{12}$  shown in Figure 4.7c are different from the 115BIC1N1 spectra in several ways. The moment estimate is 5 times larger than the variance between 2 - 20 Hz whereas it was 5 times larger than the variance between 1.5 - 50 Hz for the 115BIC1N1 inversion. The  $M'_{11}$  LPL is  $4 \times 10^{15}$  dyne-cm. This is 4 times larger than the LPL of the input source shown in Figure 4.1.

This example illustrates the source-path trade-offs. In an attempt to match the observations, even when the wrong Green's functions are specified, the inversion results in errors in the source. In this case source errors showed up as an increase on the  $M'_{33}$  components and an increase in LPL by a factor of 4.

#### 4 Station Distribution Tests

Four station distribution trials were completed to show the sensitivity of inversions to limitations in the ranges, azimuths and number of components in the data set. The following four tests were run with a 1% white noise level in the synthetics velocities. GAMMAN1 includes only the 13.5 and 27.0 meter ranges (5 stations). ALPHAN1 was limited to only the 13.5 meter ranges (3 stations). OMEGAN1 was limited to two stations; one at 13.5 and one at 27.0 meters. Trial C3N10 replicates the linear CART3 configuration. For

comparison to trial inversion 115BIC1N1, only stations at 13.5, 27.0 and 40.6 m were included.

The results are shown in table 9 in the form of the time domain peak amplitudes of the moment rate and moment estimates. GAMMAN1 moments are approximately equal to 115BIC1N1 moments in time domain amplitude and symmetry. ALPHAN1 moments are larger than 115BIC1N1 by 3%. OMEGAN1, with only 2 stations has diagonal moment rate components within 1% of each other. In terms of time domain amplitudes and effect on symmetry, the trial inversions shown above do not show sensitivities to station distribution.

### 5. Condition Numbers

Condition numbers are a measure of how sensitive the inversion procedure is in the presence of noise in the data. Inversions with good station distribution are less sensitive to noise. Condition numbers are obtained by taking the ratio of the largest to the smallest eigenvalue as discussed in Section 4.B. Condition number as a function of frequency for the above 5 trial inversions plus the 115BIC1N00 inversion are plotted in Figure 4.8. 115BIC1N10 and 115BIC1N1 have the same condition numbers as 115BIC1N00. This means that for the CART 1 station distribution (denoted C1 in the synthetic trial names), the inversion is just as sensitive to 1% noise as it is 10% noise.

The condition numbers of inversions 115BIC1N00, C3N1, GAMMAN1 and ALPHA are similar. These trials have minima

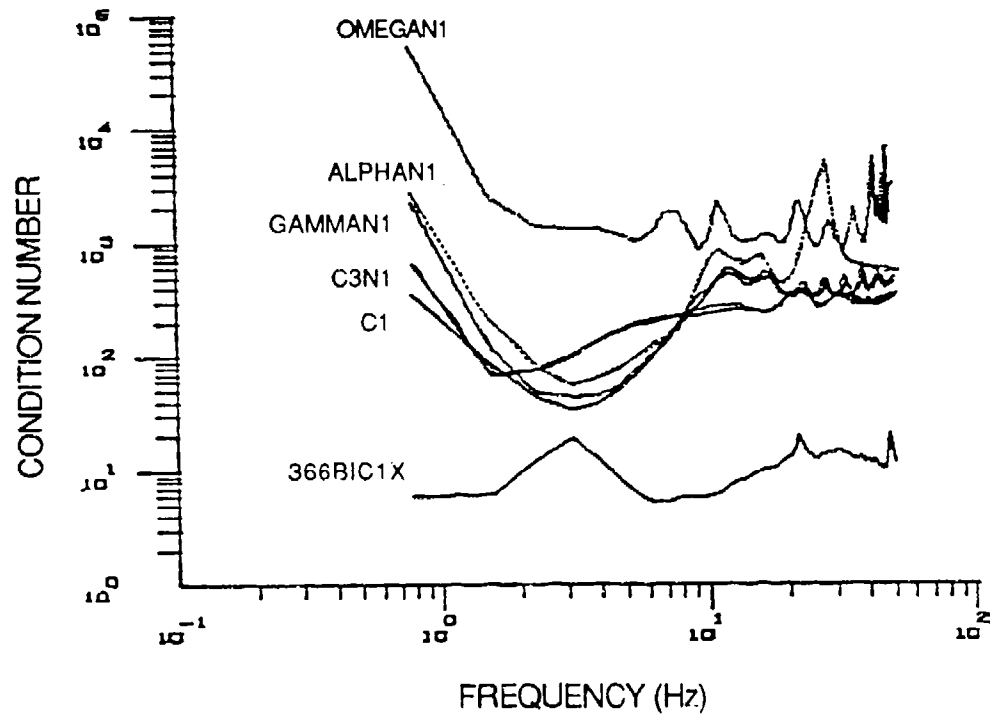


Figure 4.8. Condition numbers versus frequency for 6 synthtic inversions.

between 2 - 8 Hz where the average condition number is 50. Between 1.5 and 50 Hz the condition numbers are below 300. ALPHAN1 has a peak of 5200 at 25 Hz corresponding to a spectral hole in the Green's functions. The spectral hole results when Green's functions are all calculated for the same distance from the source. OMEGAN1 condition numbers are larger because only two stations are used. The average condition number of OMEGAN1 is 1500. In general the trial inversions with the fewest stations have the largest condition numbers.

The condition numbers associated with inversion 366BIC1X have an average value of 10, which is 10 times smaller than all other tests. This result suggests that the velocity of the test medium could affect the ability to resolve source characteristics such as size of source excitation. This observation can be explained by the peak time domain amplitudes of the Green's functions. Two sets of Green's functions calculated at the 27 meter range are plotted in Figure 4.2 with the peak amplitudes at the right of each trace. For the fast half-space model, the amplitudes of the 10 Green's functions are of the same order of magnitude. In contrast the Green's functions corresponding to the slow half-space model have amplitudes that are 400 times larger on the transverse component of the CLVD source than the radial and vertical components of the EXPL source.

This imbalance in amplitudes is related to Poisson's ratio. The HS366 model has a Poisson's ratio of .29 and the

HS115 model has a Poisson's ratio of .45. Based on information in table 6, the Poisson's ratio of .45 is believed to be more correct for the McCormick Ranch Site.

#### 6. Time Domain Fits

Equation 4.9 was used to obtain a calculated velocity from the input Green's functions and the inverted source. The correlation coefficients measuring the degree of fit between the input (synthetic) velocity and the calculated velocity are given in table 10 for all synthetic trials. Inversion 115BIC1N00 has a correlation coefficient above .9 for all radial (R) and vertical (Z) components and a value of 0 for all transverse (T) components. As the noise increases, the R and Z correlation coefficients reduce slightly. The T correlation coefficients increase to .18 - .69.

As a visual example, the fit for 115BIC1N10 is shown in Figure 4.9. Input (synthetic) velocity is plotted above calculated velocity for each component at the 3 different ranges. The fits are almost perfect for the R and Z components. The pure noise in T is not modeled very well which is a good result.

Inversion 366BIC1X with the Green's functions that were too fast shows smaller correlation coefficients in table 10. The fits are correspondingly degraded as shown in figure 4.10. The fits of the transverse components are most noticeable because the inversion erroneously put signal on the transverse velocities. This result showed up in the

TABLE 10

CORRELATION COEFFICIENTS FOR  
SYNTHETIC SOURCE INVERSIONS

RANGE (m)	13.5	13.5	13.5	27.0	27.0	40.6	40.6
AZIMUTH	90	270	0	180	35	215	325
<u>TRIAL NAME</u>							
115BIC1N00	.9973	.9950	.9952	.9991	.9997	.9877	.9946 (R)
	.0000	.0000	.0000	.0000	.0000	.0000	.0000 (T)
	.9454	.9471	.9472	.9864	.9864	.9999	.9999 (Z)
115BIC1N1	.9973	.9949	.9952	.9988	.9994	.9866	.9940 (R)
	.1891	.4288	.3716	.4641	.5165	.6415	.6956 (T)
	.9457	.9466	.9473	.9860	.9866	.9998	.9997 (Z)
115BIC1N10	.9929	.9896	.9891	.9778	.9811	.9271	.9326 (R)
	.3446	.2196	.3758	.4613	.2834	.6767	.7513 (T)
	.9397	.9443	.9391	.9750	.9755	.9828	.9819 (Z)
366BIC1X	.9030	.8193	.9260	.5561	.5124	.4579	.4107 (R)
	.1250	-.0504	.0108	.0685	.1726	.1349	.0393 (T)
	.8373	.7334	.0558	.2327	.1552	.8447	.8509 (Z)
GAMMAN1	.9991	.9993	.9960	.9991	.9980		(R)
	.0950	-.1428	.0703	.3418	.9374		(T)
	.9910	.9905	.9675	.9555	.9891		(Z)
ALPHAN1	1.0000	1.0000	1.0000				(R)
	.6993	.7341	.5992				(T)
	1.0000	1.0000	1.0000				(Z)
OMEGAN1	1.0000			1.0000			(R)
	.9999			1.0000			(T)
	1.0000			1.0000			(Z)
C3N1	1.0000			.9946		.9856	(R)
	.8615			.5753		.9122	(T)
	.9992			.9782		.9994	(Z)

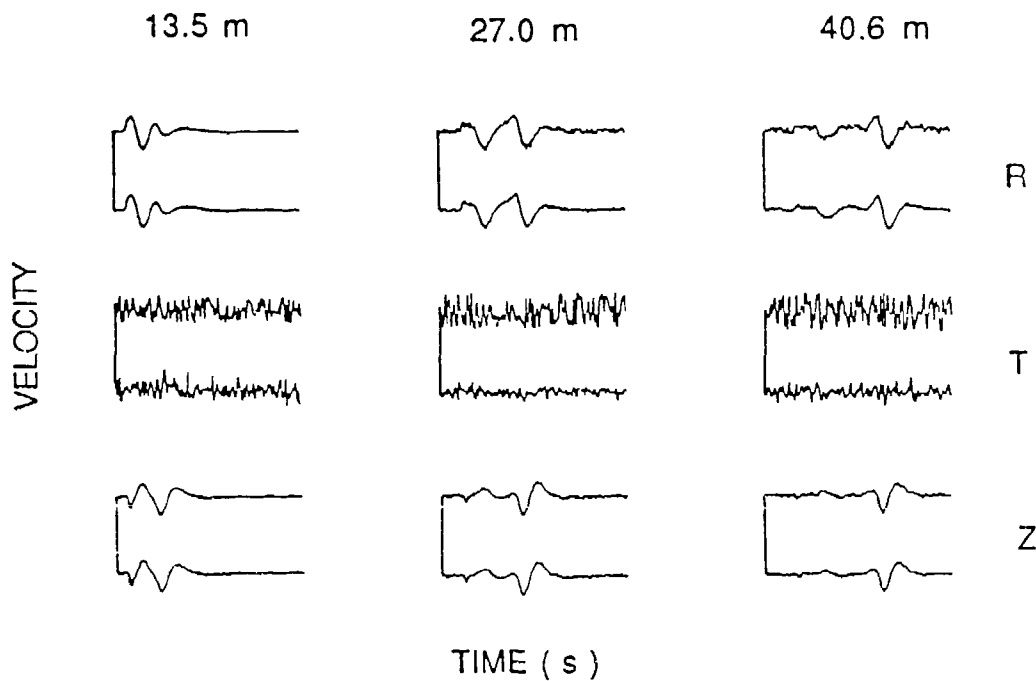


Figure 4.9. Synthetic inversion 115BIC1N10. Comparisons are made at three ranges for radial (R), transverse (T) and vertical (Z) components. In each pair, the top trace is the input velocity record and the bottom trace is the calculated velocity record. .64 seconds of data are plotted.

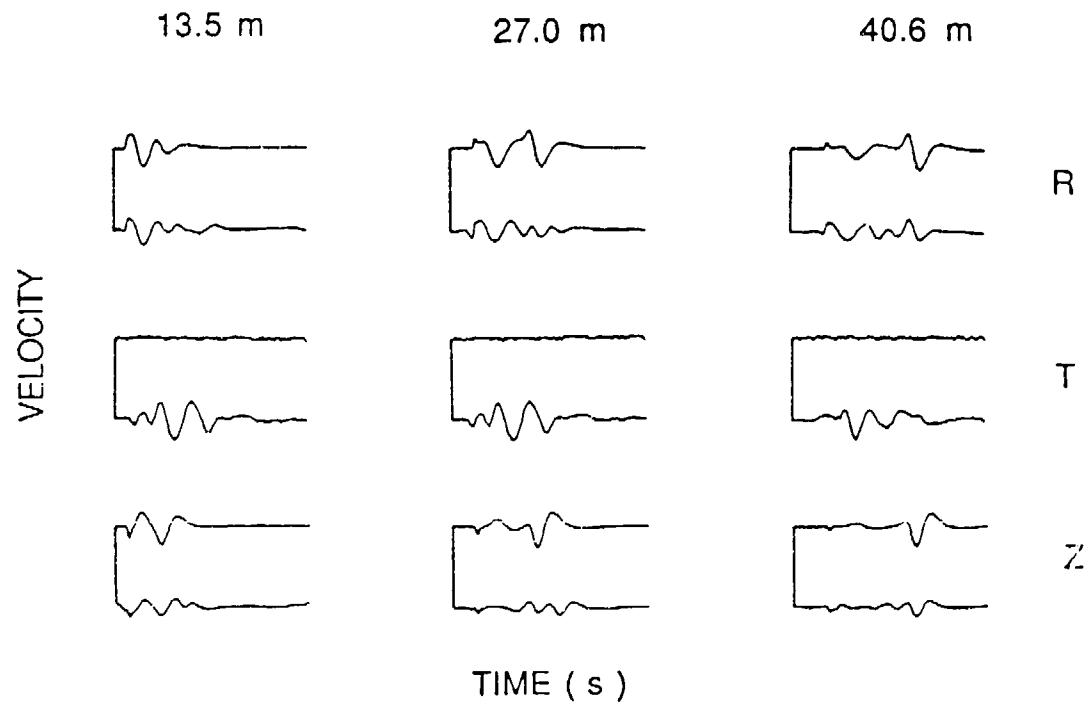


Figure 4.10. Synthetic inversion 366BIC1X. Comparisons are made at three ranges for radial (R), transverse (T) and vertical (Z) components. In each pair, the top trace is the input velocity record and the bottom trace is the calculated velocity record. .64 seconds of data are plotted.

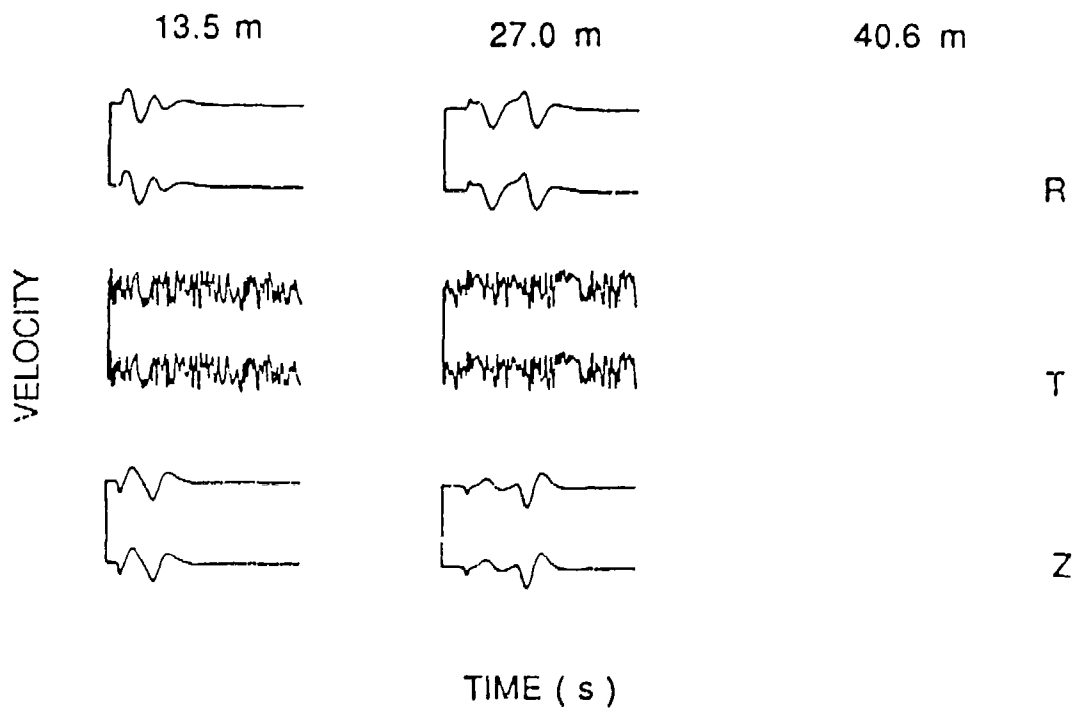


Figure 4.11. Synthetic inversion OMEGAN1. Comparisons are made at only the two ranges for radial for which data was input: 13.5 and 27 meters. Radial (R), transverse (T) and vertical (Z) components. In each pair, the top trace is the input velocity record and the bottom trace is the calculated velocity record. .64 seconds of data are plotted.

larger off-diagonal components in the moment tensors relative to the noise trials.

The correlation coefficients for the station distribution tests are similar to those of the noise tests. The difference here is that with fewer stations, the noise in the transverse is modeled because there are not enough stations to distinguish noise from signal. For example, OMEGAN1 has almost perfect correlation coefficients on all six components. Figure 4.11 shows how the noise on the transverse components was modeled.

#### D. Source Inversions with Observational Data

Table 11 gives the peak time domain amplitudes of the source inversions with the CAMT1 observational velocity records. Similar analyses to the ones completed for the synthetic trials will describe these inversions. Here the input is actual observed velocity waveforms. In Section 4.D.1 the results of inversions utilizing half-space Green's functions are given. Section 4.D.2 describes the inversion utilizing layered half-space Green's functions. Condition numbers are discussed in Section 4.D.3 and correlation coefficients and fits are discussed in Section 4.D.4.

##### 1. Halfspace Inversions

This section describes the results of inversions using the CAMT1 observational velocity seismograms and half space Green's functions. Two half space inversions were run. One

TABLE 11

PEAK TIME DOMAIN AMPLITUDES FROM  
CART OBSERVATIONAL SOURCE INVERSIONSMOMENT RATE ( dyne-cm/s  $\times 10^{16}$  )

TRIAL	NAME	M'11	M'12	M'13	M'22	M'23	M'33	M'ISO
115C1		5.086	.006168	.03768	5.062	.0433	4.938	5.030
366C1		13.64	.45160	1.869	13.60	.7028	35.56	20.90
C1F		3.302	.2254	.7868	3.492	.4632	5.912	4.155
C1H		1.659	.4189	1.208	2.210	.7223	3.154	1.705
C1N		2.515	.3103	.5248	2.596	.4600	3.427	2.769
C1O		.9724	.3260	.0789	1.134	.0412	.7122	.8019
C2N		8.665	.1403	.4585	8.340	4.039	18.03	11.64
C3N		3.250	.4354	2.671	7.227	.5965	7.305	4.871

MOMENT ( dyne-cm  $\times 10^{14}$  )

TRIAL	NAME	M <sub>11</sub>	M <sub>12</sub>	M <sub>13</sub>	M <sub>22</sub>	M <sub>23</sub>	M <sub>33</sub>	M <sub>ISO</sub>
115C1		11.98	.04672	.5132	11.81	.2492	14.49	12.76
366C1		121.6	.8632	23.68	110.9	4.184	310.4	180.9
C1F		9.787	1.587	2.935	10.16	1.160	16.93	12.23
C1H		7.226	1.703	1.032	5.799	1.449	8.253	6.611
C1N		9.337	4.796	3.063	9.380	3.130	11.68	10.13
C1O		5.551	4.554	.4050	4.769	.3540	3.078	3.463
C2N		33.55	2.562	.0579	32.36	1.933	71.35	45.75
C3N		7.207	2.014	6.635	13.71	3.876	17.08	10.91

with the slow HS Green's functions, HS115, and the other with the fast HS Green's functions, HS366. The HS115 Green's functions were used for the majority of the synthetic data inversions in the previous section. When comparing the real data inversions of this section with the synthetic data inversions of the previous section note there is a difference in the number of points calculated in the frequency domain. The observational data inversions have 256 time points (1.28 seconds) and 128 frequency points. The synthetic data inversion have 128 time points (.64 seconds) and 64 points in the frequency spectra.

The results of the HS115 inversion are shown in Figure 4.12. The moment rate tensor and its integral, the moment tensor are shown in 4.12a and 4.12b with the modulus of the  $M'_{11}$  and  $M'_{12}$  elements shown in 4.12c. Refer to Figure 4.1 for labels of the moment tensor elements. 1.28 seconds of data are plotted in the moment rate and moment time series.

The dashed curves in 4.12 are the variances as discussed in Section 4.C.2. The standard deviation is 5 times lower than the moment rate estimate between 4 and 40 Hz. A similar measurement from the synthetic inversion with 1 % noise limited the frequency band of interpretable data to 1.5 - 50 Hz. Based on these variance estimates there are less high frequencies available for interpretation than predicted by the synthetic models.

The LPL of the  $M'_{11}$  component in Figure 4.12c is  $1.4 \times 10^{15}$  dyne-cm compared to  $1.0 \times 10^{15}$  dyne-cm for synthetic

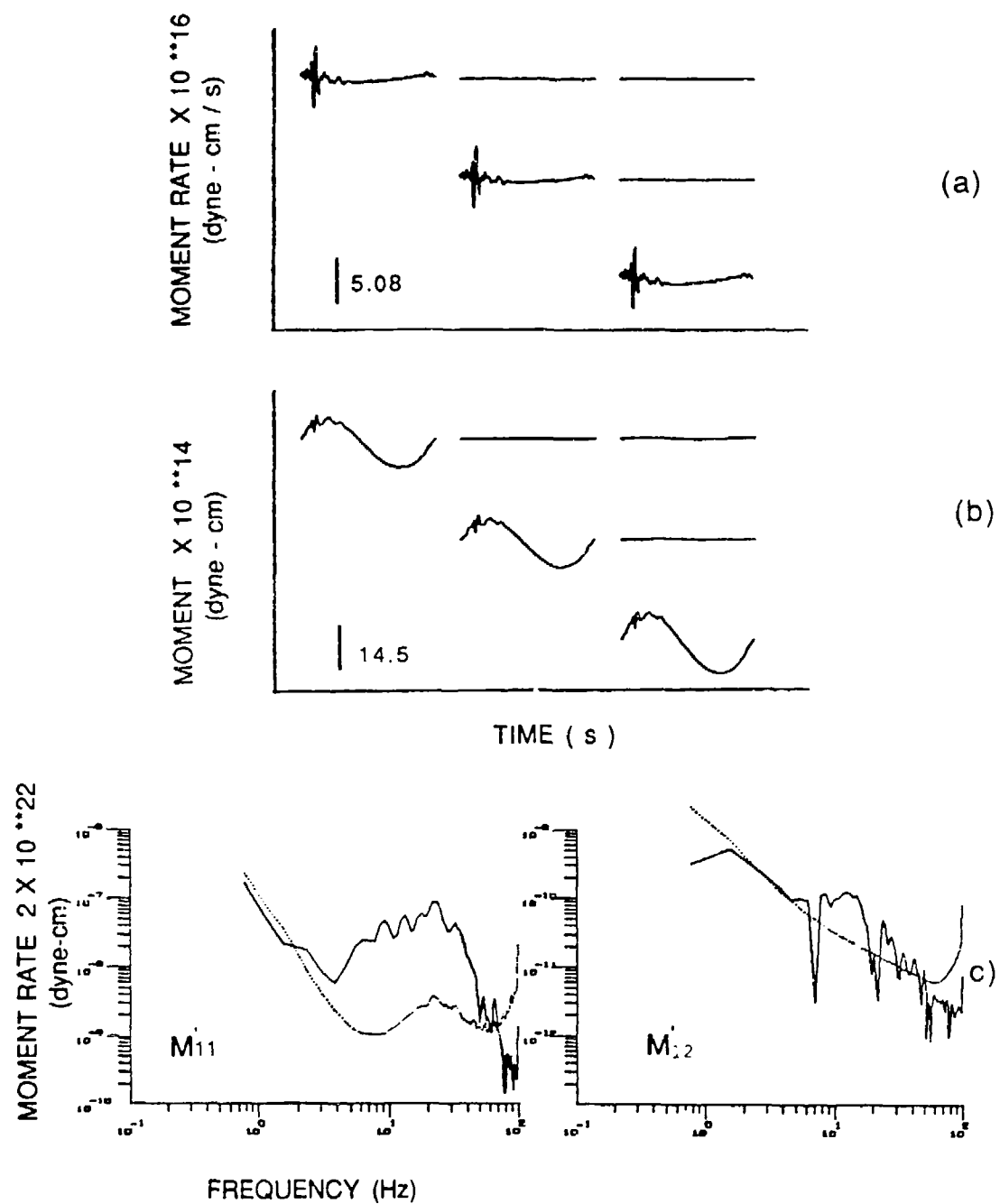


Figure 4.12. Observational inversion 115C1 using CART 1 input velocity and HS115 Green's functions (a)moment rate (b)moment (c)amplitude spectra. Refer to Figure 4.1 for labels.

inversion 115BIC1N1. The similarity of these two inversions confirms the accuracy of the peaks predicted by the forward velocity models in Chapter 3. With similar observations and same Green's functions, the moment is similar.

Time domain comparisons from table 11 show spherical symmetry in the source when the HS115 Green's functions are used. The  $M'_{11}$  and  $M'_{22}$  peaks are within 3% of each other and the off diagonal components have amplitudes of less than 1% of the isotropic amplitude. Similarly the synthetic inversion with HS115 Green's functions resulted in off diagonal components with peaks of only .1% of the isotropic component.

The Results of the HS366 inversion are shown in figure 4.13. The moment rate estimates in figure 4.13c are 5 times larger than the variance between 4 and 40 Hz. The LPL of the  $M'_{11}$  component in Figure 4.13c is difficult to pick because it is not flat between 4 and 40 Hz. The peak at 7 Hz has a LPL of  $7.6 \times 10^{15}$  dyne-cm. This difference in LPL between this inversion and the HS115 inversion is due to velocity differences between the two half-space Green's functions. The faster velocity in model HS115 results in smaller peak amplitudes in the Green's functions (see Figure 4.2). The inversions attempt to make up for the smaller amplitude by putting more energy into the source.

The difference in Poisson's ration between the two models results in a difference in overshoot in the  $M'_{11}$  spectra. Model HS115 with a high Poisson's ratio of .45 results in an increase in source strength between 4.5 and 40

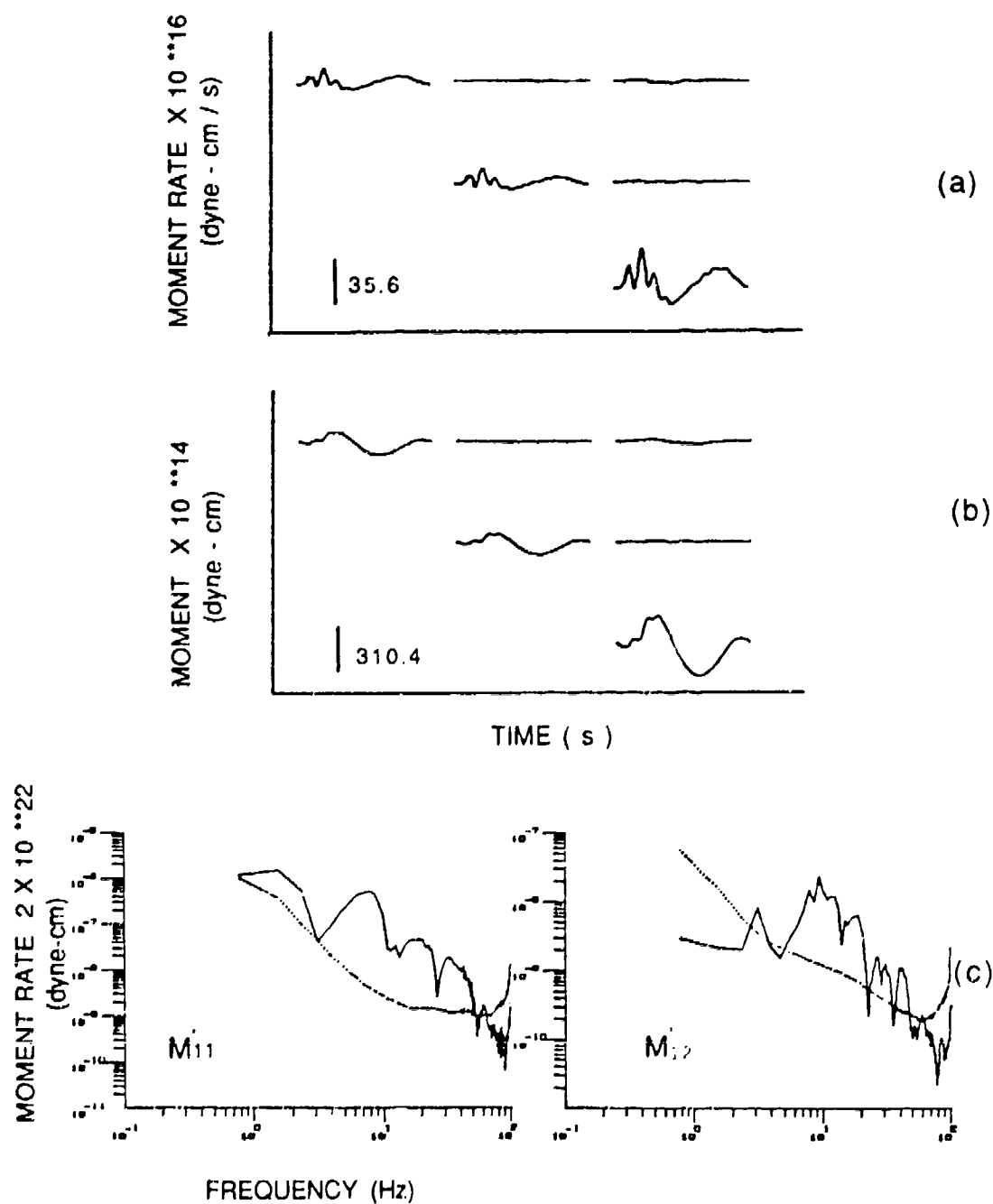


Figure 4.13. Observational inversion 366C1 using CART 1 input velocity and HS366 Green's functions (a)moment rate (b)moment (c)amplitude spectra. Refer to Figure 4.1 for labels.

Hz. Model HS366 with a lower Poisson's ratio of .29 results in a decrease in source strength between 4 and 40 Hz. This phenomenon was predicted by the Mueller-Murphy source models in Figure 3.2d.

The previous two inversions emphasize the influence that test medium velocities have on inversion results. This is even more clearly seen in the comparison of the time domain peaks in table 11.  $M_{ISO}(366)$  is 4 times larger than  $M_{ISO}(115)$ . Comparing the  $M'_{11}$ ,  $M'_{22}$  and  $M'_{33}$  components of the HS366 inversion note that they are not equalized as they were for HS115 inversion. For the HS366 inversion the  $M'_{33}$  component is three times larger than the  $M'_{11}$  and  $M'_{22}$  components. The symmetry of the moment tensors has been changed by the Green's functions. In particular the symmetry has been changed by changing the velocity of the test medium. It is worth noting that similar results were obtained in the synthetic inversion, HS366BIC1X, in which Green's functions with too fast a shear velocity were used.

The HS366 Green's functions also affect the relative strength of the deviatoric moment rate relative to the isotropic moment. While the isotropic moment rate is 88 times greater than the deviatoric for HS115, the isotropic is only 3 times greater than the deviatoric for HS366. In summary the inversion with the HS366 Green's functions results in less spherical symmetry, and increase in  $M'_{33}$  relative to  $M'_{11}$  and  $M'_{22}$  and an increase in LPL by a factor of 5.4.

## 2. Layered Halfspace Inversions

This section describes the results of CART 1 source inversions. Green's functions corresponding to LHS models F, H, N and O listed in table 7 are the path models. Peak moment rates are shown in table 11.

The first comparison is between inversion C1F and C1H. As shown in table 7, models F and H are the same model with the exception of the shear velocity in the most shallow layer. Model F has a  $\beta_1$  of 120 m/s and model H has a  $\beta_1$  of 80 m/s. The Green's functions for both models were calculated by specifying a source depth of 3 meters- just below the interface between layer one and layer two. Comparison of these two inversions allows an isolation of the effect that overburden shear velocity has on the moments. Faster shear velocity results in smaller time domain peaks. This was illustrated by the Green's functions in Figure 4.2. When the time domain peak is smaller, the inversion compensates by increasing the source peak. In table 11 the inversion using faster shear velocity (F) has larger time domain amplitude than the inversion using the slower shear velocity (H).  $M_{ISO(F)} = 4.155 \times 10^{16}$  dyne-cm/s and  $M_{ISO(H)} = 1.705 \times 10^{16}$  dyne-cm/s. Here the difference in shear velocity is 40 m/s and the isotropic components differ by a factor of 2.5.

Another difference between the two inversions can be observed in the separation of the deviatoric and isotropic components.

$$D_{ij(F)} = 0.93 \times 10^{15} \begin{bmatrix} -1.0 & -.24 & -.84 \\ & .80 & .46 \\ & & -1.8 \end{bmatrix} \text{ dyne-cm/s}$$

$$D_{ij(H)} \sim 0.68 \times 10^{15} \begin{bmatrix} -1.0 & -.64 & -1.8 \\ & .20 & -1.1 \\ & & -1.2 \end{bmatrix} \text{ dyne-cm/s}$$

While the isotropic moment rate of inversion C1F is 3 times larger than that of C1H, the deviatoric moment rate is only 1.4 times larger. The relative strength of the deviatoric source components is larger when model H is used than when model F is used to account for the path. Decreasing the shear velocity in the upper layer of model H is responsible for this difference.

The source time functions and amplitude spectra of inversion C1F and C1H are shown in Figure 4.14 and Figure 4.15. The  $M'_{11}$  estimates in C1F are 5 times larger than the variance between 4 and 40 Hz. Similarly, the  $M'_{11}$  estimates in C1H are 5 times larger than the variance between 4 and 40 Hz. An estimate of the LPL of C1F is  $3.0 \times 10^{15}$  dyne-cm compared to  $1.2 \times 10^{15}$  dyne-cm for C1H. These values are rather subjective because the source spectra are not flat between 4 - 40 Hz. These were taken from the spectral peaks.

Inversions C1N and C1O address the problem of source coupling differences. This is possible because the velocity and attenuation parameters in models N and O are identical. The only difference in computation of the Green's functions is the placement of the source. Model N places the source at

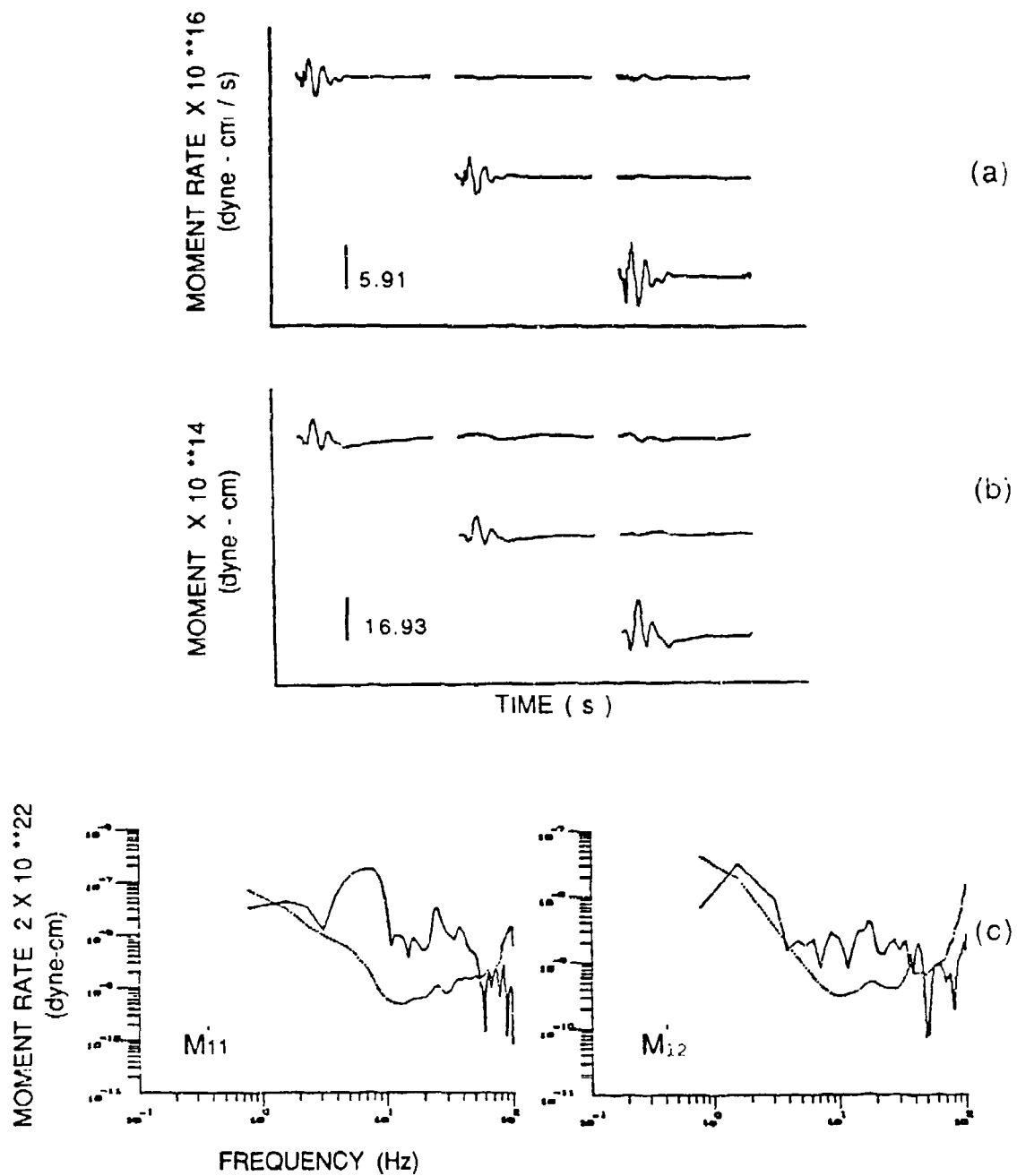


Figure 4.14. Observational inversion C1F using CART 1 input velocity and LHS F Green's functions (a)moment rate (b)moment (c)amplitude spectra. Refer to Figure 4.1 for labels.

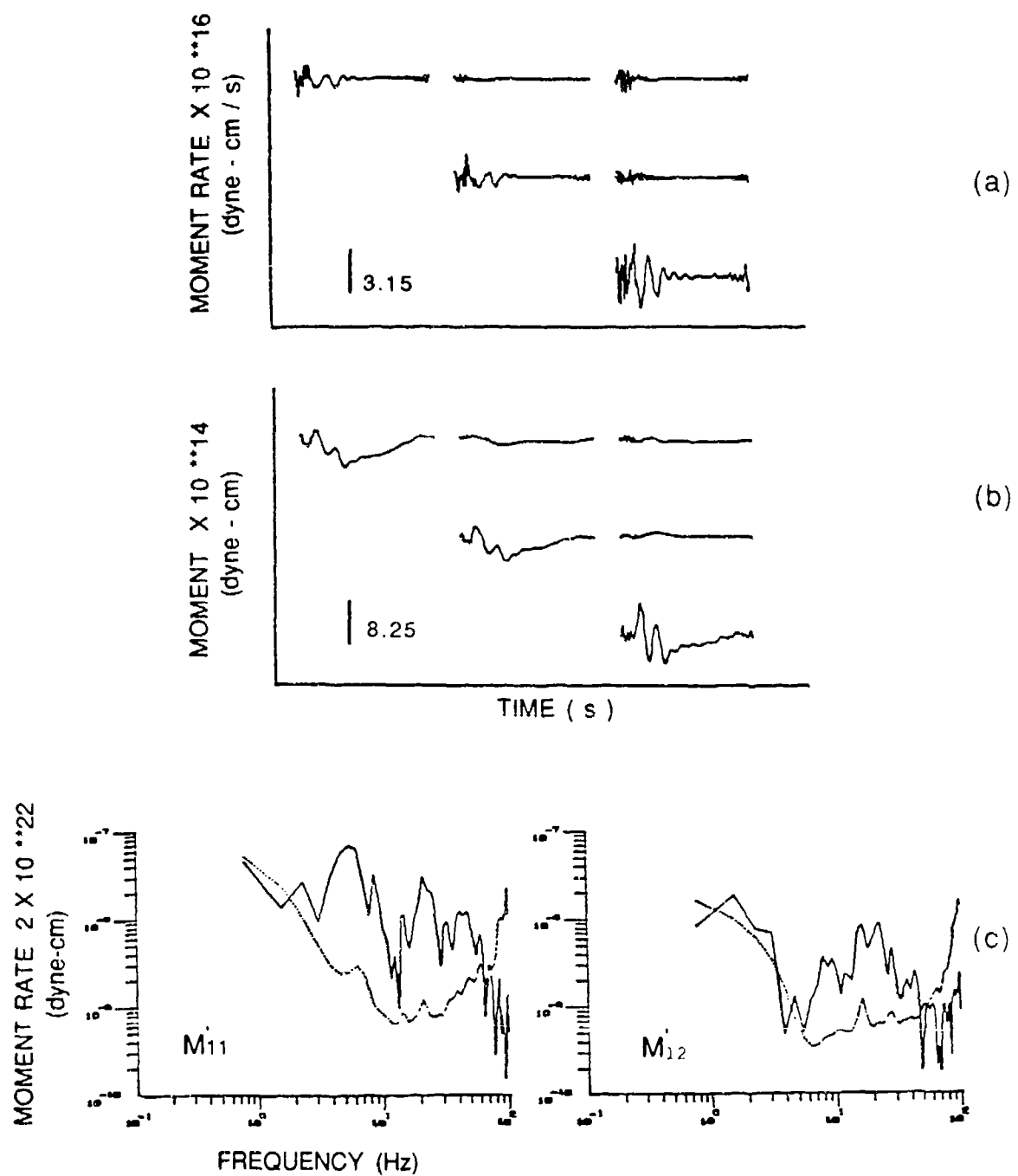


Figure 4.15. Observational inversion C1H using CART 1 input velocity and LHS H Green's functions (a)moment rate (b)moment (c)amplitude spectra. Refer to Figure 4.1 for labels.

3 meters- just below the first interface. The velocities at source depth are 670 m/s and 230 m/s for P and S velocities respectively with Poisson's ratio equal to .43. Model O places the source at 3 meters- this time just above the interface. The velocities at source depth are 270 m/s and 120 m/s with a Poisson's ratio of .38.

The isotropic moment rate peak for inversion C1N is  $2.769 \times 10^{16}$  dyne-cm/s and for C1O it is  $.8019 \times 10^{16}$  dyne-cm/s. There is over a factor of 3 decrease in isotropic moment when the velocity at source depth is decreased. The deviatoric components of C1N are larger than those of C1O relative to their isotropic components. Increasing Poisson's ratio at shot depth increases the contribution of deviatoric relative to isotropic source components.

Figures 4.16 and 4.17 compare the source time functions and spectra for the C1N and C1O inversions. LPL measured from the  $M'_{11}$  spectrum is  $2 \times 10^{15}$  dyne-cm with the N path model and  $.6 \times 10^{15}$  dyne-cm for model O. Model N, with the faster velocity at source depth results in LPL of moment that is 3.3 times greater than that of model O. The above two comparisons show how changes in the Green's functions relate to large differences in the resulting moment tensor estimates.

### 3. Condition Numbers

Condition number as a function of frequency for 4 of the observational inversions are plotted in Figure 4.18. The

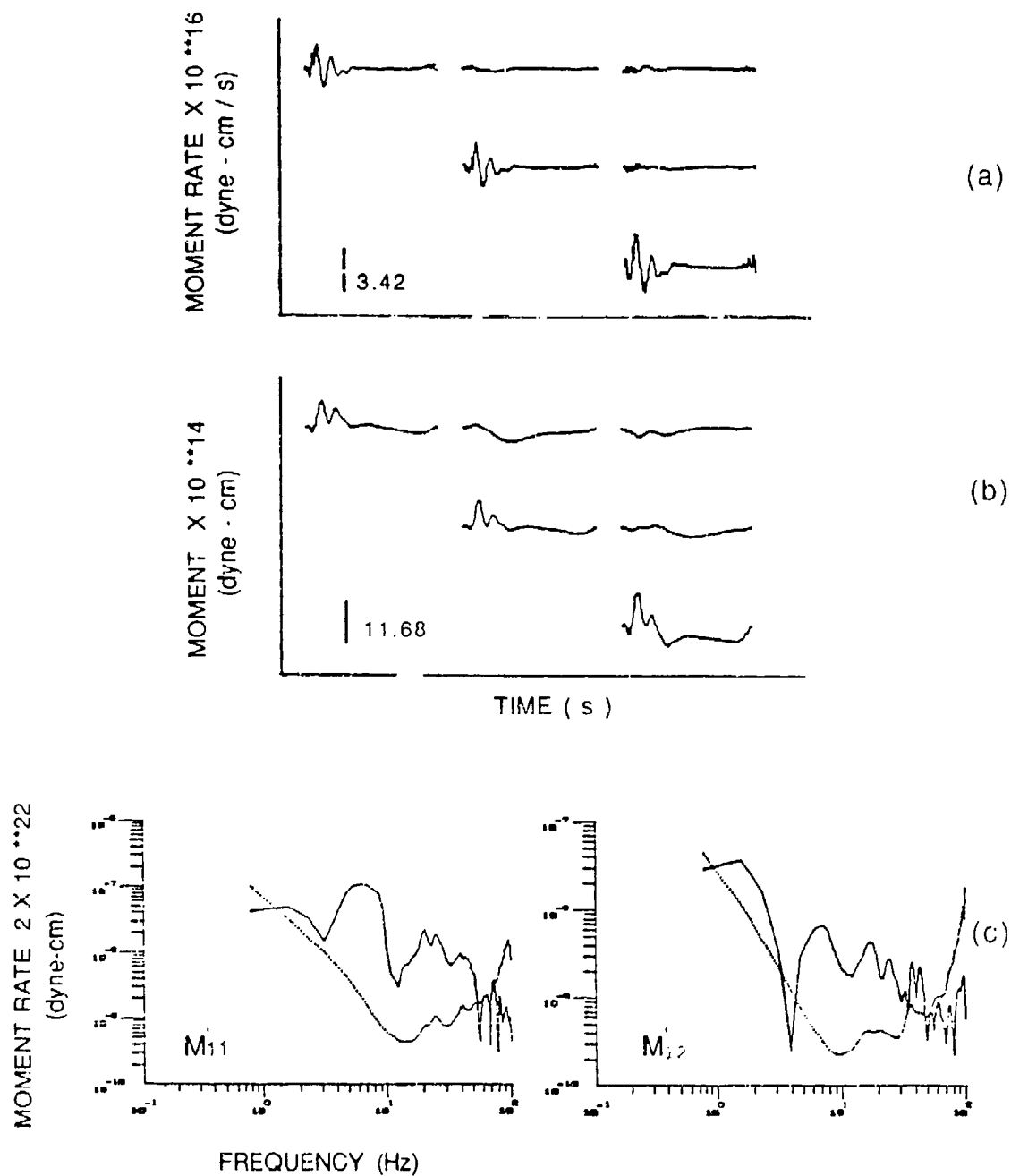


Figure 4.16. Observational inversion C1N using CART 1 input velocity and LHS N Green's functions (a)moment rate (b)moment (c)amplitude spectra. Refer to Figure 4.1 for labels.

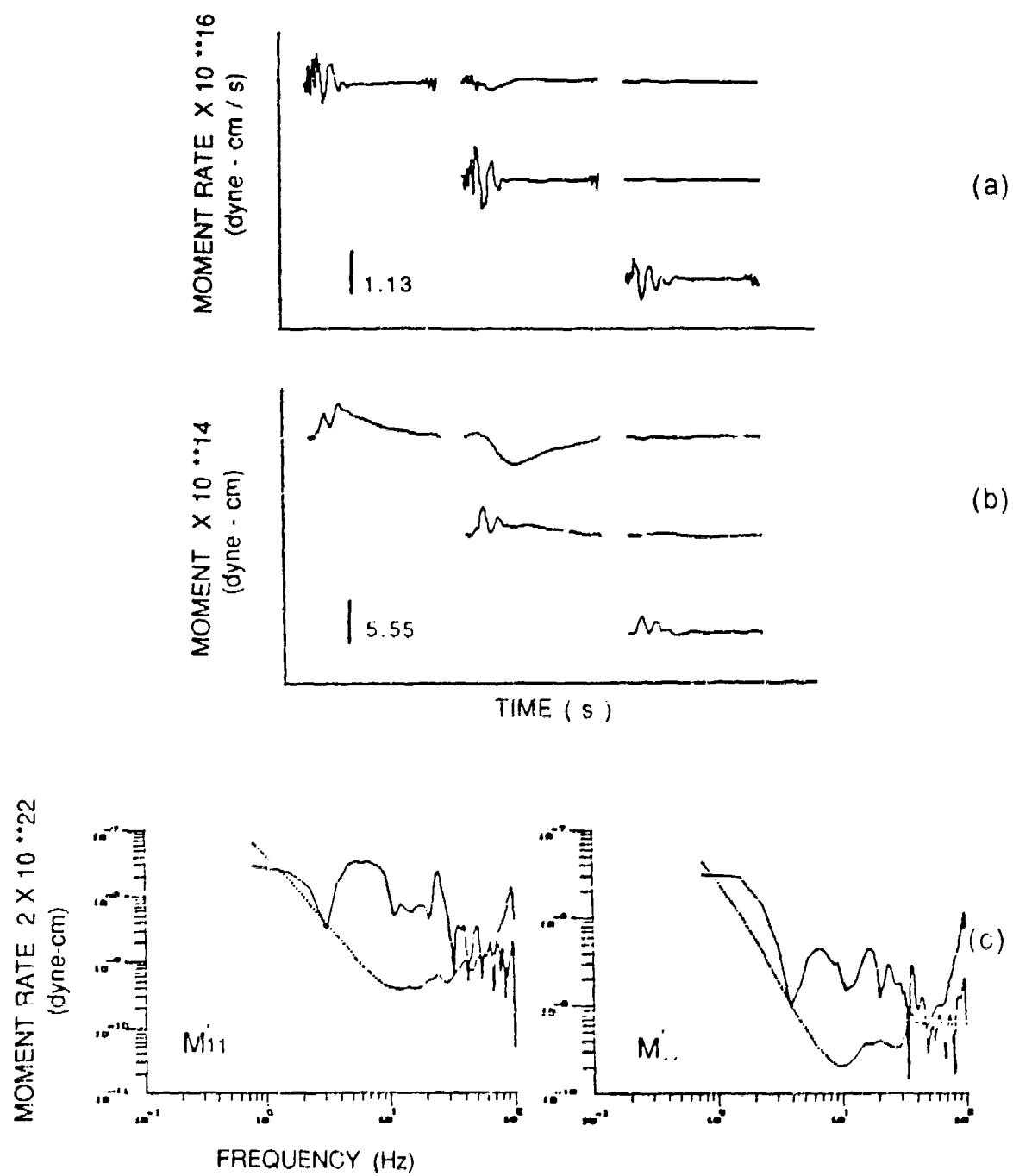


Figure 4.17. Observational inversion C10 using CMT 1 input velocity and LHS 0 Green's functions (a)moment rate (b)moment (c)amplitude spectra. Refer to Figure 4.1 for labels.

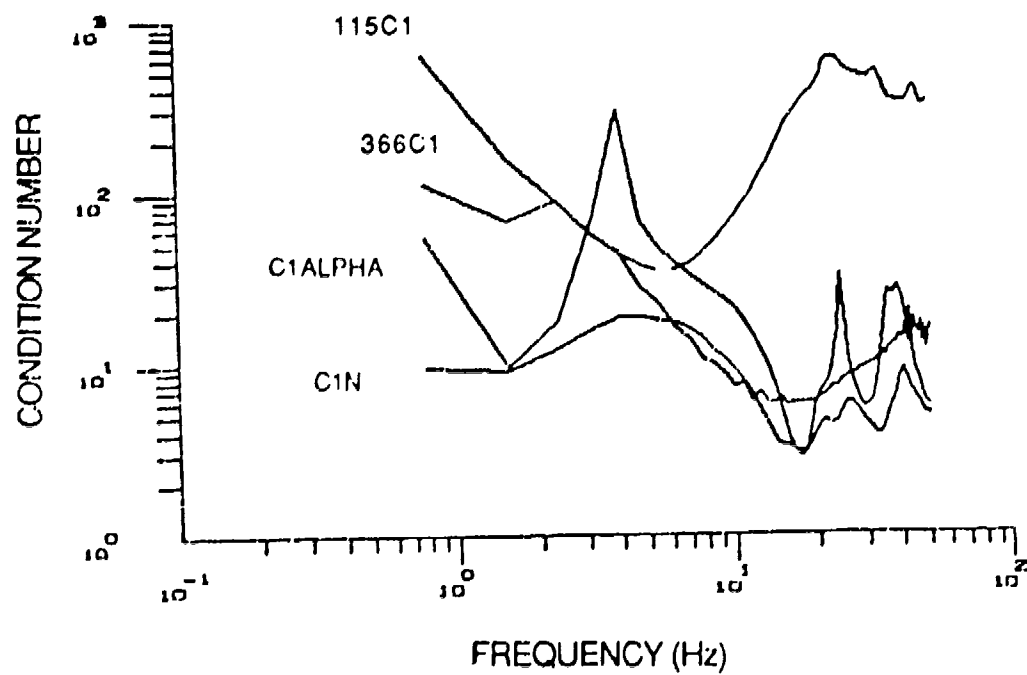


Figure 4.18. Condition numbers versus frequency for 4 observational inversions..

condition numbers for inversions C1F, C1H, C1N, C1O and all have average values of 10. Only C1N is plotted in Figure 4.18. All but 115C1 are have similar shape and values of around 10 beyond 10 Hz.

C1ALPHA has a peak of 300 at 40 Hz corresponding to a spectral hole in the Green's functions. A similar peak occurred in the synthetic inversion, ALPHAN1, when the same Green's functions were used and the input velocities were limited to one range.

The condition numbers associated with inversion 115C1 are larger than all others with the exception of the peak in C1ALPHA. As was discussed in Section 4.C.5, the inversions with the slowest shear velocities produce the largest condition numbers.

#### 4. Time Domain Fits

Correlation coefficients for the 9 CART 1 observational data inversions are listed in table 12. The input seismograms are compared to the calculated seismograms in Figures 4.19 - 4.20. Comparisons are made at the three ranges representative of the CART 1 data set: 13.5, 27.0 and 40.6 meters. In each pair, the top trace is the input velocity record and the bottom trace is the velocity record calculated from the input Green's functions and the inverted moment rate tensor.

Figure 4.19 shows the time domain fits to the CART 1 data using the slow path model, HS115. Figure 4.20 shows the

TABLE 12

 CORRELATION COEFFICIENTS FOR  
 CART I OBSERVATIONAL SOURCE INVERSIONS

RANGE (m)	13.5	13.5	13.5	27.0	27.0	40.6	40.6
AZIMUTH	90	270	0	180	35	215	325
<b>TRIAL NAME</b>							
115C1	.8399	.8742	.9365	.7130	.6064	.6889	.7355
	.1720	.3665	.2727	-.0388	.4888	.5647	.2253
	.2189	.7611	.6304	.2027	.0591	.6573	.7717
366C1	.9112	.9118	.7123	.8855	.7330	.9104	.8410
	.4866	-.1501	.5584	-.0897	-.2005	.5791	.4078
	.6928	.5851	.6205	.8615	.7260	.8113	.7602
C1F	.9550	.9657	.8729	.9408	.7780	.8974	.9162
	.3111	.4154	.6921	.2074	.2636	.6850	.1269
	.5852	.6993	.6688	.6827	.6066	.6636	.4747
C1H	.9263	.9489	.8740	.8089	.8599	.6700	.6427
	.4333	-.1449	.5746	.2112	.0696	.2491	.1180
	.3729	.5396	.4495	.4961	.1807	.1745	.1622
C1N	.9584	.9501	.7800	.6364	.5430	.8132	.8418
	.5016	.6531	-.1258	.0644	.7026	-.1943	-.0248
	.4801	.5897	.5689	.0639	-.0403	.4550	.4195
C1O	.9715	.9726	.7788	.8014	.7574	.6196	.6510
	.5577	.6457	.0817	.3276	.6716	-.0894	.1748
	.4294	.5201	.4345	-.0109	-.1275	.2404	.3998
C1GAMMA	.9581	.9647	.6508	.8525	.7379		(R)
	.5849	.6773	-.1847	.1932	.7040		(T)
	.4449	.5629	.4818	.1983	.2239		(Z)
C1ALPHA	.9920	.9924	.9967				(R)
	.8630	.9396	.7981				(T)
	.9684	.9801	.9567				(Z)
C1OMEGA	1.0000	1.0000					(R)
	1.0000	1.0000					(T)
	1.0000	1.0000					(Z)

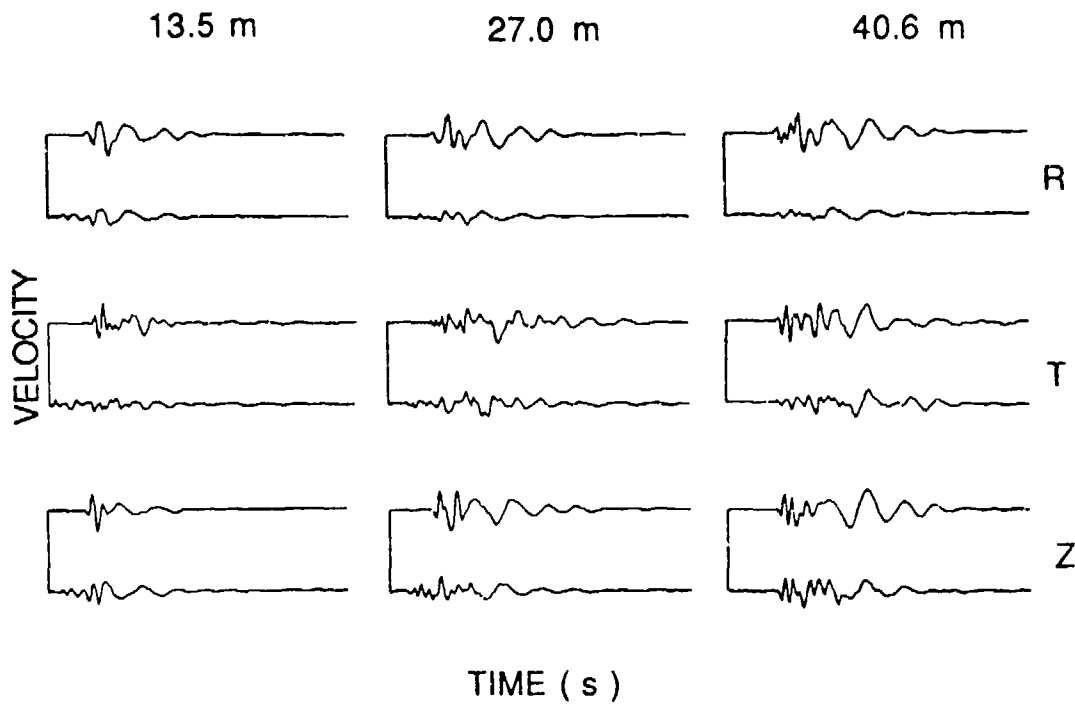


Figure 4.19. Observational inversion 115C1. Comparisons are made at three ranges for radial (R), transverse (T) and vertical components. In each pair, the top trace is the input velocity record and the bottom trace is the calculated velocity record.

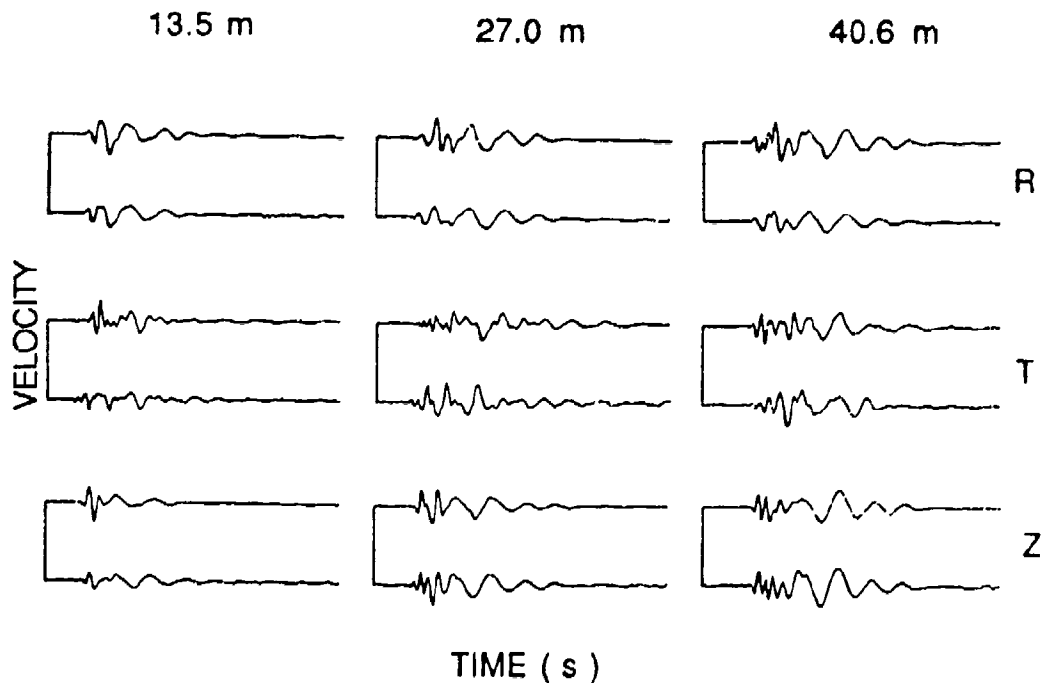


Figure 4.20. Observational inversion 366C1. Comparisons are made at three ranges for radial (R), transverse (T) and vertical components. In each pair, the top trace is the input velocity record and the bottom trace is the calculated velocity record.

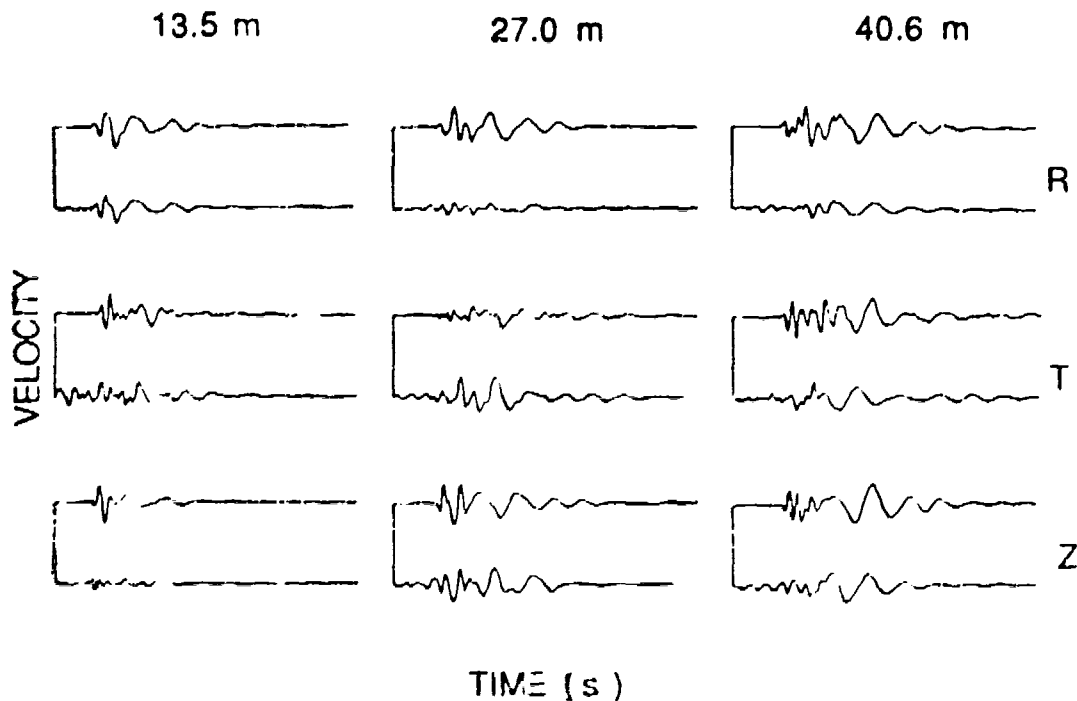


Figure 4.21. Observational inversion C16. Comparisons are made at three ranges for radial (R), transverse (T) and vertical components. In each pair, the top trace is the input velocity record and the bottom trace is the calculated velocity record.

fits when the fast HS model, HS366 is used. The peak amplitudes of the input seismograms are matched better by the HS366 inversion than the HS115 inversions. The HS366 inversion also does a better job of matching the surface waves.

As a representative of the LHS fits, inversion C1N velocities are plotted in Figure 4.21. At 13.5 meters the radial peak is matched but the vertical peak is underestimated. At 27.0 and 40.6 meters the radial peaks are underestimated while the vertical peaks are better matched.

## CHAPTER 5

### SUMMARY AND CONCLUSIONS

The CART/ART tests have been useful in demonstrating a method of experimental seismology to constrain source characteristics for small explosions. One advantage to this approach is that physical parameters, such as velocities of the source medium, can be measured in the field to enhance modeling procedures. Trade-offs in the source and path effects are unavoidable even on the small scale. This study has attempted to quantify these trade-offs as they relate to uncertainties in the McCormick Ranch site model. Conclusions from this study fall into three main categories: increased knowledge of the path effects, increased knowledge of the source physics and recommendations for future tests.

#### A. McCormick Ranch Geological Model

Low velocities, low Q-values, and high Poisson's ratio of the McCormick Ranch test site are factors that contribute to some unique problems in the source models. The best model for the site was given in Table 3. P-velocities are believed to be reliable as are depths to interfaces. Upper layer Q values are very low (5-10).

The hardest parameter to define is shear velocity. Because there was insufficient data to resolve the shear

velocities, a range of shear values was carried into Chapter 3 on forward modeling and Chapter 4 on inverse modeling. Uncertainty in shear velocity strongly affects the relative amplitudes of the path functions and thus influences the symmetry and strength of the source functions. As an example, inversions C1F and C1H illustrate the importance of overburden shear velocity. Decreasing the top layer shear velocity from 80 to 120 m/s had the effect of decreasing the source strength from  $3 \times 10^{15}$  dyne-cm to  $1.2 \times 10^{15}$  dyne-cm.

### B. Source Physics

An iterative process of refining the proportionality constants in the 1971 Mueller-Murphy forward models produced a range of possible CART source interpretations. These constants can be used as a starting point for future studies in which dry alluvium is the source medium.

The best forward model (BASIC) was obtained by using the following constants: a compaction factor ( $k_1$  in equation 3.7) of 0.4, an elastic radius factor ( $k_2$  in equation 3.8) of 417; a cavity radius factor ( $k_3$ , Equation 3.9) of 28.5 and decay constant factor ( $k_4$ , Equation 3.10) of 1.5. Errors in cavity radius were shown to be of particular importance because of the relation between cavity radius and the long-period-level of the moment rate spectrum which is interpreted directly as source strength.

Errors in the Green's function can lead to changes in the symmetry of the source. The inverted source functions

were predominantly spherical when the slow HS Green's functions were used. When fast HS Green's functions were used, the deviatoric source components increased in size relative to the isotropic source. In particular synthetic tests with the wrong Green's functions resulted in diagonal components of the moment tensor with the  $M_{33}$  increased in amplitude by a factor of almost 3. There was also a factor of 4 error in source strength.

This study serves as an investigation into methods of determining yield scaled source models for small sources. Although absolute measurements of source strength are dependent on accurate velocity models, a site-specific scaling model is obtainable using the experimental method outlined in this study. The next step would be to repeat the study in the same source medium at similar scaled ranges but with incrementally larger yields. In this way a yield-scaling would be developed for alluvium. The same series of tests would then be conducted in other rock types.

#### E. Recommendations

Site parameterization should be done before explosion tests. Because of their importance in determining the long-period-level of the isotropic source, it is essential to constrain velocities of the source medium. In addition, preliminary site characterization could help avoid placing the source near an interface.

Forward modeling can be done after the site is characterized and before the explosions.

When alluvium is the source medium, Poisson's ratio can be high. The result is that the Green's functions have very large amplitudes with respect to the shear components. The method may not be so sensitive to shear velocities errors when a medium with lower Poisson's ratio is used.

Slightly larger sources should be used so the burial depth for containment is deeper. This should reduce the problems of the near-surface inhomogeneities.

CART I design is recommended because it has the best range coverage and azimuthal coverage. Designs can be tested through inversion of synthetic data. The condition numbers indicate whether the design is particularly sensitive to noise in the data.

To compare contained and uncontained shots, stations should be placed in the same relative locations so the same Green's functions can be used for the two different sets of inversions. This will improve bias of comparisons. Even if the Green's functions are not known with more certainty at least the error will be systematic allowing direct comparison of source functions.

Finally, the development of two additional field techniques would be useful: an improved method of obtaining shear velocities and empirical measurements of the final cavity radius. Both of these measurements could help determine the source strength in an absolute sense.

APPENDIX A  
DATA CORRECTIONS

Data corrections refer to those steps taken to convert the observed accelerograms to velocity and displacement records. The processing steps (PS) are listed, discussed and illustrated below. In order to maintain continuity in illustrating the processing steps, some figures are presented that are not referred to in the text.

- 1.0 Deglitch
- 2.0 Rescale
- 3.0 Integrate to velocity
  - 3.1 Remove slopes
  - 3.2 Hi-pass filter
- 4.0 Integrate to displacement
- 5.0 Window

PS 1.0 Deglitch. Instrument glitches were removed using a maximum threshold amplitude with all values in the series above the maximum replaced by an arithmetic mean of surrounding data points. Six channels out of sixty were deglitched.

PS 2.0 Rescale. Each point in the acceleration time series was multiplied by a scale factor to convert digital counts to  $\text{cm}/\text{s}^2$ . The peak accelerations for each channel of data are listed in Appendix C.

PS 3.0 Integrate. Observed accelerations were integrated in the time domain using the trapezoid rule. Integration had the effect of boosting the long-period end of the spectrum. Because slopes and long-period noise made the signal look noncausal, corrections were necessary to return the records to realistic velocity records. Long-period noise estimates are not available at the time of this writing.

PS 3.1 Remove slopes. Slopes were subtracted using cursors on a graphics terminal with an interactive plotting routine. Slope removal was the most time consuming of the processing step, because several attempts were made on each channel of data before the proficiency was acquired to do this step in a consistent manner.

The observed slopes are grouped into the six different types listed in table 13. Also given in the table are the percentages of occurrence of each type. Discussion of each type follows.

Type 1 is just a constant slope in velocity. An example is given in Figure A.1b (file 2D3). A constant DC offset in acceleration causes this type of slope. To illustrate this point the DC offset ( $1.2 \text{ cm/s}^2$ ) in acceleration was removed before integration. The resulting uncorrected velocity (Figure A.1e) did not exhibit the ramp as in Figure A.1b. The spectra in Figures A.1b, 1c and 1e show great similarity between 3 and 70 Hz. Below 3 Hz the effect of the ramp is seen as a rise in long-period energy.

Although removing a DC term in acceleration or removing a ramp in velocity are equivalent processing steps, several tests such as the one described above lead to the conclusion that it is preferable to remove the slope after integration. The reasoning behind the preference is that in calculating the DC offset, only the first 30 points are used whereas slope removal in velocity uses more points for the average.

Type 2 was the most commonly observed slope. An example is given in Figure A.2 ( file 2A3 ). The step was identified and located by drawing one line through the points before the onset of the signal and another line through the points after the signal had passed. Location of the step is coincident with the first peak of the signal in each case. The slopes before and after the step are equal for half of the channels with this slope type suggesting that the step is superimposed on the type 1 slope. In other words, if the DC offset were removed before integration, type 2 would not have a slope but rather a step in uncorrected velocity. Note that the step occurs at the time for signal arrival ( types 2 and 5 ) in 16 of 20 channels on the radial component ( see table 13 ).

One explanation for the step is that it is related to a sampling problem. If the recording system failed to reproduce all the high frequency components of the signal, the error would be largest on the first cycle of the accelerogram for a dispersive wave. In other words, the area under the curve for the first two cycles is not balanced.

TABLE 13  
TYPES OF OBSERVED SLOPES WITH PERCENTAGES

	R	T	Z	Total %
(1) Constant	5	2	4	18.3
(2) Step	7	3	14	40.0
(3) Two Ramps	6	2	0	3.3
(4) Three Ramps	2	10	0	20.0
(5) Step and Ramp	5	2	2	15.0
(6) Other	1	1	0	3.3

A test of this hypothesis was to reproduce a step in a file that did not exhibit a step in uncorrected velocity (see Figure A.1e). A 4-pole low-pass Butterworth filter with the corner at 50 Hz was applied to the DC-corrected acceleration data of file 2D3 (Figure A.1a). The file was then integrated to yield uncorrected velocity. The results were marginal in reproducing a step.

Continuing the test, a similar filter with corner at 30 Hz was applied to acceleration. In addition, a filter at 60 Hz with a 12-pole roll-off was applied to the DC-corrected acceleration. Steps in uncorrected velocity resulting from these filter tests are negligible compared with those observed for the type 2 slope.

The above tests failed to reproduce steps because the high frequencies were reduced throughout the signal time window. In order to explain the location of the step at the first arrival, the high frequency depletion should affect only the first cycle.

In a different test to replicate the steps, the amplitude of only the first positive peak was reduced. As illustrated in Figures A.3a and A.3b, the first peak was reduced from  $1505 \text{ cm/s}^2$  to  $1305 \text{ cm/s}^2$  (13.3%) by editing the acceleration file. As shown in Figure A.3c, this procedure has replicated the slope observed in Figure A.2b where the step is 5% of the maximum velocity. Comparison of spectra in Figures A.1b and A.3c shows similarity above 3 Hz.

Now, comparing Figures A.3d and 1f, the slope-correction process is validated. Figure A.1f represents the original file which had no step in uncorrected velocity and in Figure A.3d an artificial step has been successfully removed. The same test was repeated with a 90 % reduction in peak amplitude (see Figure A.4). Again the correction process is validated comparing Figure A.4c with Figure A.1f. Note that the spectra in Figures A.1f, A.3d and A.4c are almost identical below 40 Hz.

The conclusion is that loss of energy above the anti-alias filter corner frequency (70 Hz) may have affected the representation of the signal but that due to dispersion, this effect is only important in the first cycle. While the slope correction procedure cannot restore high frequencies, it does improve the representation of the signal by increasing the amplitude of the first arrival by an appropriate amount.

Slope types 3 and 4 are similar to the type 1 ramp in uncorrected velocity with the addition of slope changes at various times throughout the signal. An example of slope type 3 is given in Figure A.5b (file 2G2). Note that the slopes in Figure A.3b could be redrawn with 3 instead of 2 slopes. That would have made file 2G2 an example of the type 4 slope with three ramps, one occurring at the arrival of the signal.

Type 3 and 4 slopes may be related to tilt of the accelerometer. If this is the case, the changes in slope should occur on both horizontal components at the same point.

in time. A comparison should be made with files 2G2 and 2G3 (Figures A.5b and A.5c) for verification. Otherwise, if the changes do not occur at the same time, then the tilt was with respect to only one axis. The lesson learned by comparing Figures A.5b (transverse component) and 5c (radial component) is that a better interpretation is made when all three components are corrected simultaneously.

Peak amplitudes in acceleration, velocity and displacement are given in Appendix C. Peak acceleration amplitude of the transverse component is an average of 25% of the radial. One explanation for the apparent slope changes on the transverse components is that tilt is more obvious due to smaller transverse amplitudes. The instrument tilt required to cause the change in slope in Figure A.5b is 0.06 mm. The calculation was made for an instrument box 18 inches (460 mm) in length. Tilts of this magnitude could be caused by shifting of the instrument box in the dry alluvium after the signal has passed.

Type 4 slope is similar to type 3 except that two changes in slope occur. The first change is coincident with signal arrival and the second change is after the signal has passed. Half of the transverse components required the removal of slope type 4.

Slope types 3 and 4 are difficult to remove consistently because of the placement of the change in slope. In attempts to repeat the corrections, it was noted that the placement of the change in slope affects the appearance of the long-period

noise in the slope-corrected velocity (Figure A.5d). However, the high-pass filter applied in the next processing step (PS 3.2) does a good job of removing the long-period oscillations before and during the signal (Figure A.5e). After repeating the entire processing sequence for a file such as 3A2 the corrected velocity records look the same even if the slope corrections were slightly different.

Types 5 and 6 are combinations of types 1-4. Type 5 slope is a step followed by a ramp. Type 6 slopes are similar to the others but with an extra change in slope. In one case (file 1A2) the change in slope occurred before signal arrival. In another case (file 2B1) the uncorrected velocity was similar to type 5 except that the step at the signal arrival was very large and there was an extra slope change after passage of the signal. Both of these channels are excluded from analysis because of their unusual characteristics.

PS 3.2 High-pass filter. In the discussion of slope type 3, the long-period noise resulting from the integration and slope removal was pointed out. The best filter design was determined by finding the corner that would eliminate most of the long-period noise and retain the broadest frequency band possible. The optimal corner was found to be 3.5 Hz as illustrated in Figure A.1.

During early work with the data different 4-pole filters were designed for each file. Later, it was determined that the 4-pole filter had too steep a roll-off and introduced

significant acausal arrivals. This effect is illustrated by comparing Figures A.6 (4-pole) with Figure A.2d (2-pole).

The final filter design is a 2-pole high-pass Butterworth filter with corner at 3.5 Hz. Every channel of data was passed through this same filter after slope removal. The non-zero phase characteristics of this filter are compensated in the inversions.

PS 4.0 Integrate to displacement. The corrected velocity records are integrated a second time to yield displacement. Figures A.7a and A.7b illustrate the problems with the long-period noise if the filter in PS 3.2 is not applied before the second integration. When the filter is applied before the second integration, no further corrections are necessary.

PS 5.0 Window. The corrected velocity records are windowed from 600 points to 256 points with 25 points before the signal arrival and 231 points after the signal arrival.

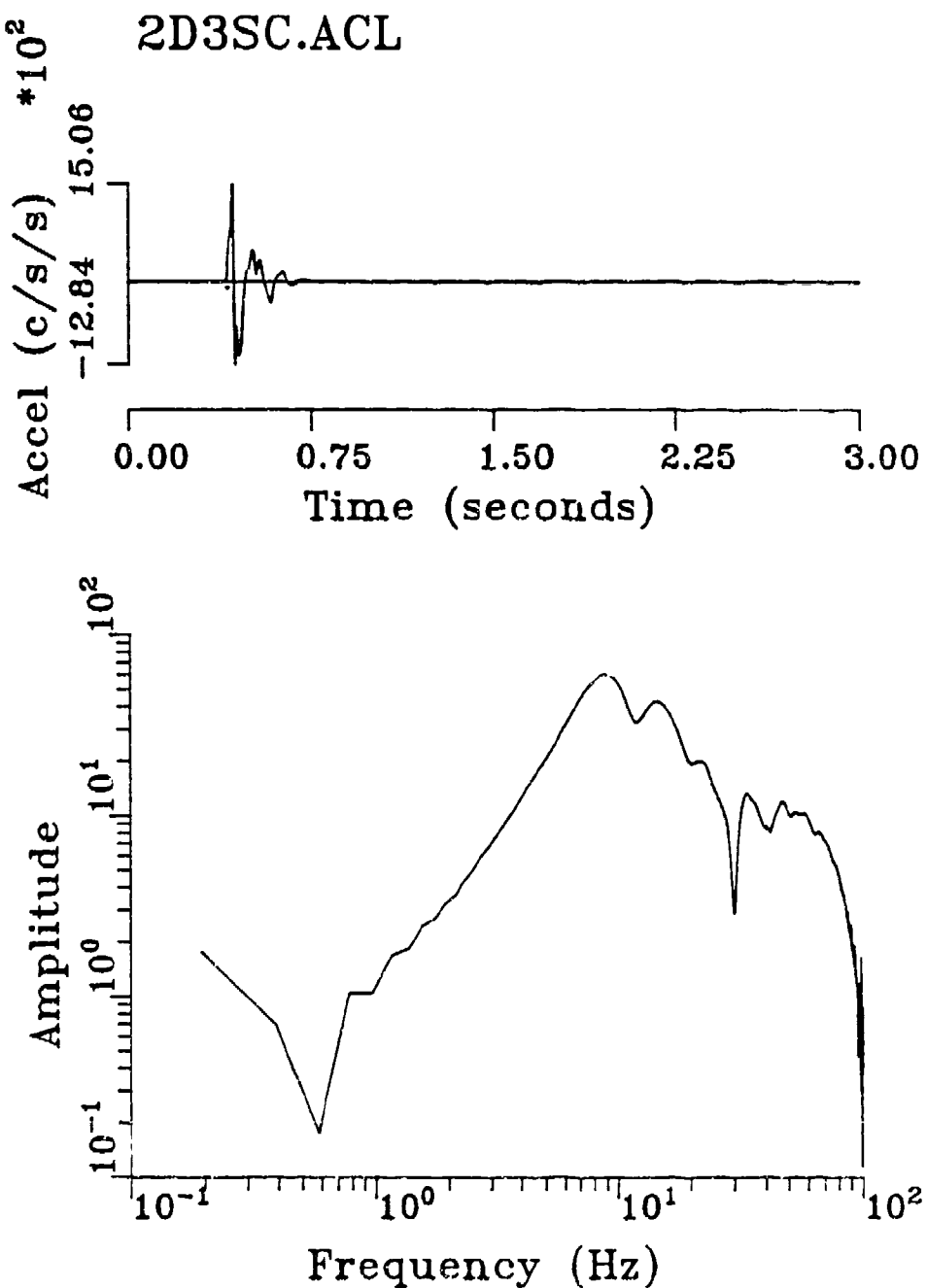


Figure A.1a. Observed acceleration scaled to  $\text{cm}/\text{s}^2$ . File 2D3 is the radial component observed at the 5 meter range. Peak amplitude is 1.56 g. PS2.0

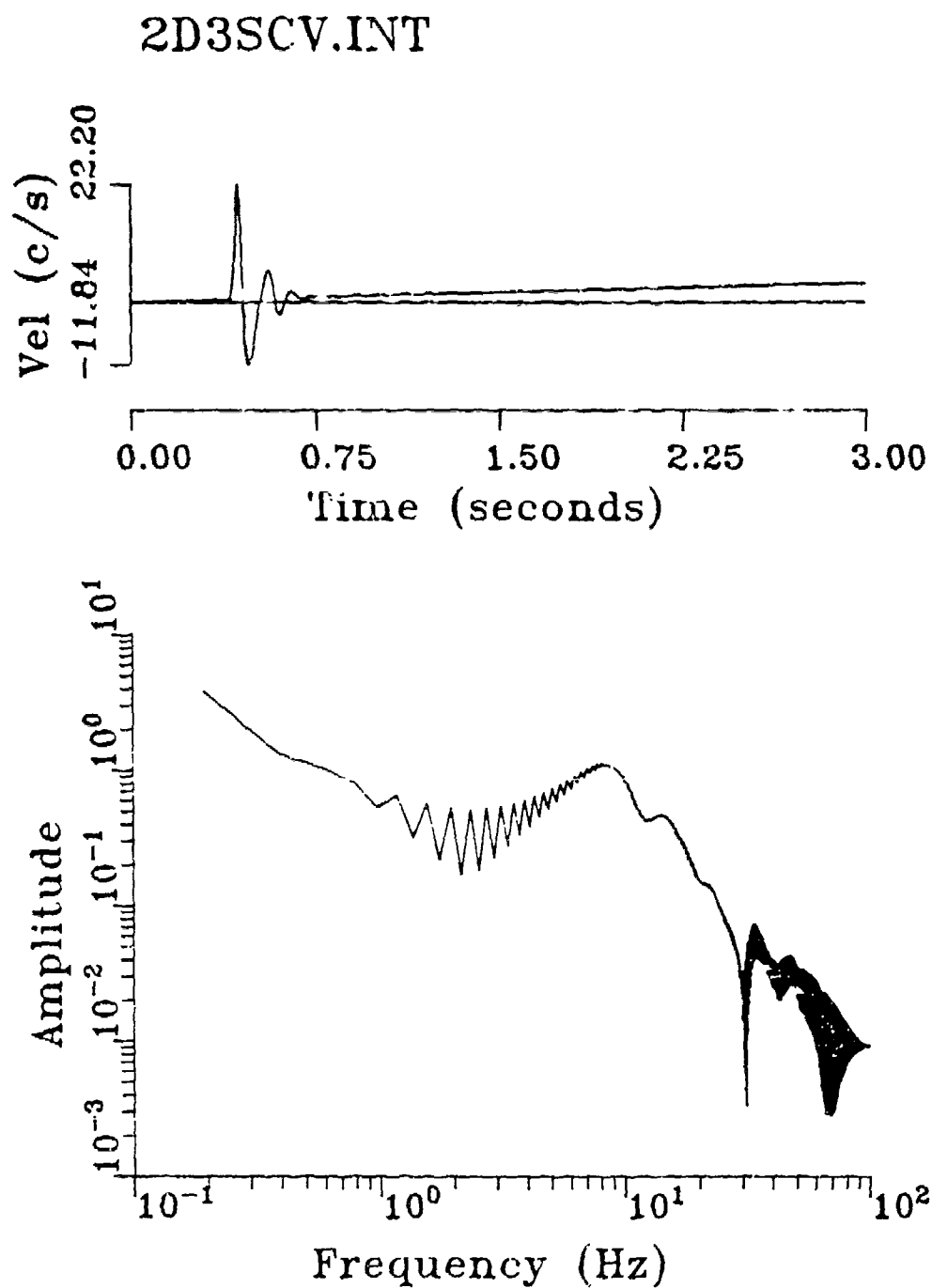


Figure A.1b. Example of slope type 1, a constant slope in uncorrected velocity. Record obtained by integration of Figure A.1a. PD3.0

## 2D3SCV.SLP

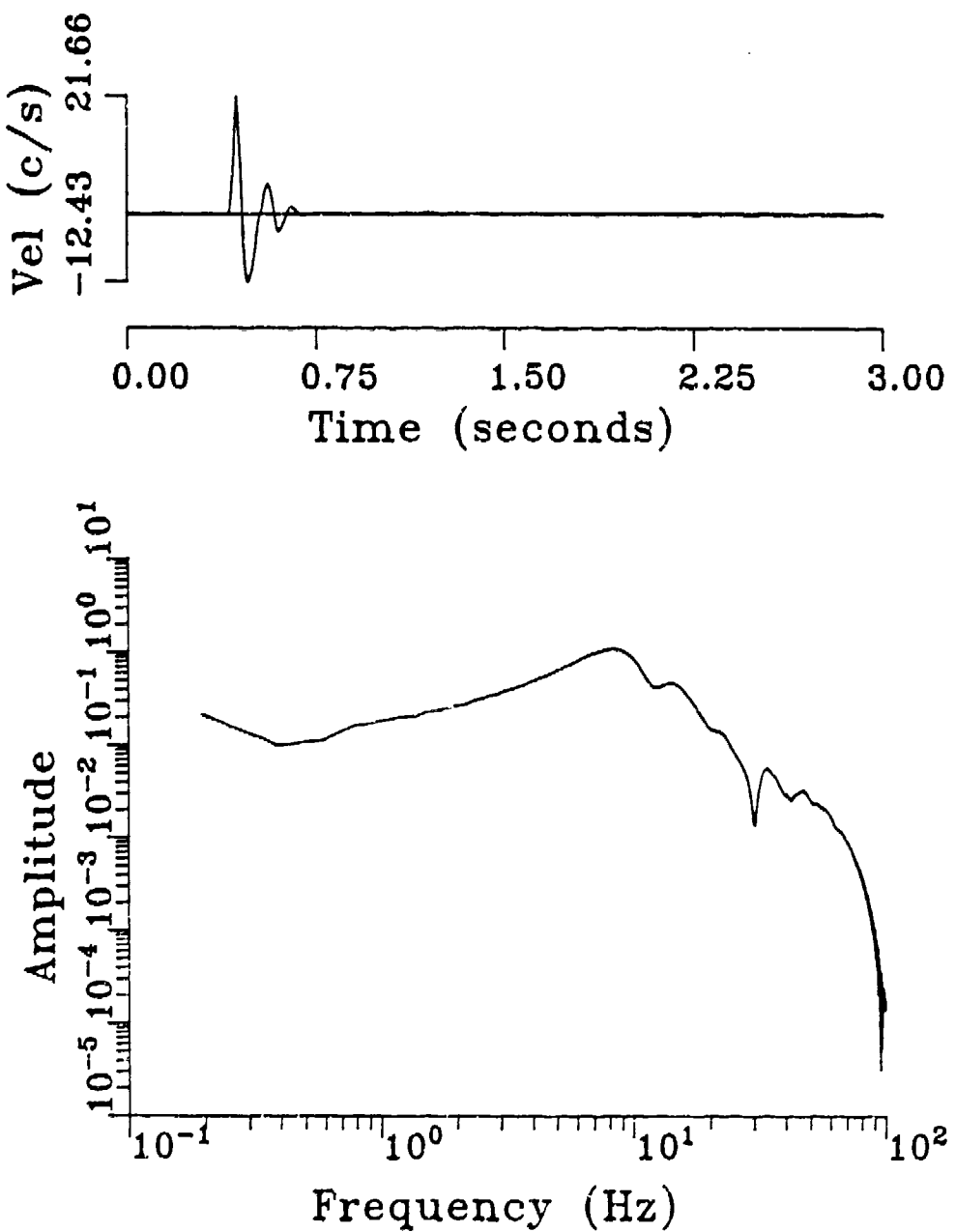


Figure A.1c. Slope subtracted from Figure A.1b. PS3.1

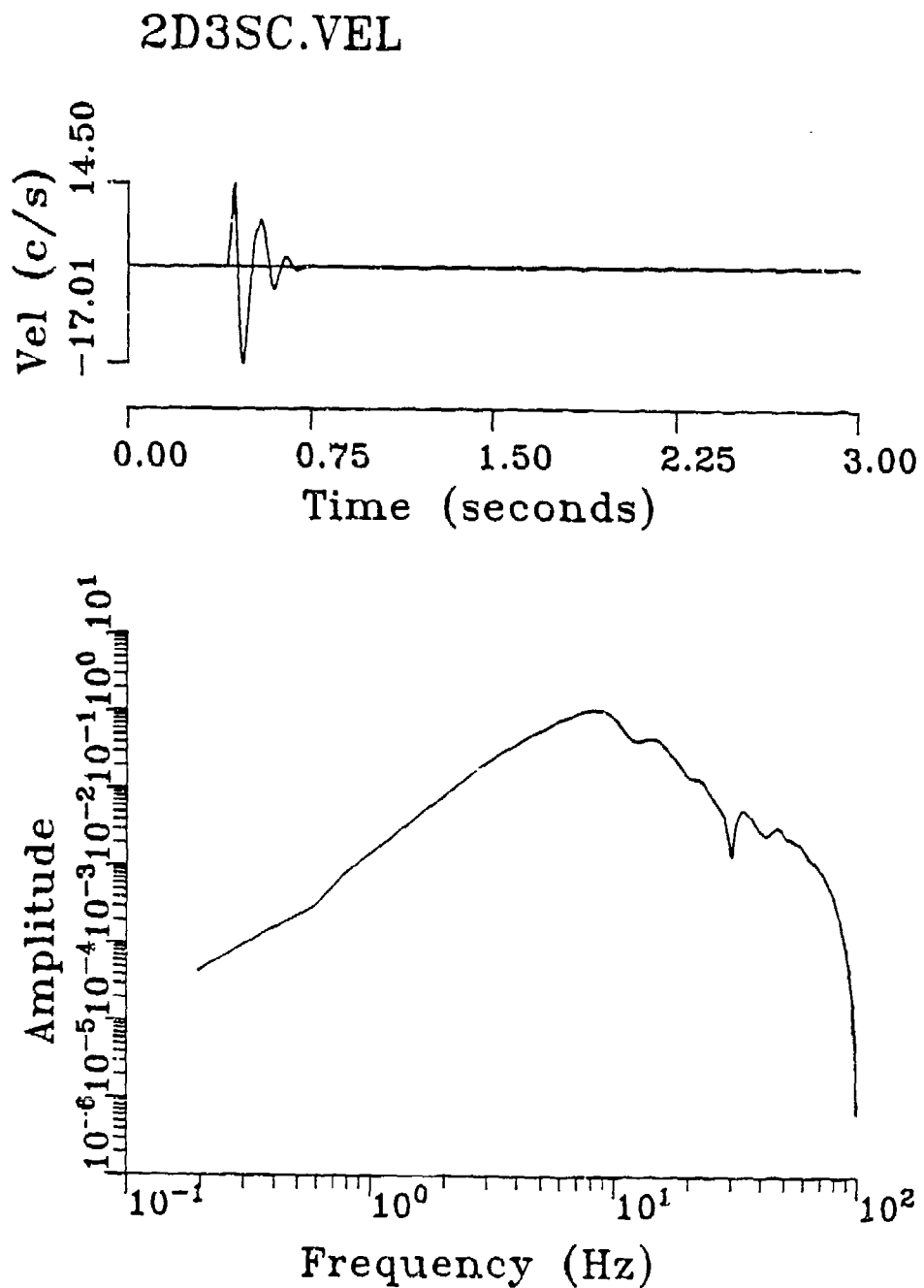


Figure A.1d. Corrected velocity. Record obtained by application of high-pass filter with corner at 3.5 Hz to Figure A.1c. PS3.2

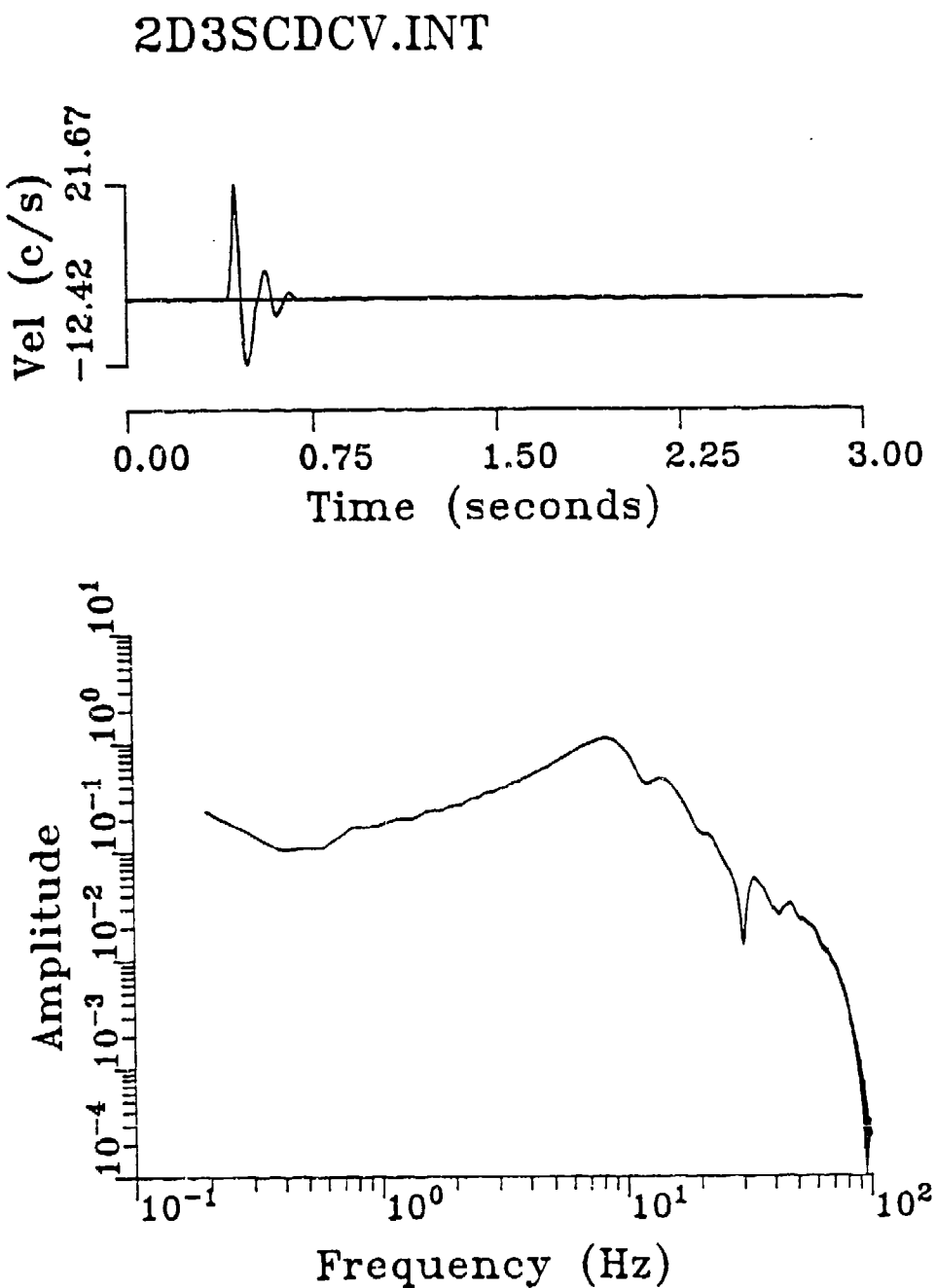


Figure A.1e. Uncorrected velocity. Record obtained by removing a DC offset from Figure A.1a before integrating. Compare to Figure A.1b. where the DC term was not removed before integration. Removing DC in acceleration is equivalent to removing a slope from velocity.

## 2D3SCDC.VEL

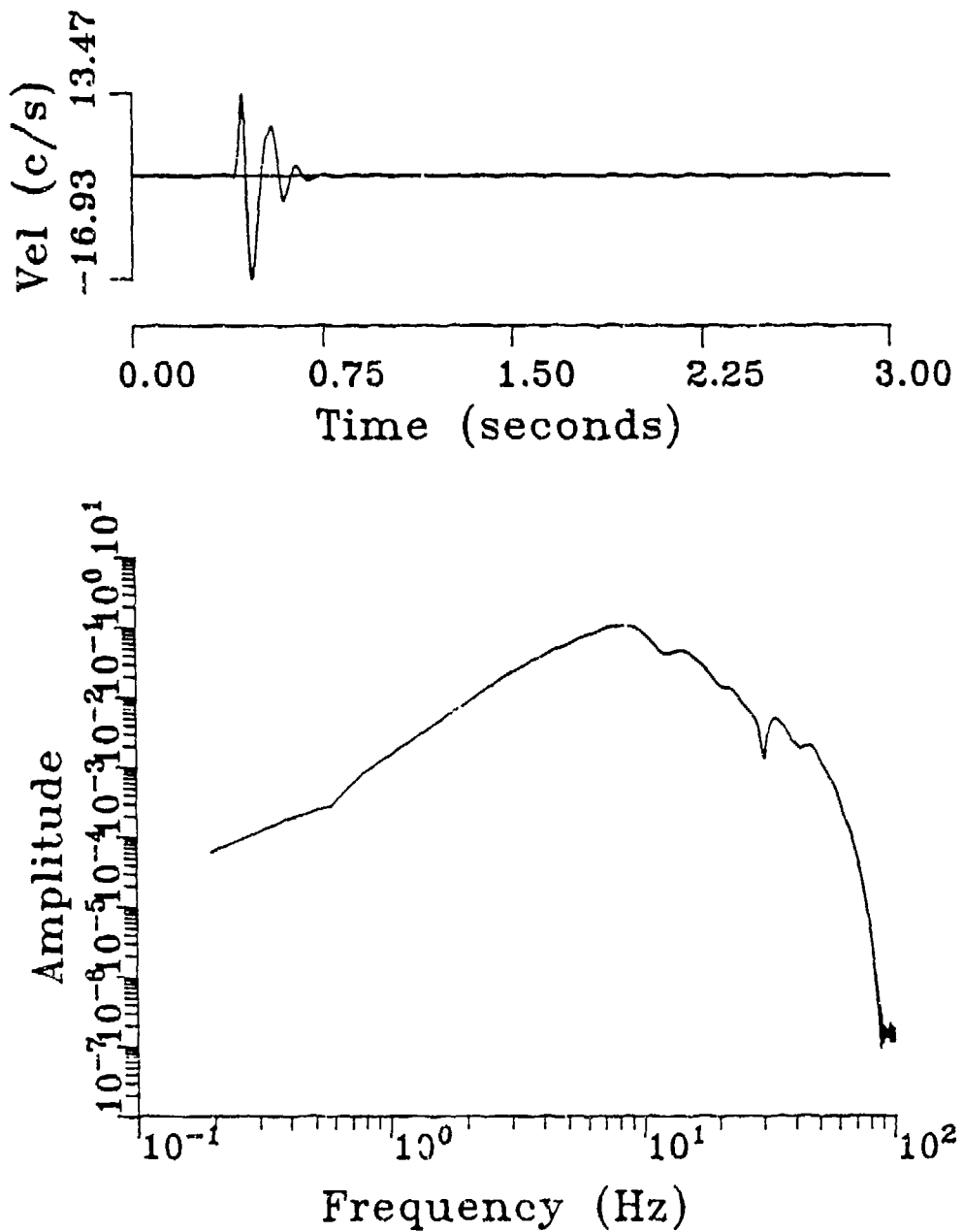


Figure A.1f. Corrected velocity. Compare to Figure A.1d. Figures A.1d and A.1f are almost identical and support the statement that removing DC in acceleration is equivalent to removing a slope from velocity.

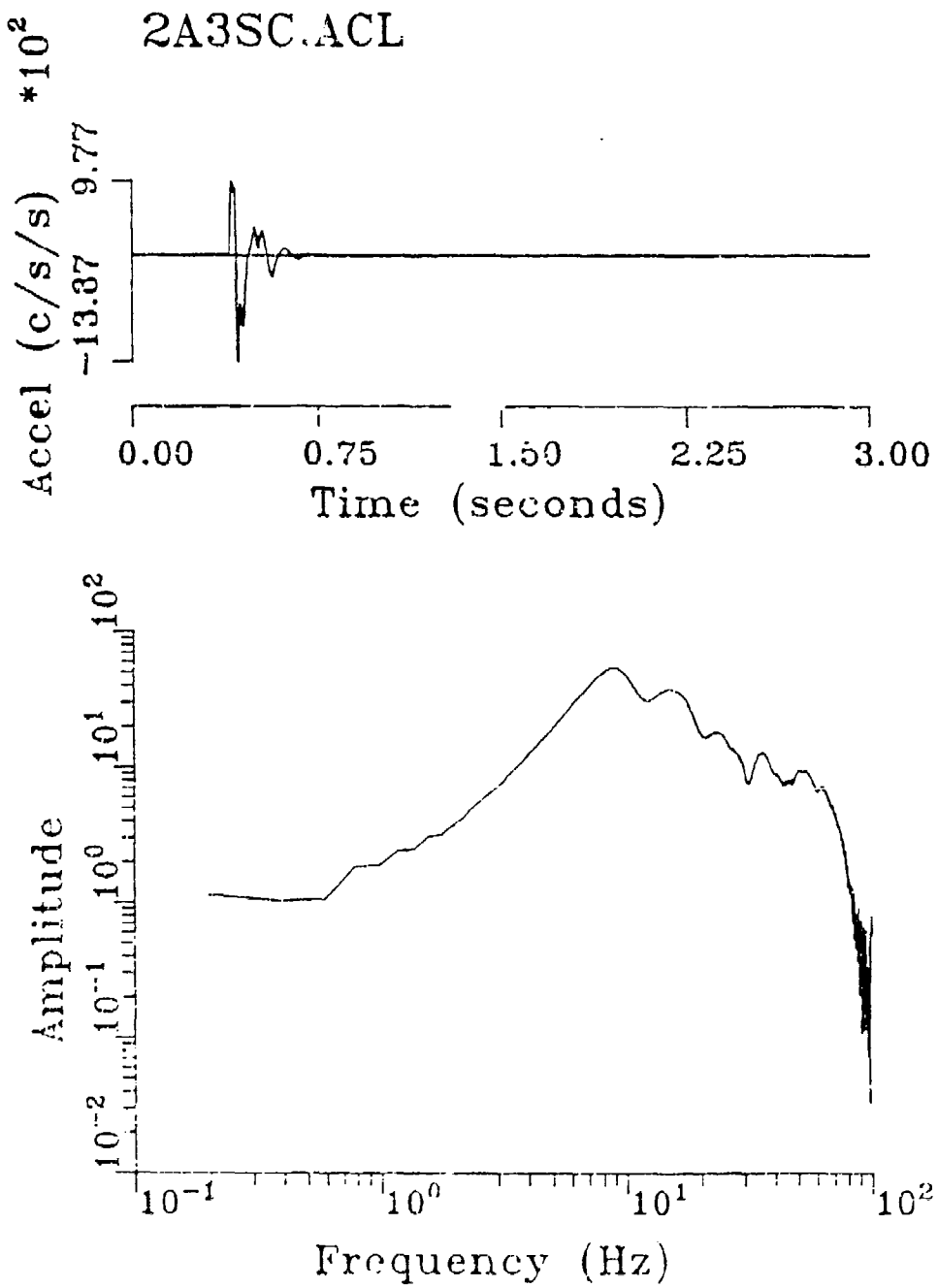


Figure A.24. Observed acceleration scaled to unit<sup>2</sup>, for 2A3SC, radial component observed at the S station during Park City, 1970, 10:11:00.

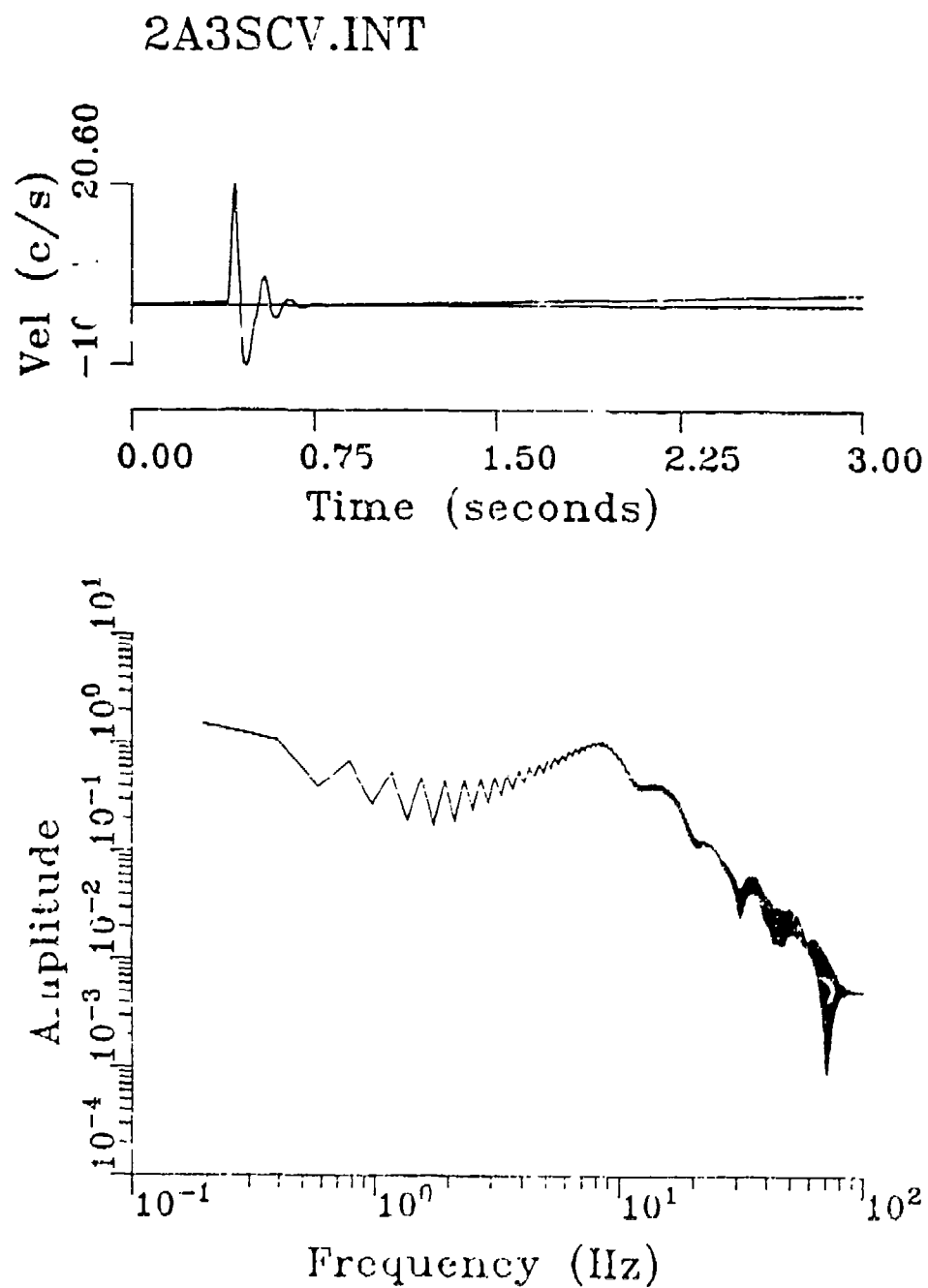


Figure A.21. Example of slope type 2, a step in microseismic velocity. Record obtained by integration of Figure A.20. The step is 4% of the peak velocity, 10.3%.

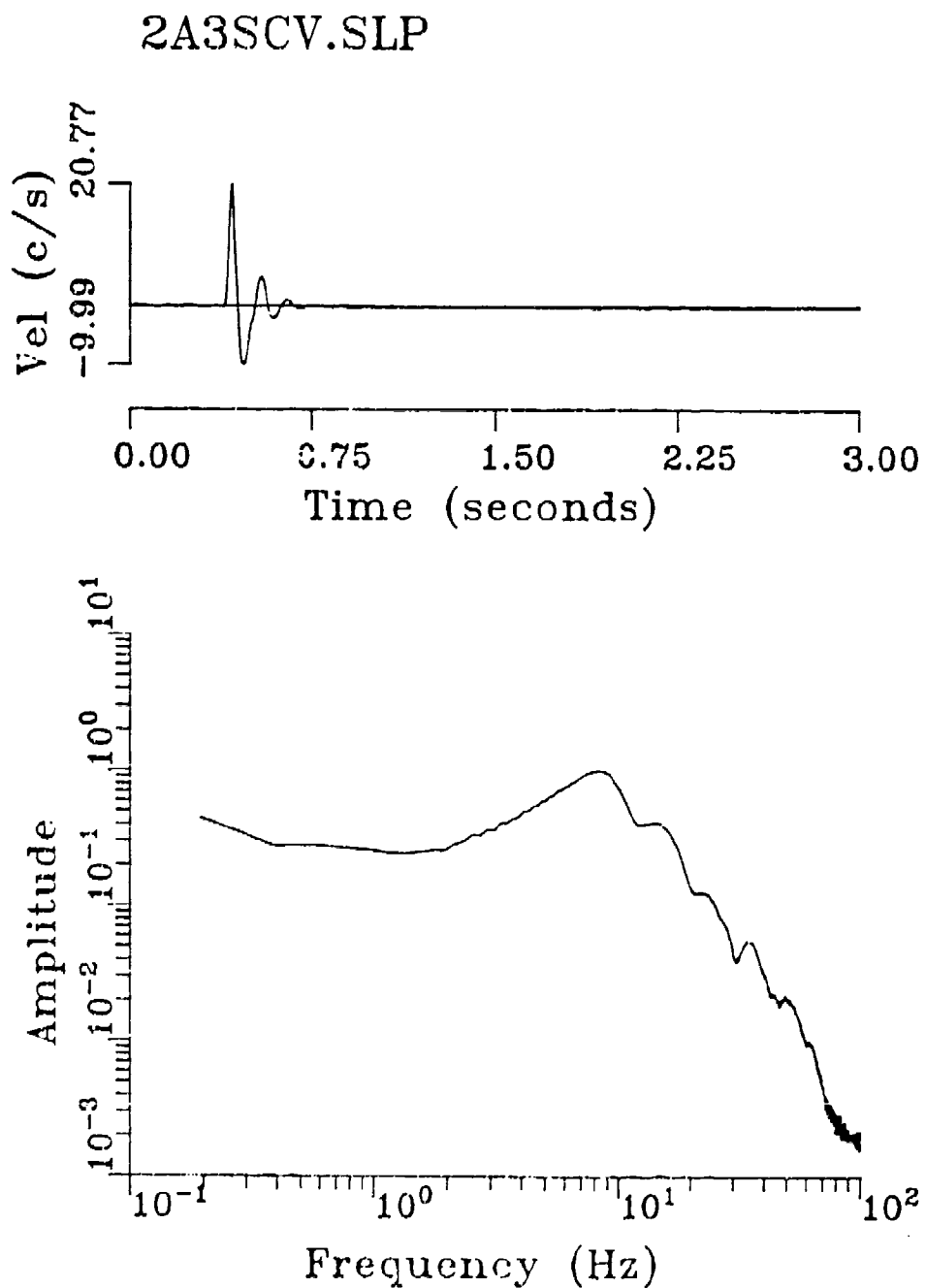


Figure 4.2a. Slope (type 2) subtracted from Figure 4.2b, PL 3.1.

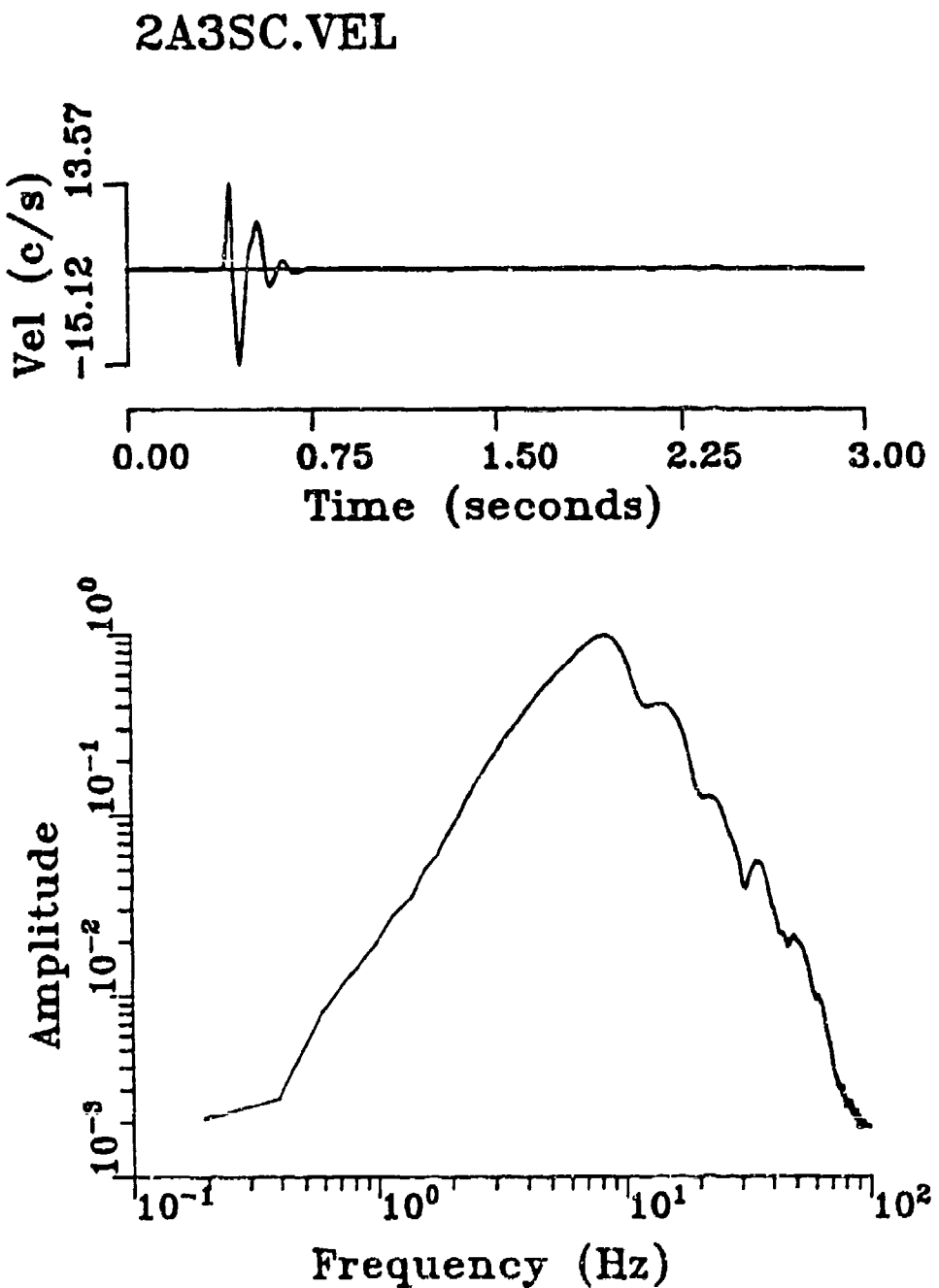


Figure A.2a. Corrected velocity. Record obtained by the application of a high-pass 2-pole Butterworth filter with corner at 3.1 Hz to Figure A.2a.

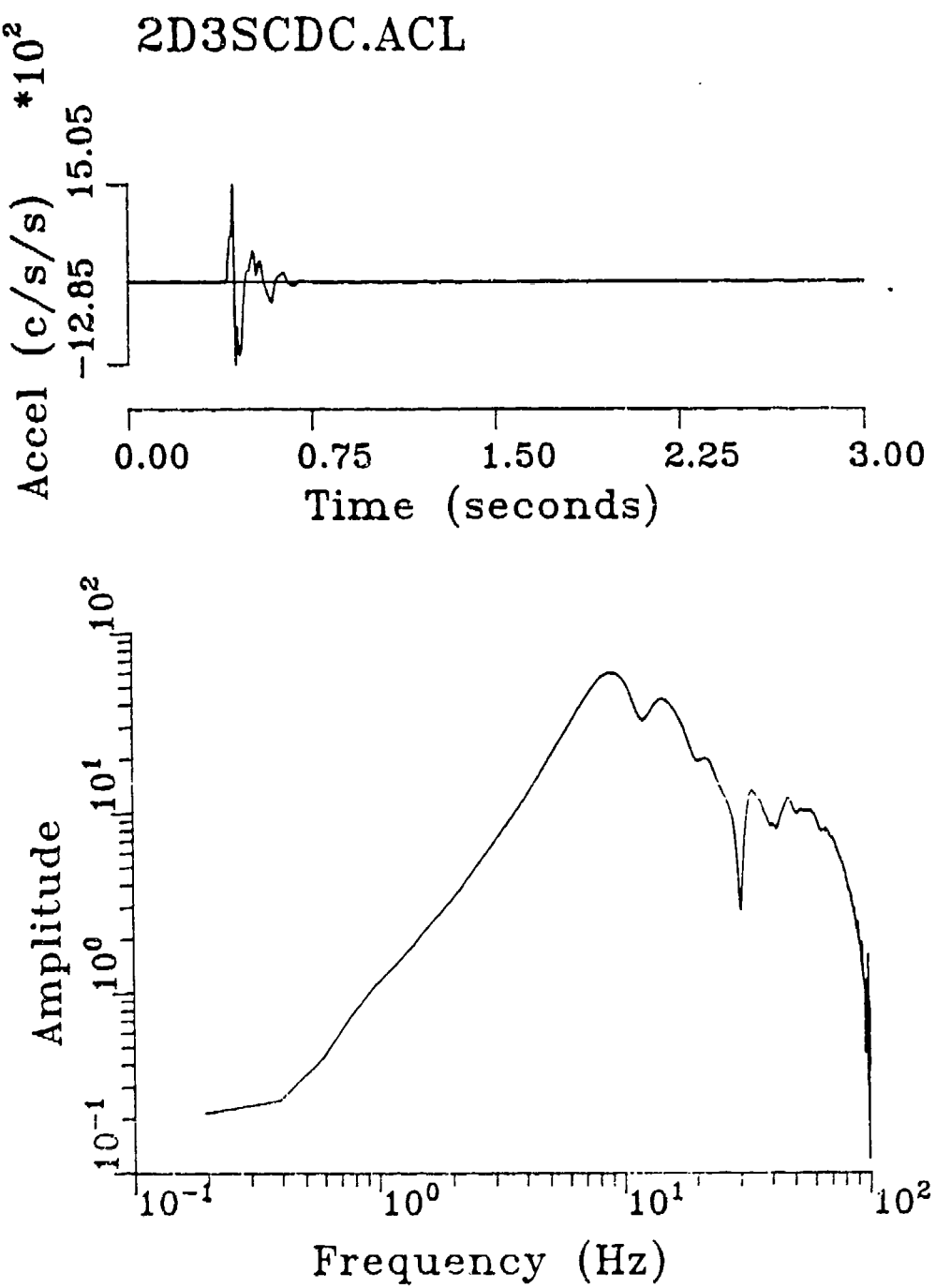


Figure E.3a. Observed acceleration with DC removed. Compare to Figure 1a with no DC removed.

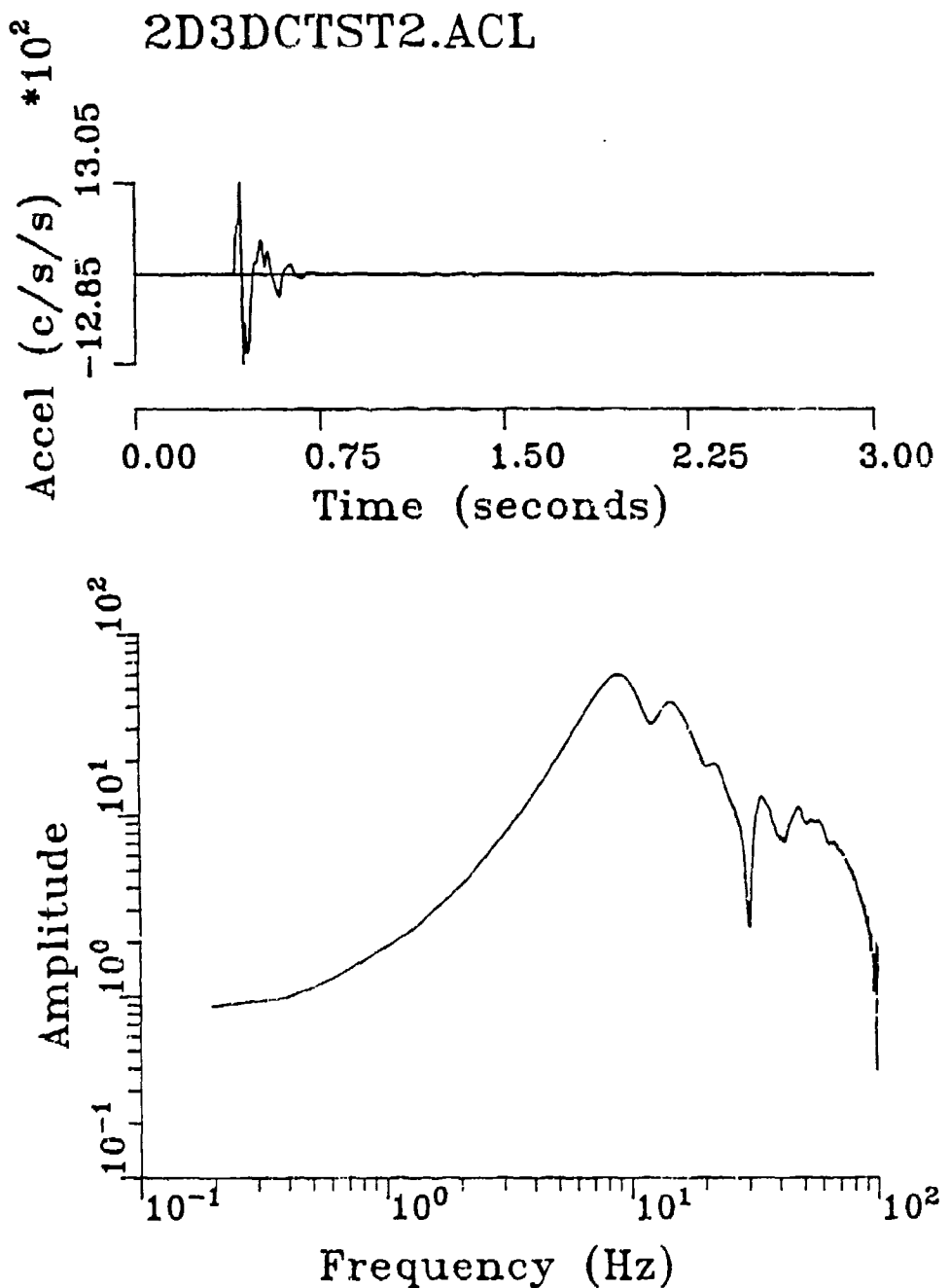


Figure A.3b. File 2D3 with first peak in acceleration reduced by 13.3%. This is a test to replicate the  $t_j = 2$  slope as illustrated in file 2A3, Figure A.2b.

## 2D3DCTST2V.INT

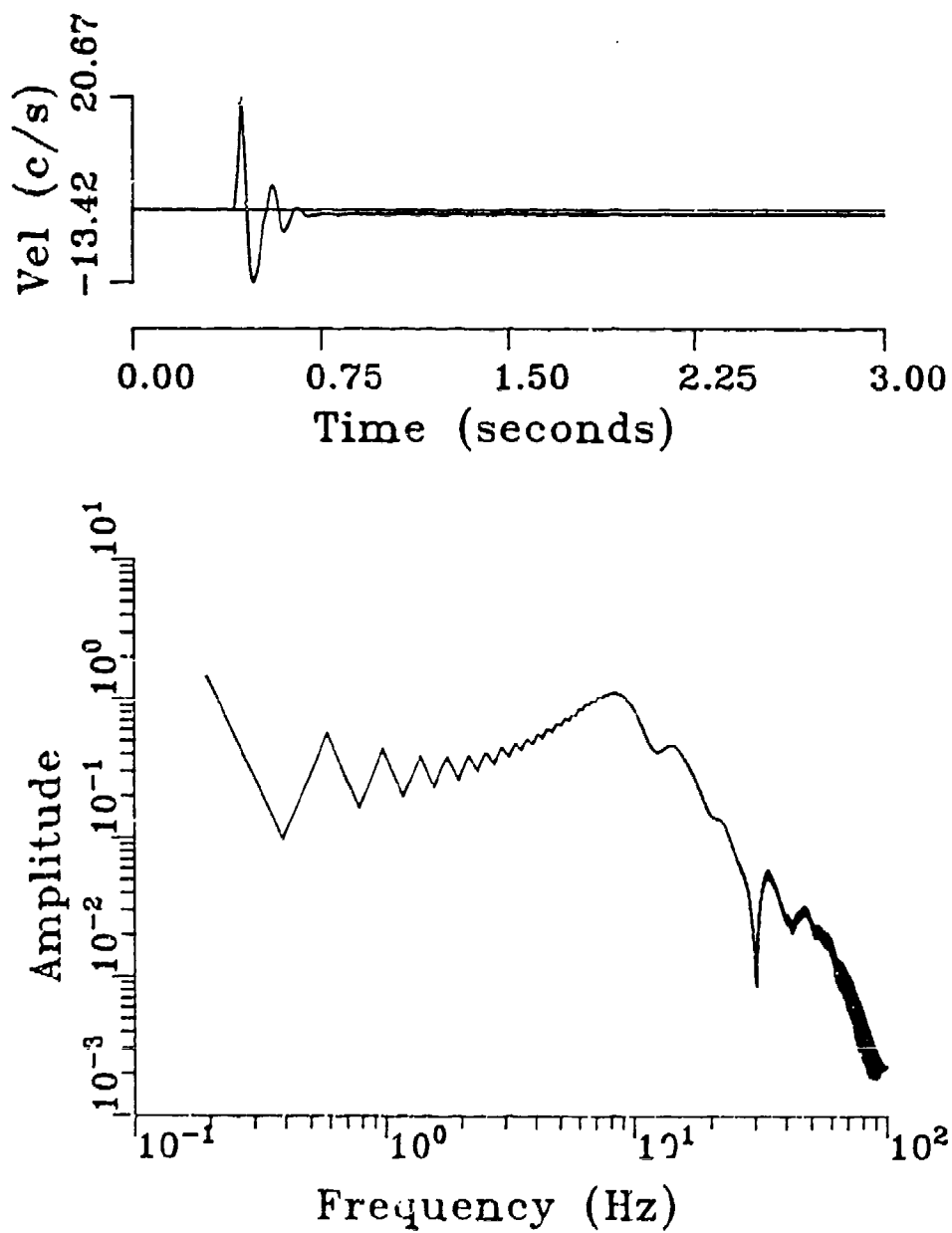


Figure A.3c. Uncorrected velocity obtained by integration of Figure 3b. The 3.3% reduction in peak acceleration resulted in a step that was 5% of the peak velocity.

## 2D3DCTST2.VEL

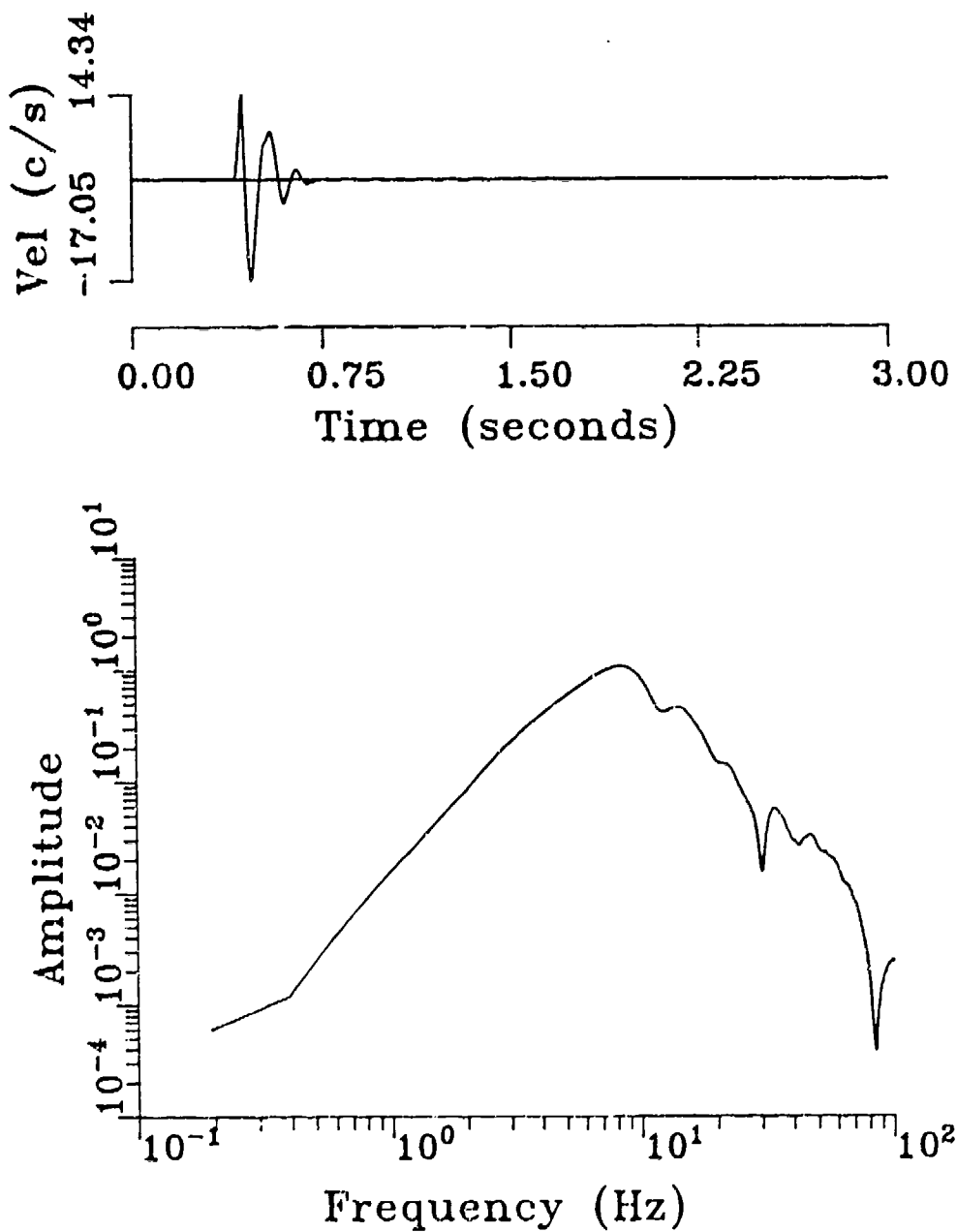


Figure A.3d. Corrected velocity. The corrected velocity is almost identical to that of Figure A.1d even though there has been a step induced in the uncorrected velocity by reducing the amplitude of the first peak of the original acceleration record.

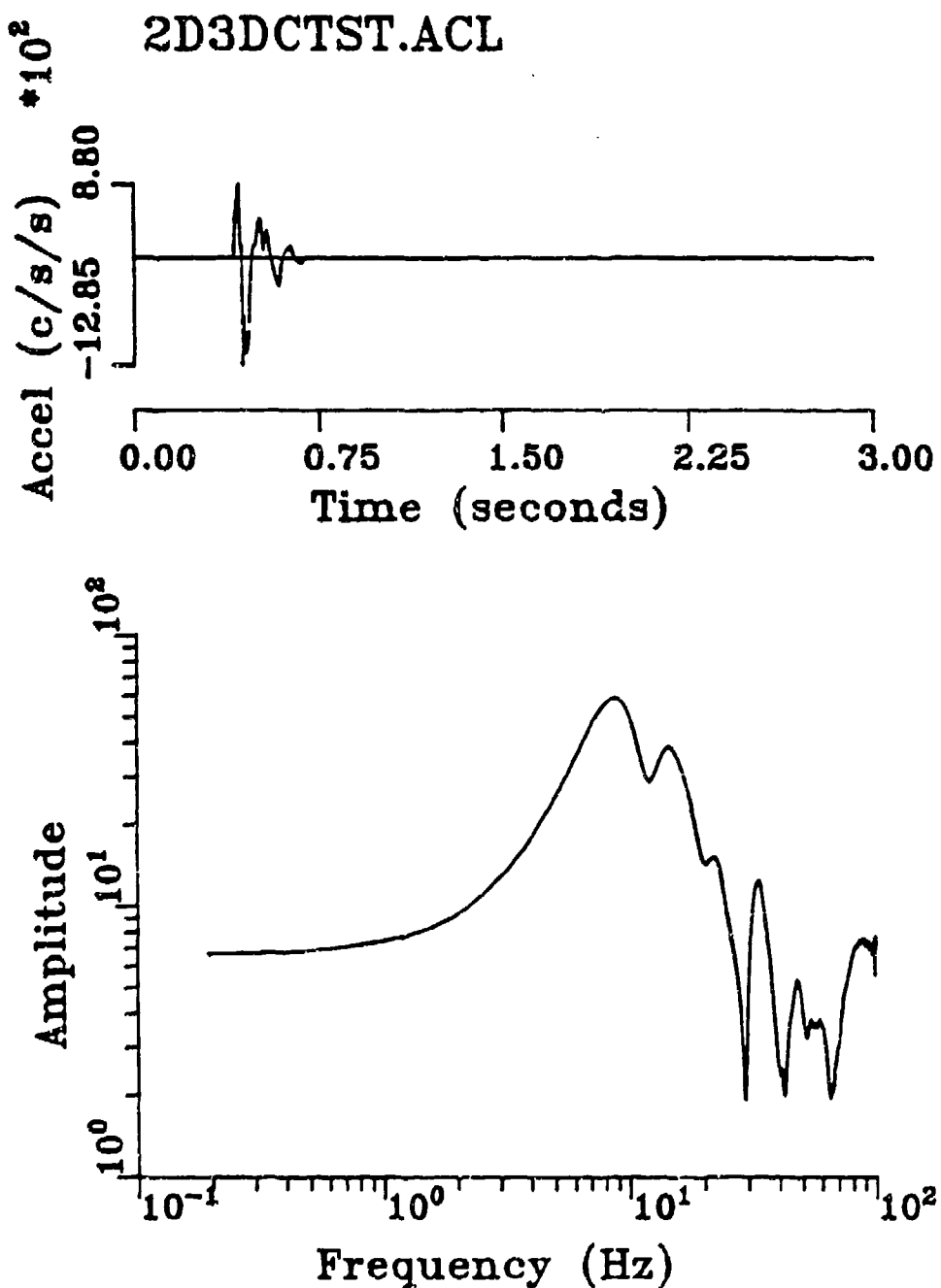


Figure A.4a. File 2D3 with first peak in acceleration reduced by 90% (from 1505 to 150  $cm/s^2$ ). This is a test to replicate the type 2 slope as illustrated in file 2A3. Same as Figure A.3b but with a greater reduction in amplitude.

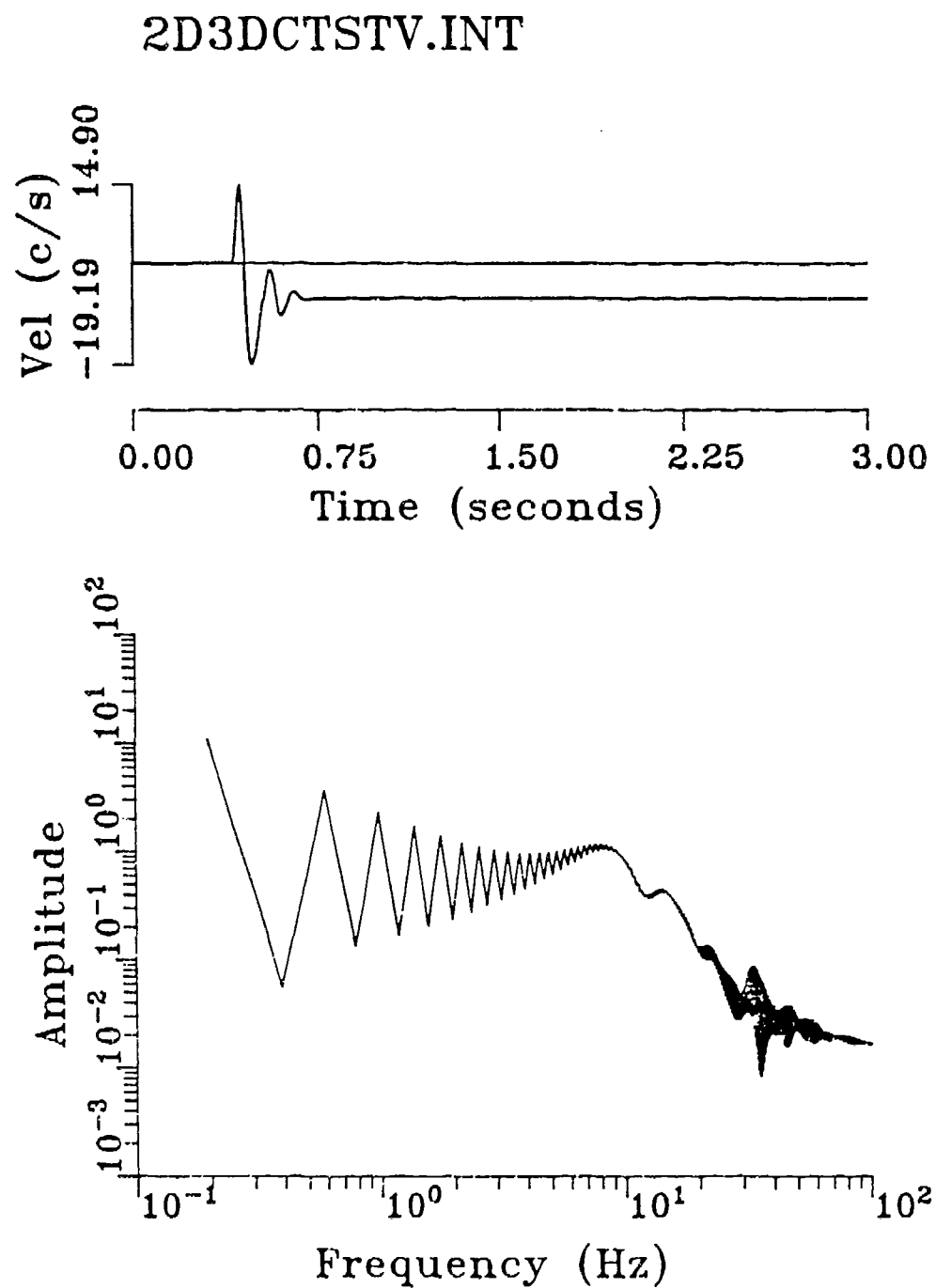


Figure A.4b. Uncorrected velocity obtained by integration of Figure A.4a. The 90% reduction in peak acceleration resulted in a step that is 33.2% of the peak velocity.

## 2D3DCTST.VEL

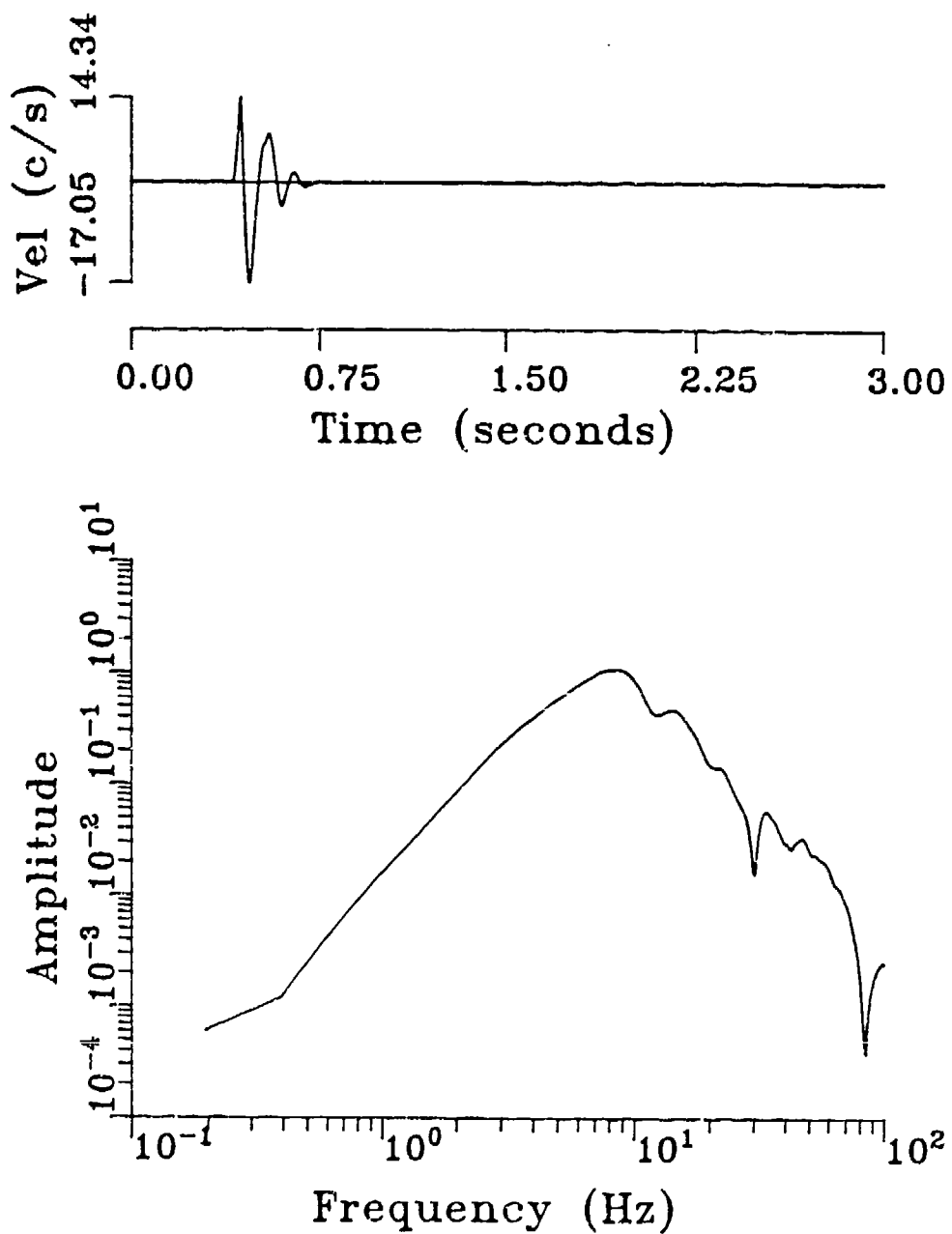


Figure A.4c. Corrected velocity. The corrected velocity is almost identical to that of Figure A.1d even though there has been a step induced in the uncorrected velocity by reducing the amplitude of the first peak of the original acceleration record.

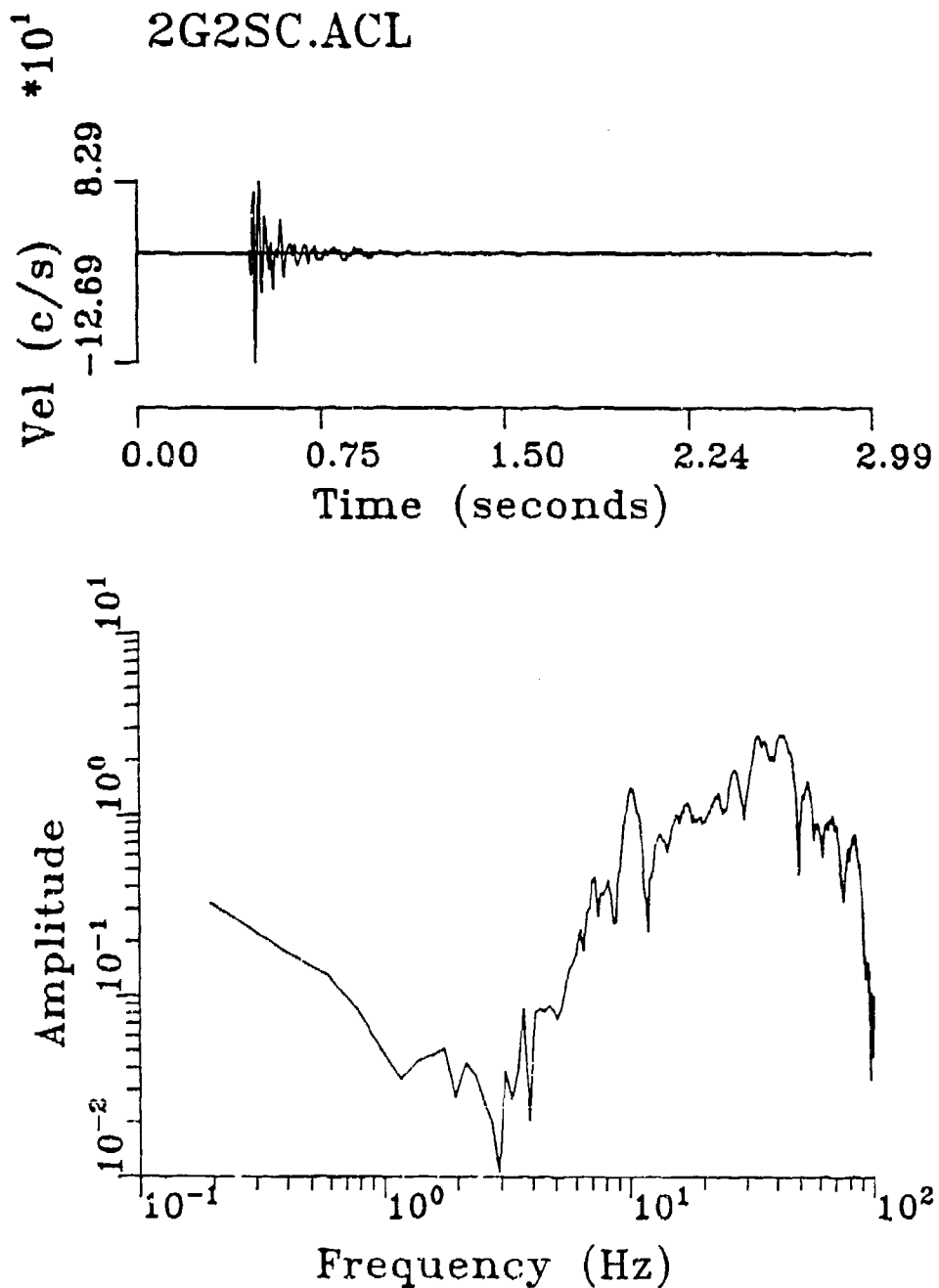


Figure A.5a. Observed acceleration scaled to  $cm/s^2$ . File 2G2 is the transverse component observed at the 13.5 meter range. Peak acceleration is  $0.13g$ .

2G2SCV.INT

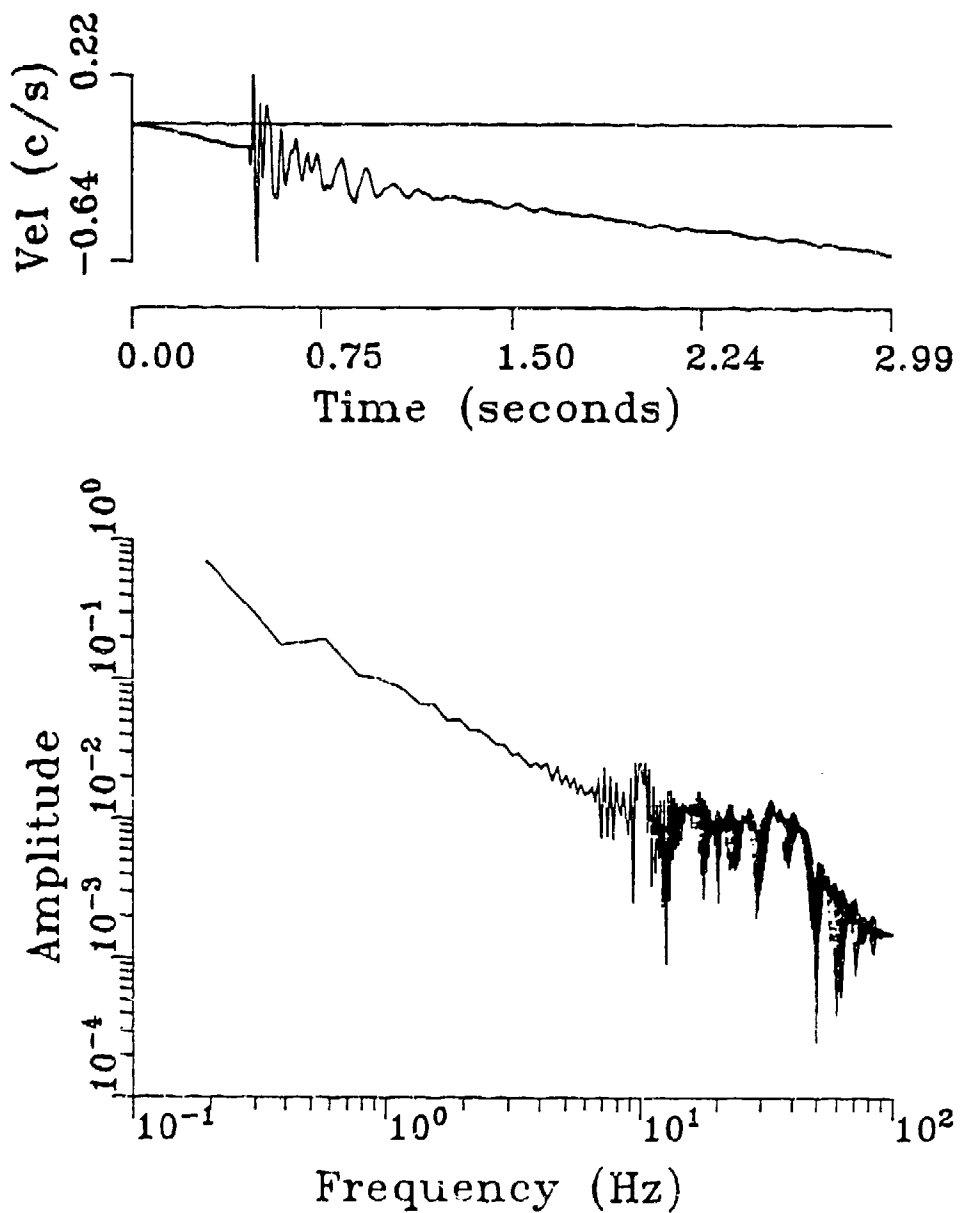


Figure A.5b. Example of slope type 3, two ramps in uncorrected velocity. The change in slope, indicated by the arrow, occurs after the signal has passed.

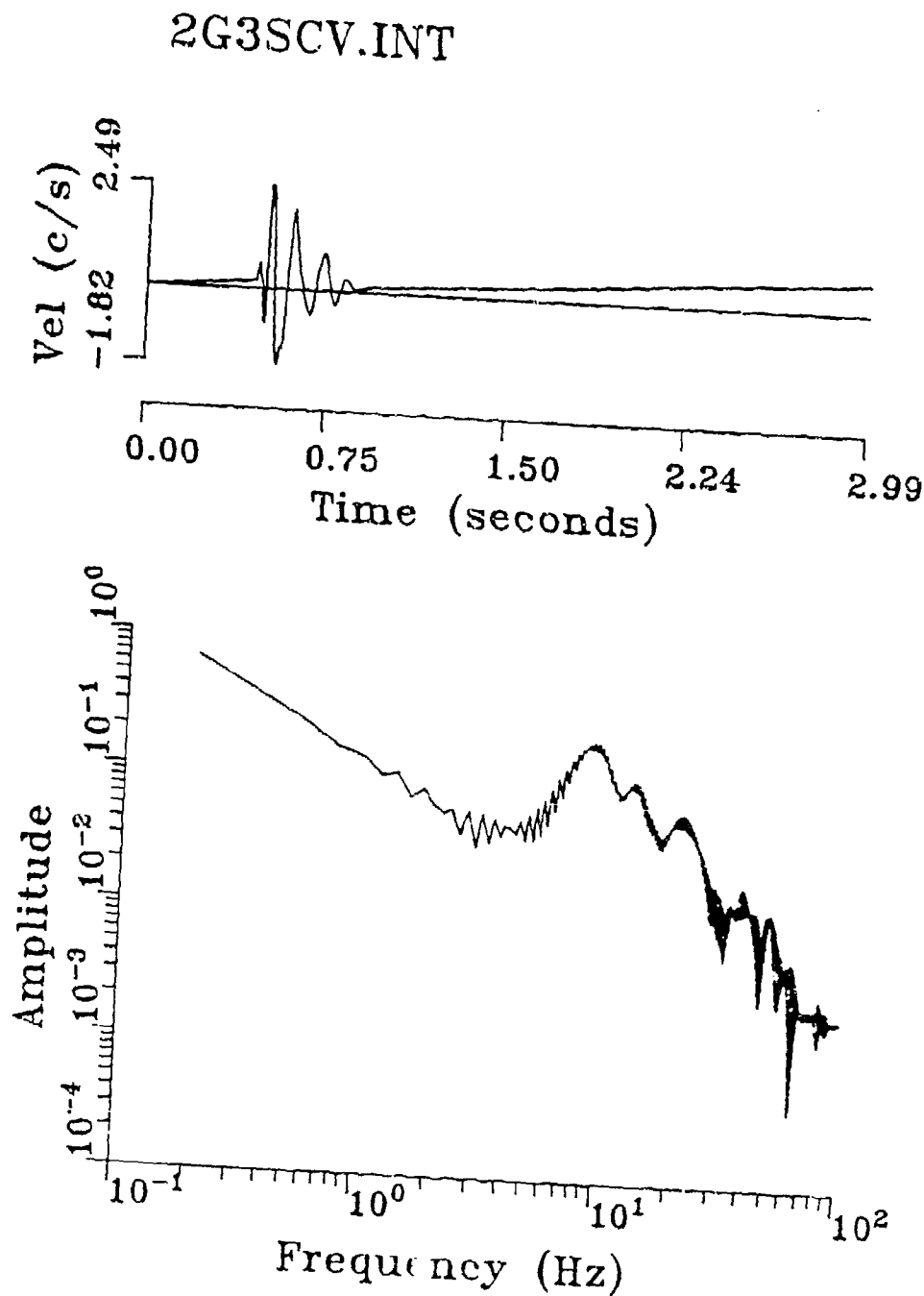


Figure A.5c. Uncorrected velocity. File 2G3 is the radial component corresponding to file 2G2. If the change in slope (arrow) is taken into account, then the tilt interpretation will be consistent with file 2G2.

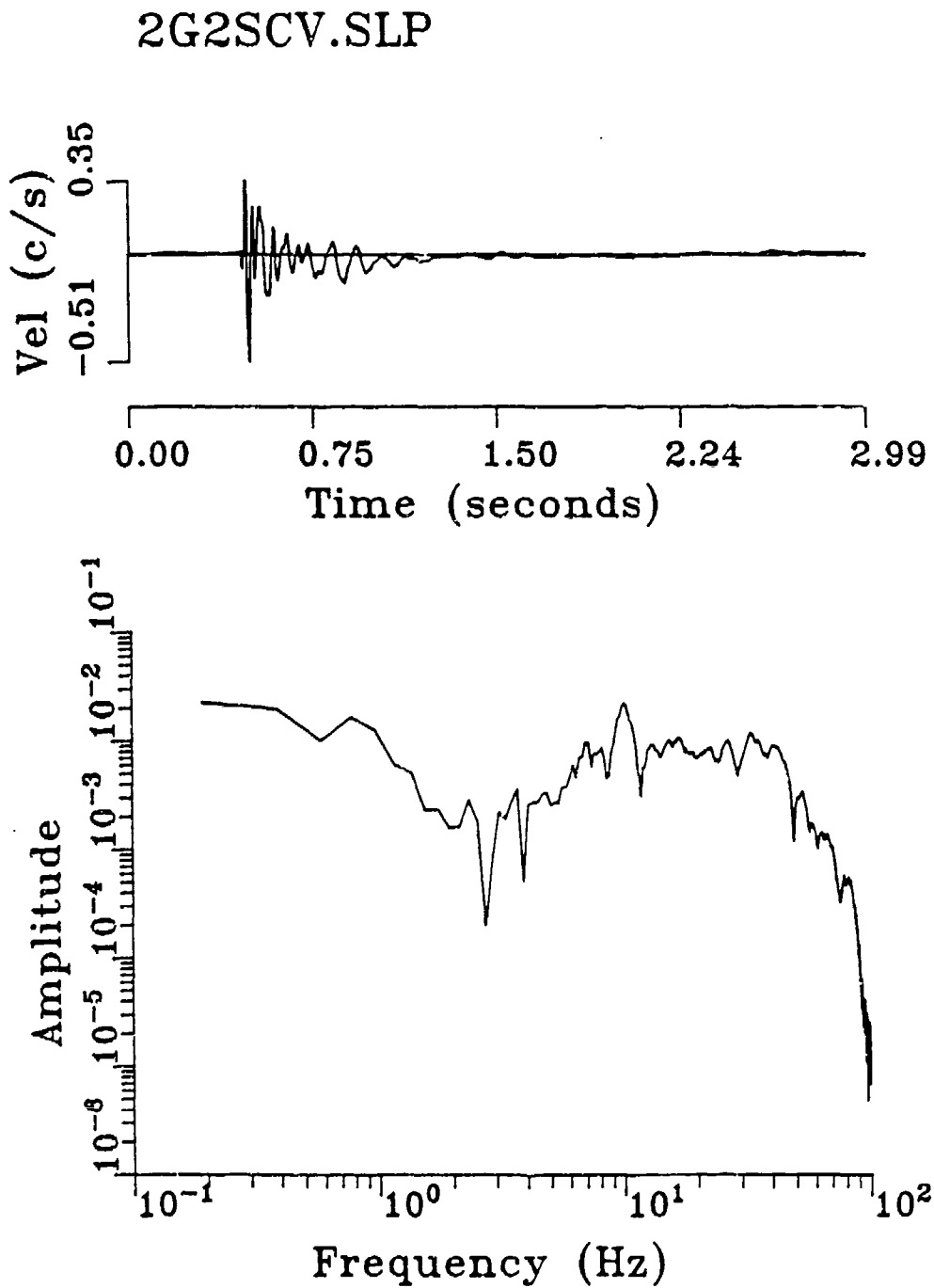


Figure A.5d. Velocity record obtained by subtracting the two slopes from Figure A.5b. The departure from the zero line shows up as a peak in the amplitude spectrum below 1 Hz. This boost in long period noise is a result of integration.

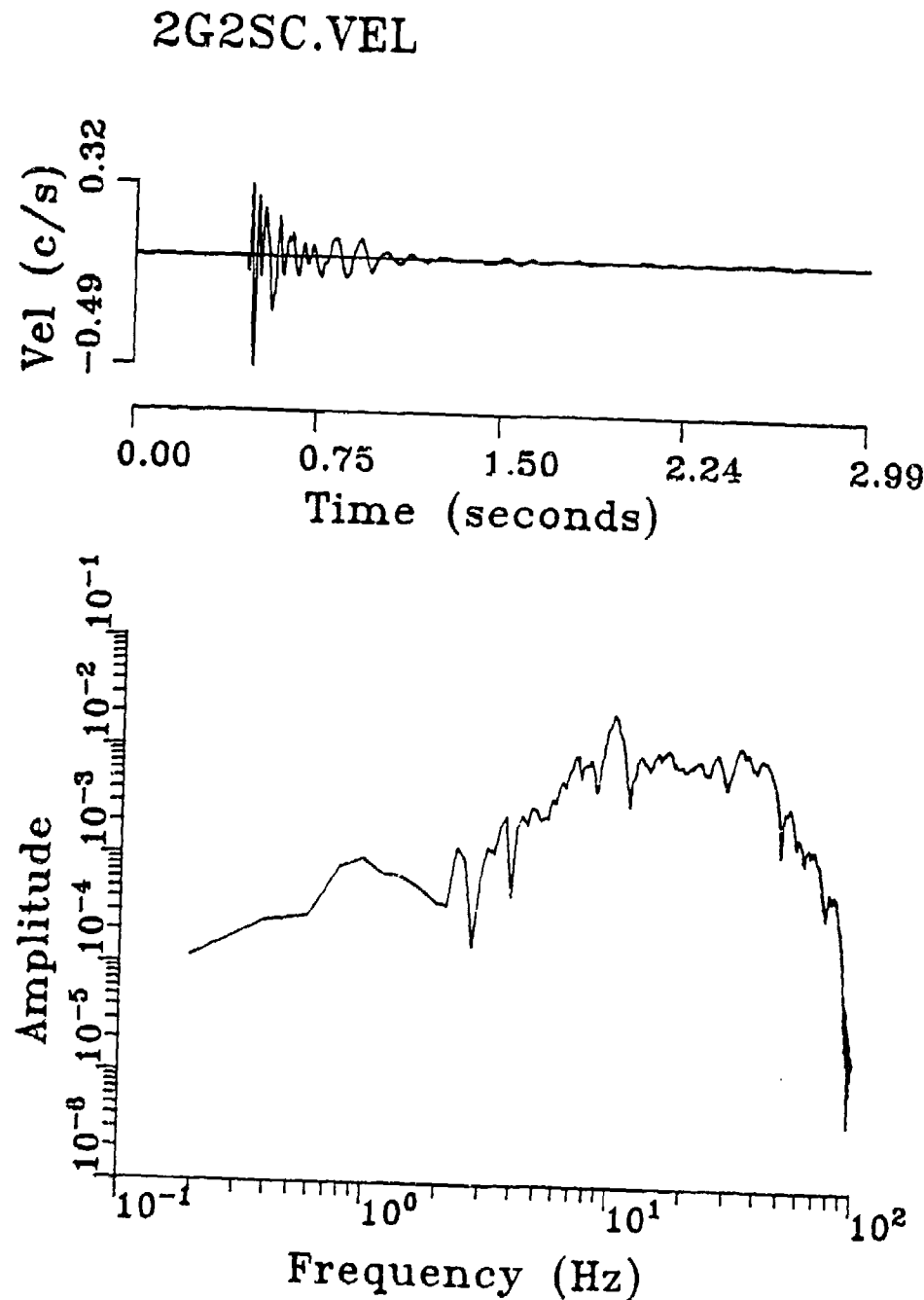


Figure A.5e. Corrected velocity. Record obtained by filtering slope-corrected velocity with a high-pass, 2-pole Butterworth filter with corner at 3.5 Hz.

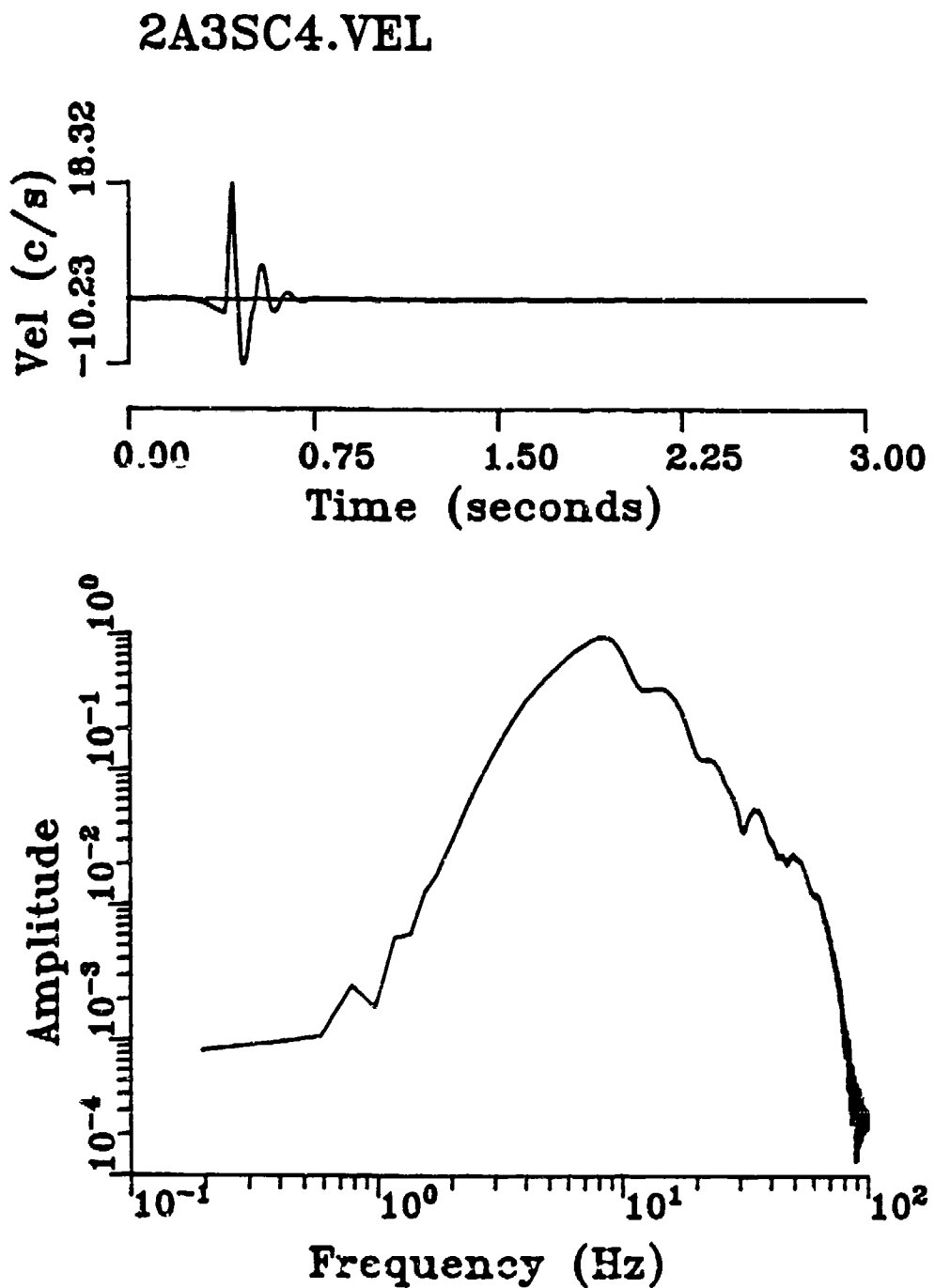


Figure A.6. Filter test. The 4-pole filter design was rejected because of the significant acausal arrivals induced by the filter. Compare to Figure A.2d where the high-pass filter in PS 3.2 has a 2-pole roll-off.

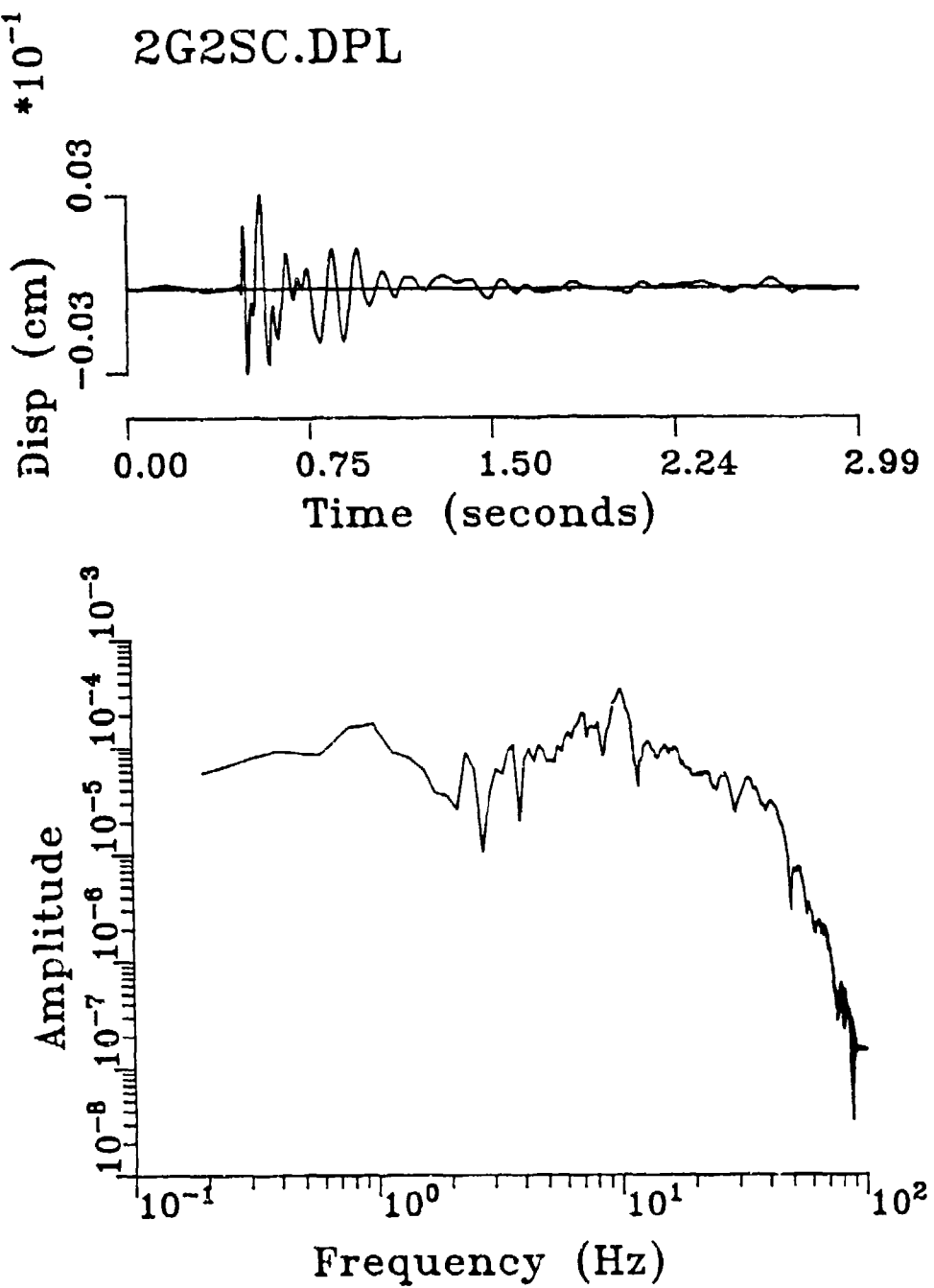


Figure A.7a. Corrected displacement. Record obtained by integration of Figure 5d. The displacement signal is affected by long-period noise remaining in the corrected velocity.

## 2G2SCP.DPL

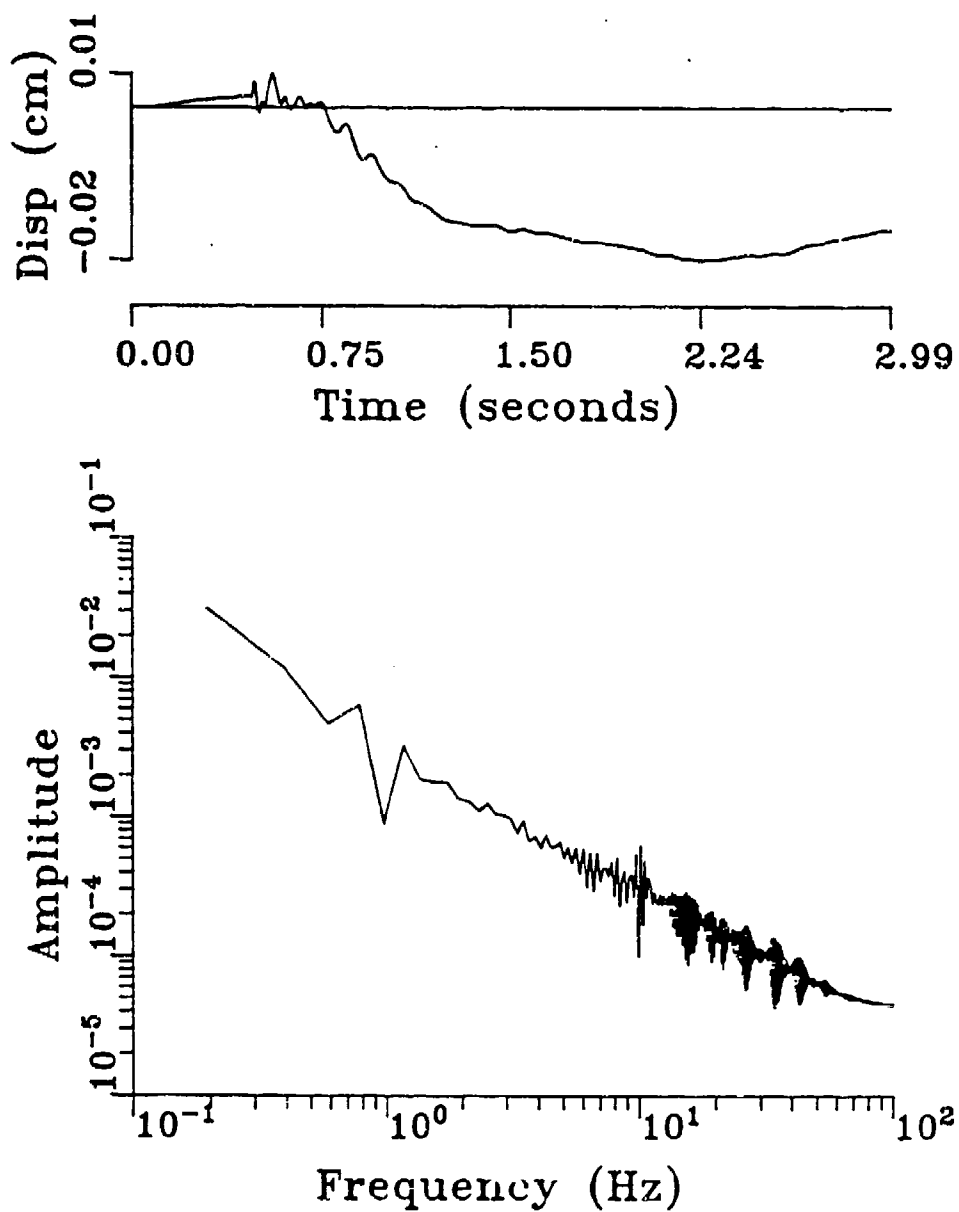


Figure 7b. Displacement record obtained by integration of Figure A.5d. The poor quality of this displacement record illustrates the importance of the high pass filter in Fig. 1.

APPENDIX B  
COMPLETE EXPLOSION DATA SET

## PLAN VIEW OF CART1 SOURCE AND RECEIVER LOCATIONS

♦ G

● E

▲ C

▲ A

▲ B

⊕

● D

♦ F

⊕ SHOT LOCATION

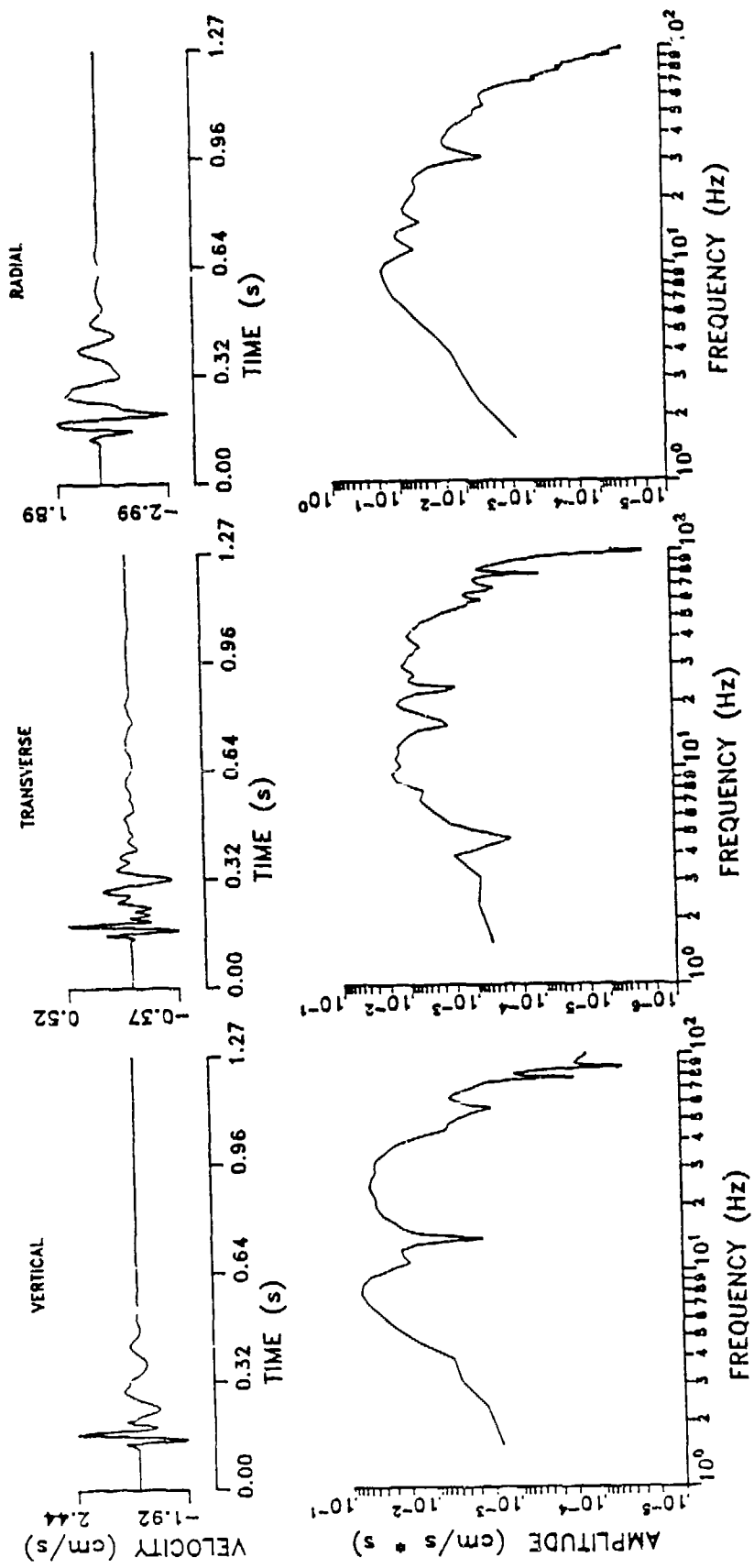
▲ 13.5 m

● 27.0 m

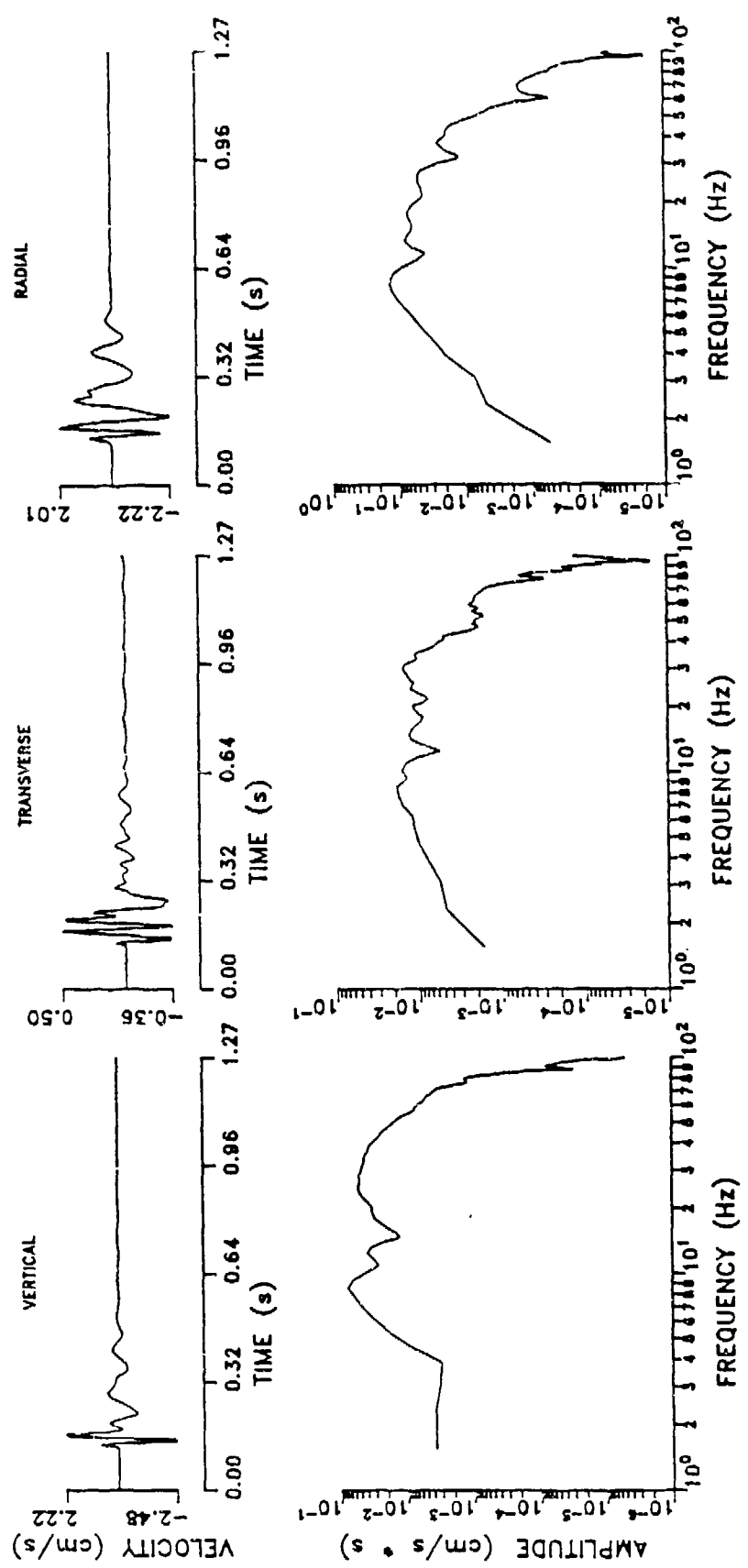
♦ 40.6 m

↑ 0° NORTH

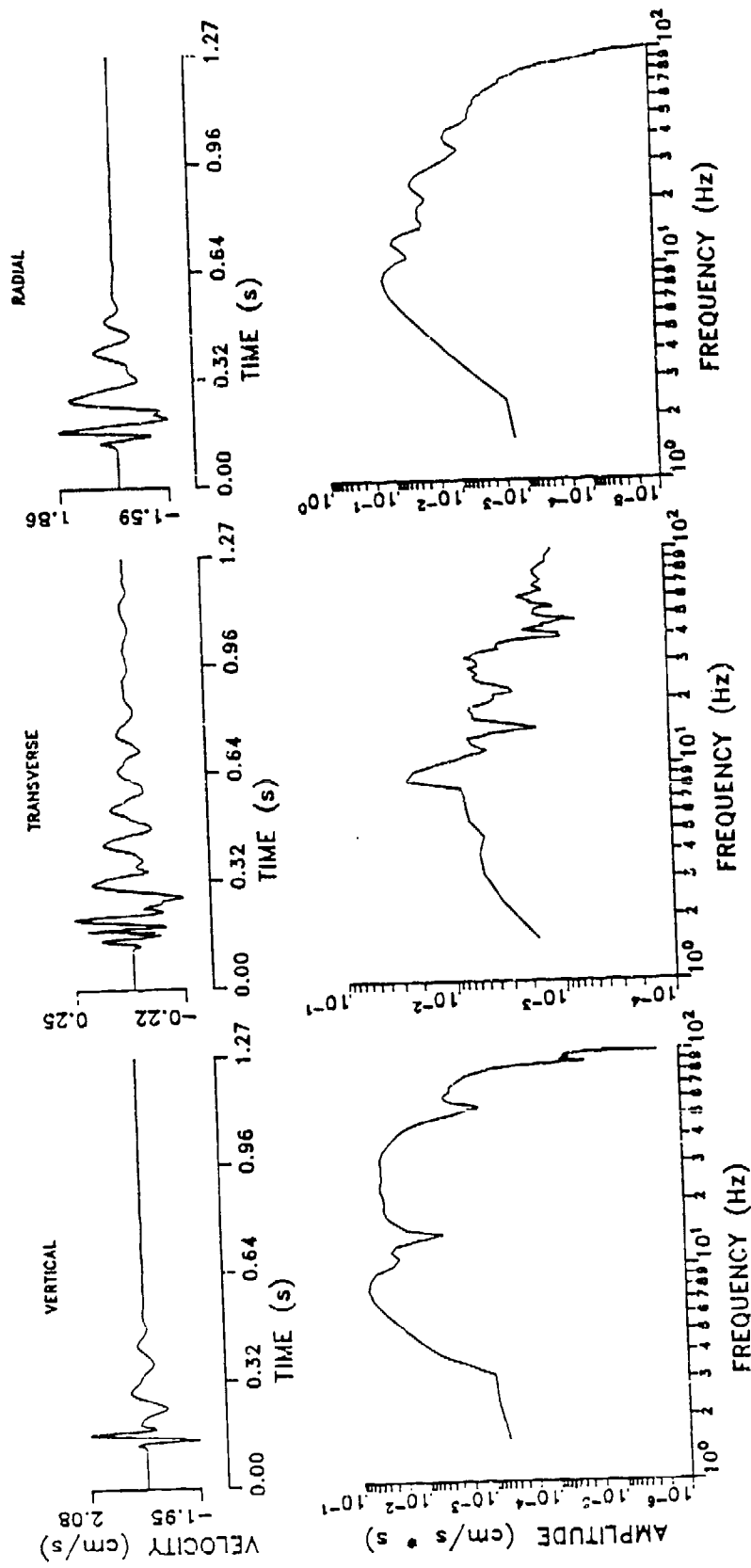
CART 1A: 90 DEGREES AT 13.5 METERS



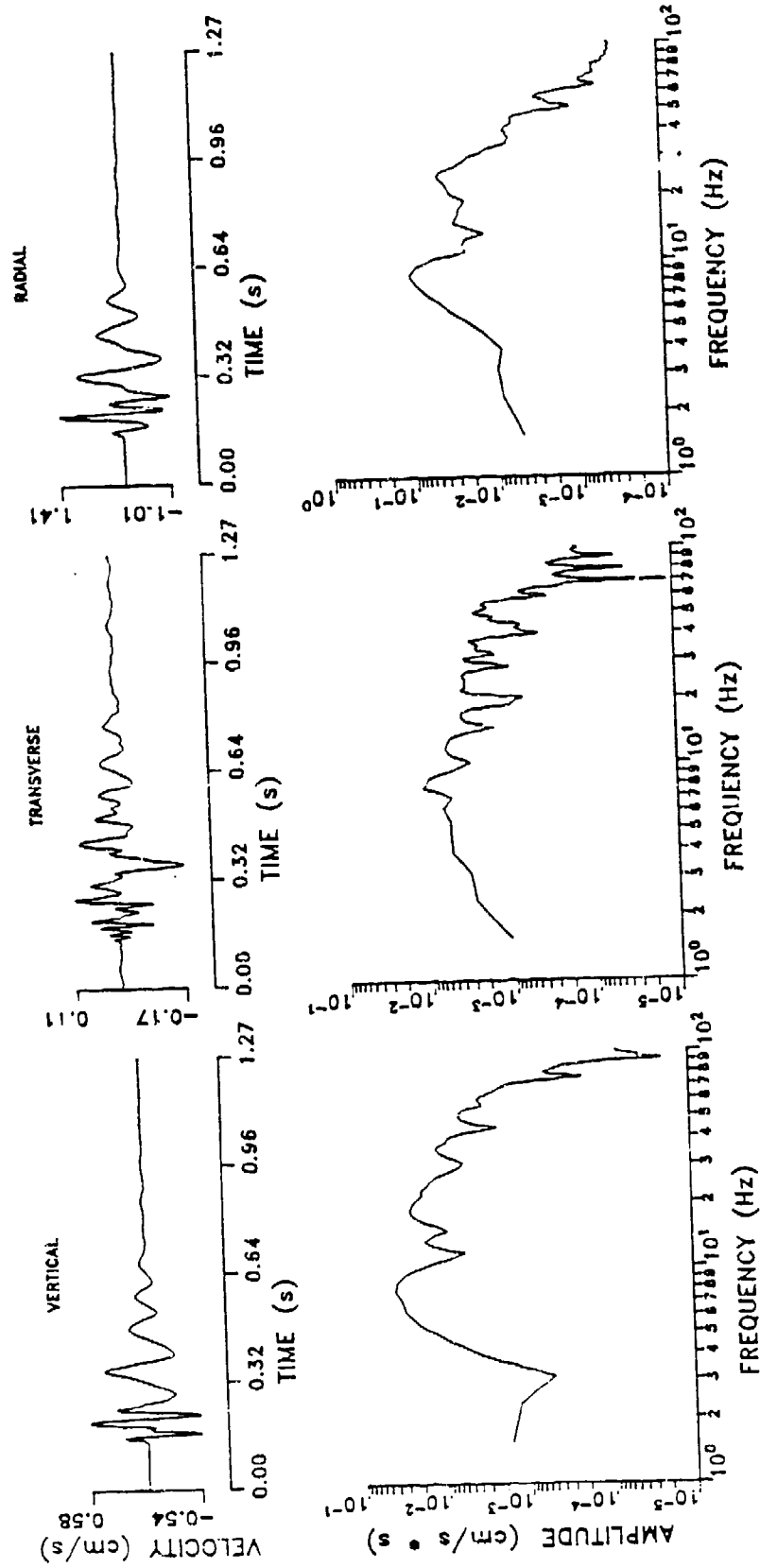
CART 1B: 270 DEGREES AT 13.5 METERS



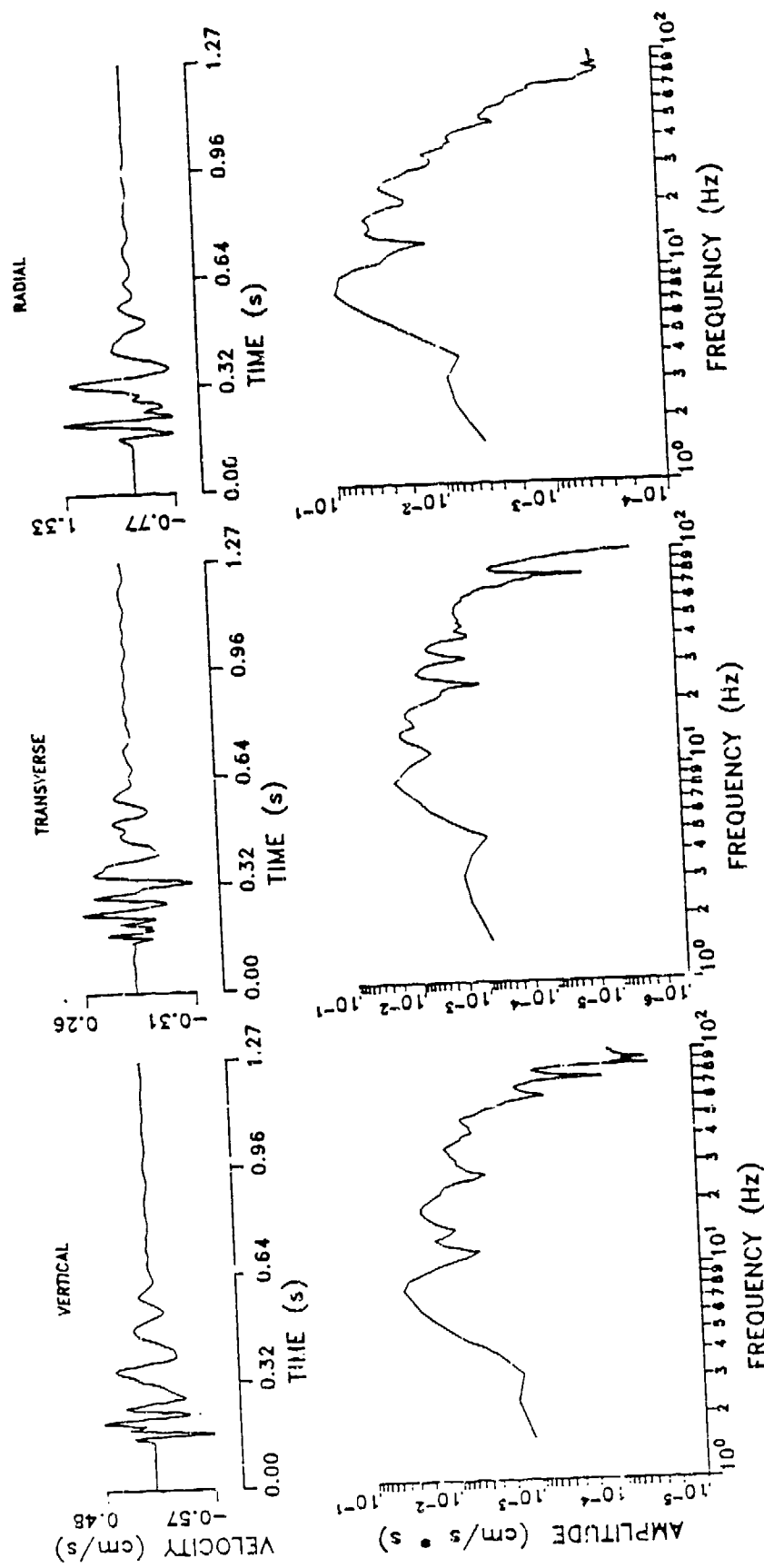
CART 1C: 0 DEGREES AT 13.5 METERS



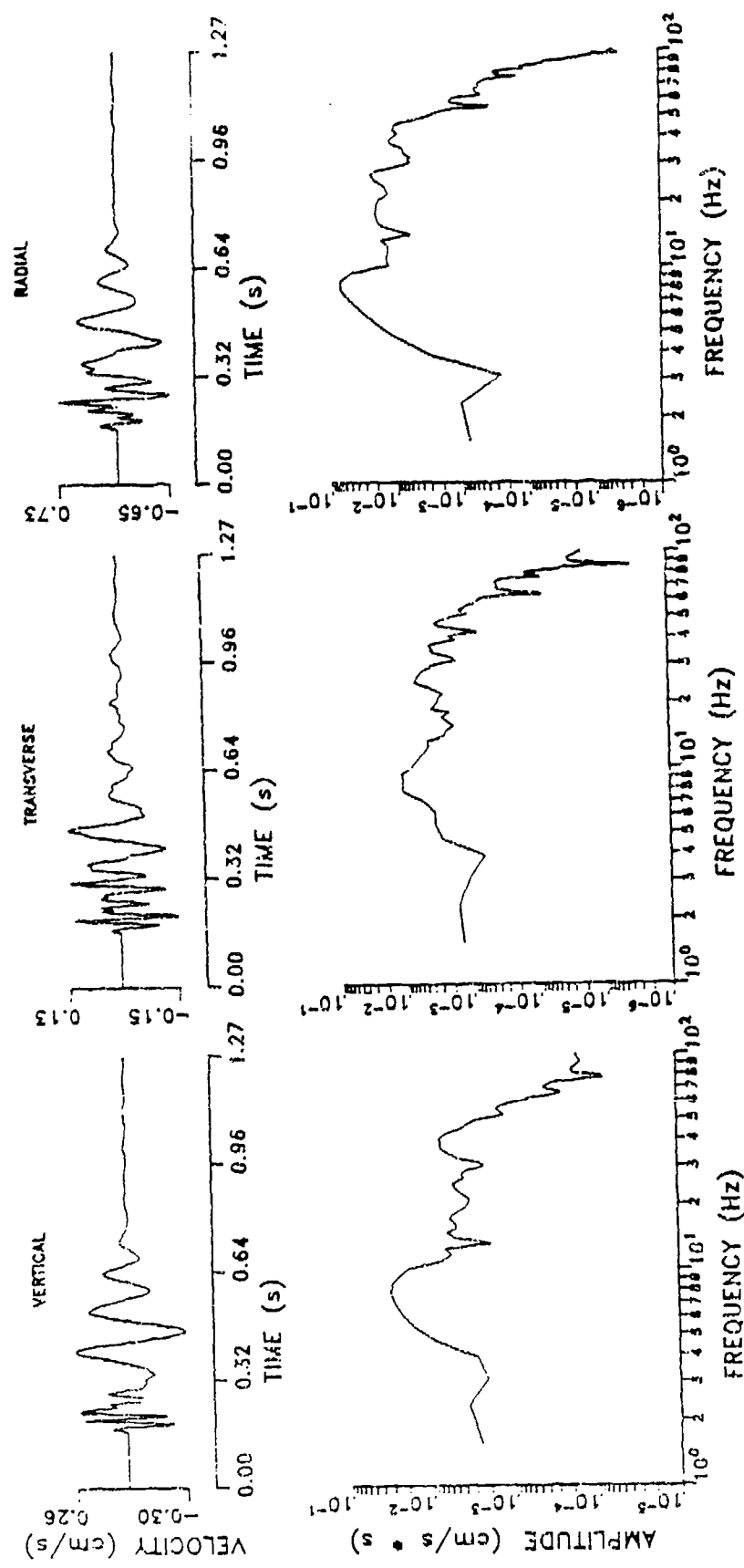
CART 1D: 180 DEGREES AT 27.0 METERS



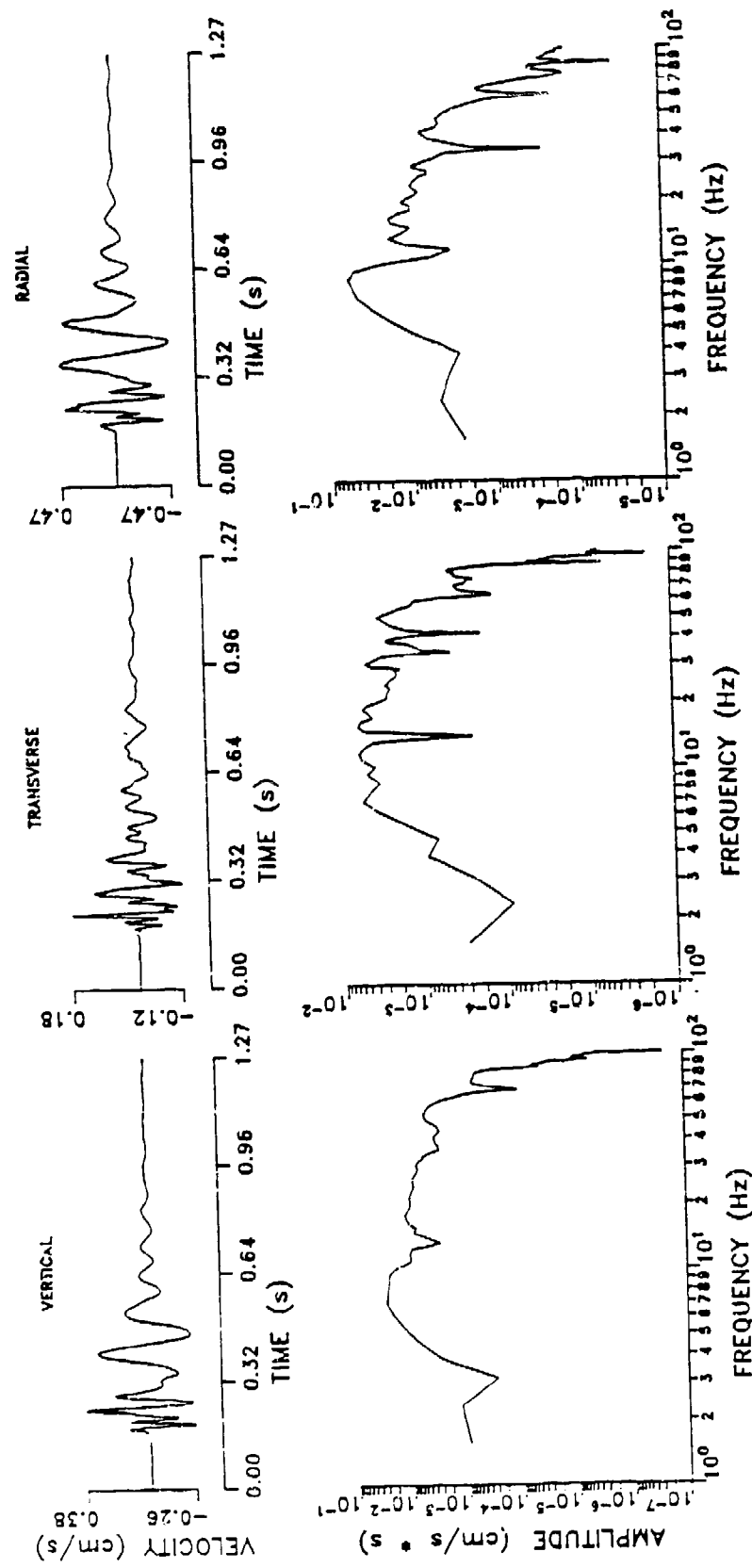
CART 1E: 35 DEGREES AT 27.0 METERS



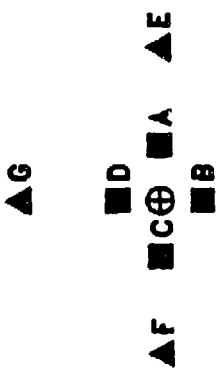
CART 1F: 215 DEGREES AT 40.6 METERS



CART 1G: 325 DEGREES AT 40.6 METERS



## PLAN VIEW OF CART2 SOURCE AND RECEIVER LOCATIONS

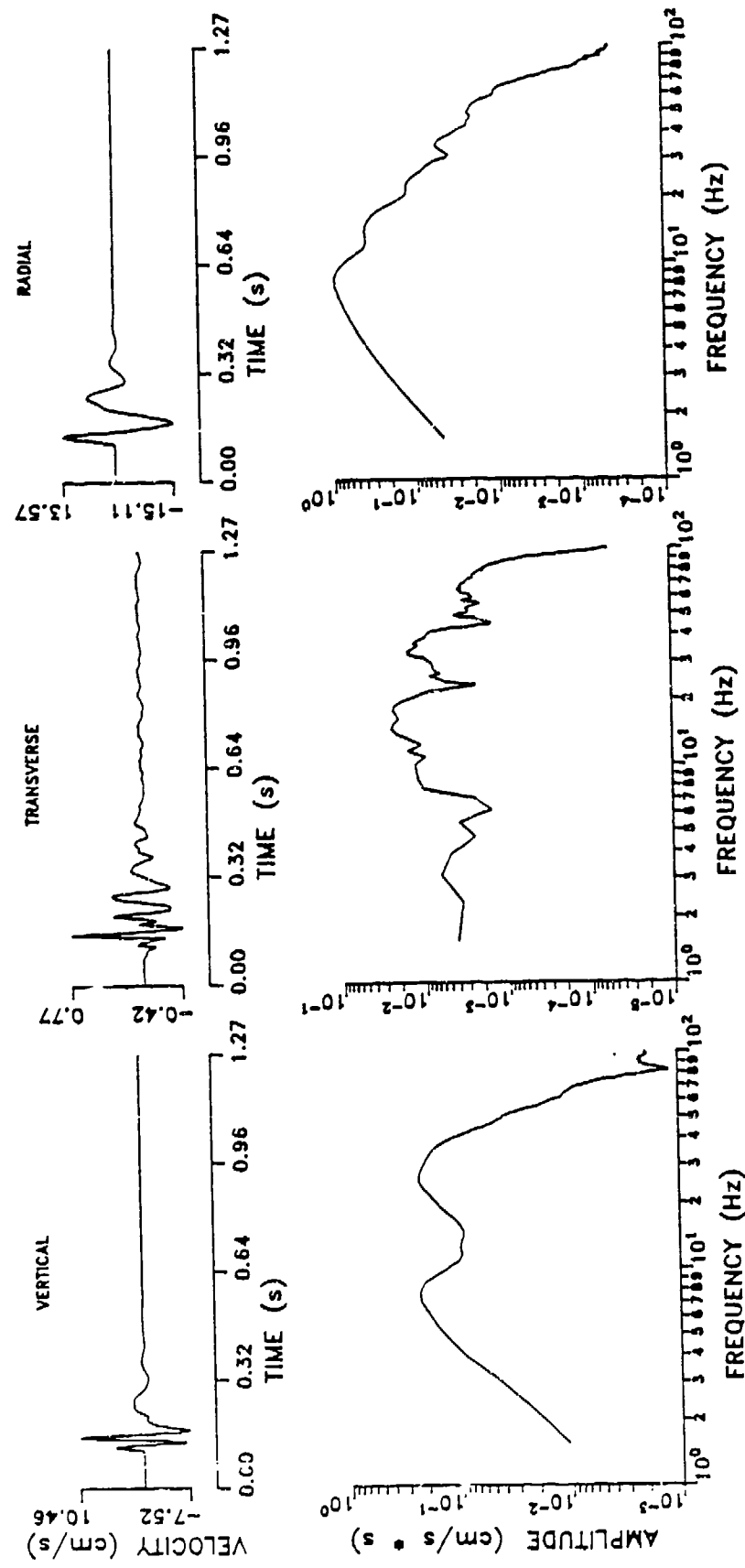


⊕SHOT LOCATION

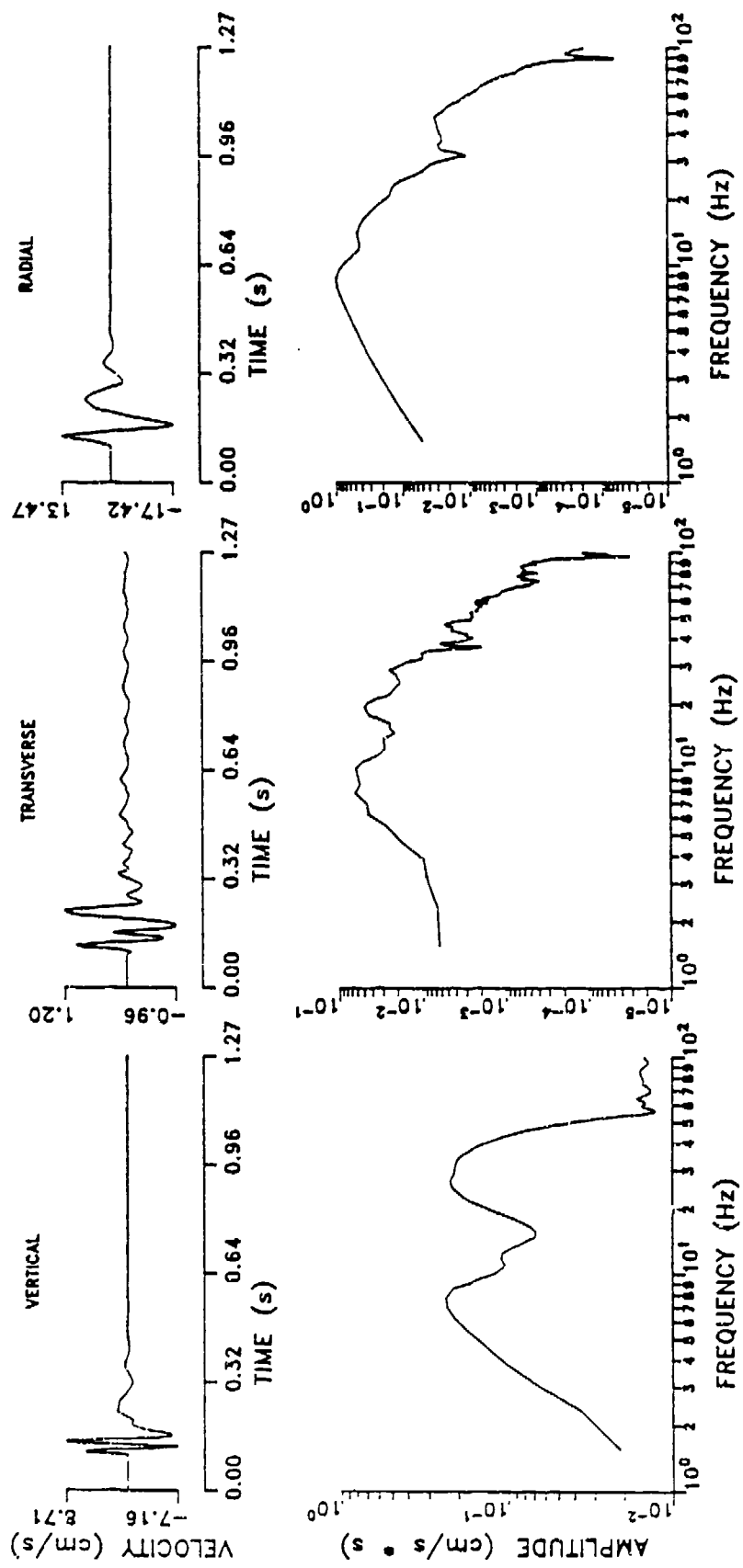
| 0° NORTH

■ 5.0 m  
▲ 13.5 m

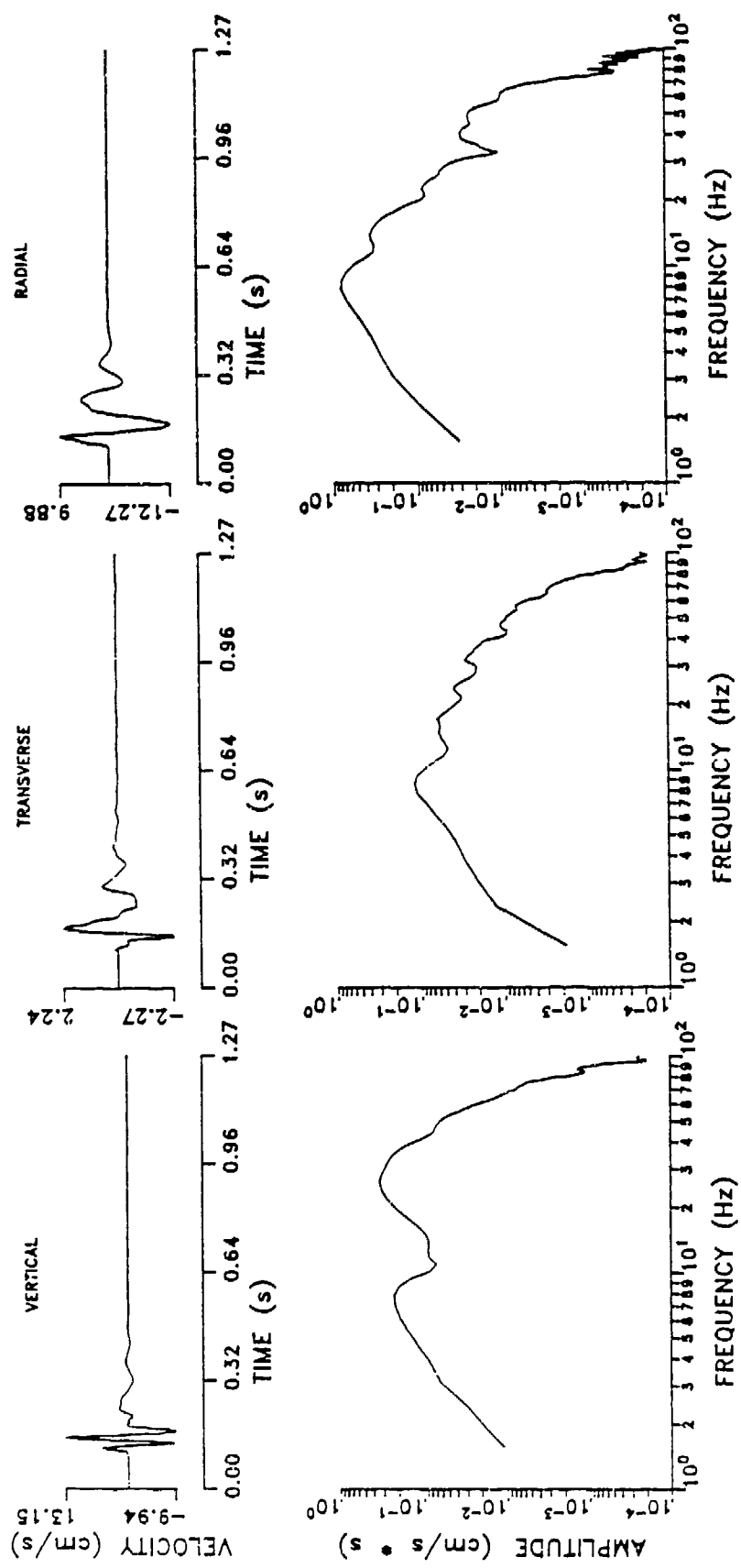
CART 2A: 90 DEGREES AT 5.0 METERS



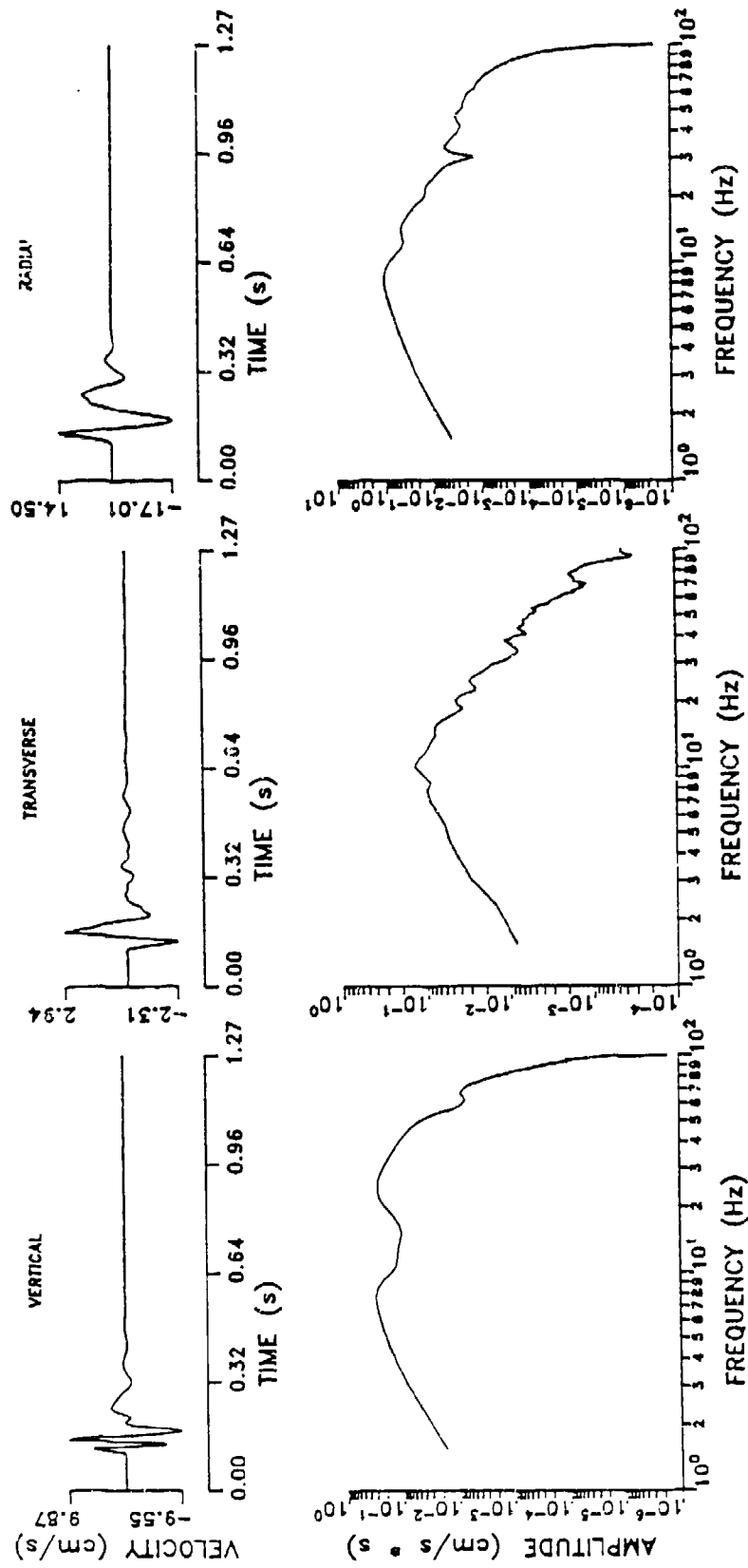
CART 2B: 180 DEGREES AT 5.0 METERS



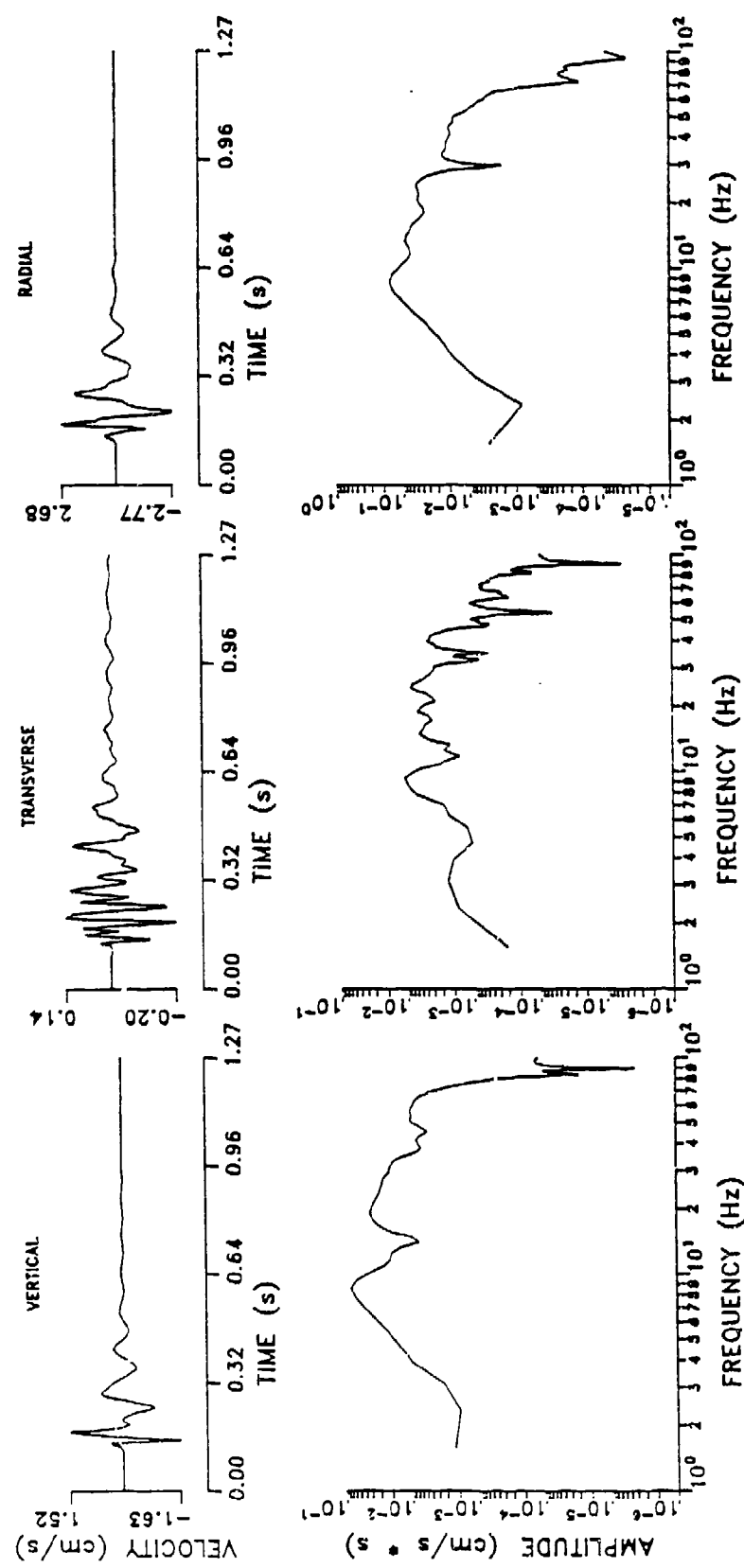
CART 2C: 270 DEGREES AT 5.0 METERS



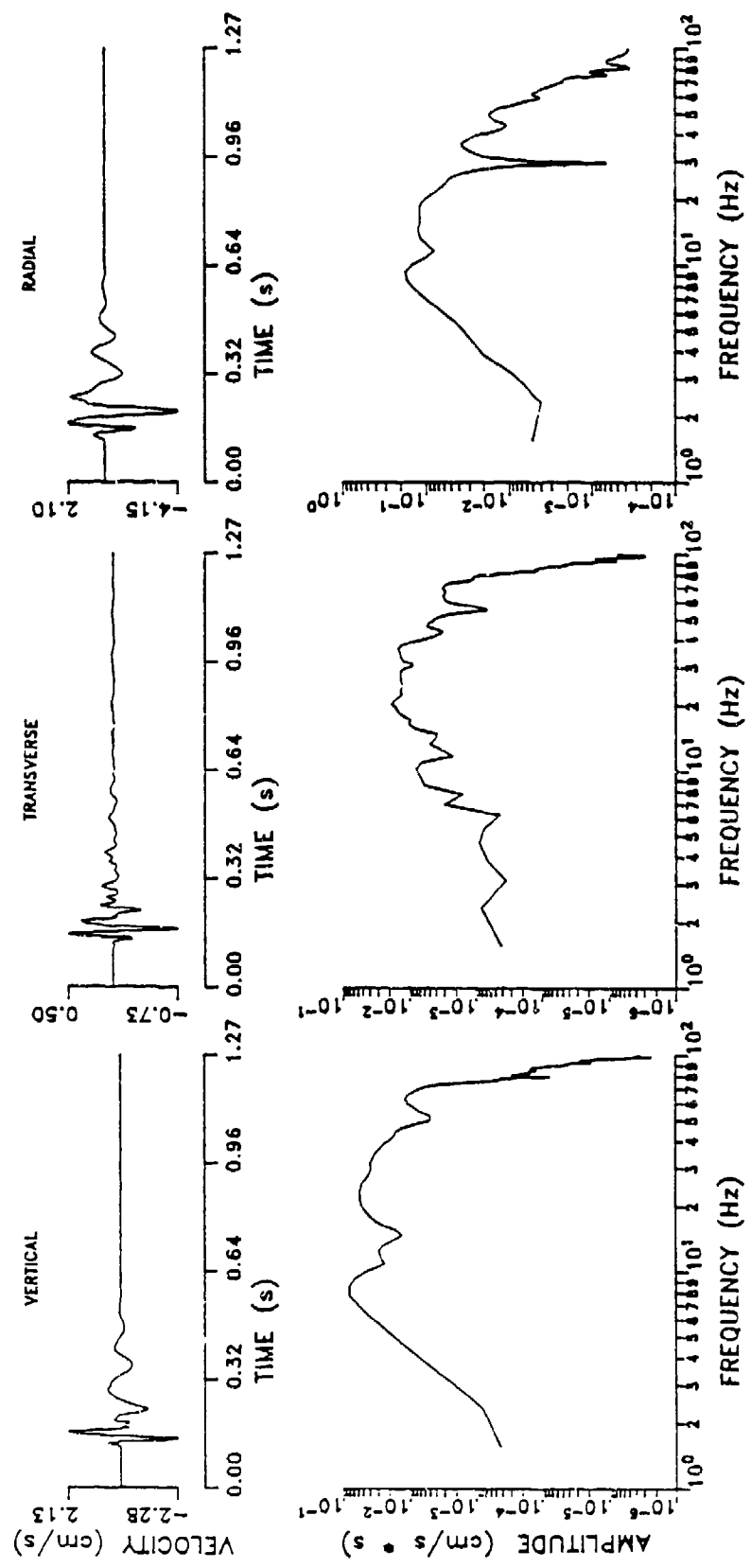
CART 2D: 0 DEGREES AT 27.0 METERS



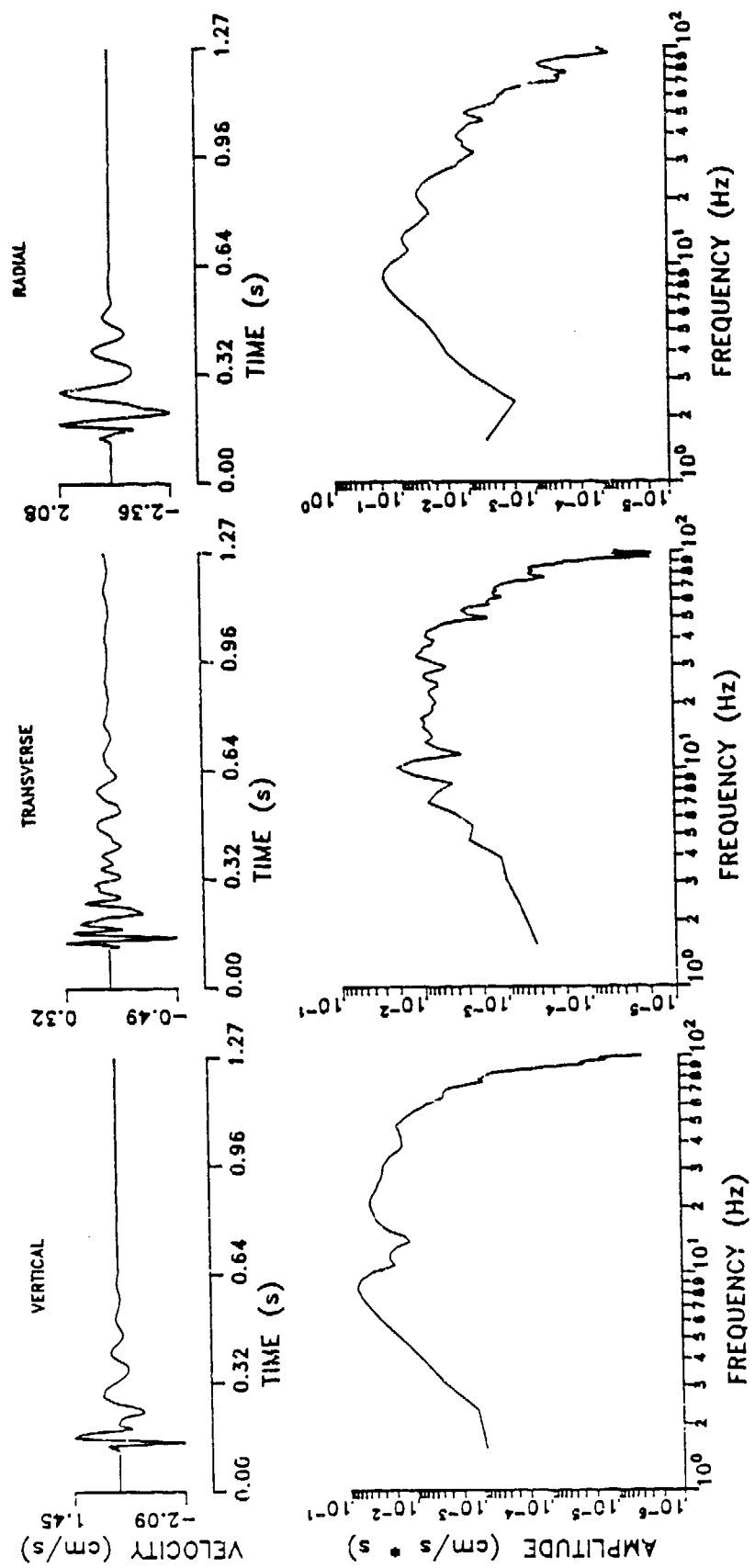
CART 2E: 90 DEGREES AT 13.5 METERS



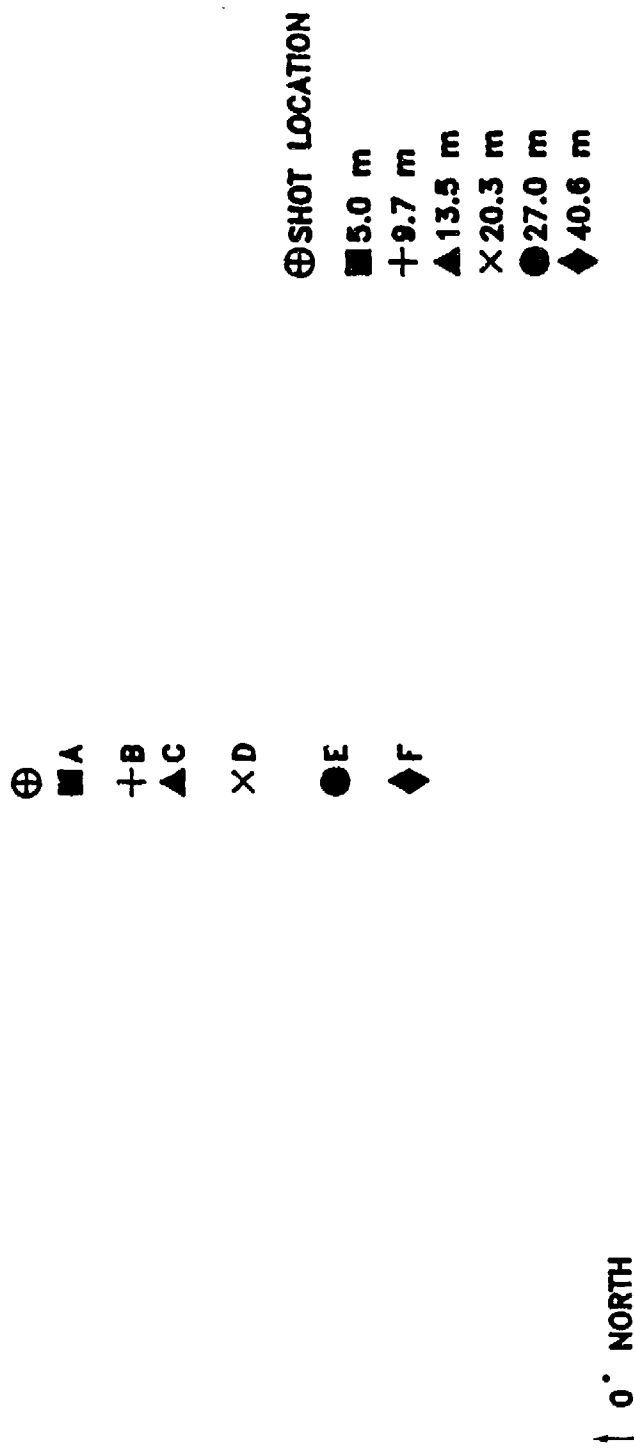
CART 2F: 270 DEGREES AT 13.5 METERS



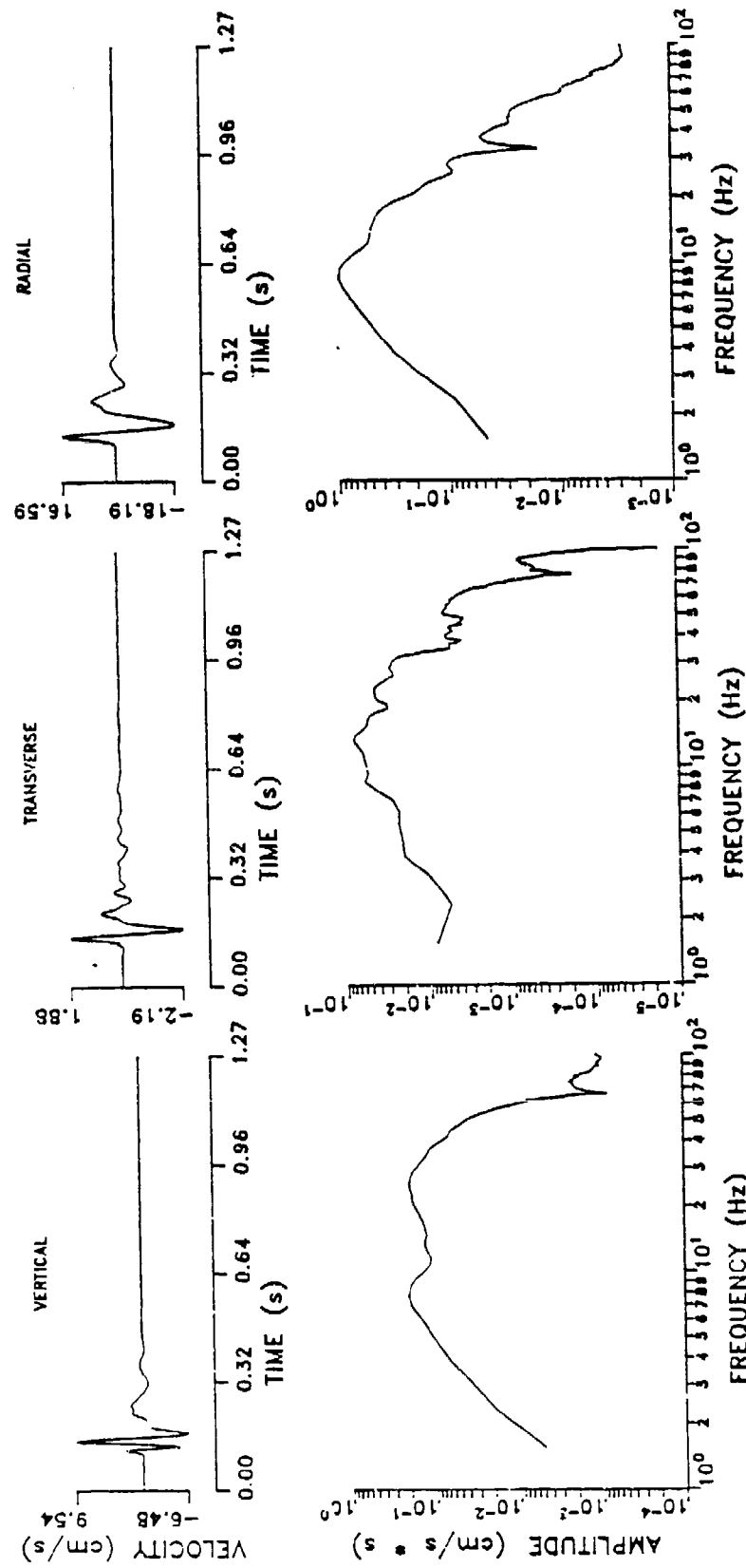
CART 2G: 0 DEGREES AT 13.5 METERS



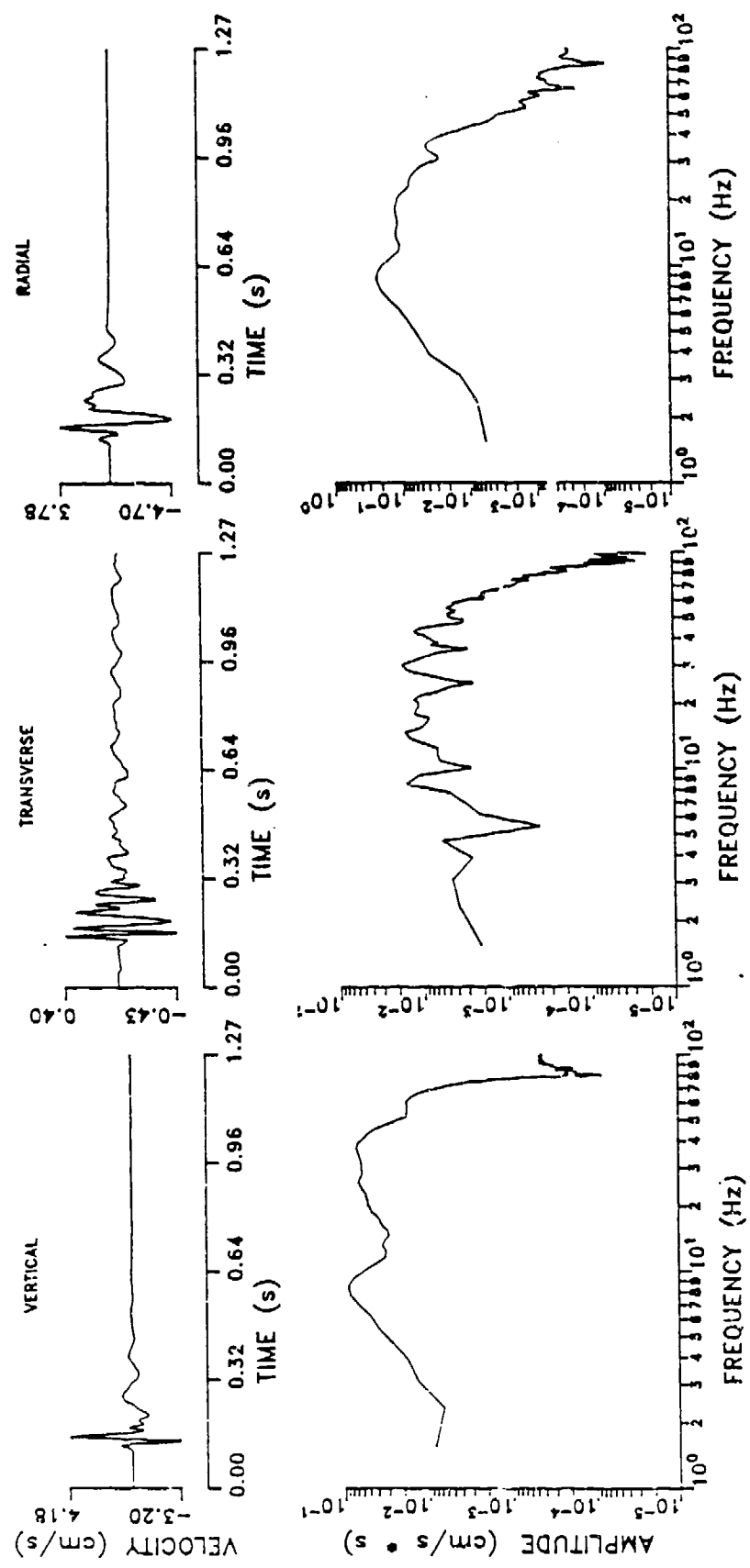
## PLAN VIEW OF CART3 SOURCE AND RECEIVER LOCATIONS



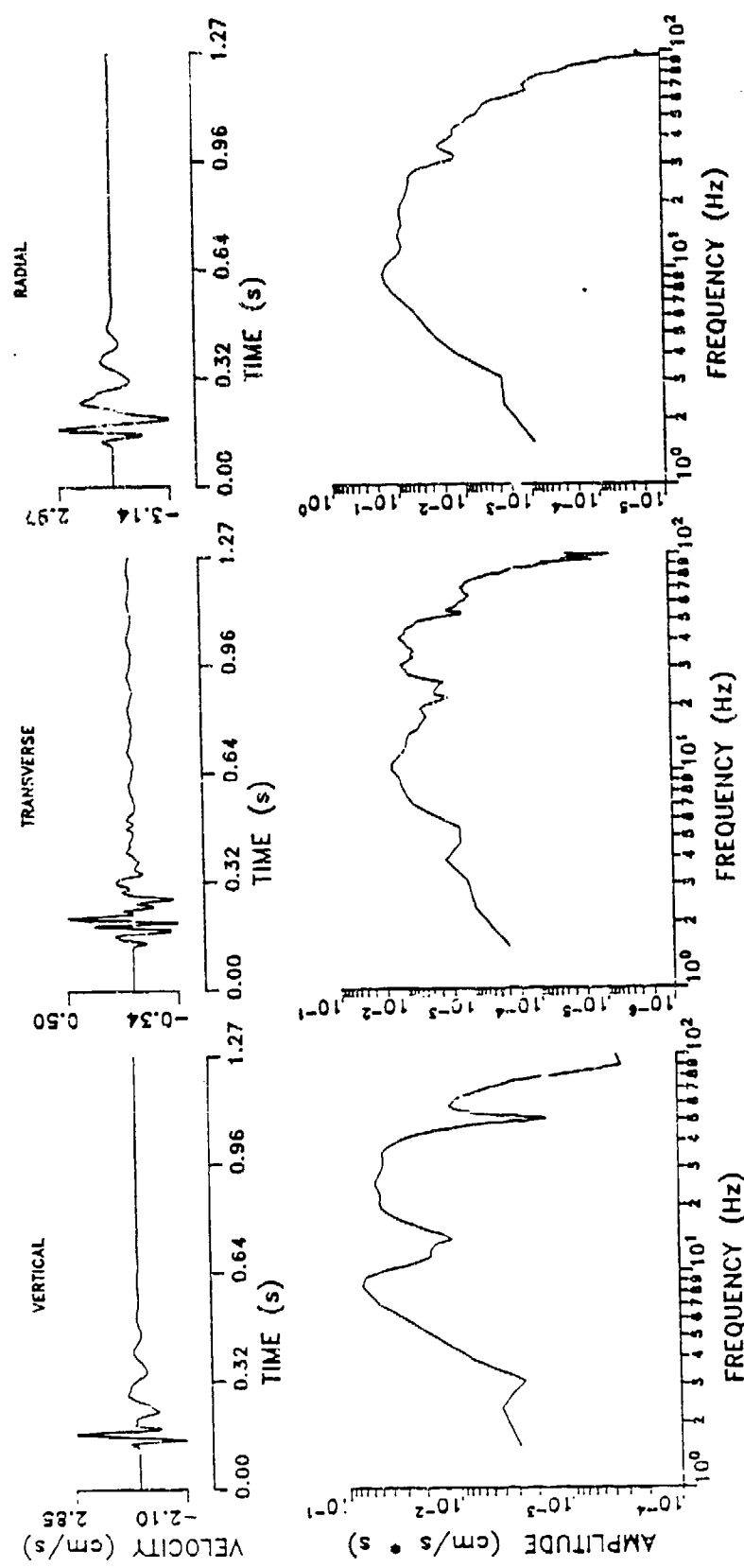
CART 3A: 180 DEGREES AT 5.0 METERS



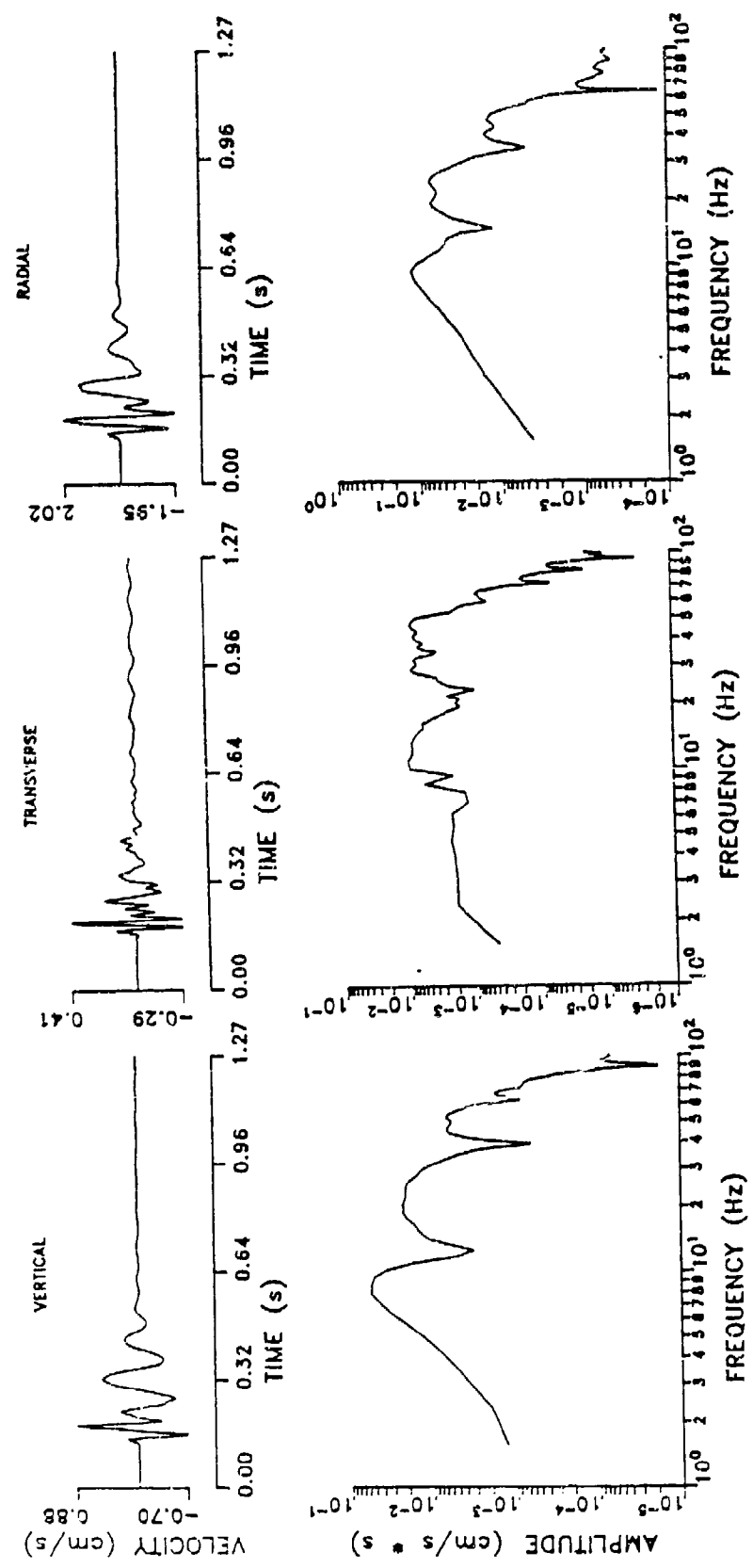
CART 3B: 180 DEGREES AT 9.7 METERS



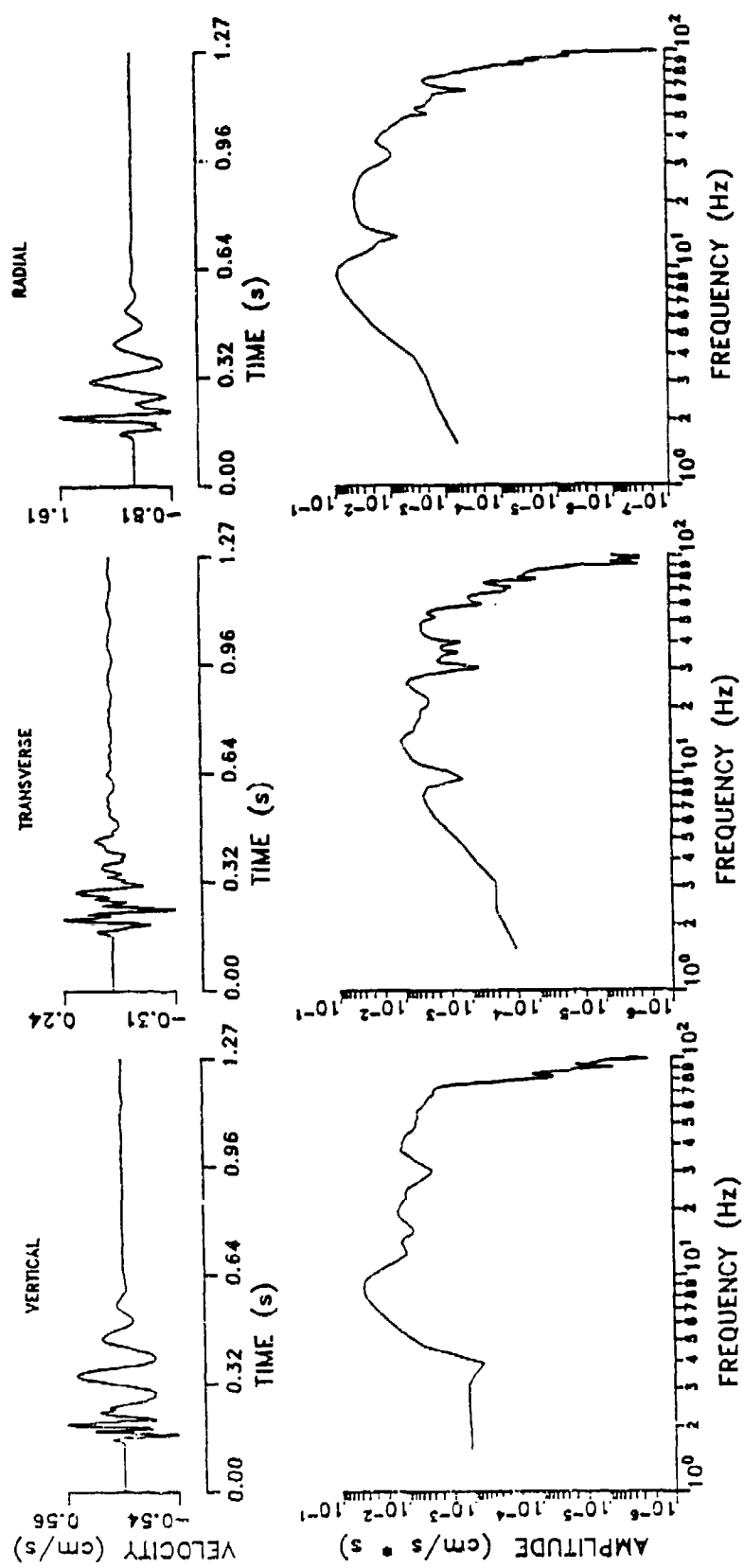
CART 3C: 180 DEGREES AT 13.5 METERS



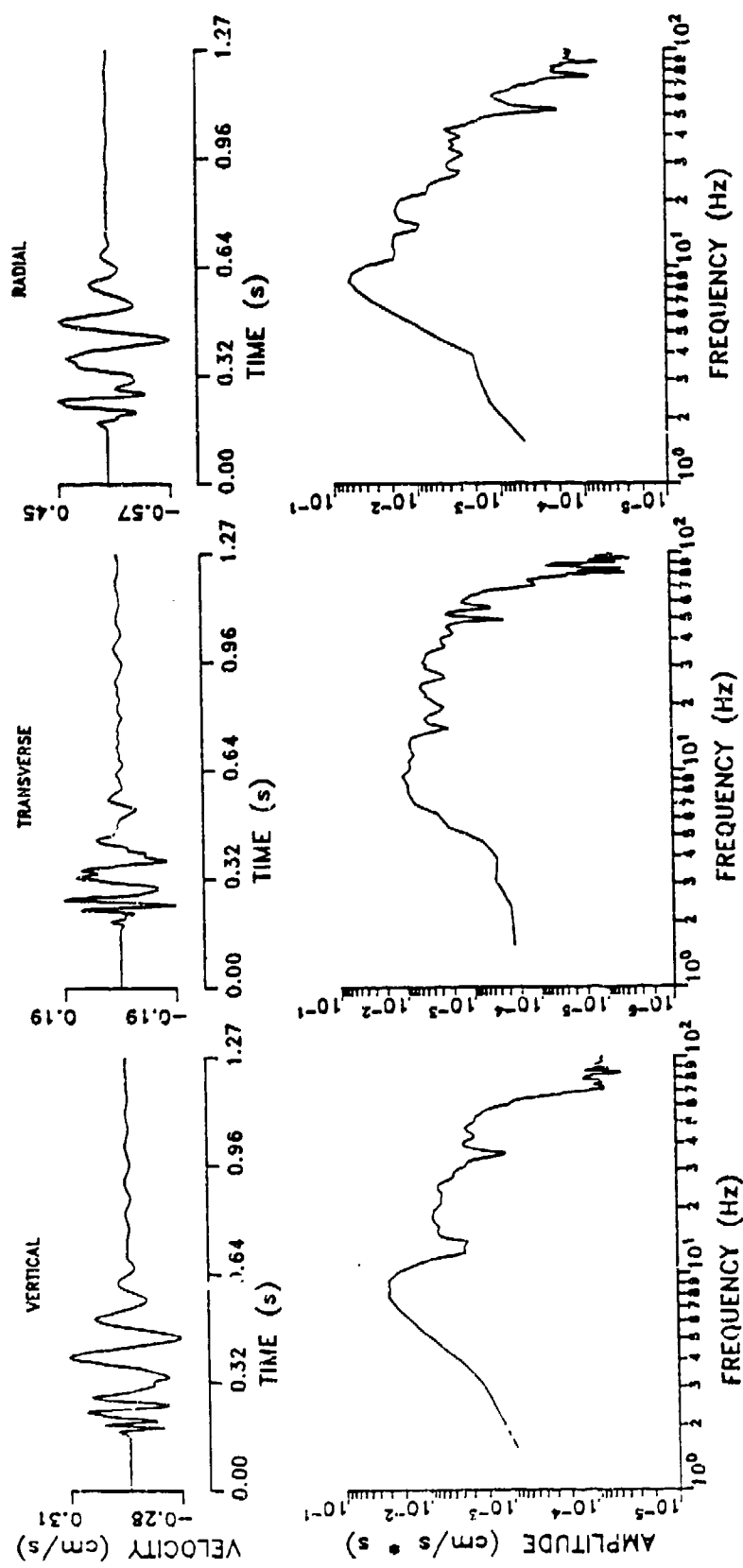
CART 3D: 180 DEGREES AT 20.3 METERS



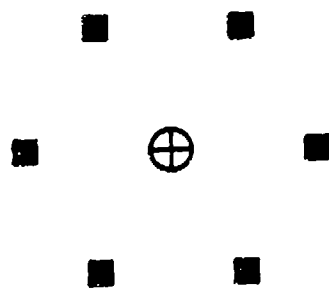
CART 3E: 180 DEGREES AT 27.0 METERS



CART 3F: 180 DEGREES AT 40.6 METERS



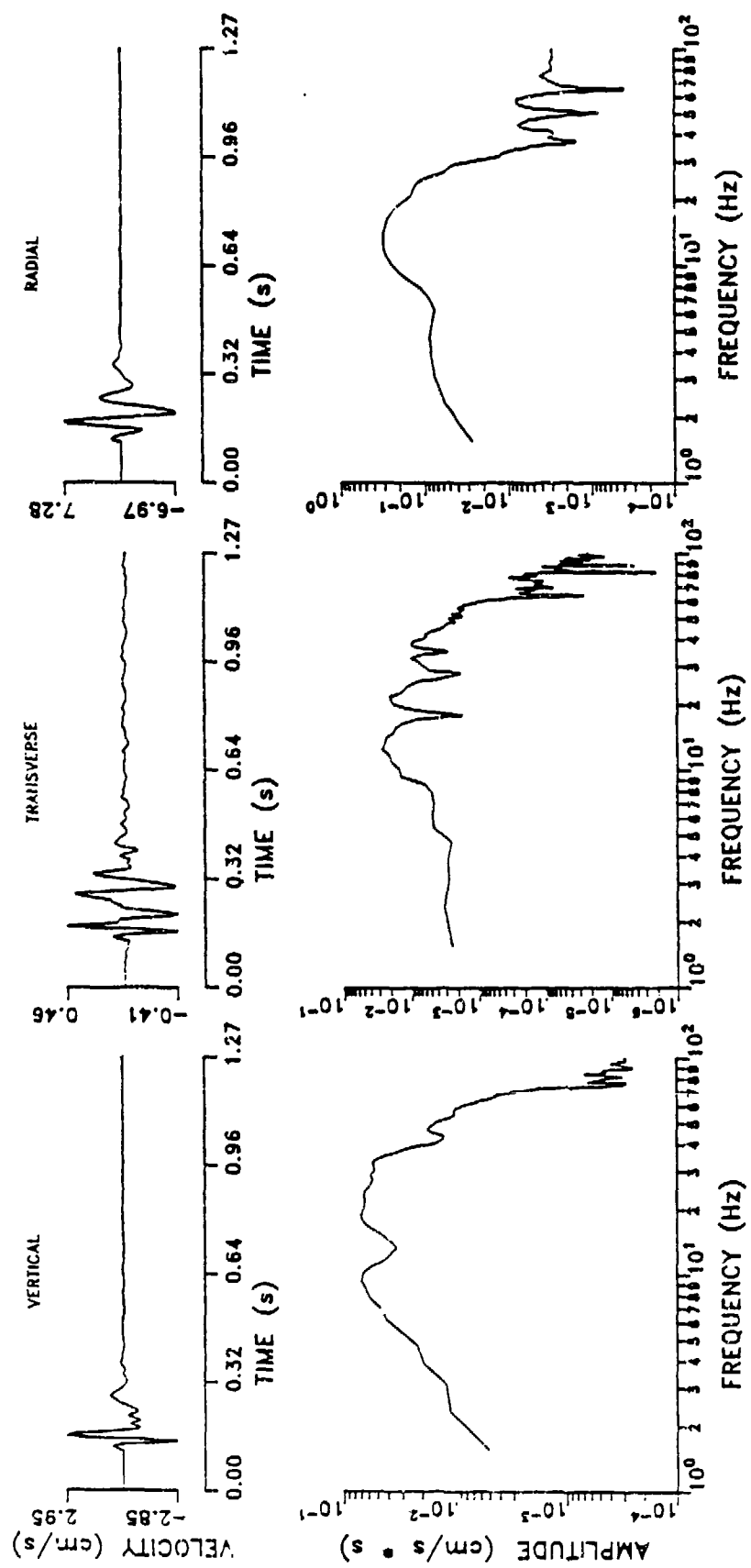
PLAN VIEW OF ART1 SOURCE AND RECEIVER LOCATIONS



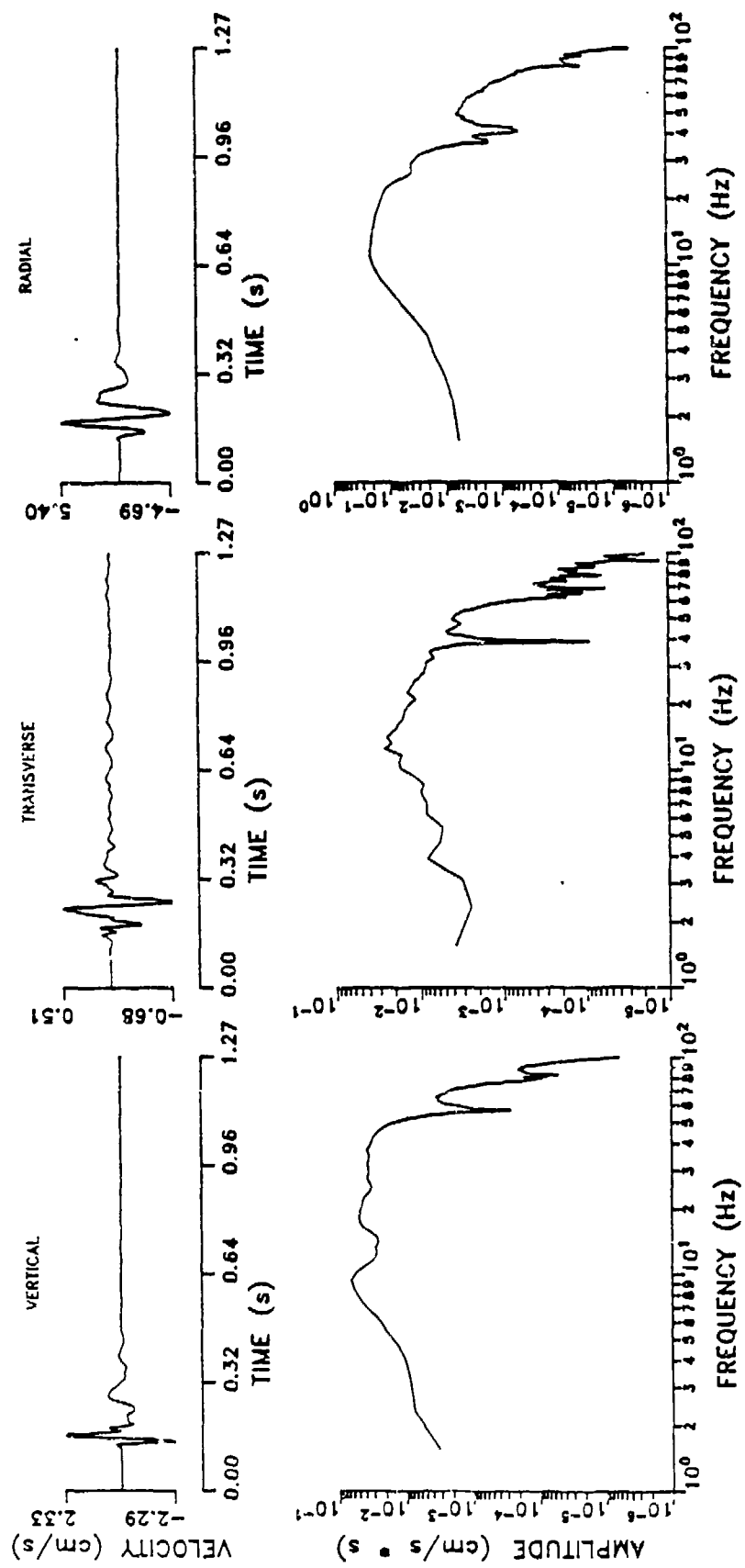
⊕ SHOT LOCATION  
■ RECEIVER AT 10 m

↑ 0° NORTH

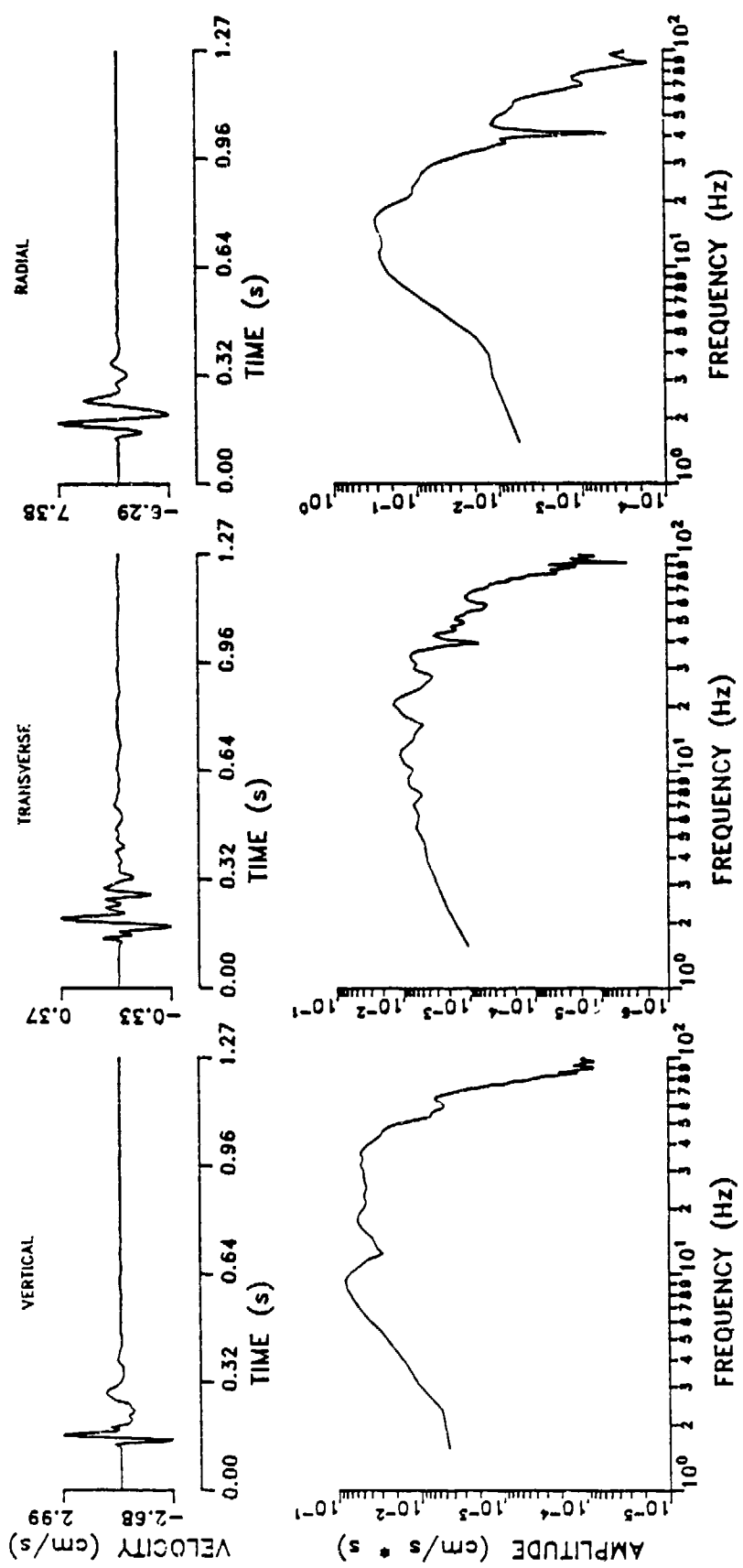
ART 1: 0 DEGREES AT 10 METERS



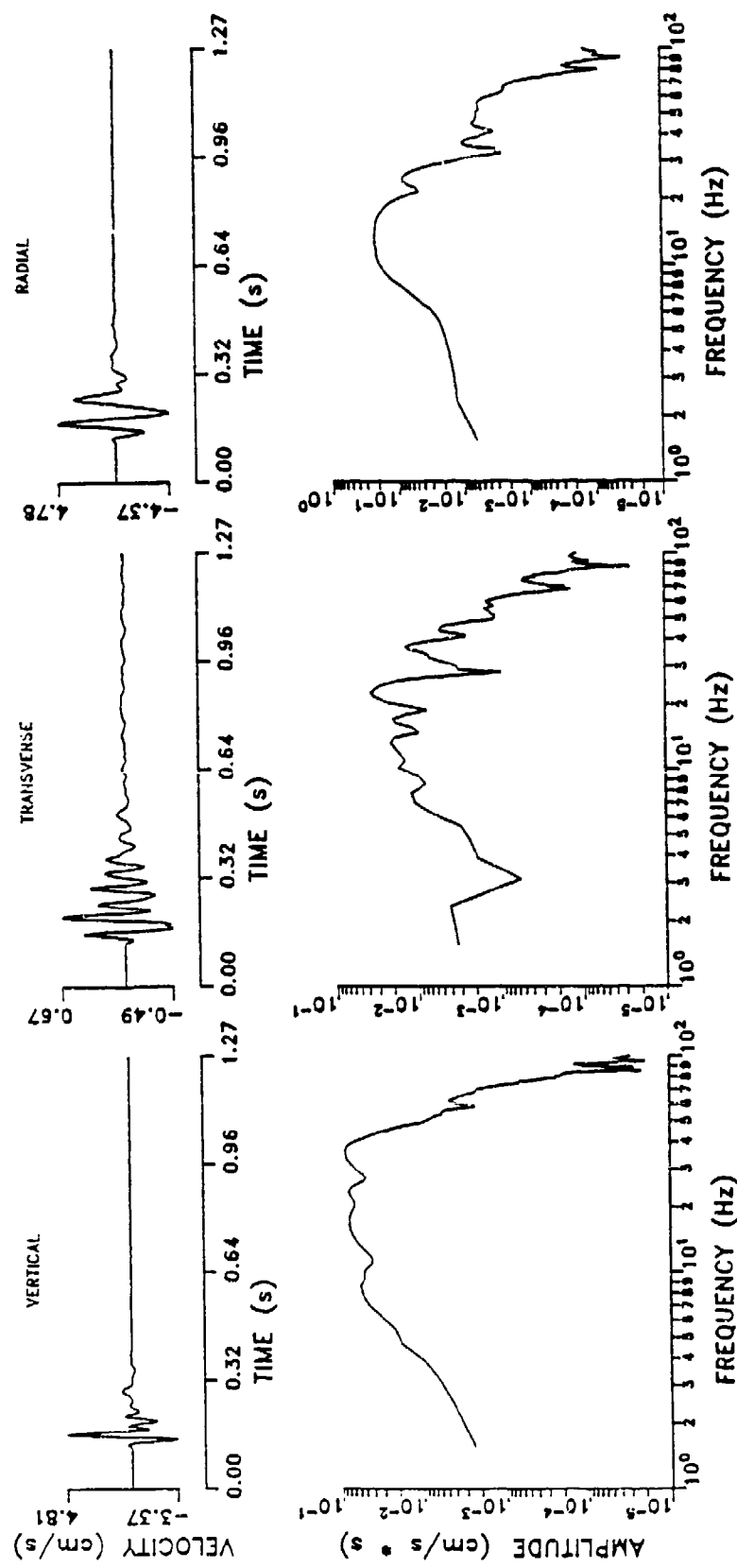
ARR 1: 60 DEGREES AT 10 METERS



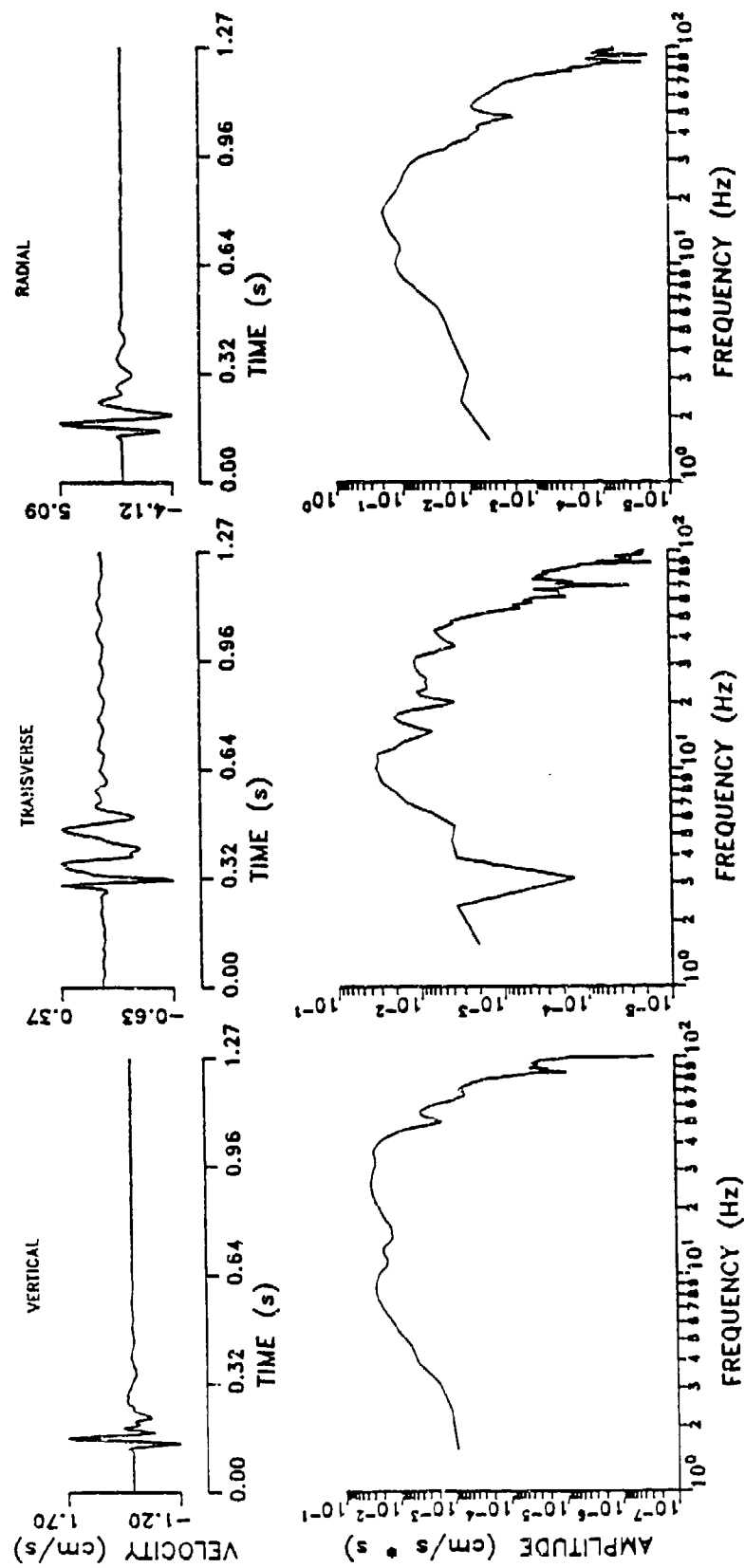
ART 1: 120 DEGREES AT 10 METERS



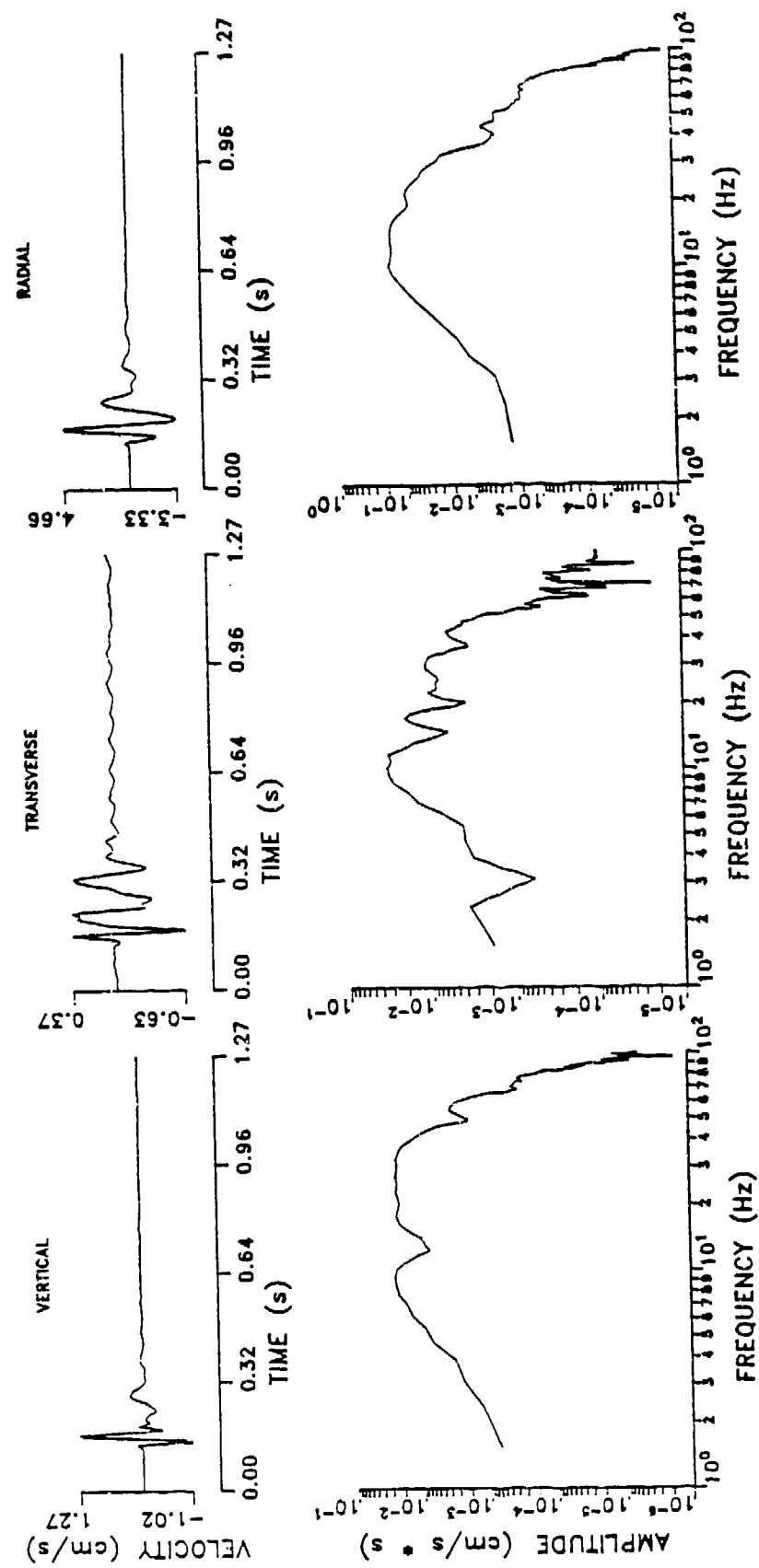
ART 1: 180 DEGREES AT 10 METERS



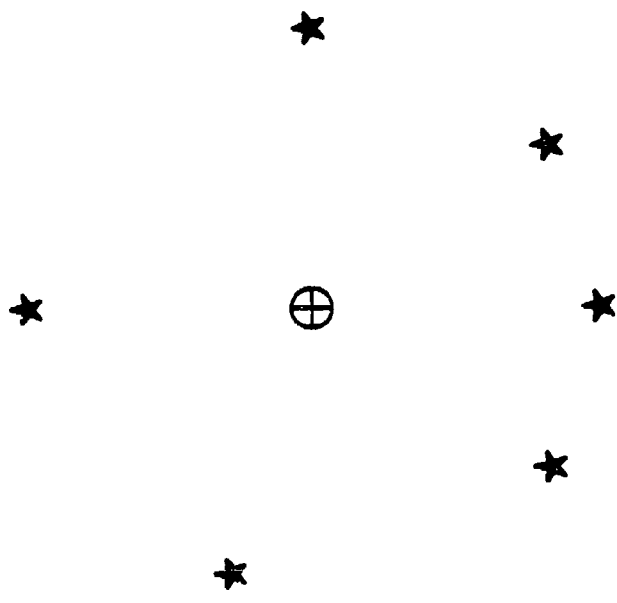
ART 1: 240 DEGREES AT 10 METERS



ART 1: 300 DEGREES AT 10 METERS



## PLAN VIEW OF ART2 SOURCE AND RECEIVER LOCATIONS

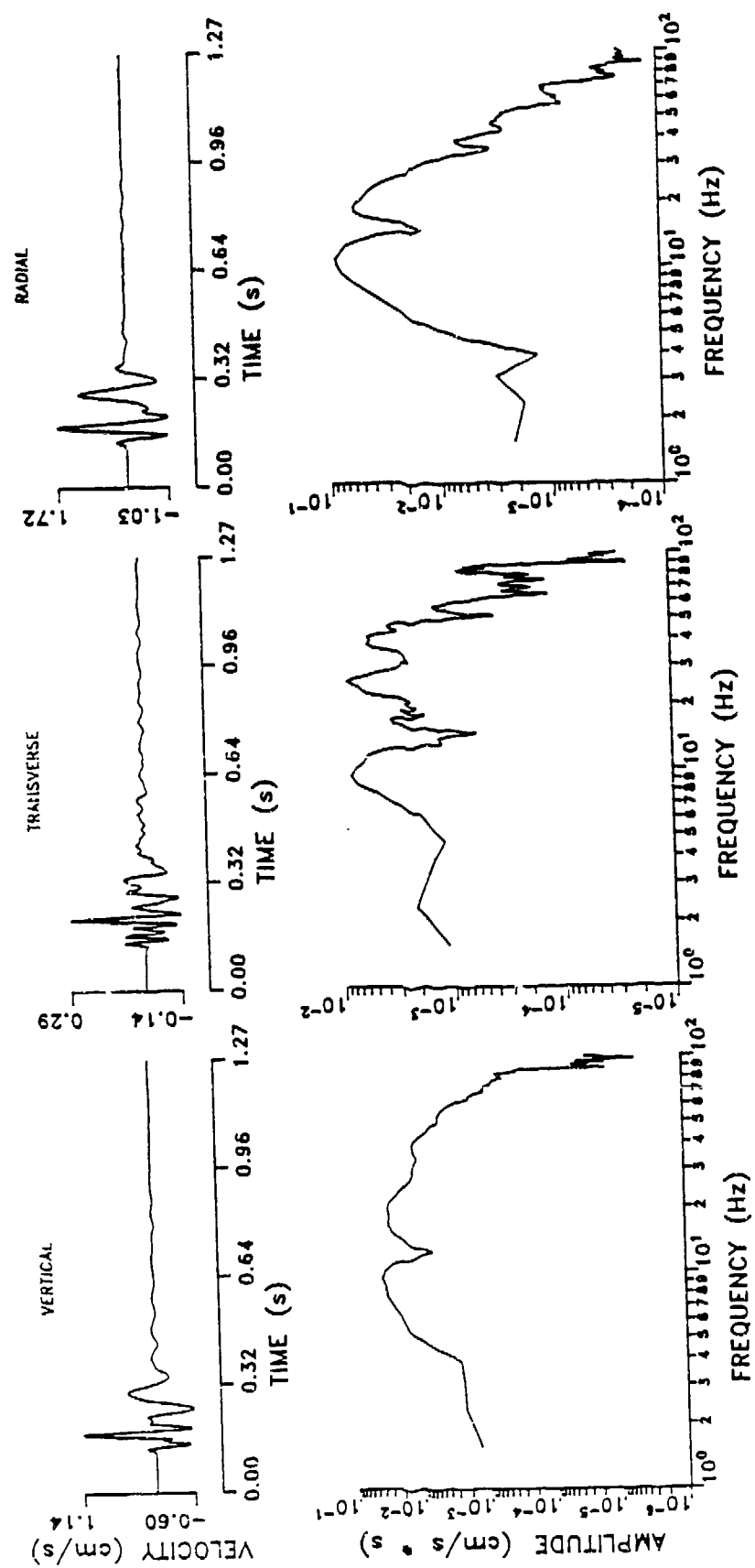


⊕ SHOT LOCATION

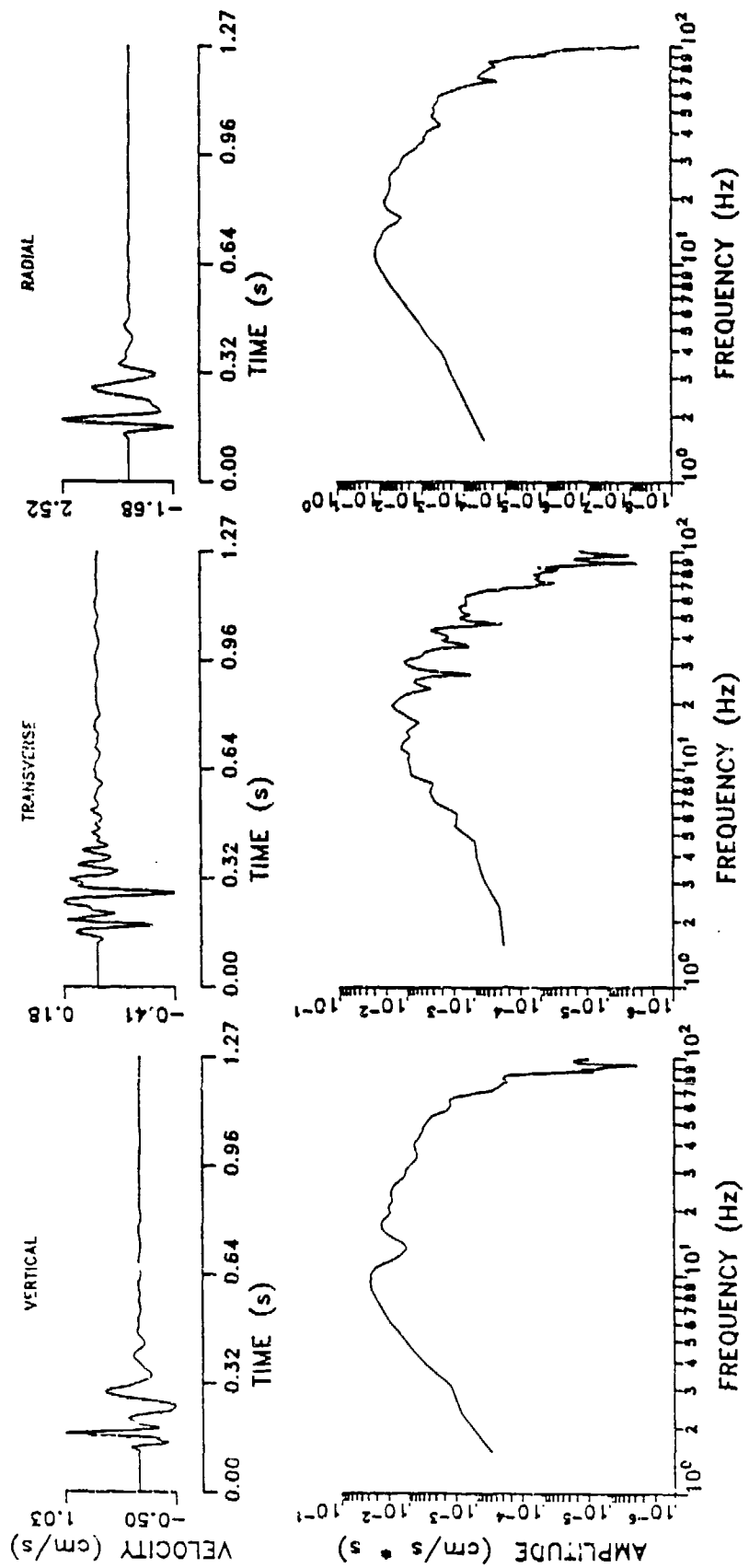
★ RECEIVER AT 20 m

↑ 0° NORTH

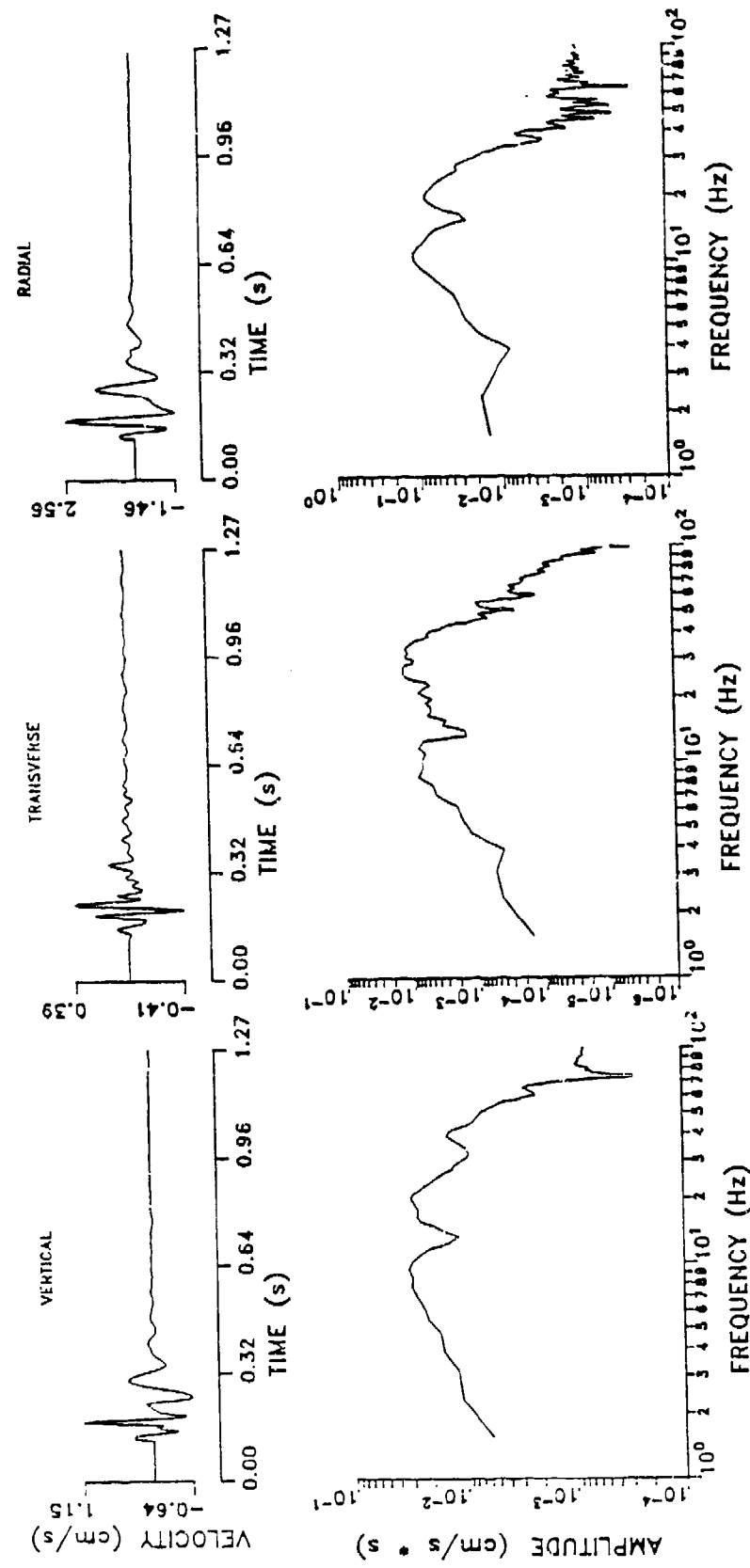
ART 2: 0 DEGREES AT 20 METERS



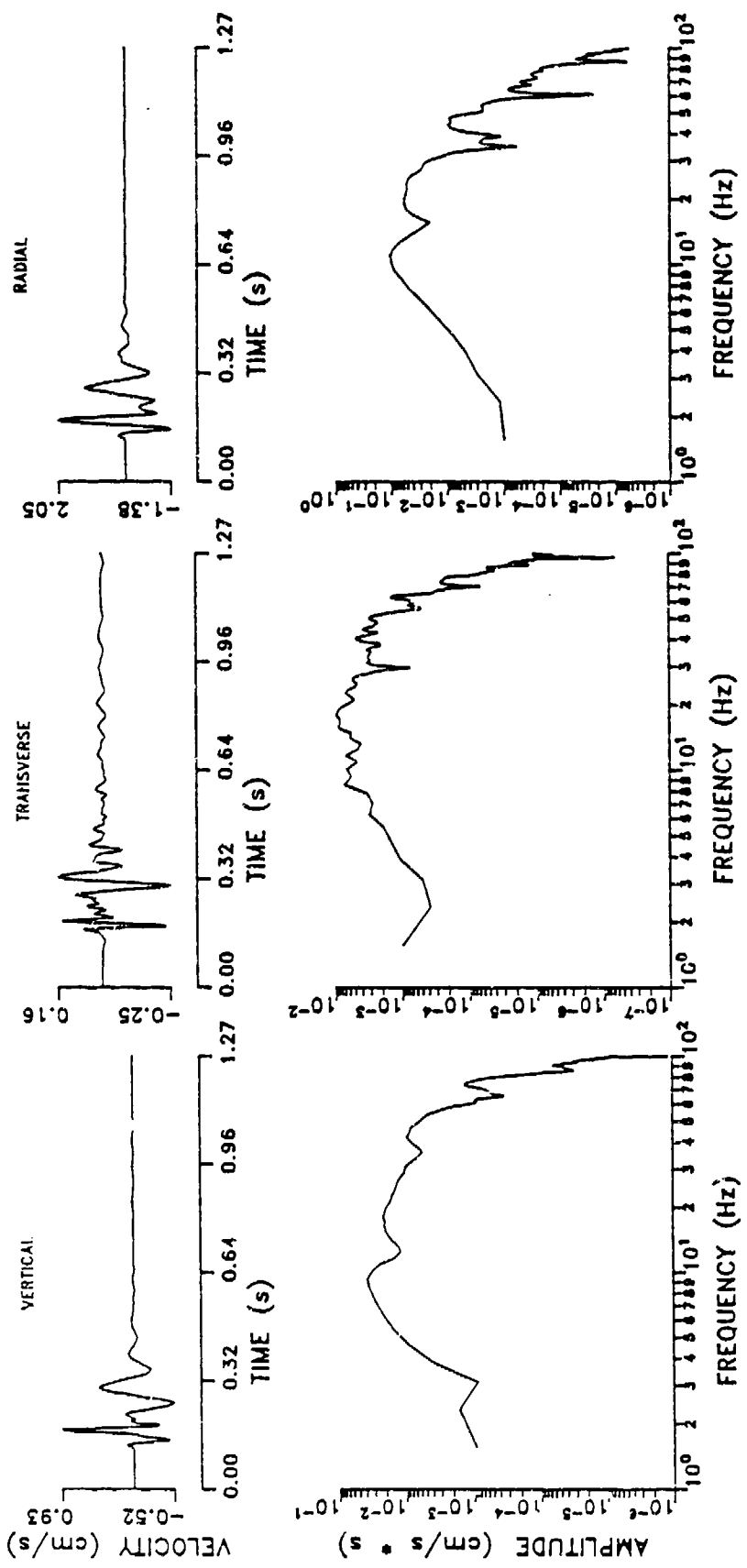
ART 2: 90 DEGREES AT 20 METERS



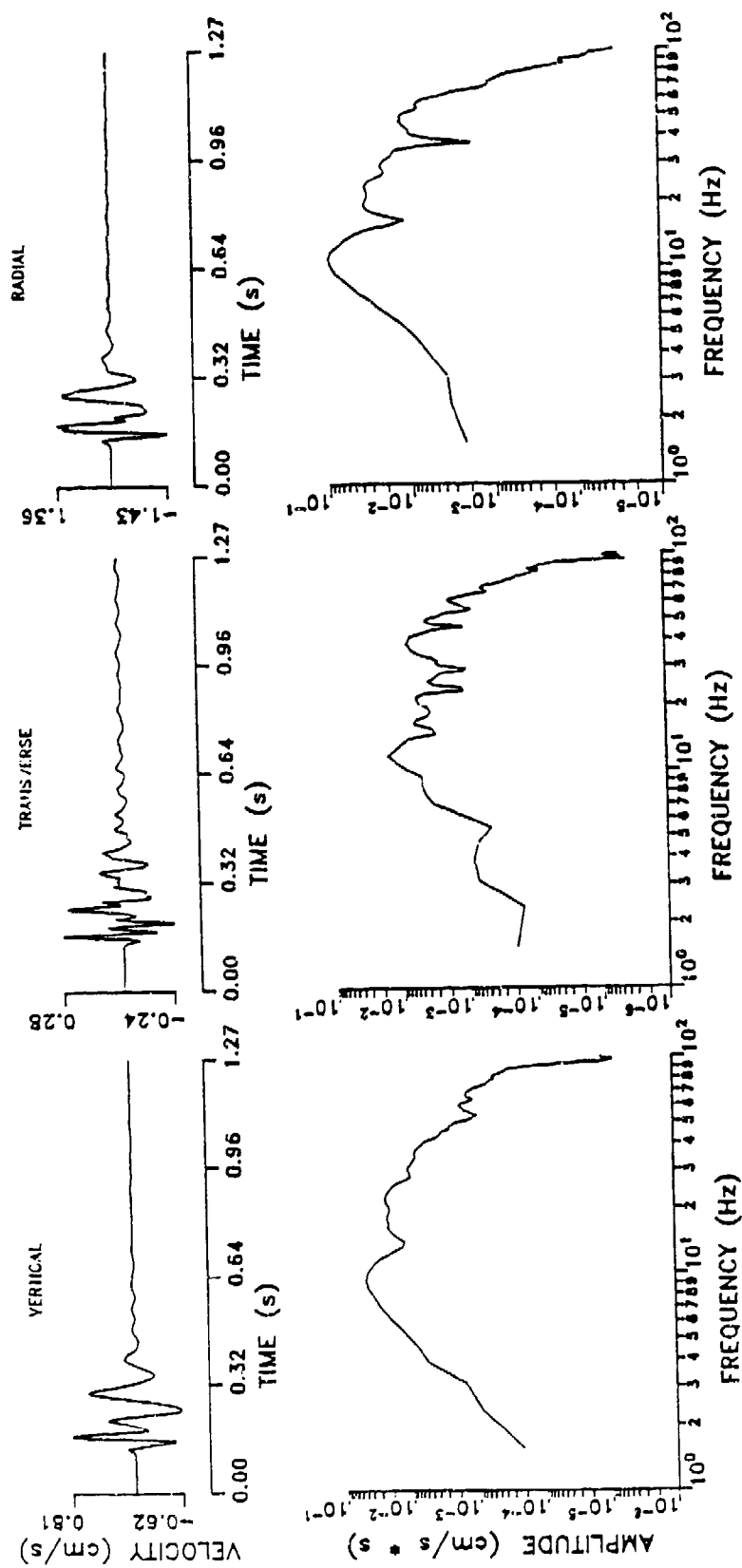
ART 2: 144 DEGREES AT 20 METERS



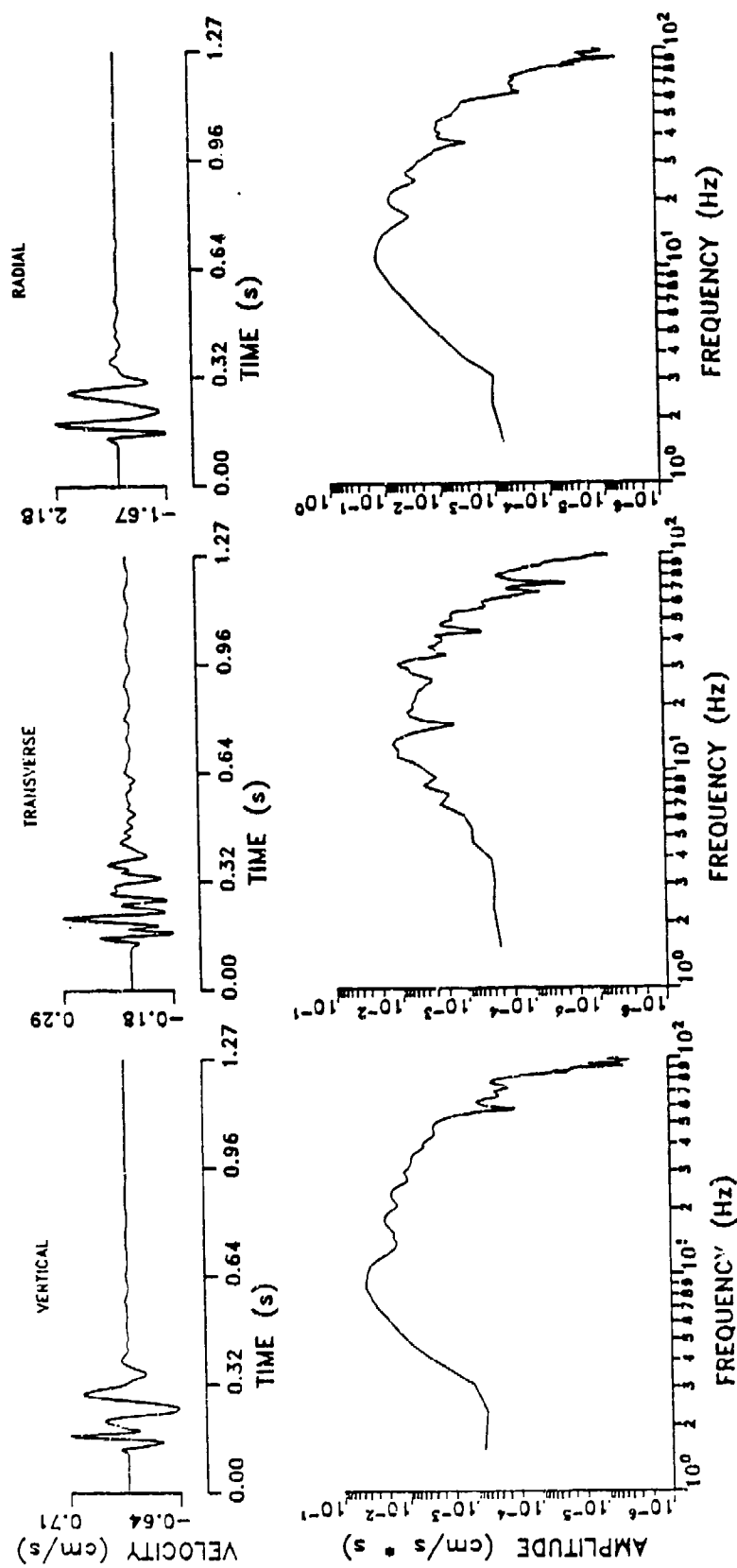
ART 2: 180 DEGREES AT 20 METERS



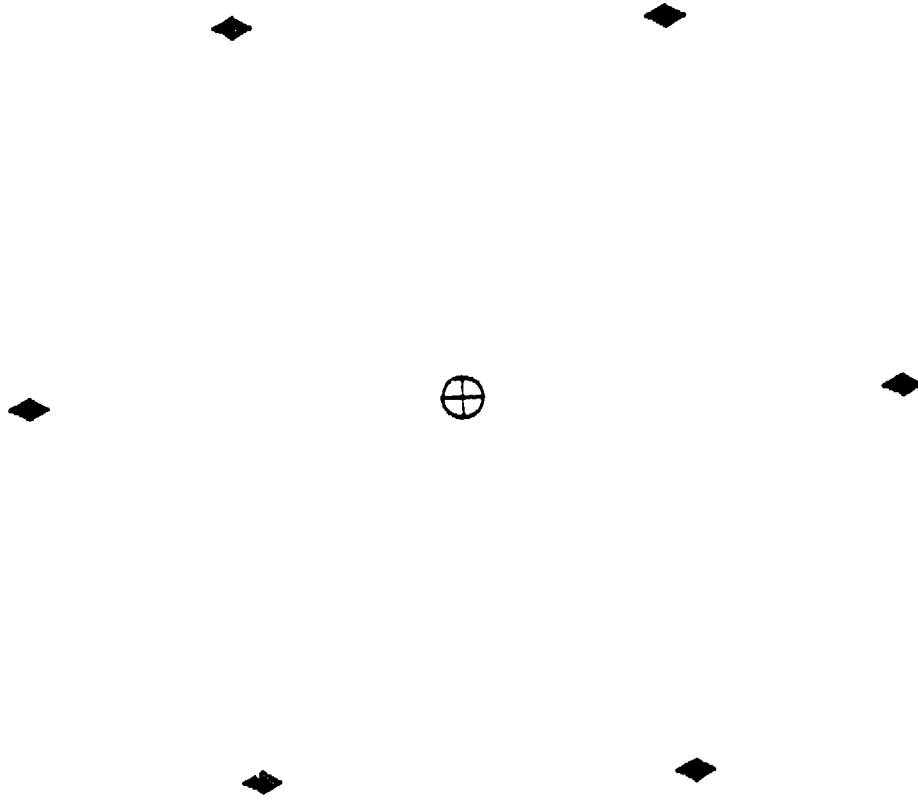
ART 2: 216 DEGREES AT 20 METERS



ART 2: 288 DEGREES AT 20 METERS



PLAN VIEW OF ART3 SOURCE AND RECEIVER LOCATIONS

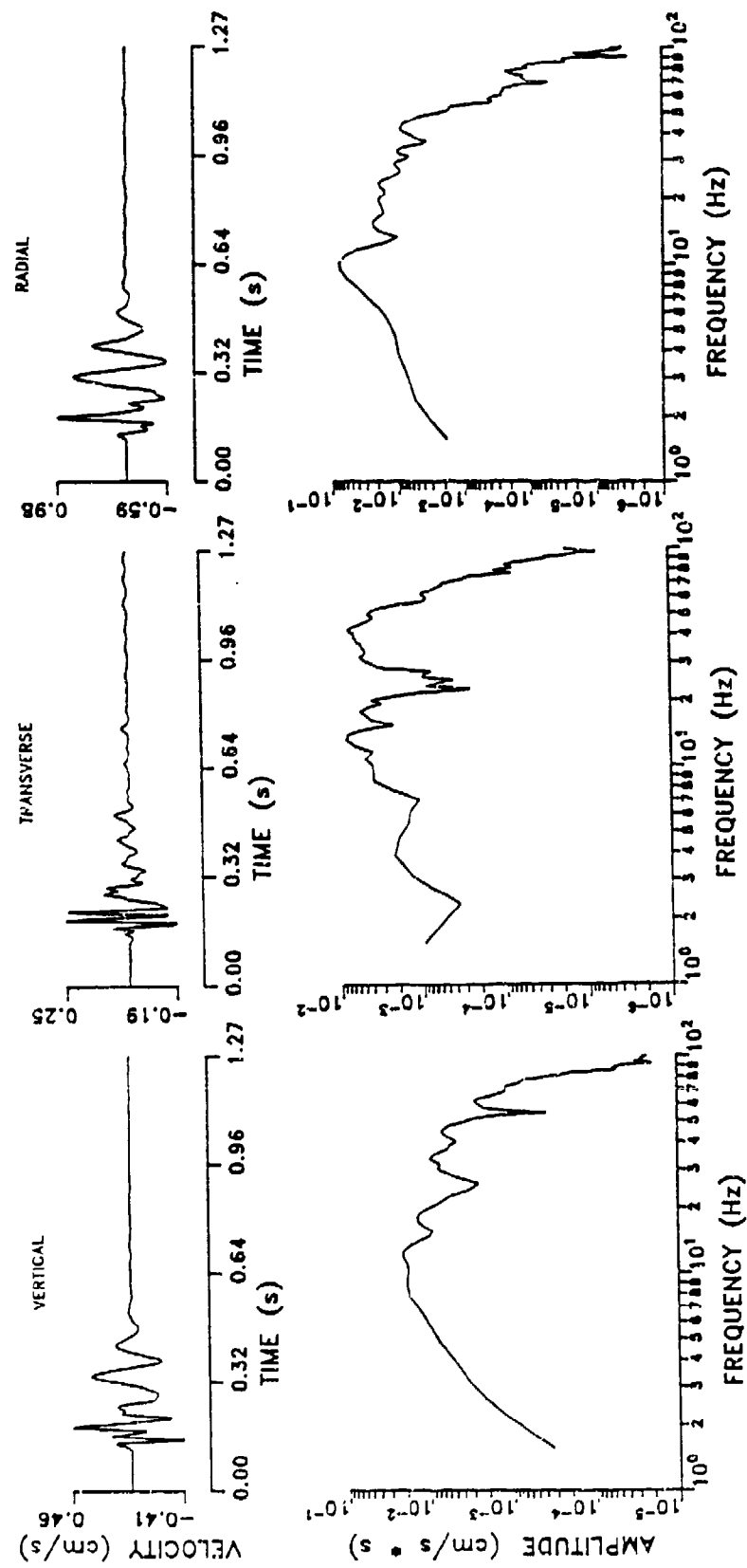


10° NORTH

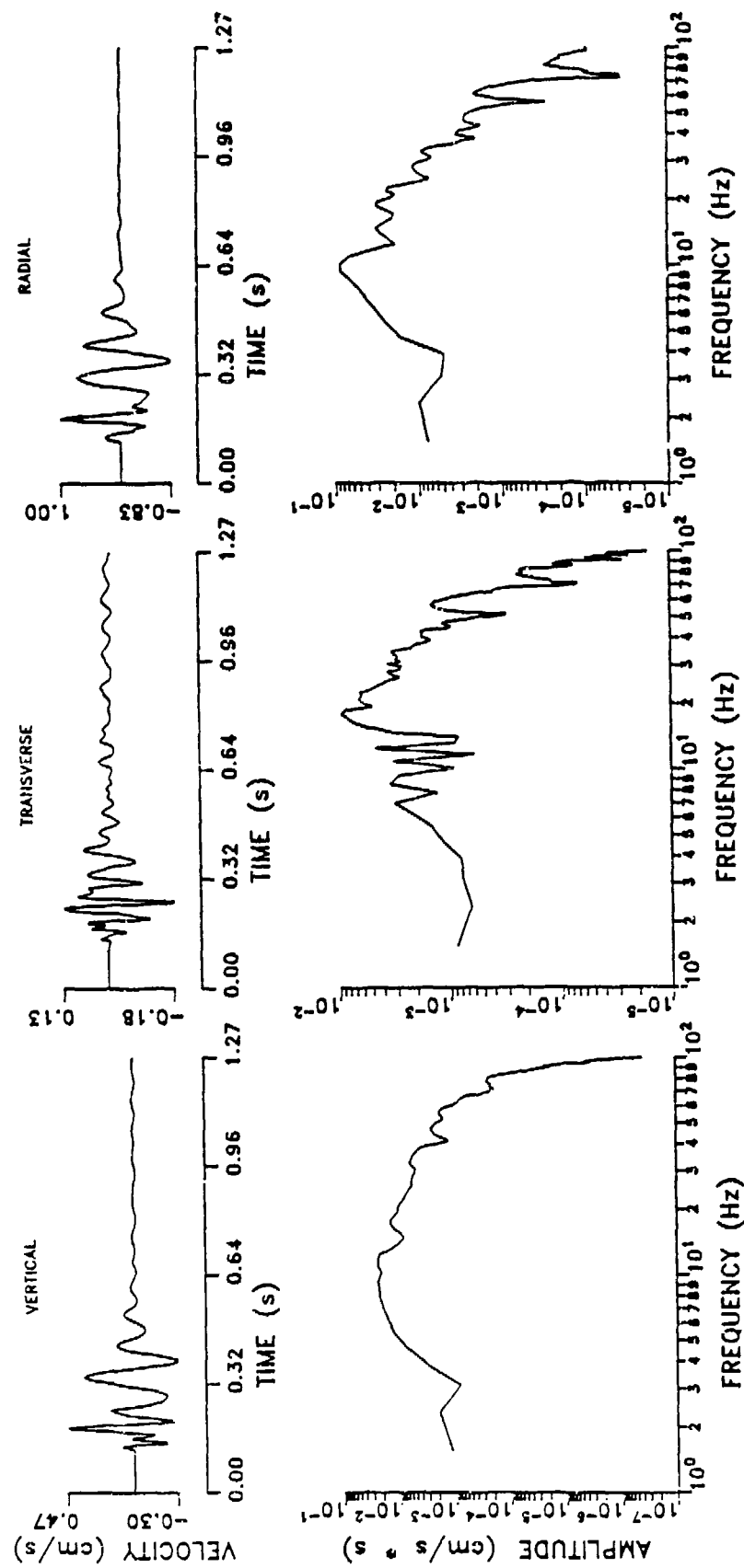
⊕ SHOT LOCATION

◆ RECEIVER AT 30 m

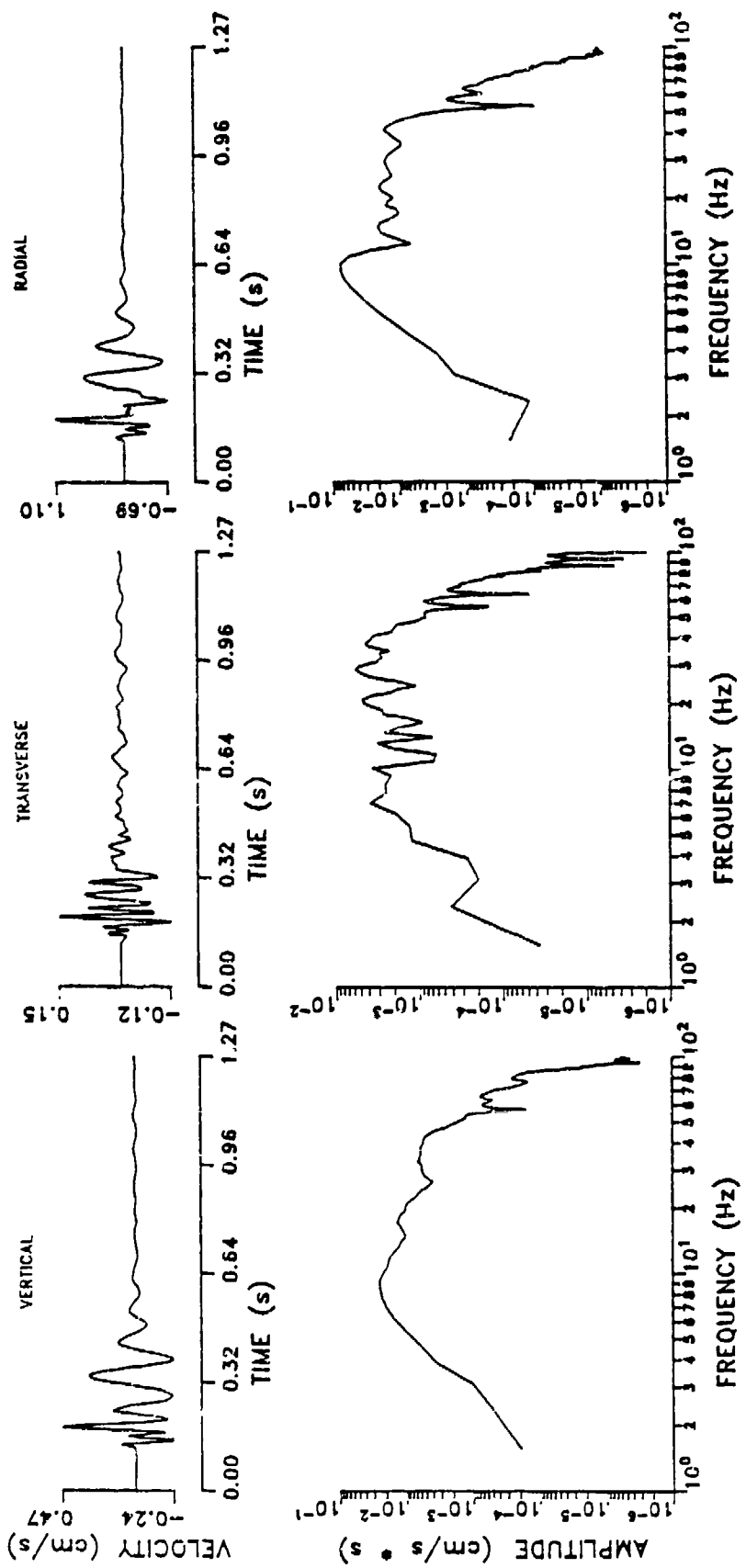
ART 3: 0 DEGREES AT 30 METERS



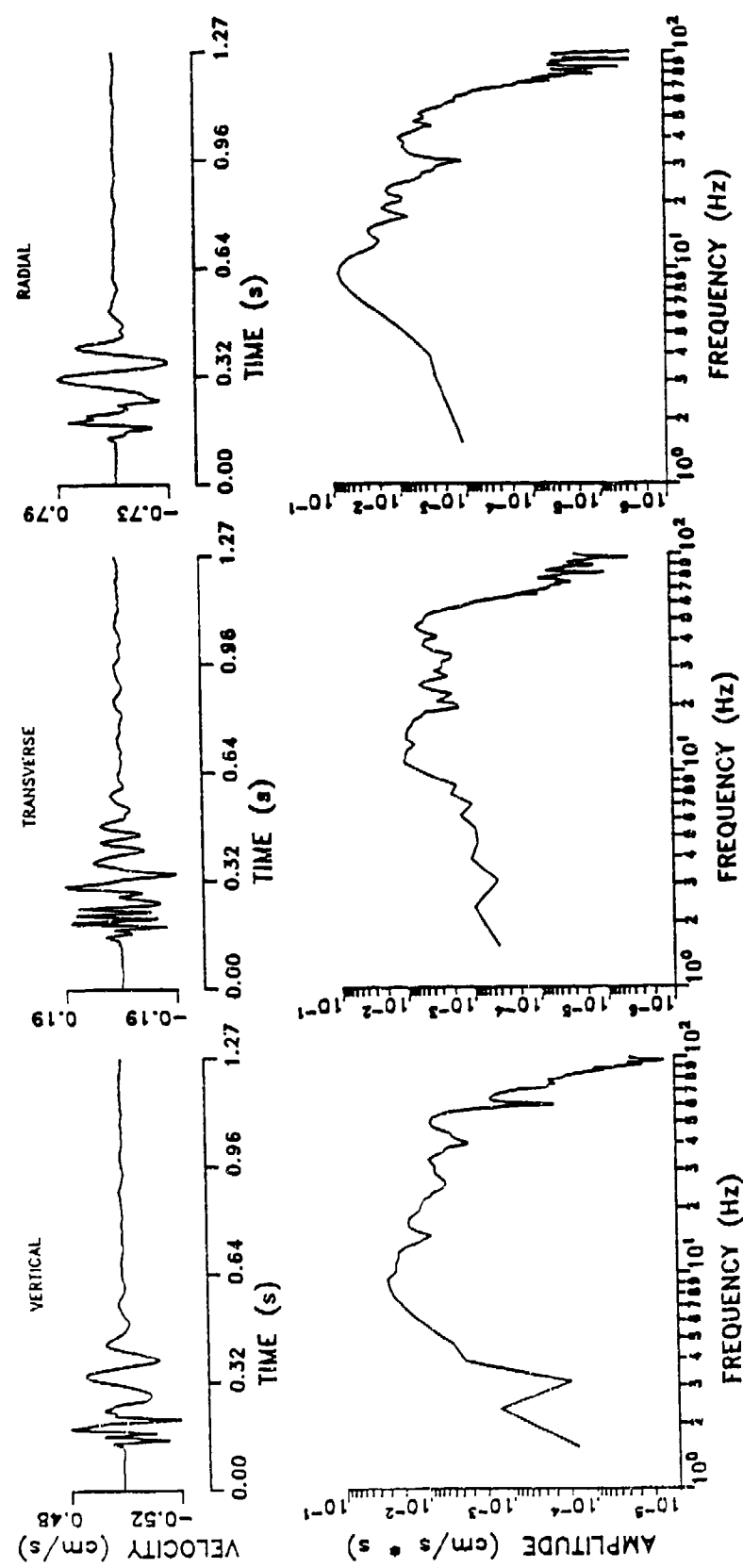
ART 3: 60 DEGREES AT 30 METERS



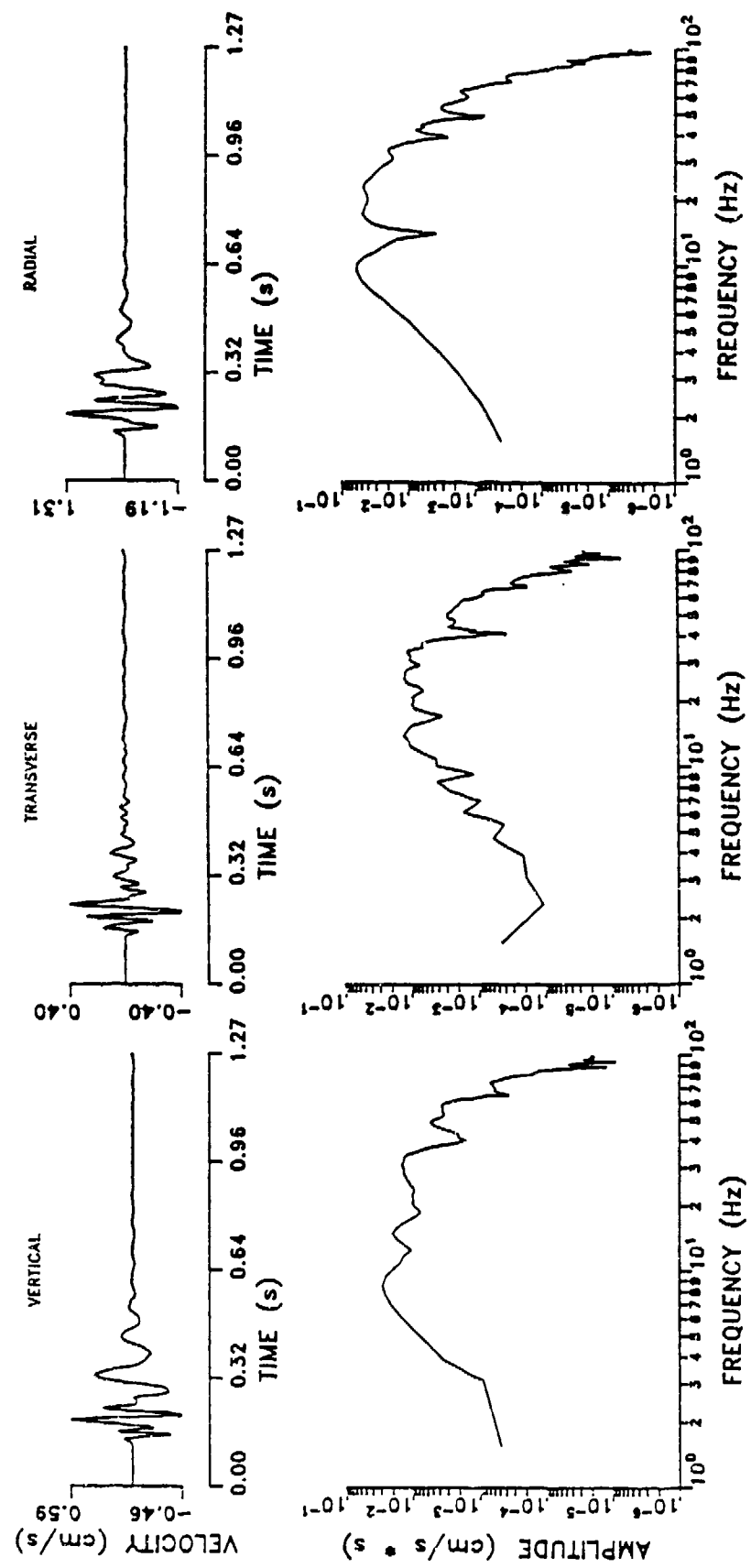
ART 3: 120 DEGREES AT 30 METERS



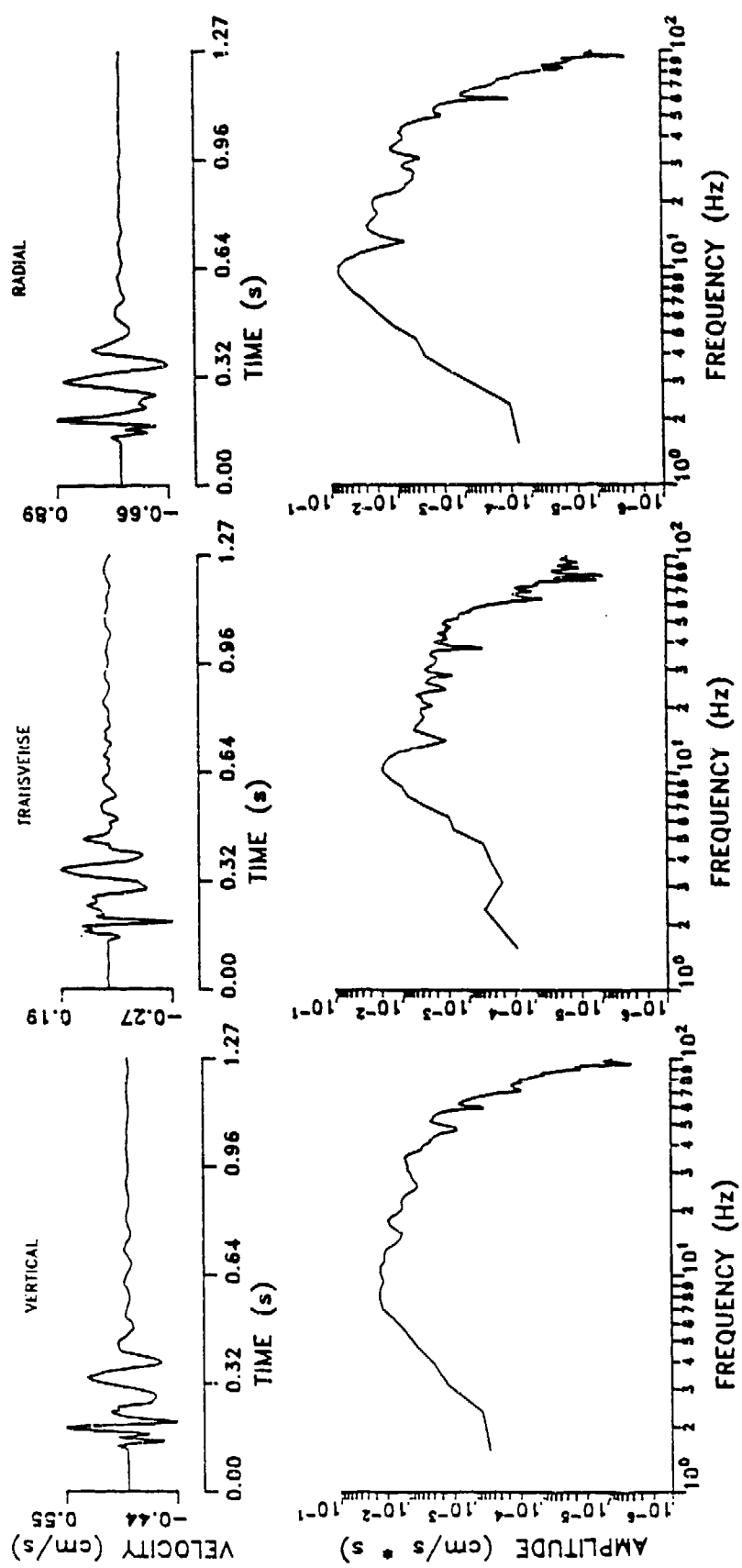
ART 3: 180 DEGREES AT 30 METERS



ART 3: 240 DEGREES AT 30 METERS



ART 3: 300 DEGREES AT 30 METERS



PLAN VIEW OF ART LINE SOURCE AND RECEIVER LOCATIONS

⊕

□ 10 m



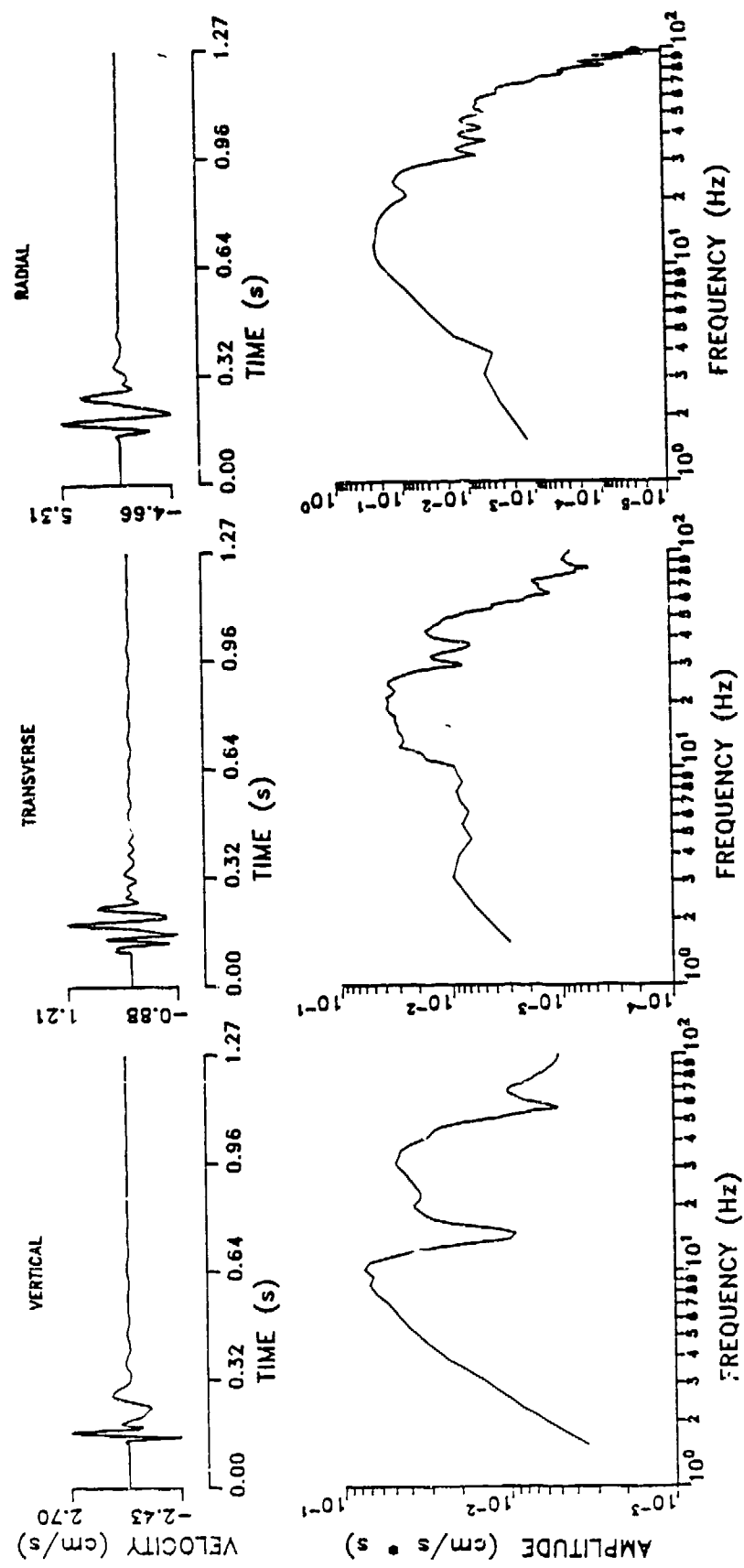
□ 60 m

⊕ SHOT LOCATION

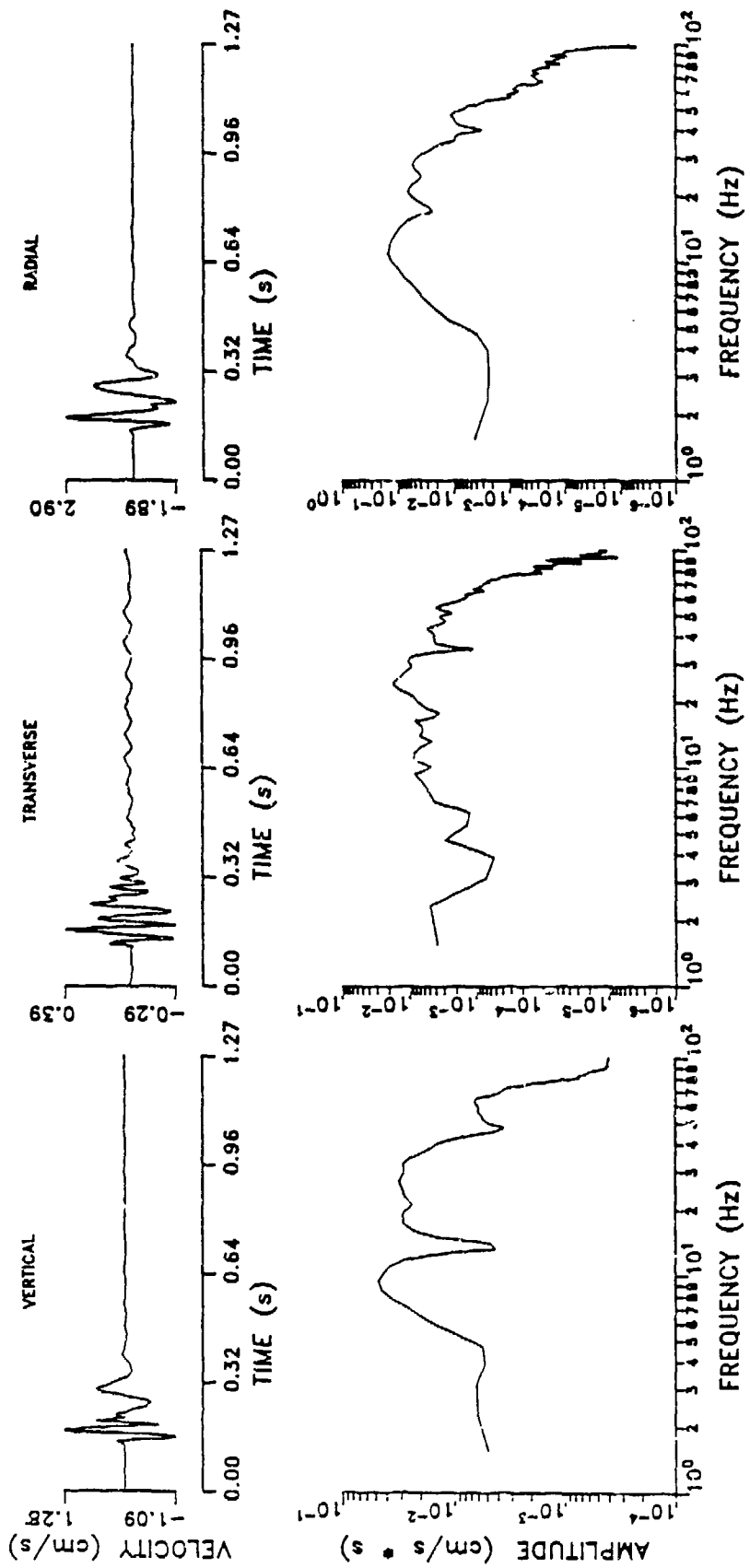
□ RECEIVER LOCATIONS

| 0° NORTH

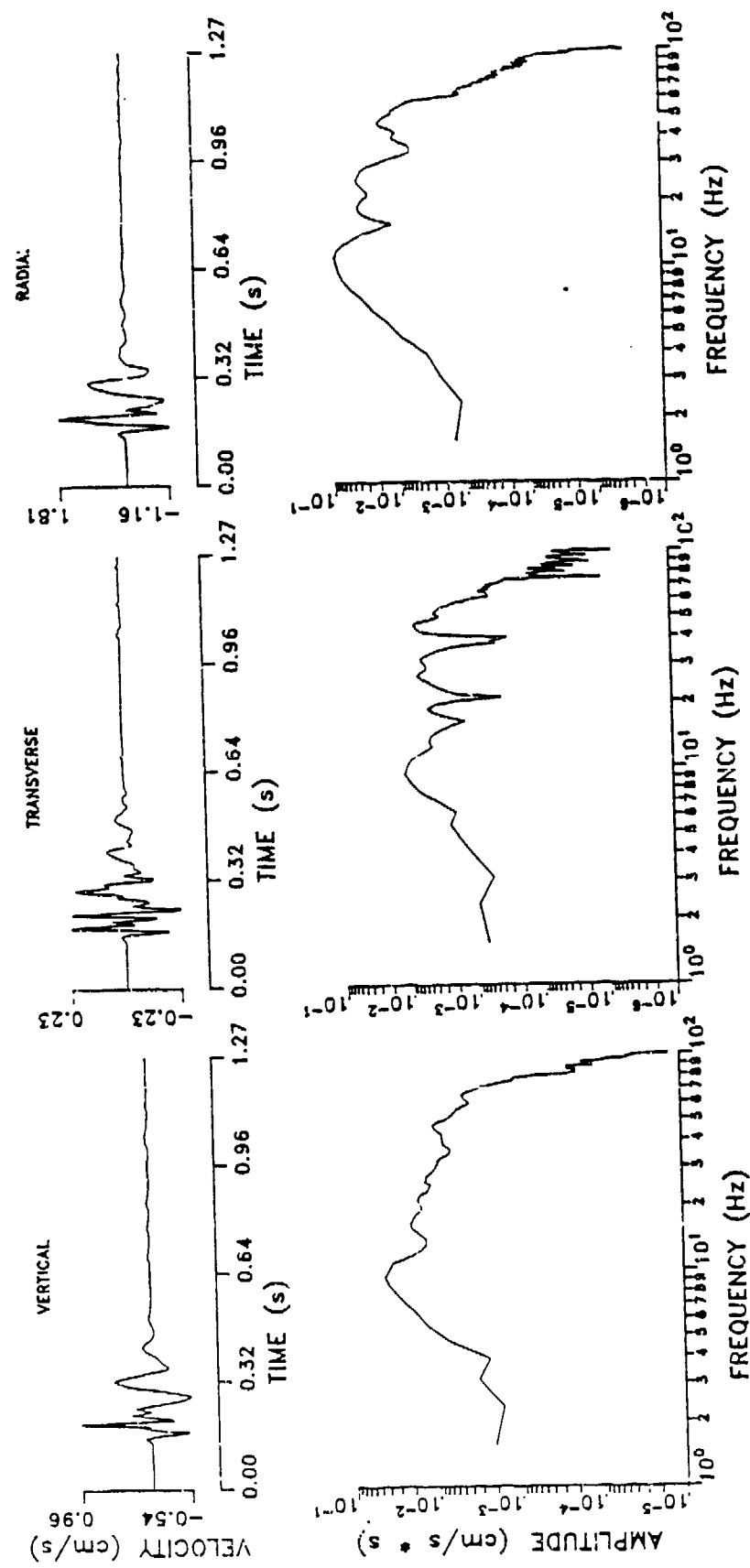
## ART LINE TEST: 10 METERS

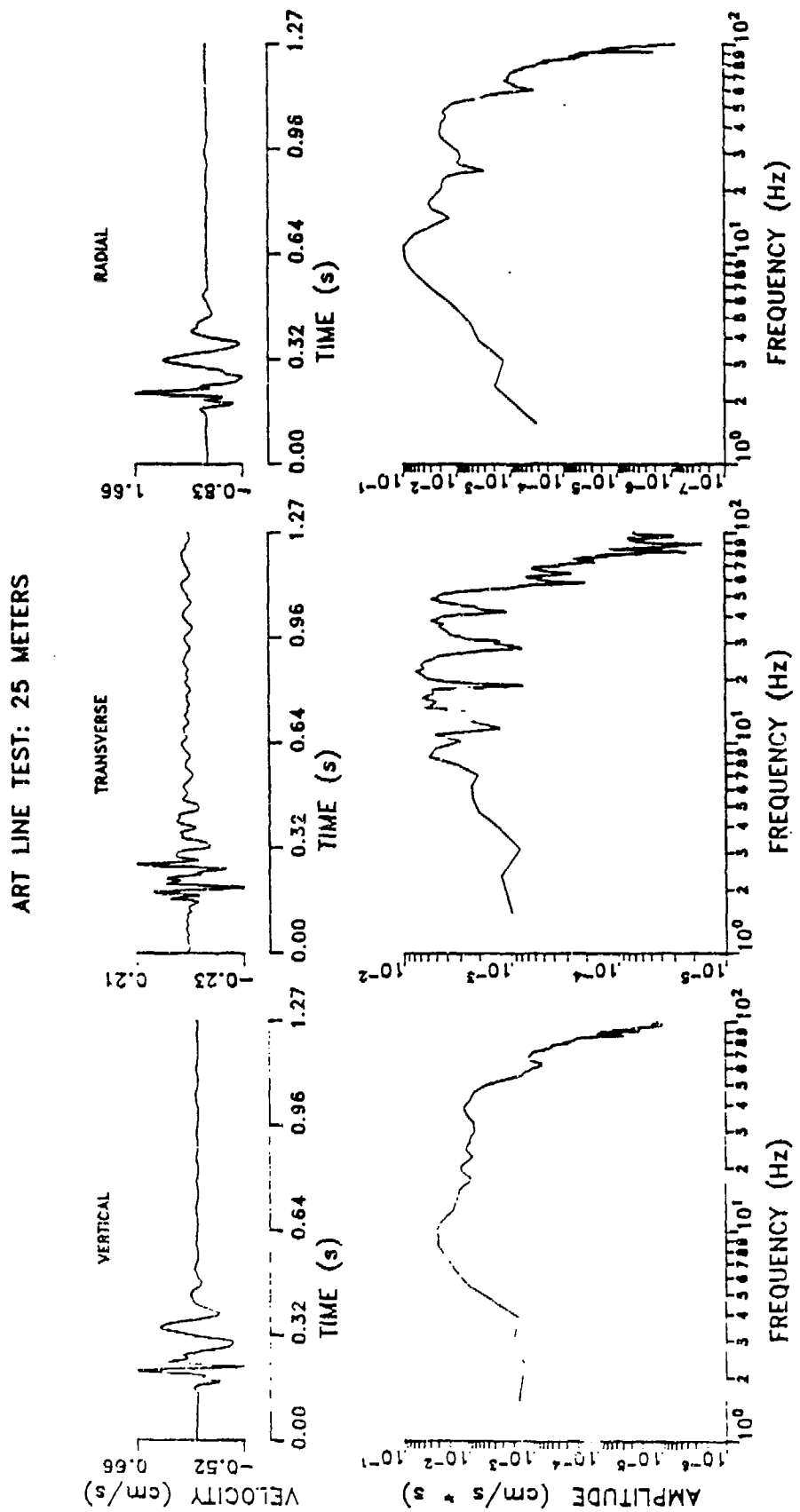


## ART LINE TEST: 15 METERS

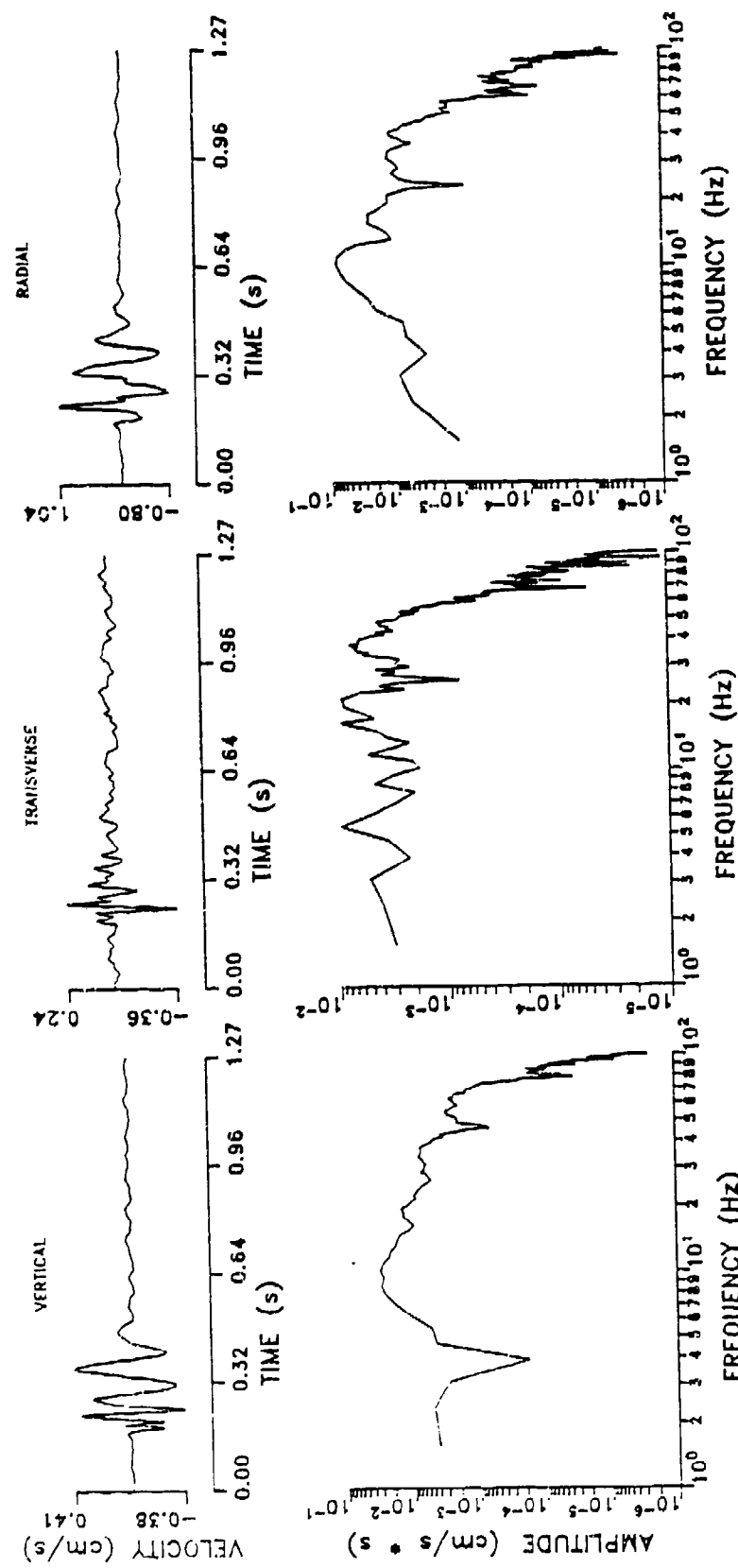


## ART LINE TEST: 20 METERS

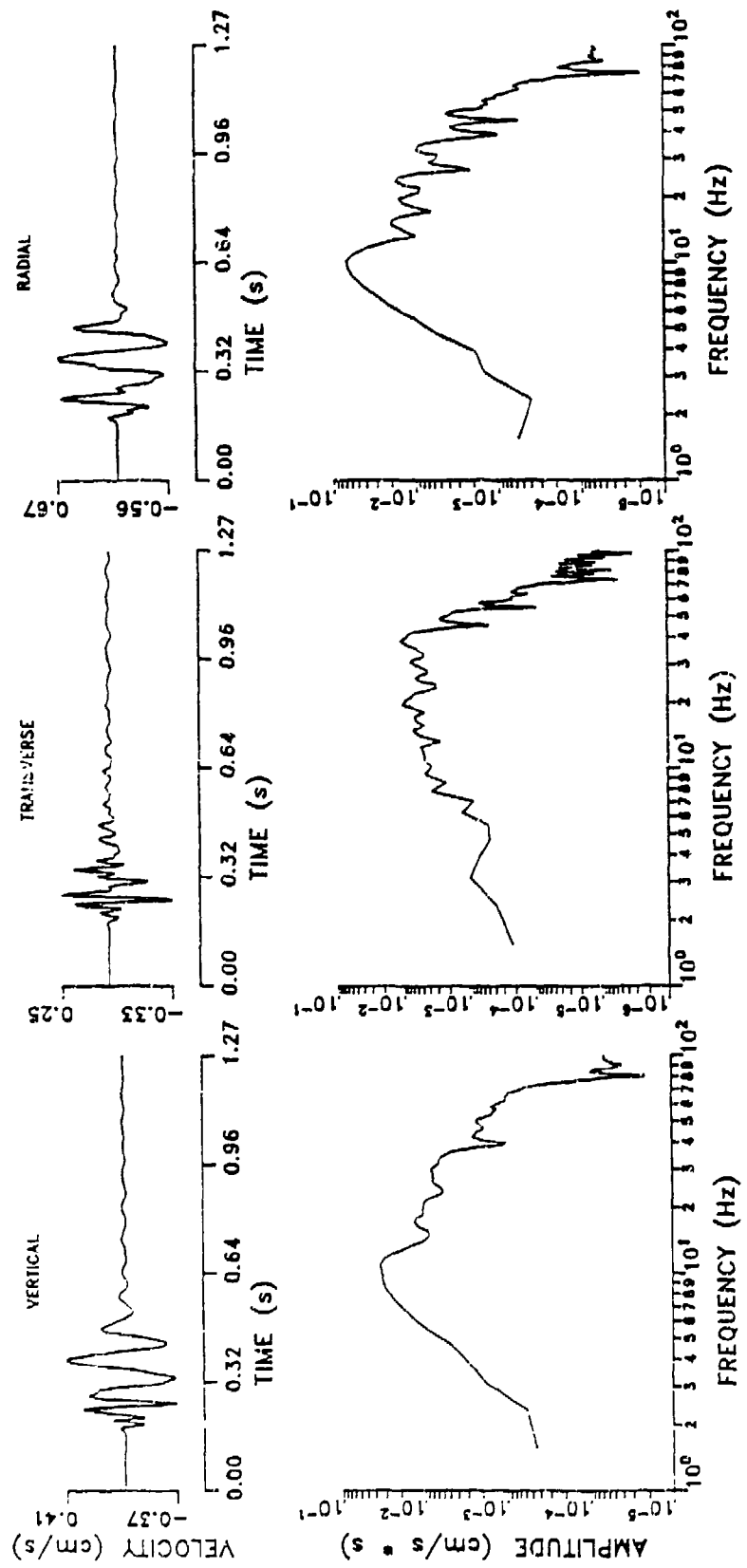




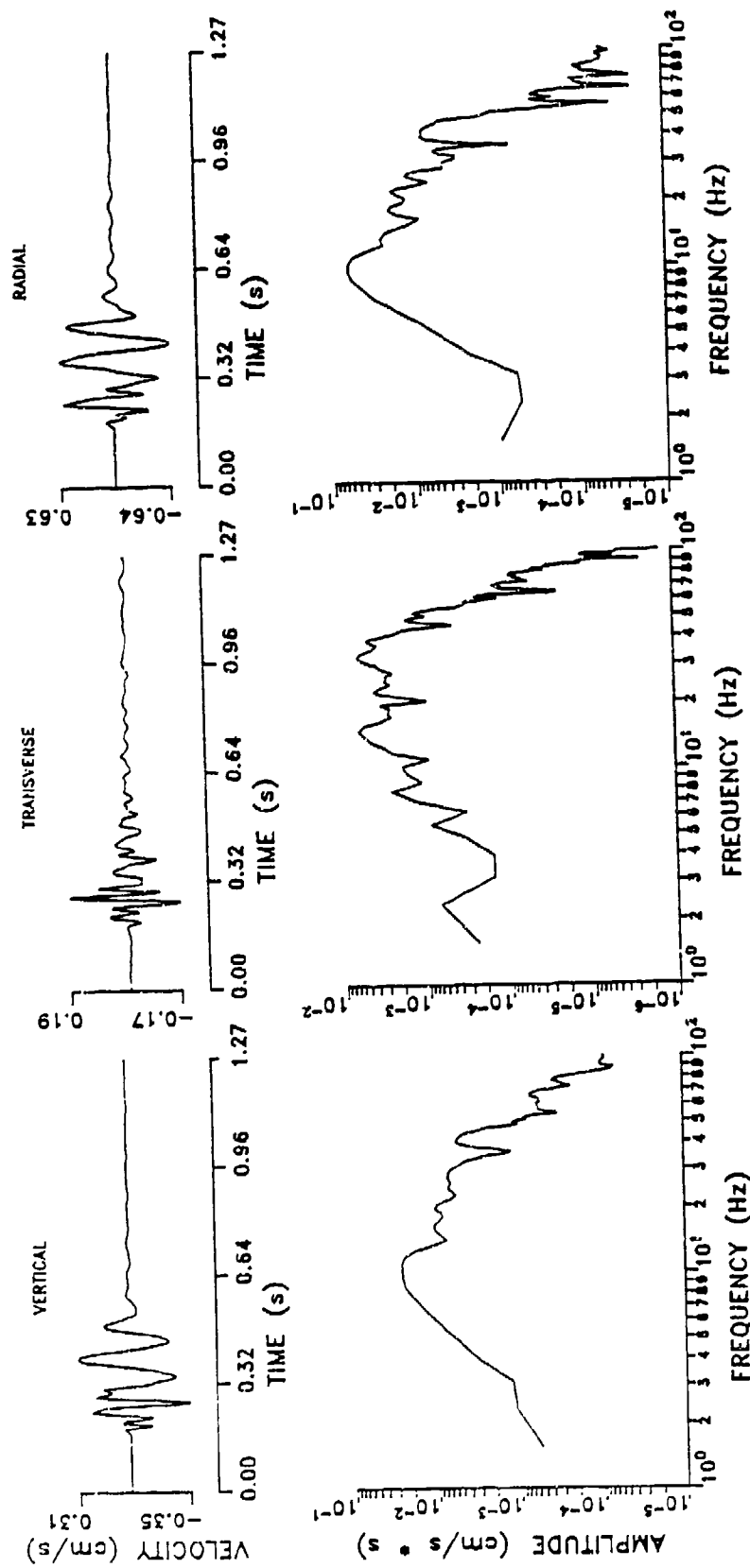
## ART LINE TEST: 30 METERS



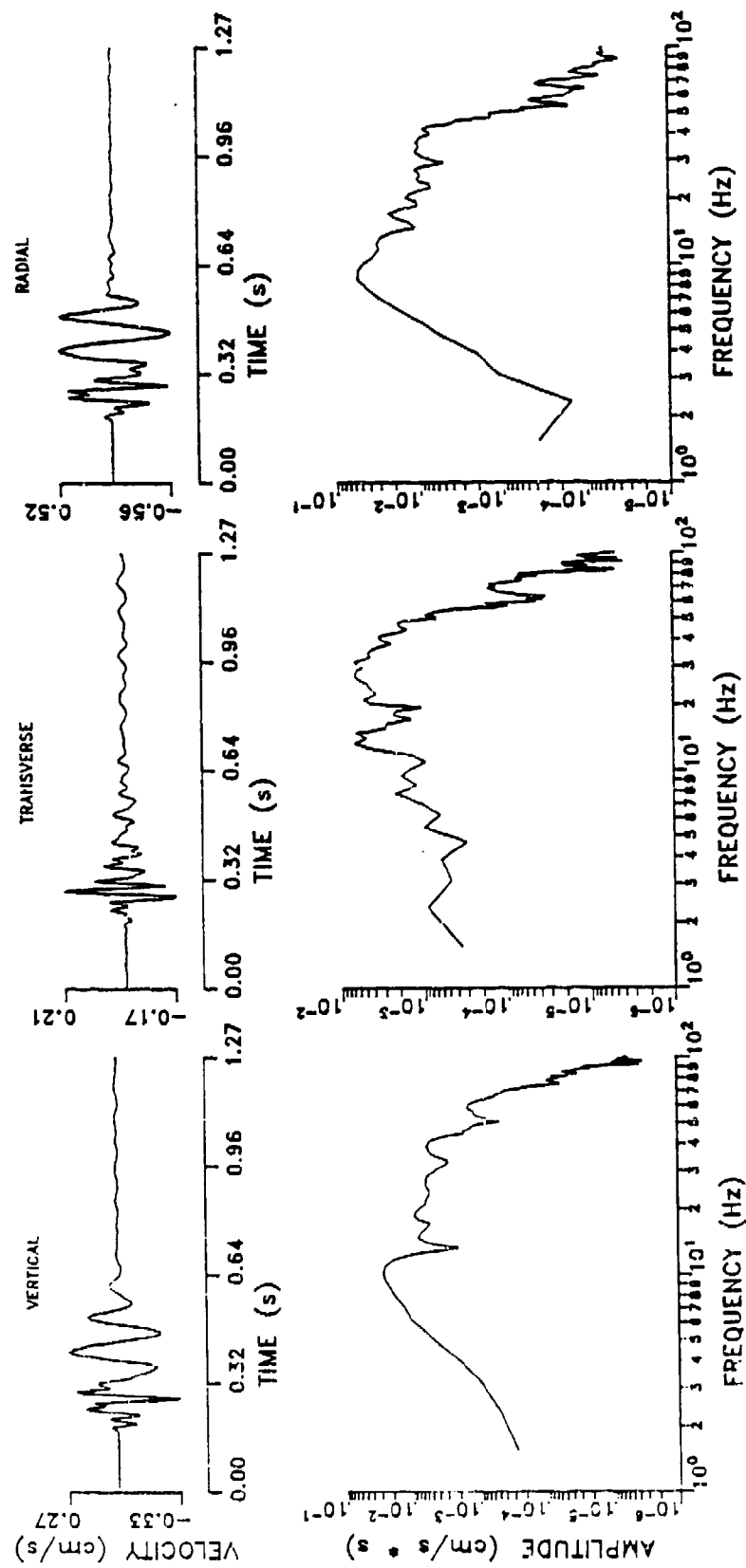
## ART LINE TEST: 35 METERS



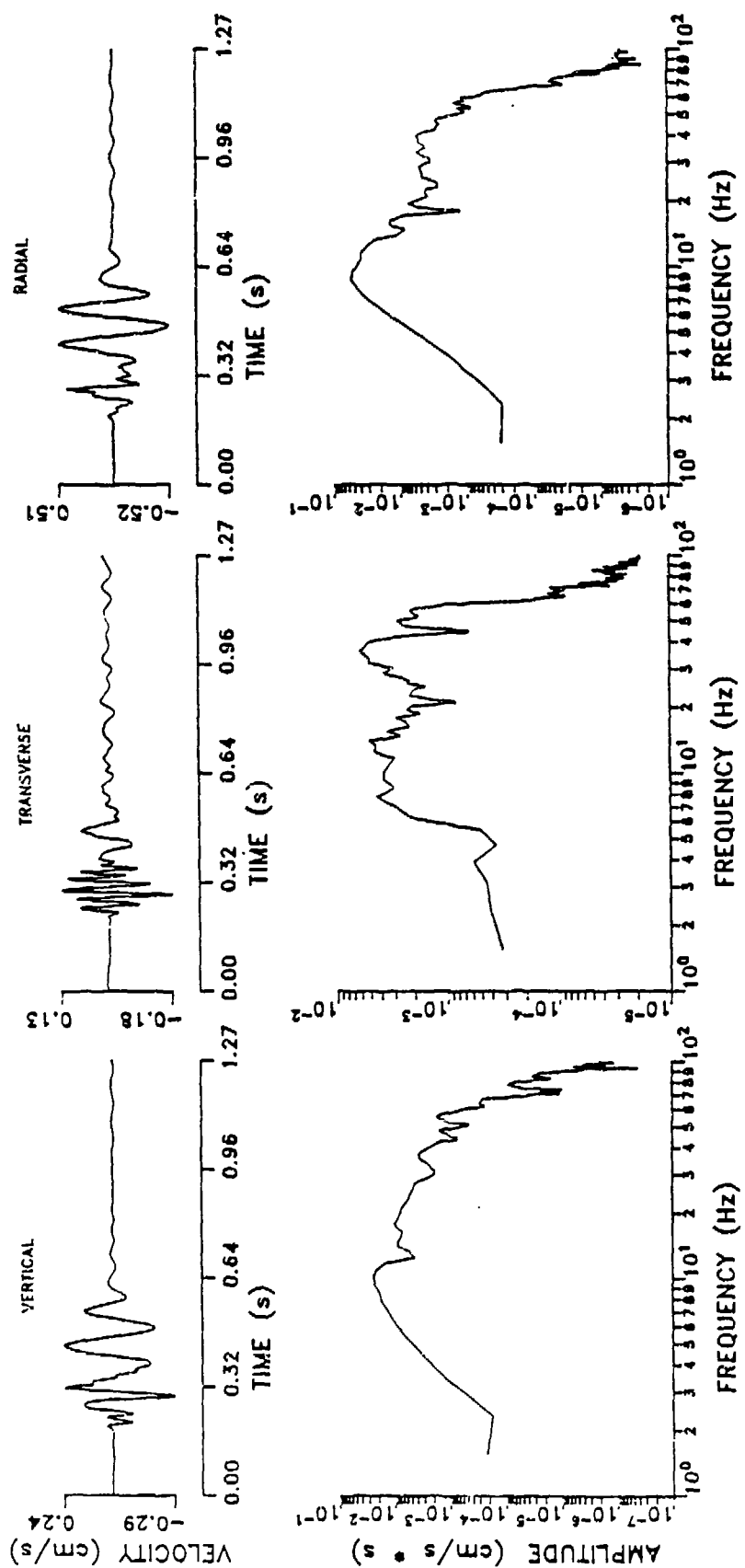
## ART LINE TEST: 40 METERS



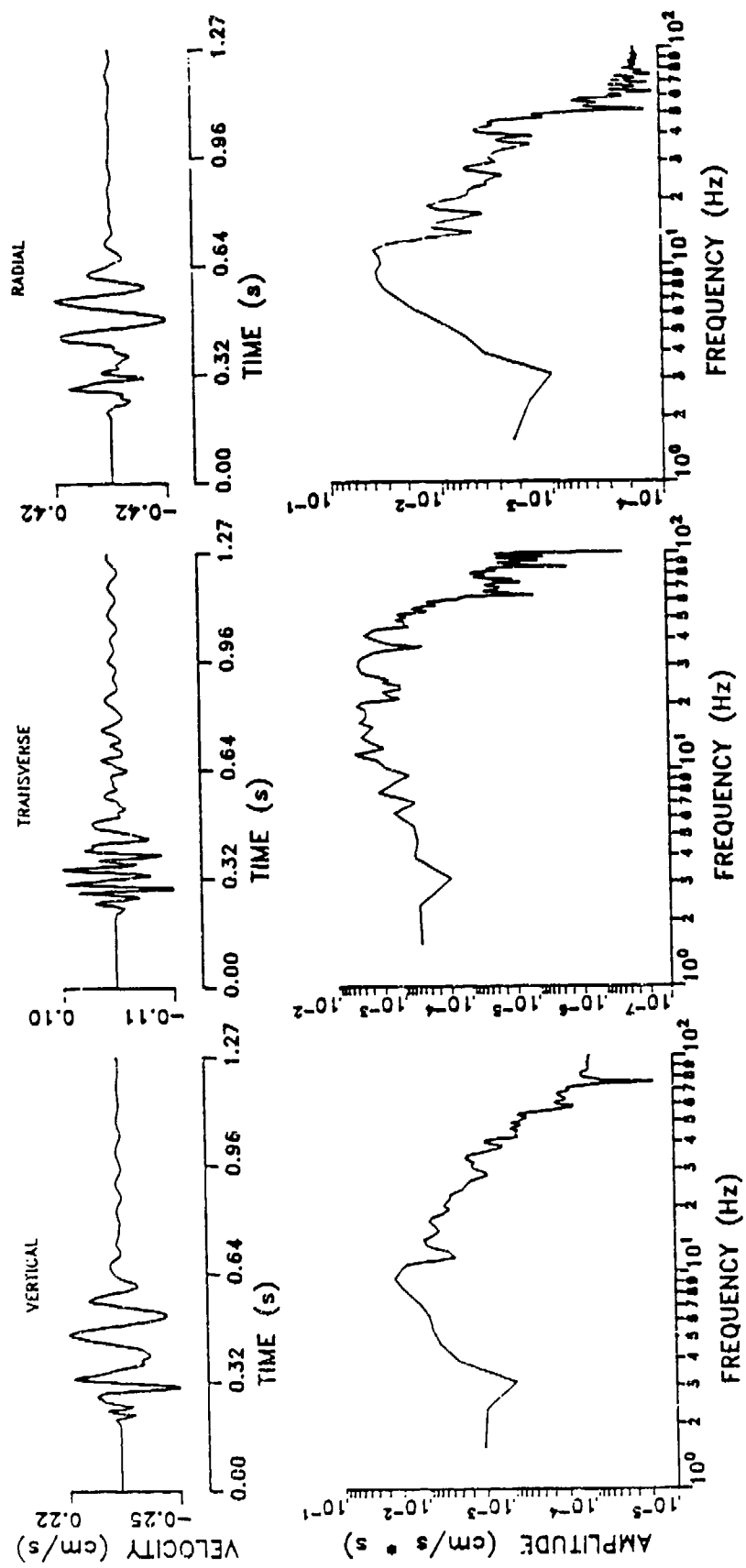
## ART LINE TEST: 45 METERS



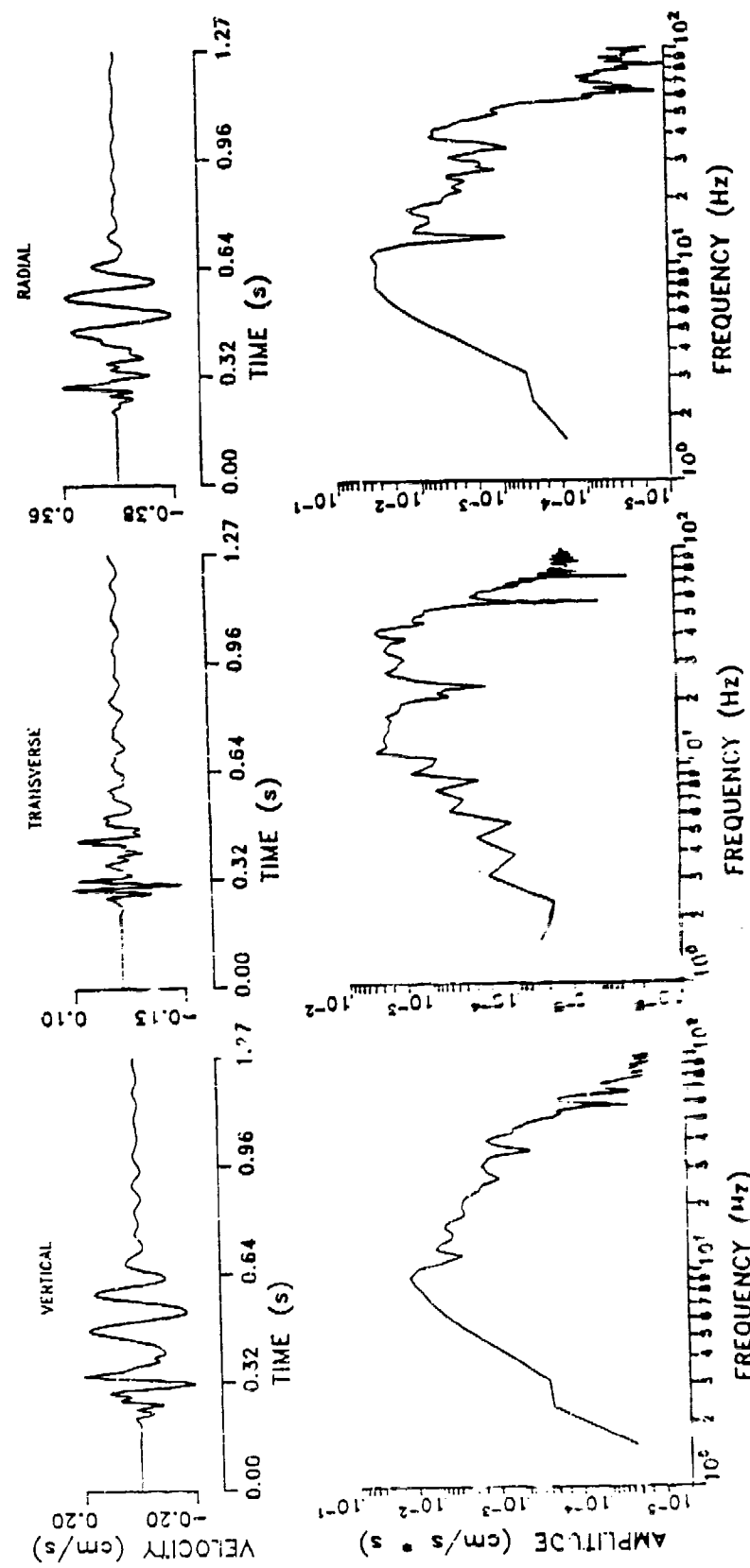
## ART LINE TEST: 50 METERS



## ART LINE TEST: 55 METERS



## ART LINE TEST: 60 METERS



APPENDIX C  
CART PEAK AMPLITUDES

File Name	Range (m/kt <sup>1/3</sup> )	Range ( m)	Peak Accel. (cm/s <sup>2</sup> )	Peak Vel. (cm/s)	Peak Displ (cm)	Slope Type
1A1	1019.0	13.5	373	2.44	1.6	4
1A2			130	.52	.4	6
1A3			342	1.89	3.5	1
1B1	1019.0	13.5	598	2.22	1.9	1
1B2			113	.50	.8	4
1B3			441	2.01	3.1	5
1C1	1019.0	13.5	404	2.08	1.5	1
1C2			99	.25	.4	5
1C3			344	1.86	3.2	2
1D1	2001.9	27.0	122	.58	.7	2
1D2			31	.11	.2	2
1D3			186	1.41	1.8	2
1E1	2001.0	27.0	115	.48	.6	5
1E2			46	.26	.4	4
1E3			184	1.33	1.7	2
1F1	2999.5	40.6	62	.26	.6	2
1F2			37	.15	.2	2
1F3			136	.73	1.0	1
1G1	2999.5	40.6	75	.38	.6	2
1G2			52	.18	.1	1
1G3			95	.47	.9	2
2A1	429.6	5.0	2156	10.46	9.3	5
2A2			273	.77	.4	4
2A3			1387	13.57	28.9	2
2B1	429.6	5.0	2342	8.71	10.4	6
2B2			144	1.2	1.8	4
2B3			1401	13.47	27.8	2
2C1	429.6	5.0	2950	13.15	10.5	4
2C2			366	2.24	3.6	2
2C3			965	9.88	21.6	2

File Name	Range (m/kt <sup>1/3</sup> )	Range ( m)	Peak Accel. (cm/s <sup>2</sup> )	Peak Vel. (cm/s)	Peak Displ (cm)	Slope Type
2D1	429.6	5.0	2479	9.87	10.5	1
2D2			271	2.94	3.6	5
2D3			1506	14.50	21.6	1
2E1	1019.0	13.5	390	1.52	10.5	2
2E2			38	.14	4.0	4
2E3			536	2.68	29.2	2
2F1	1019.0	13.5	494	2.28	1.8	1
2F2			153	.73	.4	4
2F3			562	4.15	4.4	2
2G1	1019.0	13.5	440	1.45	1.5	1
2G2			127	.32	.3	3
2G3			331	2.08	3.5	2
3A1	429.6	5.0	1875	9.54	8.2	5
3A2			263	1.88	2.6	4
3A3			1581	16.59	31.4	2
3B1	747.8	9.7	1209	4.18	2.2	5
3B2			153	.40	.3	4
3B3			596	3.70	5.6	2
3C1	1019.6	13.5	554	2.85	1.6	2
3C2			127	.50	.3	3
3C3			493	2.97	3.4	5
3D1	1511.9	20.3	138	.88	1.1	2
3D2			113	.41	.2	4
3D3			392	2.01	2.6	2
3E1	2001.9	27.0	189	.56	.8	2
3E2			63	.24	.2	4
3E3			219	1.61	1.5	1
3F1	2999.5	40.6	53	.24	.6	5
3F2			43	.19	.2	1
3F3			72	.45	.9	2

APPENDIX D  
ART PEAK AMPLITUDES

File Name	Azimuth. Degrees	Range ( m)	Range (m/kt <sup>1/3</sup> )	Peak Accel (cm/s <sup>2</sup> )	Peak Vel. (cm/s)	Peak Displ (cm)
ART1	0	10.0	742.26	637	2.94	2.5
				105	.46	.6
				745	7.28	11.1
ART1	60	10.0		563	2.33	2.2
				96	.51	.8
				632	5.39	5.8
ART1	120	10.0		831	2.99	2.6
				148	.37	.5
				764	7.38	7.8
ART1	180	10.0		960	4.81	2.9
				96	.66	7.9
				515	4.78	5.3
ART1	240	10.0		752	1.70	1.0
				113	.37	.7
				594	5.09	4.5
ART1	300	10.0		642	1.27	.9
				113	.37	.7
				506	4.66	5.2
ART2	0	20.0	1476.4	221	1.14	1.0
				67	.29	.19
				191	1.72	1.8
ART2	90	20.0		204	1.03	.9
				59	.18	.3
				402	2.52	2.4
ART2	144	20.0		225	1.15	1.3
				86	.39	.3
				228	2.56	3.3
ART2	180	20.0		131	.93	
				50	.16	
				221	2.05	

File Name	Azimuth. Degrees	Range ( m)	Range (m/kt <sup>1/3</sup> )	Peak Accel (cm/s <sup>2</sup> )	Peak Vel. (cm/s)	Peak Displ (cm)
ART	216	20.0		167 71 315	.81 .28 1.36	1.1 .2 2.0
ART2	288	20.0		127 43 280	.71 .29 2.18	1.1 .2 2.4
ART3	0	30.0	2212.2	116 77 149	.46 .25 .98	.5 .1 1.2
ART3	60	30.0		55 34 122	.45 .13 1.00	.6 .1 1.5
ART3	120	30.0		80 33 179	.47 .15 1.10	.5 .09 1.2
ART3	180	30.0		116 58 113	.52 .19 .69	.6 .2 1.4
ART3	240	30.0		109 89 192	.58 .40 1.31	.7 .3 1.4
ART3	300	30.0		88 49 153	.55 .19 .89	.6 .3 1.2
ART LINE		10.0	742.3	510 199 575	2.70 1.21 5.31	
ART LINE		15.0	1108.8	338 74 462	1.28 .39 2.90	
ART LINE		20.0	1476.4	233 65 333	.96 .23 1.81	
ART LINE		25.0	1844.2	141 50 309	.66 .21 1.66	

File Name	Azimuth. Degrees	Range ( m)	Scaled Range	Peak Accel (cm/s <sup>2</sup> )	Peak Vel. (cm/s)	Peak Disp (cm)
ART LINE	30.0	2212.2		88	.36	
				77	.24	
				136	1.04	
ART LINE	35.0	2580.4		65	.33	
				76	.25	
				64	.64	
ART LINE	40.0	2948.6		64	.21	
				61	.19	
				102	.60	
ART LINE	45.0	3316.8		61	.18	
				39	.12	
				104	.42	
ART LINE	50.0	3685.1		46	.24	
				43	.13	
				66	.43	
ART LINE	55.0	4053.2		29	.21	
				29	.10	
				45	.32	
ART LINE	60.0	4421.6		25	.20	
				37	.10	
				64	.36	

## REFERENCES

- Bache, T. C., Estimating the Yield of Underground Nuclear Explosions, Bull. Seism. Soc. Am., Vol. 72, 131-168, 1982.
- Blake, F. G., Spherical Wave Propagation in Solid Media, J. Acoust. Soc. Am., Vol. 24, 211, 1952.
- Burdick, I. J. and D. V. Helmberger, Time Functions Appropriate for Nuclear Explosions, Bull. Seism. Soc. Am., Vol. 67, 957-973, 1973.
- Burger, R. W., T. Lay, and L. J. Burdick, Average Q Yield Estimates from the Pahute Mesa Test Site, Bull. Seism. Soc. Am., Vol. 77, 1274-1294, 1987.
- Day, S. M., N. Rimer and J. T. Cherry, Surface Waves from Underground Explosions with Spall. Analysis of Elastic and Nonlinear Source Models, Bull. Seism. Soc. Am., Vol. 73, 247-264, 1983.
- Dobrin, M. B., R. F. Simon and Lawrence, Rayleigh Waves from Small Explosions, Trans. Am. Geoph. Union. Vol. 32, 822-832, 1951.
- Flynn, E., Effects of Source Depth on Near Source Seismograms, M.S. Thesis, Southern Methodist University, 104, 1988.
- Fuchs, K. and G. Muller, Computation of Synthetic Seismograms with the Reflectivity Method and Comparison with Observations, Geophys. J. R. Astr. Soc.. Vol. 23, 417-433, 1971.
- Gilbert, F., Derivation of Source Parameters from Low-Frequency Spectra, Phil. Trans. Roy. Soc. London, Ser. A 274, 251-255, 1973.
- Gupta, I.N. and C. Kisslinger, Radiation of Body Waves from Near-Surface Explosive Sources, Geophysics, Vol. 31, 1057, 1966.
- Haskell, N. A., Analytic Approximation for the Elastic Radiation from a Contained Underground Explosion, J. Geophys. Res., Vol. 72, 2585-2587, 1967.

- Helmberger, D.V., and D.M. Hadley, Seismic Source Functions and Attenuation from Local and Teleseismic Observations of NTS Events Jorum and Handley, Bull. Seism. Soc. Am., Vol. 71, 51-68, 1981.
- Latter, A.L., R.E. LeLevier, and W.G. McMillan, A Method of Concealing Underground Explosions, J. Geophysics Res., Vol. 66, 943-48, 1961.
- Lay T., T.C. Wallace, and D.V. Helmberger, The Effects of Tectonic Release on Short-Period P Waves from NTS Explosives, Bull. Seis. Soc. Am., Vol. 74, 819-842, 1984.
- Masse, R.P., Review of Seismic Source Models for Underground Nuclear Explosions, Bull. Seism. Soc. Am., Vol. 71, 1249-1268, 1981.
- Minster, J. B., 25 Years of Source Theory, The Vela Program: A 25 Year Review of Seismic Research, A. U. Kerr, Editors, Dianne L. Carlson, 964 pp 1985.
- Mooney, H. M. and B. A. Bolt, Dispersive Characteristics of the First Three Rayleigh Modes for a Single Surface Layer, Bull. Seism. Soc. Am., Vol. 56, 43-67, 1966.
- Mueiller, R. A. and J. R. Murphy, Seismic Characteristics of Underground Nuclear Detonations Part I. Seismic Spectrum Scaling, Bull. Seism. Soc. Am., Vol. 61, 1675-1692, 1971.
- Murphy, J. R., Seismic Source Functions and Magnitude Determinations for Underground Nuclear Detonations, Bull. Seism. Soc. Amer., Vol. 67, 135-158, 1977.
- Perret, W. R. and R. C. Bass, Free-field Ground Motion Induced by Underground Explosions, SAND74-0252, Sandia Corporation, 121 pp., 1975.
- Reinke, R. E. and B. W. Stump, Stochastic Geologic Effects on Near-field Ground Motions in Alluvium, Bull. Seis. Soc. Am., 1037-1059, 1988.
- Sharpe, J. A., The Production of Elastic Waves by Explosion Pressures. I. Theory and Empirical Field Observations, Geophysics, Vol. 7, 144-154, 1942.
- Stump, B.W., Investigation of Seismic Sources by the Linear Inversion of Seismograms, PhD. Thesis, University of California, Berkeley, 1979.

- Stump, B.W., Constraints on Explosive Sources with Spall from Near-Source Waveforms, Bull. Seis. Soc. Am., Vol. 75, 361-377, 1985.
- Stump, B.W., Mathematical Representation and Physical Interpretation of a Continued Chemical Explosion in Alluvium, Bull. Seis. Soc. Am., Vol. 77, 1312-1325, 1987.
- Stump, B. W. and L. R. Johnson, The Determination of Source Properties by the linear Inversion of Seismograms, Bull. Seismol. Soc. Amer., Vol. 67, 1489-1502, 1977.
- Stump, B. W., Resolution of Complex Explosive Source Functions in the Frequency Domain, Geophys. J. R. astr. Soc., 1987.
- Stump, B.W. and R.E. Reinke, Experimental Seismology: In Situ Source Experiments, Bull. Seis. Soc. Am., Vol. 77, 1295-1311, 1987.
- Stump, B. W. and R. E. Reinke, Spall-Like Waveforms Observed in High-Explosive Testing in Alluvium, AFWL-TR-82-15, Air Force Weapons Laboratory, Kirtland AFB, New Mexico, 122 pp., 1982.
- U. S. Congress, Office of Technology Assessment, Seismic Verification of Nuclear Testing Treaties, OTA-ISC-361, Washington, DC: U.S. Government Printing Office, 1988.
- Von Seggern, D. H. and R. R. Blanford Source Time Functions and Spectra for Underground Nuclear Explosions, Geophys. J. R. Astr. Soc., Vol. 31, 83-97, 1972.
- Werth, G. C. and R. F. Herbst, Comparison of Amplitudes of Seismic Waves from Nuclear Explosions in Four Mediums, J. Geophys. Res., 68, 1463-1475, 1963.

## Seismological Research Letters, Volume 59, No. 1, January - March, 1988

This shows that  $Q_c$  is independent of the data sets and the data reduction procedure used. The  $Q_c$  value for the present data set has a strong frequency dependence:  $Q_c$  increases with frequency proportional to  $f^n$ , where  $n$  was found to be 0.95. This  $n$  value is nearly the same as that estimated for the active continents and is probably representative of the active island arcs.

**9:45**

### CHARACTERISTICS OF SCATTERING AND ATTENUATION STRUCTURE IN NORTHEASTERN JAPAN

MATSUMOTO, S. and HASEGAWA, A.

Observation Center for Prediction of Earthquakes and Volcanic Eruptions, Faculty of Science, Tohoku University, Sendai, Japan.  
Based on the single scattering model, back scattering coefficient ( $g$ ) and coda-Q value ( $Q_c$ ) are estimated for several frequency bands from the amplitude ratio of coda-to-S-wave and from the time decay of the ratio. The estimated  $g$ -value at each station ranges from  $10^{-1}$  to  $10^{-2}$  at 4-24Hz. The  $Q_c$  value shows a regional variation and frequency dependence of the form  $Q_c \propto f^n$ , where  $n$  is found to be 0.7-1.0.

A method to estimate two-dimensional  $Q_c$  structure is developed to see the regional variation of the  $Q_c$ . The  $Q_c$  value at each grid point spatially distributed was estimated by averaging the  $Q_c$  values of many event-station pairs with adequate weighting factor. The weighting factor at each grid point was calculated by using the distance from each grid to the station and the source. The obtained two-dimensional  $Q_c$  structure shows its relation to S-wave velocity structure: the low- $Q_c$  region corresponds to the low velocity region, and the high- $Q_c$  region to the high velocity region.

**10:00**

### VARIATION OF CODA Q DURING AN EARTHQUAKE SEQUENCE

WANG, C.H., TENG, T.L., and MA, K.F., Institute of Earth Sciences, Academia Sinica, P.O. Box 23-59, Taipei, Taiwan, 10754, R.O.C.

The May 26, 1986 Hualien earthquake sequence occurred in the northeastern Taiwan. The M=6.9 main shock was followed by a large number of shallow and closely-clustered aftershocks with the largest being a M=5.4 event. Afternoons formed two clusters centered at, respectively, 5 km and 15 km depth. One station TWO of the Taiwan Seismograph Network is located in the middle of these two clusters and gives excellent coda-wave recordings of the entire earthquake sequence. During the three plus hours of tremor, which occurred in the same source area, offer a unique opportunity in the study of spatial and temporal variation of coda-Q in a region of active subduction. From recordings of a peak response band centered about 5 Hz, we have found that 1) the ambient coda-Q near an active subduction region can be as low as 10<sup>-2</sup>. There is a significant drop of coda-Q immediately after the main shock. This drop lasted about two days before returning to the ambient level; 2) There is a noticeable difference of coda-Q for sources originating from the two different aftershock clusters. No significant decrease in coda-Q is found before the main shock.

**10:15**

### LG-WAVE ATTENUATION AND SITE EFFECTS OF TAIWAN AREA

Tzay-Chyn Shiu, Central Weather Bureau, Taipei, Taiwan, R.O.C.

Digital seismograms of 55 earthquakes recorded by Central Weather Bureau Seismic Network (CWSN) are used to study the characteristics of lg-wave in Taiwan area. All earthquakes are uniformly distributed in three main tectonic regions of Taiwan. Nevertheless, the averaged group velocity 3.2-3.5 km/sec and conspicuous wave trains show that the propagation of lg-wave is not apparently affected by the structural variation. From spectral analysis, lg-wave attenuation is of the form of  $100f^n$  in the frequency range of 0.7 to 6 Hz. Comparing to the Coda-Q obtained from the same area, 1 Hz Coda-Q is comparable to 1 Hz Coda-Q, but coda-wave attenuates fast at high frequency. The residual ratio of observed spectral amplitude to theoretical value is found to be independent of epicentral distance and azimuth. These results imply that the variation of spectral amplitude is not caused by the variation of geological structure and the different excitation of source. Thus, station site amplification amounts for the residuals. By repeating regression analysis, results from the band 0.7 to 6 Hz indicate that the site amplification depends strongly on site geology and frequency. The amplification of stations at sediment site is large by a factor of 2 to 3 relative to the average stations. Two sites at fault zone exhibit decreasing amplification with respect to increasing frequency, while the hard rock sites behave reversely.

**10:30**

### SCATTERING AND INTRINSIC ABSORPTION IN THE LITHOSPHERE BEATH NORTHERN AUSTRALIA

KORN, M., Research School of Earth Sciences, Australian National University, Canberra, ACT 2601, Australia.

I have studied the P coda of Indonesian earthquakes recorded at the Warramunga Array (WRA) in central Australia for a broad range of source depths. An increase of coda energy relative to the direct arrival is observed when source depth decreases. Coherency measurements by means of semblance-enhanced stacks exhibit that the coda of deep-focus events is mostly incoherent across the array, while the coda of shallower events contains a certain amount of coherent energy. The coherent arrivals are produced by reflections from plane layering and possibly by larger-scale heterogeneities in the deeper lithosphere. Small-scale heterogeneities close to the receiver, however, are responsible for the generation of the incoherent part of the coda. To further study the small-scale fluctuations of the seismic parameters I have computed the time decay of the power spectral density of the P coda of deep-focus events. An energy-flux model which assumes multiple scattering and allows for the independent determination of intrinsic Q and scattering Q has been fitted to the data. The results show an almost linear increase of intrinsic Q with frequency. Q is about 300 at 1 Hz. The frequency dependence of scattering Q is somewhat less pronounced with a value of about 340 at 1 Hz and an exponent of 0.85. A comparison of this frequency dependence with results from single scattering theory imply a correlation length of about 5.5 km and a rms velocity fluctuation of 5% for the scattering medium.

**10:45**

### NEAR SURFACE GEOLOGIC SITE CHARACTERIZATION - SEPARATION OF DETERMINISTIC AND STOCHASTIC EFFECTS

STUMP, B.W., BOGDARD, M.A., Department of Geological Sciences, Southern Methodist University, Dallas, Texas 75275; REINKE, R.E., AFRL/NTESD, Kirtland AFB, NM 87117-6000.

Geologic structures can be divided into stochastic and deterministic components. From the point of view of seismic wave propagation the deterministic component often involves a model in which velocities change in the vertical direction. The stochastic model is classified as a distribution of inhomogeneities and is characterized in terms of inhomogeneity size and velocity contrast. The separation of these geological properties have implications on ground motion prediction and the utilization of seismic information. A set of site characterization procedures were designed and implemented for the resolution of such properties. The field technique involved the retrieval of full wave seismograms at closely spaced sites along eight radials emanating from a central source. The goal of this particular experiment was the characterization of the top cm of the site which resulted in 12m spreads at 1m increments. Treating the eight observations at variance as an ensemble, frequency domain mean and variance estimates were made. The mean normalized variance, coefficient of variation ( $C_V$ ), is then used as a measure of lateral variation in waveforms. At low frequencies (<30 Hz) the  $C_V$  values are small (<1%) reflecting little spatial variation in the wavefield. As frequency or range increases, the  $C_V$  exponentially approaches 1 indicative of strong lateral variations in the wavefield. This information is utilized in constraining the stochastic site model. In order to focus on the separation of wave types and constrain velocities each one dimensional arm of the array is used in frequency/wavenumber( $\lambda$ ) estimates. A finite number of  $V$  values are assumed leading to a Burg model for the  $V$  spectra. These estimates are used in constraining the deterministic model.

**11:00**

### AN EXPERIMENTAL EVALUATION OF STOCHASTIC GELOGIC EFFECTS ON NEAR-FIELD GROUND MOTION

REINKE, R.E. AND FELICE, C.W., Air Force Weapons Laboratory, Kirtland AFB NM 87117-6000; STUMP, B.W., Dept. of Geological Sciences, Southern Methodist University, Dallas, TX 75275.

A high explosive experiment was designed to quantify the effects of random geologic inhomogeneities upon the small-scale variability in ground motion and to determine the relative importance of the deterministic and stochastic components of the ground motion wave field. The experiment involved the detonation of small (100 lbs) explosive charges upon a test bed where the subsurface geology has been characterized in a high resolution manner. The explosive-induced ground motions were recorded by accelerometers placed at six azimuths at a rate of 10, 20, and 30 meters. The subsurface site characterization effort included high resolution seismic surveys and closely-spaced cone penetrometer tests as well as drilling and sampling. The site characterization process was designed to yield a good statistical characterization of the geological variability present in the test bed subsurface. This statistical characterization will be incorporated into stochastic models of the observed ground motion field.

**11:15**

### HIGH STRESS ATTENUATION MEASUREMENTS AND WAVE FORM MODELLING

ANDERSON, R.P. and REINKE, R.E., Air Force Weapons Laboratory, Kirtland AFB NM 87117-6000.

A linear viscoelastic constant Q model was used to model explosively induced high stress ground motions in alluvium. Data sets from two high explosive tests conducted at seismite sites were modeled using this technique. One test consisted of a 20-mm spherical nitrotriazole charge detonated in alluvium at a depth of 70 meters, the other, also detonated in alluvium, was a 200-lb TNT sphere detonated at a depth of 5 meters. The smaller test was designed as a scaled non-yield static version of the larger test. Very near source acceleration records (1 meter from 250 lbs, 10 meters from 20 lbs) were used as source functions for the constant Q propagation model, and qualitative comparisons were obtained between the synthetic and observed waveforms using this technique. Theory is required to obtain a good match for the

This shows that  $Q_c$  is independent of the data sets and the data reduction procedure used. The  $Q_c$  value for the present data set has a strong frequency dependence;  $Q_c$  increases with frequency proportional to  $f^n$ , where  $n$  was found to be 0.95. This  $n$  value is nearly the same as that estimated for the active continents and is probably representative of the active island arcs.

**9:45**

CHARACTERISTICS OF SCATTERING AND ATTENUATION STRUCTURE IN NORTHEASTERN JAPAN

MATSUMOTO, S. and HASEGAWA, A.

Observation Center for Prediction of Earthquakes and Volcanic Eruptions, Faculty of Science, Tohoku University, Sendai, Japan

Based on the single scattering model, back scattering coefficient ( $g$ ) and coda-Q value ( $Q_c$ ) are estimated for several frequency bands from the amplitude ratio of coda to S-wave and from the time decay of the ratio. The estimated  $g$ -value at each station ranges from  $10^{-1}$  to  $10^{-2}$  at 4-24Hz. The  $Q_c$  value shows a regional variation and frequency dependence of the form  $Q_c \propto f^n$ , where  $n$  is found to be 0.7-1.0.

A method to estimate two dimensional  $Q_c$  structure is developed to see the regional variation of the  $Q_c$ . The  $Q_c$  value at each grid point spatially distributed was estimated by averaging the  $Q_c$  values of many event-station pairs with adequate weighting factor. The weighting factor at each grid point was calculated by using the distance from each grid to the station and the source. The obtained two dimensional  $Q_c$  structure shows its relation to S-wave velocity structure; the low- $Q_c$  region corresponds to the low velocity region, and the high- $Q_c$  region to the high velocity region.

**10:00**

VARIATION OF CODA Q DURING AN EARTHQUAKE SEQUENCE

WANG, J.H., TENG, T.L., and MA, K.F., Institute of Earth Sciences, Academia Sinica, P.O. Box 23-59, Taipei, Taiwan, 10764, R.O.C.

The May 27, 1995 Hualien earthquake sequence occurred in the northeastern Taiwan. The M=5.9 main shock was followed by a large number of shallow and closely-clustered aftershocks with the largest being a M=5.5 event. Aftershocks formed two clusters centered at 31°N and 10°E depth. One station TWO of the Taiwan Telemetered Seismic Network is located in the middle of these two clusters and gives excellent close-in recordings of the entire earthquake sequence. There are 11ings plus 11 of foreshocks occurred in the same source area offer a unique opportunity in the study of spatial and temporal variation of coda Q in a region of active subduction. From recordings of a peak response band centered about 5 Hz, we have found that: 1. The ambient coda Q near an active subduction region can be as low as 100. 2. There is a significant drop of coda Q immediately after the main shock. This drop lasted about two days before returning to the ambient level. 3. There is a noticeable difference of coda Q for sources originating from the two different aftershock clusters. No significant decrease in coda Q is found before the main shock.

**10:15**

LG-WAVE ATTENUATION AND SITE EFFECTS OF TAIWAN AREA  
Tzay-Chyn Shin, Central Weather Bureau, Taipei, Taiwan, R.O.C.

Digital seismograms of 55 earthquakes recorded by Central Weather Bureau Seismic Network(CWSN) are used to study the characteristics of Lg-wave in Taiwan area. All earthquakes are uniformly distributed in three main tectonic regions of Taiwan. Nevertheless, the averaged group velocity 3.2-3.5 Km/sec and conspicuous wave trains show that the propagation of Lg-wave is not apparently affected by the structural variation from spectral analysis. Lg-wave attenuation is of the form of  $100f^2$  in the frequency range of 0.7 to 6 Hz. Comparing to the Coda-Q obtained from the same area, 1 Hz Lg-Q is compatible to 1 Hz Coda-Q, but coda-wave attenuates fast at high frequency. The residual ratio of observed spectral amplitude to theoretical value, is found to be independent of epicentral distance and azimuth. These results imply that the variation of spectral amplitude is not caused by the variation of geological structure and the different excitation of source. Thus, station site amplification accounts for the residual. By repeating regression analysis, results from the band 0.7 to 6 Hz indicate that the site amplification depends strongly on site geology and frequency. The amplification of stations at sediment site is large by a factor of 2 to 3 relative to the average station. Two sites at fault zone exhibit decreasing amplification with respect to increasing frequency, while the hard rock sites behave reversely.

**10:30**

SCATTERING AND INTRINSIC ABSORPTION IN THE LITHOSPHERE  
BENEATH NORTHERN AUSTRALIA

KORN, M., Research School of Earth Sciences, Australian National University, Canberra, ACT 2601, Australia.

I have studied the P coda of Indonesian earthquakes recorded at the Warramunga Array (WRA) in central Australia for a broad range of source depths. An increase of coda energy relative to the direct arrivals is observed when source depth decreases. Coherency measurements by means of semblance-enhanced stacks exhibit that the coda of deep-focus events - mostly incoherent across the array, while the coda of shallower events contain a certain amount of coherent energy. The coherent arrivals are produced by reflections from plane layering and possibly by larger-scale heterogeneities in the deeper lithosphere. Small-scale heterogeneities close to the receiver, however, are responsible for the generation of the incoherent part of the coda. To further study the small-scale fluctuations of the seismic parameters I have computed the time decay of the power spectral density of the P coda of deep-focus events. An energy-flux model which assumes multiple scattering and allows for the independent determination of intrinsic Q and scattering Q has been fitted to the data. The results show an almost linear increase of intrinsic Q with frequency. Q is about 300 at 1 Hz. The frequency dependence of scattering Q is somewhat less pronounced with a value of about 340 at 1 Hz and an exponent of 0.85. A comparison of this frequency dependence with results from single scattering theory imply a correlation length of about 3.5 km and a rms velocity fluctuation of 5% for the scattering medium.

**10:45**

NEAR SURFACE GEOLOGIC SITE CHARACTERIZATION - SEPARATION OF DETERMINISTIC AND STOCHASTIC EFFECTS

STUMP, B.W., BOOGARDS, M.A., Department of Geological Sciences, Southern Methodist University, Dallas, Texas 75275; REINKE, R.E., AFML/NETSC, Kirtland AFB, NM 87117-6000

Geologic structures can be divided into stochastic and deterministic components. From the point of view of seismic wave propagation the deterministic component often involves a model in which velocities change in the vertical direction. The stochastic model is classified as a distribution of inhomogeneities and is characterized in terms of inhomogeneity size and velocity contrast. The separation of these geologic properties have implications on ground motion prediction and the utilization of seismic information. A set of site characterization procedures were designed and implemented for the resolution of such properties. The field technique involves the retrieval of full wave seismograms at closely spaced sites along eight radials emanating from a central source. The goal of this particular experiment was the characterization of the top 2m of the site which resulted in 2D spreads at 1m increments. Treating the eight observations at each range as an ensemble, frequency domain mean and variance estimates were made. The mean normalized variance, coefficient of variation (CV), is then used as a measure of lateral variation in waveforms. At low frequencies (<30 Hz) the CV values are small (~.4) reflecting little spatial variation in the wavefield. As frequency or range increases, the CV exponentially approaches 1 indicative of strong lateral variations in the wavefield. This information is utilized in constraining the stochastic site model. In order to focus on the separation of wave types and constrain velocities each one dimensional arm of the array is used in frequency/wavenumber/Fourier estimates. A finite number of V values are assumed leading to a Burg model for the K spectra. These estimates are used in constraining the deterministic model.

**11:00**

AN EXPERIMENTAL EVALUATION OF STOCHASTIC GEOLOGIC EFFECTS ON NEAR-SITE GROUND MOTION

REINKE, R.E. AND FELICE, C.W., Air Force Weapons Laboratory, Kirtland AFB NM 87117-6008; STUMP, B.W., Dept. of Geological Sciences, Southern Methodist University, Dallas, TX 75275

A high explosive experiment was designed to quantify the effects of random geologic inhomogeneities upon the small-scale variability in ground motion and to determine the relative importance of the deterministic and stochastic components of the ground motion wave field. The experiment involved the detonation of small (100 lb) explosive charges upon a test bed where the subsurface geology had been characterized in a high resolution manner. The explosive induced ground motions were recorded by accelerometers placed at six azimuths at ranges of 10, 20, and 30 meters. The subsurface site characterization effort included high resolution seismic surveys and closely spaced cone penetrometer tests as well as drilling and sampling. The site characterization process was designed to yield a good statistical characterization of the geological variability present in the test bed subsurface. This statistical characterization will be incorporated into stochastic models of the observed ground motion field.

**11:15**

HIGH STRESS ATTENUATION MEASUREMENTS AND WAVE FORM MODELLING  
ANDERSON, K.P. and SHAW, R.A., Air Force Weapons Laboratory, Kirtland AFB NM 87117-6000

A linear viscoelastic, constant Q model was used to model explosively induced high stress ground motions in alluvium. Data sets from two high explosive tests conducted at separate sites were modeled using this technique. One test consisted of a 20-ton spherical high-explosive charge detonated in alluvium at a depth of 20 meters, the other, also conducted in alluvium, was a 156-lb TNT sphere detonated at a depth of 5 meters. The smaller test was designed as a scaled low yield scaled version of the larger test. Zero near-source acceleration recordings (11 meter from 20m site, 5.5 meters from 5m site) were used as source functions for the constant Q propagation model. Good qualitative comparisons were obtained between the synthetic and measured waveforms using this technique. The Q's required to obtain a good match for the

EFFECTS OF SOURCE DEPTH ON NEAR-SOURCE SEISMOGRAMS

Elizabeth C. Flynn and Brian W. Stump

Department of Geological Sciences, Southern Methodist University  
Dallas, Texas

**Abstract.** Source depth effects are examined for five 115-kg trinitrotoluene (TNT) explosions buried at depths ranging from the optimum cratering depth of 1.8 m to the fully contained depth of 11.5 m. Data were recovered at near source ranges from 17 to 228 m. The waveforms are dominated by P and SV-Rayleigh energy. Depth effects are evident in the increase of P to SV-Rayleigh amplitude ratios and in the twofold increase of high-frequency energy for the deeper sources. Theoretical propagation depth effects are modeled by Green's functions calculated for a velocity gradient which approximates the velocity structure of the experimental site. The effects of depth on the explosion source function are predicted using the scaling laws of Mueller and Murphy (1971). These models did not reproduce the observed twofold increase of high-frequency energy. The discrepancy between the model and observations is attributed to increased coupling of high frequency P wave energy for fully contained sources. Energy calculations confirm that the shallowest event coupled 40% and the fully contained event 80% of the total seismic energy into the P wave. Source coupling efficiencies ranged from 0.7-1.0% for the near surface source to 1.5-2.9% for the fully contained explosion.

#### Introduction

The object of this study is a quantitative and theoretical investigation of the physical processes which act as a function of source depth in producing near-source explosion waveforms. An understanding of these processes is essential to the problem of characterizing the depth of the seismic event. The ability to determine source depth is important to discrimination and yield studies, where estimates of yield are dependent on the burial depth of the source [Mueller and Murphy, 1971].

The problem of characterizing the depth of a seismic event is one which involves two broad aspects: propagation effects which act as a function of depth, and changes in the nature of the source function as its burial depth changes. A spherically symmetric explosion is a good source of compressional wave energy, while a cylindrically symmetric explosion, one that is close to the free surface and only partially contained, is a richer source of SV and Rayleigh wave energy. Thus there is a relationship between the P and Rayleigh wave energy of an explosion

that is dictated to some extent by the burial depth of the event.

The free surface contributes the most important propagation effects to the source depth problem. Rayleigh wave excitation is directly attributed to the presence of the free surface boundary. The source's proximity to this boundary affects its ability to excite surface wave energy. The dependence of Rayleigh amplitudes on earthquake source depths has been observed by many authors. [Eissler and Kanamori, 1956] estimated source depths of Hawaiian earthquakes from the ratios of body to surface wave amplitudes. On a smaller scale, [Dobrin et al., 1951] quantified the decay of Rayleigh amplitudes for explosions buried from 20 to 300 ft. The Rayleigh decay is predominantly a function of the change in propagation path with depth, but for very shallow sources an increase in source coupling serves to increase the Rayleigh amplitude with depth.

The interference of pP and other free surface reflections with the direct P arrival is another phenomenon dependent on the depth of the source. The free surface reflection creates interference phenomena that present difficulties in the frequency domain where spectral techniques are used to estimate various source parameters [Langston, 1978].

With both source and propagation effects contributing a depth dependence to the P and the surface wave, the relationship between these two arrivals can be a complicated function of source depth. This study is intended to quantitatively assess the effects of the depth of the source on P and Rayleigh arrivals, and to distinguish the effects of depth on the source function and the propagation terms.

This study is unique to those mentioned above for two reasons. First, this investigation focuses on near-source observations for which the scale is much smaller, although the physical phenomena are the same. The near-source observations are dominated by upgoing rather than downgoing energy and are thus strongly influenced by the free surface and near-surface structure. Second, the experimental configuration is well controlled; the source depths and recording distances are accurately known, as is the velocity structure of the experimental site. The data set provides not only depth-dependent observations, but also range-dependent observations which allow the characterization of spatial propagation effects.

The separation of source and propagation effects is attempted by matching observed depth effects with theoretical depth effects. Propagation effects are modeled by theoretical Green's functions. Source effects for the fully contained events are calculated from the depth scaling

Copyright 1988 by the American Geophysical Union.

Paper number 78B024.  
0148-0227/88/0078-0024\$05.00

## OBSERVATIONAL DATA

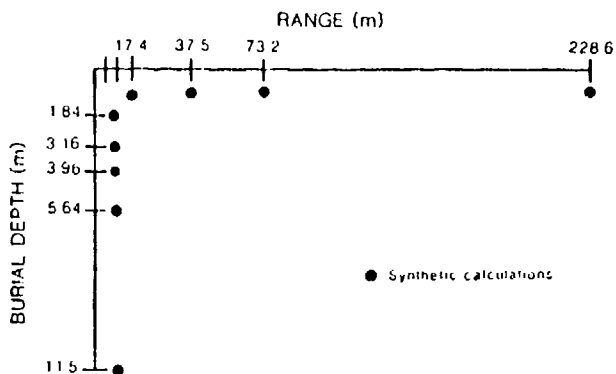


Fig. 1. Schematic of the experimental configuration. Sources were buried at 1.84, 3.16, 3.96, 5.64, and 11.5 m. Data were recorded at ranges of 17.4, 37.5, 73.2, and 228.6 m.

proposed by [Mueller and Murphy, 1971]. The increase in source coupling with increased containment is quantified by the calculation of total seismic energy as a function of burial depth.

### Observational Data

#### Range Effects

The data set was generated by five 115 kg chemical explosions fired in dry alluvium and buried from 1.8 to 11.5 m below the free surface. The explosions ranged from partially contained, 1.8 m being the optimum cratering depth, to a fully contained event at a depth of 11.5 m. Radial (to the source) and vertical acceleration was recorded at 17, 37, 73, and 228 m from each of the five events. The data were sampled at 2000 samples/s. The recording ranges and source depths are summarized in Figure 1. The velocity waveforms for one range (73 m) are shown in Figure 2, which displays the radial and vertical components for each explosion. The complete data set is displayed in the work by [Flynn, 1986].

The waveforms are dominated by a P phase and an SV-Rayleigh phase. The SV and Rayleigh arrivals are treated as one because at the closest ranges their arrival times are separated by only a few hundredths of a second, while the SV-Rayleigh pulse width is of the order of 0.2 s. In Figure 2 the SV-Rayleigh pulse is distinguished by a large amplitude and a shift to longer periods relative to the P arrival. Propagation effects at the farthest range (228 m) have separated the P and SV-Rayleigh phases by some intermediate multipathed arrivals, but as close as 37 and 73 m the waveforms consist almost entirely of the P and the SV-Rayleigh phases (Figure 4a). At the closest range (17 m), even the P and SV-Rayleigh phases are not completely separated.

The dominance of P and SV-Rayleigh motion is verified by particle motion diagrams. In Figure

3 the 228-m radial and vertical components are plotted with particle motions for the indicated P and SV-Rayleigh windows. Particle motion in the P window is rectilinear, with the radial and vertical motions roughly equal. In the indicated SV-Rayleigh window, the radial and vertical components have fallen out of phase and particle motion has become retrograde, representing surface wave motion.

The effect of range in separating the body and surface wave phases is illustrated in Figure 4 by the particle motions of a single event. At 17 m the P wave motion is not strongly linear, nor is it sharply distinguished from the onset of the SV-Rayleigh wave. The separation of body and surface waves becomes more distinct with the evolution of strongly linear and retrograde motions observed at more distant ranges.

The effect of propagation distance is evident in the decay of P and SV-Rayleigh amplitudes. In Figure 5, decay rates of the phases are estimated by a linear least squares fit to the log of the amplitude versus the log of the range. The P and SV-Rayleigh waves display faster decay rates than are expected for spherical and cylindrical wave fronts, respectively. Radial P decays as  $r^{-1.6}$ , vertical P as  $r^{-1.3}$ , radial Rayleigh as  $r^{-1.0}$ , and vertical Rayleigh as  $r^{-0.9}$ . These decay rates include the effects of geometrical spreading, complex structural interactions, scattering, and intrinsic attenuation.

## VELOCITY WAVEFORMS observed at 73 meters

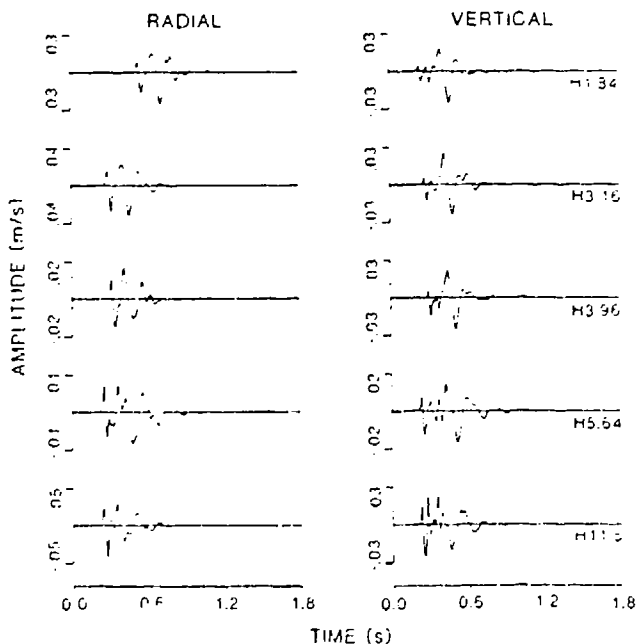


Fig. 2. Observed velocity waveforms. Radial and vertical components are shown for each source depth at the 73 m range. H indicates source burial depth.

RADIAL and VERTICAL VELOCITY  
at 228 meters

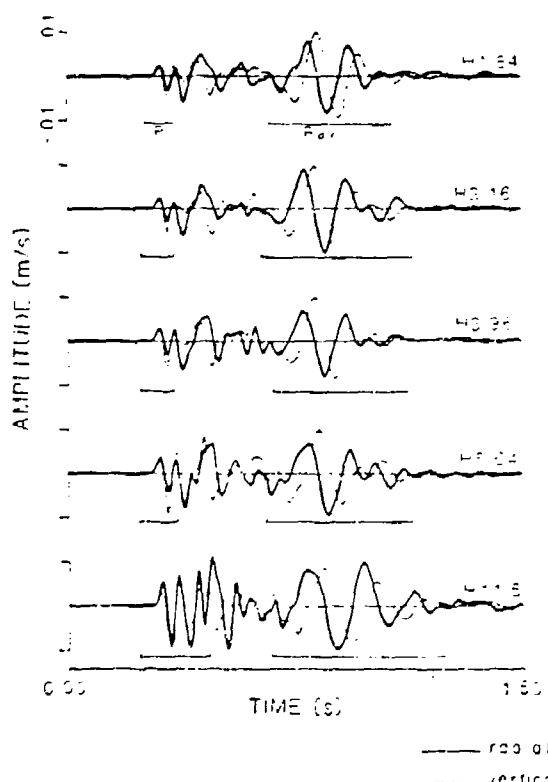


Fig. 3a

Fig. 3. Velocity waveforms and corresponding P and SV-Rayleigh particle motions observed at 228 m. (a) Radial (solid line) and vertical (dashed line) velocity waveforms. H indicates source burial depth. Bars indicate P and SV-Rayleigh time window for which particle motions are plotted. (b) Particle motions for the P and SV-Rayleigh time windows.

#### Depth Effects

**Time domain.** In the time domain the P and SV-Rayleigh arrivals were identified by particle motion diagrams. The vertical P wave amplitude increases by twofold to sixfold (depending on range) from a source depth of 1.6 m to a depth of 11.5 m (Figure 6). The radial P wave amplitude shows a less pronounced depth dependence, increasing by 1.5-fold to threefold over the range of source depths. The SV-Rayleigh waves display very little depth dependence, decreasing by 20–40% over the range of source depths. The ratios of P to SV-Rayleigh amplitudes plotted in

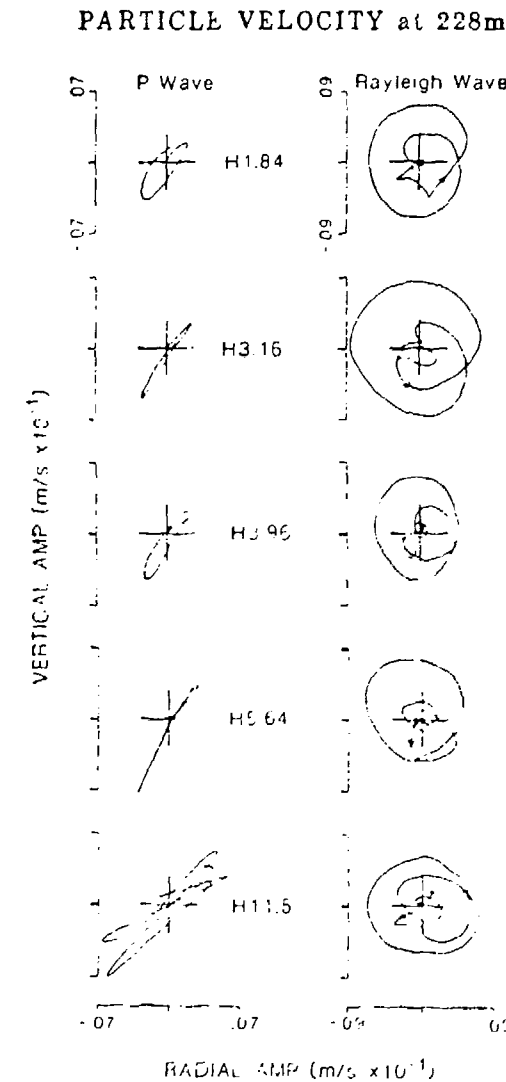


Fig. 3b

Figure 7 are largely a reflection of the depth dependence of P wave amplitudes.

**Frequency domain.** The displacement spectra for each event as recorded at 73 m are given in Figure 8a. The signal is above background noise in the 2- to 60-Hz band (Figure 8b). The displacement spectra at each range are characterized by a long period level and a corner frequency that were estimated from an overlay of a four-pole Butterworth filter. In Table 1 it is seen that an average 2- or 3-Hz increase in corner frequency accompanies the increase of source depth from 1.6 to 11.5 m. This estimate of the corner is subject to error, as the difference

### PARTICLE VELOCITY for 5.64m event

#### RADIAL and VERTICAL VELOCITY for 5.64m event

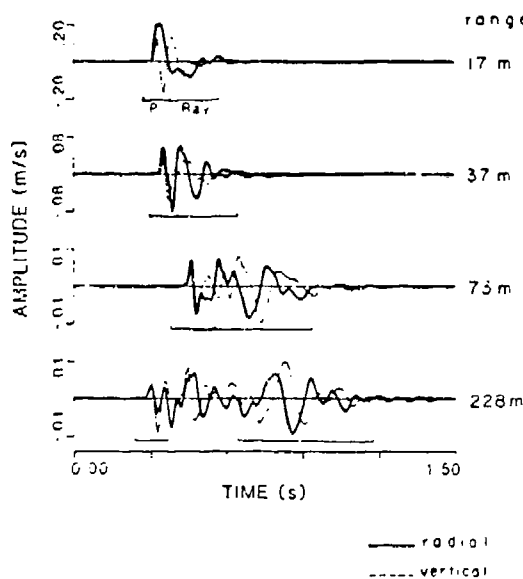


Fig. 4a

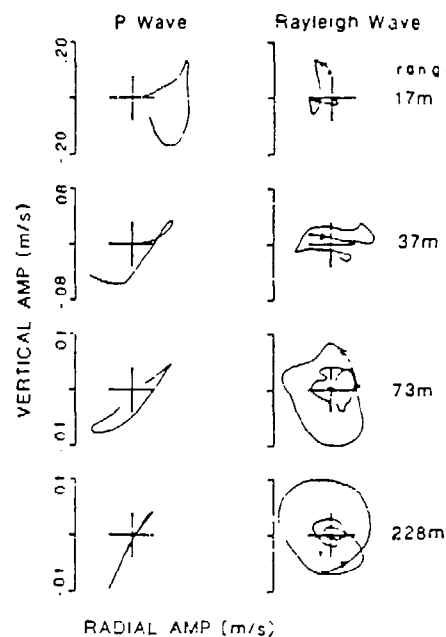


Fig. 4b

Fig. 4. Velocity waveforms and corresponding P and SV-Rayleigh particle motions for the 5.6 m event at four recording ranges. (a) Radial (solid line) and vertical (dashed line) velocity waveforms. Bars indicate P and SV-Rayleigh time windows. (b) Particle motions for the P and SV-Rayleigh windows.

in corner frequency between the radial and vertical components at the same range or the difference between two different ranges is comparable to the 2- to 3-Hz variation. Corner frequency variations for this data set are small, of the order of 20% at most. No appreciable increase or decrease in the long period level of the spectra occurs with changing source depth.

A comparison in Figure 9 of the spectra of the deepest and the shallowest events illustrates the change in spectral shape that coincides with an increase of source burial depth. The higher corner frequency of the deeper event is reflected in the increase of high-frequency spectral amplitudes. At the long periods the two spectra converge for the depths and ranges studied.

Spectral ratios of the deepest to the shallowest sources were calculated in the frequency domain and smoothed by a five-point running mean (Figure 10). The increase in high-frequency spectral amplitude of the deeper event is represented by a spectral ratio greater than 1. At low frequencies (<10 Hz) the spectral ratios are not consistently smaller or greater than 1, but at high frequencies (10-4 Hz) the deepest event has a factor of 2 increase in spectral amplitude. Time domain windows of the P and SV-Rayleigh waveform and Fourier analysis identifies the 10- to 40-Hz band as the P contribution and the 4- to

10-Hz band as the SV-Rayleigh contribution [Flynn, 1986]. The increase of 10- to 40-Hz spectral amplitudes that accompanies an increase of source depth agrees with the time domain P amplitudes in suggesting a larger contribution of P wave energy for the deeper events. The low-frequency band of 4-10 Hz lacks a consistent increase or decrease of spectral amplitudes with depth, suggesting that for the events under study the amount of SV-Rayleigh energy produced is not a strong function of source depth.

#### Modeling of Source and Propagation Effects

The depth effects that have been outlined in the time and frequency domains contain both source and propagation depth effects. The observations can be expressed in general terms as a convolution of the source function with propagation path effects, or in the frequency domain as

$$U(f) = G(f) S(f) \quad (1)$$

where  $U$  are the observations,  $S$  the source function, and  $G$  the Green's function or impulse response of the medium.

### RADIAL AMPLITUDE vs RANGE

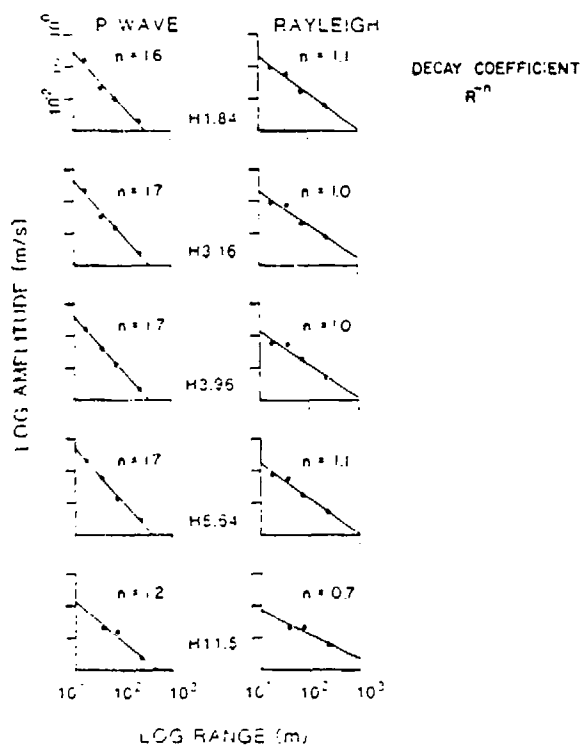


Fig. 5a

### VERTICAL AMPLITUDE vs RANGE

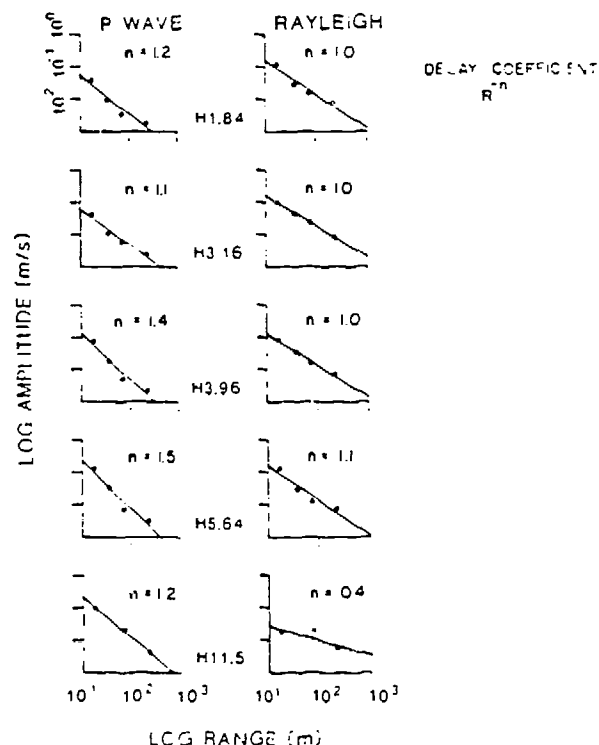


Fig. 5b

Fig. 5. Spatial decay of P and SV-Rayleigh velocity amplitudes. Amplitude decay is approximated by a least squares line on each plot. (a) Radial P and SV-Rayleigh amplitudes. (b) Vertical P and SV-Rayleigh amplitudes.

#### Source Effects

In an attempt to create a reference against which the data can be judged, the [Mueller and Murphy, 1971] source model was used to predict source effects for source depths between 1.8 and 11.5 m. This model is for fully contained sources and acts as a standard against which the cratering explosions can be compared. Shown in Figure 11 are the predicted effects of source depth on the far-field source potential. From 1.8- to 11.5-m source depth, the corner frequency of the source is predicted to increase by approximately a factor of 2, a much larger increase than observed in the data. The long period level of the spectra drop by a factor of 2 from the 1.8- to 11.5-m source. The observations show no consistent decrease in the long period level (Table 1). The spectral ratio of the 1.8- to 11.5-m sources has a twofold increase in high-frequency amplitudes (Figure 12) and is comparable to the observed amplitude ratios (Figure 10). The observations appear to demonstrate some of the predicted source depth effects, but they lack other of the predicted source effects, namely, the drop in long period level.

#### Propagation Effects

The contribution of propagation effects to the depth-dependent observations can be tested with synthetic waveforms generated by idealized propagation models. The velocity model which best fit the test site [Stump and Reinke, 1982] consisted of compressional velocity, shear velocity, and density which increased smoothly from surface values of 375 m/s, 244 m/s, and 1.67 g/cm<sup>3</sup>, respectively to values of 1128 m/s, 610 m/s, and 2.1 g/cm<sup>3</sup> in the half-space at 25-m depth (Figure 13). The depths and P velocities at the site are well constrained, while the shear velocities are not as well known. The P and S Qs in this initial model were assumed to be 100 and 44, respectively.

Green's functions were calculated by a modified reflectivity method and convolved with the theoretical source function for the 11.5-m depth. This convolution was completed so that direct comparisons with the band-limited observational data could be made. The resulting waveforms are given in Figure 14. The P amplitude can be seen to increase with source depth relative to the SV-Rayleigh amplitude. The model produces a factor

## RADIAL AMPLITUDE vs SOURCE DEPTH

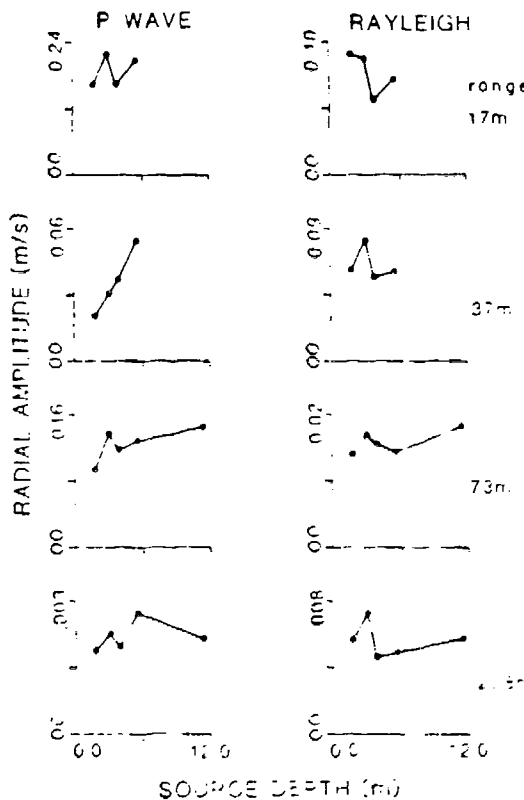


Fig. 6a

## VERTICAL AMPLITUDE vs SOURCE DEPTH

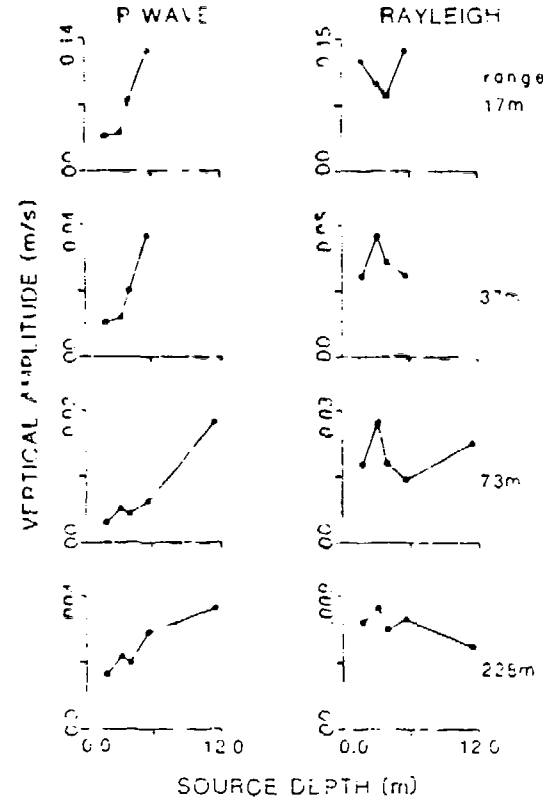


Fig. 6b

Fig. 6. P and SV-Rayleigh amplitudes as a function of source depth. (a) Radial P and SV-Rayleigh amplitude versus source depth. (b) Vertical P and SV-Rayleigh amplitude versus source depth.

of 1.7-4.0 increase in P amplitude with source depth, which is comparable to the increase of observed P amplitudes (2-6). The SV-Rayleigh amplitude decreases by a factor of 3-5, which is more pronounced than the 20-40% decrease that was observed.

Comparison of the spatial decay of the Green's functions can be made with the data. For the 1.84-m synthetic source the vertical P wave decays as  $r^{-1.2}$  and the Rayleigh wave decays as  $r^{-0.6}$ . The observed decay values for this source depth (Figure 5b) are  $r^{-1.2}$  and  $r^{-1.0}$ , respectively. The radial synthetics for the 1.84-m source give P and Rayleigh decay rates of  $r^{-1.1}$  and  $r^{-0.7}$  compared with observed values of  $r^{-1.6}$  and  $r^{-1.1}$  (Figure 5a). For the 11.5-m source the vertical synthetics (P and Rayleigh) decay as  $r^{-0.6}$  and  $r^{-0.4}$  compared with observed values of  $r^{-1.2}$  and  $r^{-0.4}$ . The radial synthetic values for the deeper source are  $r^{-0.9}$  and  $r^{-0.3}$  compared with observed values of  $r^{-1.2}$  and  $r^{-0.7}$ . Both the synthetics and the observations show reduced decay rates as the source depth increases

and the effects of the shallow low-velocity layers are reduced. Although the synthetics more closely replicate the observed spatial decay than a simple elastic half-space, the observational data in most cases decay faster than the synthetics. This observation indicates that effects such as intrinsic attenuation and scattering could be underestimated in this model.

In the frequency domain the corner frequency decreases by approximately 2 Hz, which is unlike the shift to higher frequencies observed in the data. The long period level displays a slight increase with source depth.

In summary, the Green's functions can account for an increased P wave amplitude with depth, but they cannot account for an increasing corner frequency or a nondecaying long period level, and they produce an SV-Rayleigh wave that is too strongly depth dependent.

### Combined Source/Propagation Effects

Predicted source depth effects were combined with theoretical propagation depth effects by

## P:R RATIO vs SOURCE DEPTH

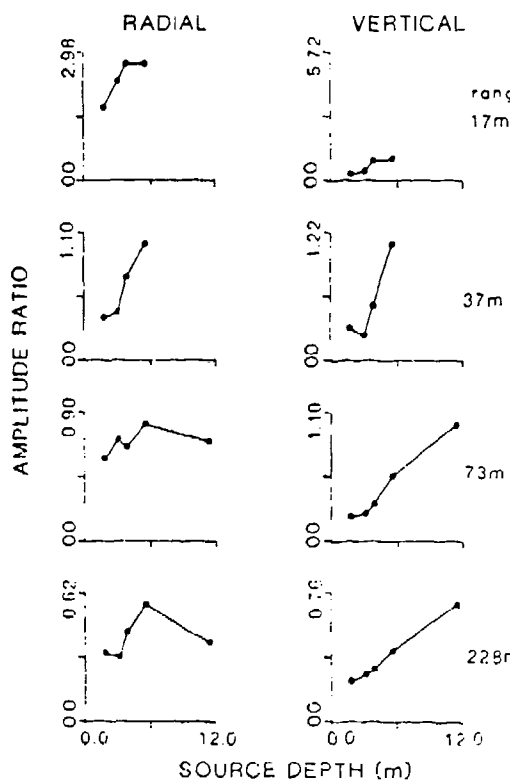


Fig. 7. Ratio of P to SV-Rayleigh amplitude as a function of source depth, for both the radial and vertical components.

convolving the Green's functions with the appropriate Mueller-Murphy source function derived for each source depth. The Mueller-Murphy predictions are strictly for fully contained sources. The spectral ratios resulting from these combined source and propagation effects are given in Figure 15. The shift of source energy to high-frequencies is roughly balanced by the decrease in high-frequency energy for the deep propagation path. At long periods the spectral ratio is slightly greater than 1, particularly at the 228-m range.

Comparing the observed (Figure 10) and calculated (Figure 15) spectral ratios, it is evident that the observations contain depth effects beyond those that can be accounted for by the Mueller-Murphy source model and the layered Green's functions. The depth effect that is not satisfactorily modeled is the two to one spectral ratio at high frequencies ( $10^{-4}$  Hz).

The physical depth effect that is addressed by neither the Green's functions nor the Mueller-Murphy source scaling laws is the effect of moving from a partially contained to a fully contained burial depth. Based upon the modeling exercise, it is concluded that the fully contained source generates more high-frequency

energy as a result of an increase in coupling over the near-surface source. In order to experimentally quantify the increased coupling efficiency with increased burial depth, the total seismic energy in the observed waveforms is calculated as a function of source depth.

## DISPLACEMENT SPECTRA OBSERVED at 73m

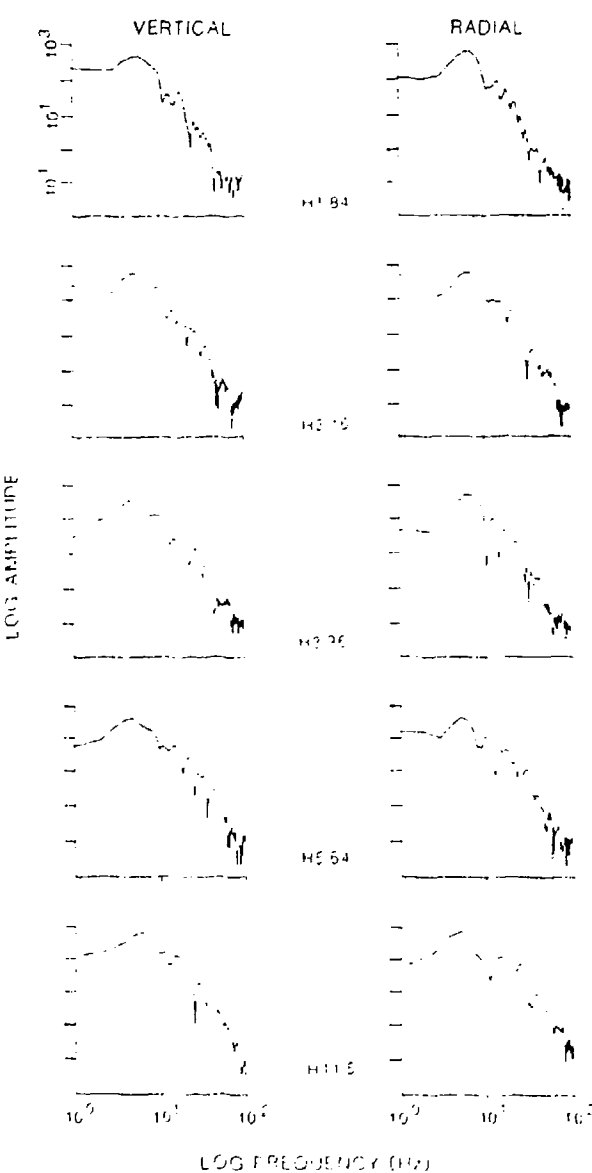


Fig. 8a. Displacement spectra for all events recorded at 73 m. Here 2048 time points were windowed by a 10% cosine taper applied to the displacement waveforms.

## ACCELERATION AND NOISE SPECTRA

Range 7.3 m

II 3.16

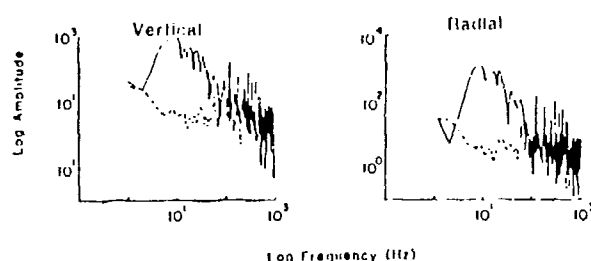


Fig. 8b. Acceleration and noise spectra for a typical event, illustrating the effective bandwidth of 2-50 Hz.

TABLE 1b. Levels of Observed Displacement Spectra,  $\times 10^4$

Range, m	Source Depth, m				
	1.84	3.16	3.96	5.64	11.5
	<u>Radial</u>				
17	3.20	3.20	3.00	6.00	
37	1.00	1.00	0.70	0.80	
73	0.70	0.70	0.50	0.40	1.20
228	0.22	0.40	0.28	0.31	0.40
	<u>Vertical</u>				
17	1.10	0.90	0.80	1.20	
37	0.70	0.75	0.55	0.90	
73	0.48	0.60	0.40	0.42	0.72
228	0.28	0.37	0.30	0.38	0.40

## Energy Calculations

Attenuation and Q

Energy as a function of depth is best quantified after spatial dependencies have been removed from the data. The data set lends itself to an empirical determination of range-dependent propagation effects which are represented as the spatial decay of P and SV-Rayleigh energy. The P and SV-Rayleigh energy displays a range dependence which is greater than simple geometrical spreading. Since the goal of this part of the investigation was the quantification of coupled energy in the wave field, an empirical spatial decay was determined. The total decay could then be used to quantify the energy in the wave field at any observational range. The apparent attenuation can be represented as a decaying function of range

$$A = A_0 \exp(-\alpha r), \quad (2)$$

where  $\alpha$  is the apparent attenuation and  $r$  is the range. The apparent attenuation is a combination

of mechanisms such as scattering, intrinsic attenuation, and wave propagation phenomena as illustrated in the synthetic calculations. Apparent attenuation is estimated from the seismic energies which are calculated from observational velocity records.

Calculation of seismic energy begins with the energy flux [Wu, 1966; Perret, 1973]:

$$F = \rho c \int [v(t)]^2 dt \quad (3)$$

where  $F$  is energy flux in ergs per square centimeter,  $\rho$  is density ( $\text{g/cm}^3$ ),  $c$  is propagation velocity ( $\text{cm/s}$ ), and  $v(t)$  is recorded particle velocity ( $\text{cm/s}$ ).

The energy flux,  $F$ , was calculated for both P and SV-Rayleigh arrivals. The P arrival corresponds to the time duration over which the particle motion was linear; the SV-Rayleigh arrival was marked by the onset of retrograde motion (Figures 3 and 4).

Using Parseval's theorem, the energy flux was calculated in the frequency domain

$$\int [v(t)]^2 dt = 1/(2\pi) \int [V(\omega)]^2 d\omega \quad (4)$$

where  $V(\omega)$  is the Fourier transform of  $v(t)$ .

The advantage of calculating the energy flux in the frequency domain is that the apparent spatial attenuation can be derived for each of the two frequency bands considered, a P band and the SV-Rayleigh band, where the apparent attenuation is assumed to be frequency independent within each of these bands.

The P and SV-Rayleigh time windows were tapered and transformed, padding to 256 points for the P window and 512 points for the SV-Rayleigh window. The function  $[V(\omega)]$  is plotted in Figure 16 for the P and SV-Rayleigh windows. The P wave energy is peaked in the 10- to 40-Hz band and the SV-Rayleigh energy is in the 4- to 10-Hz band. The amplitude of the P wave spectrum has fallen off by nearly a factor of 10 at 40 Hz, which means that  $[V(\omega)]^2$  has fallen off by a factor of 100. The P wave energy was taken to be

TABLE 1a. Corner Frequencies of Observed Displacement Spectra

Range, m	Source Depth, m				
	1.84	3.16	3.96	5.64	11.5
	<u>Radial</u>				
17	10.0	10.5	11.0	10.5	
37	10.0	11.0	12.0	15.0	
73	10.0	10.5	10.5	11.5	12.0
228	10.0	10.0	10.5	10.5	11.5
	<u>Vertical</u>				
17	12.0	12.0	15.0	15.0	
37	11.0	11.0	14.0	16.0	
73	10.0	10.5	11.0	12.0	12.0
228	9.0	9.5	10.0	10.5	11.0

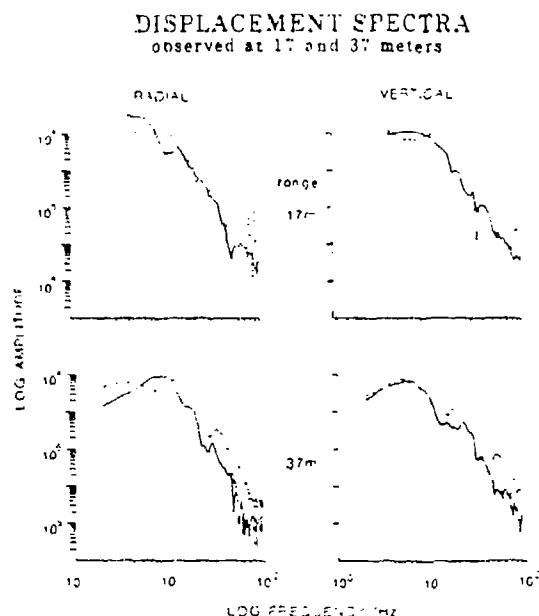


Fig. 9a

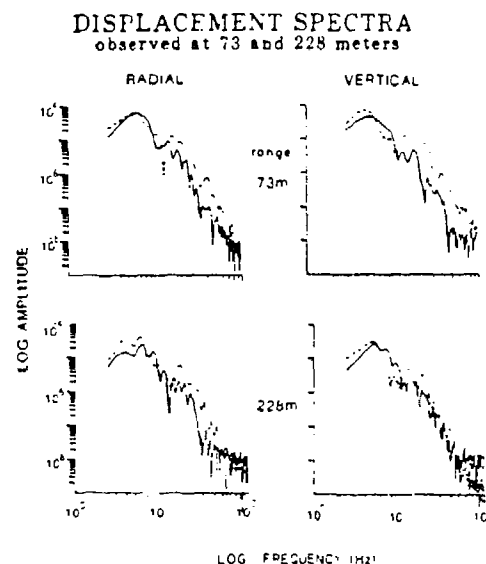


Fig. 9b

Fig. 9. Comparison of displacement spectra of the deepest and shallowest events. The shallowest event (solid line) is the 1.8-m event. The deepest event (dashed line) recorded at 17 and 37 m is the 5.6-m event; the deepest event recorded at 73- and 228-m is the 11.5-m event. (a) Displacement spectra for the 17- and 37-m ranges. (b) Displacement spectra for the 73- and 228-m ranges.

the sum of the energies contributed by frequencies between 8 and 40 Hz. The SV-Rayleigh energy is determined by summing energy in the 4- to 12-Hz band. Inclusion of a wider frequency band

changes the energy estimates by no more than 5%. The total energy in a spherical wave front becomes

$$E = 4\pi R^2 F \quad (5)$$

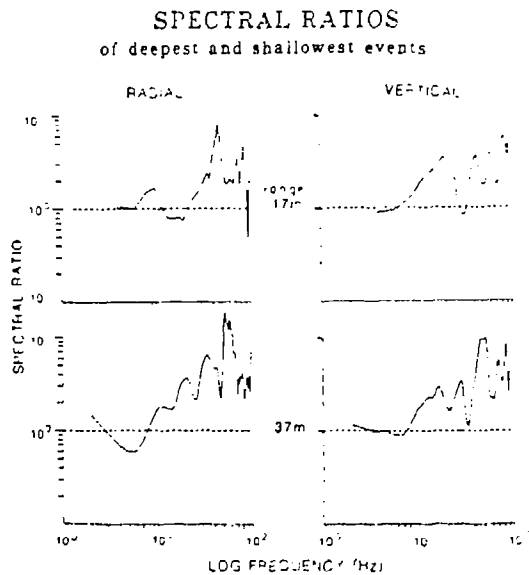


Fig. 10a

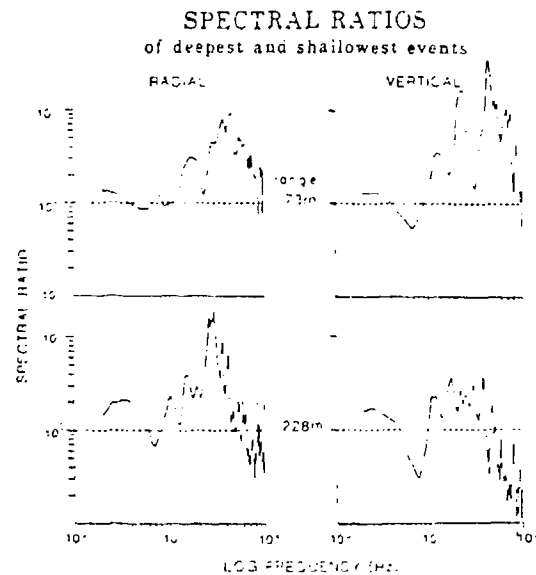


Fig. 10b

Fig. 10. Spectral ratio of the deepest to the shallowest events. Dashed lines represent a spectral ratio of 1. (a) Spectral ratios for the 17- and 37-m ranges. (b) Spectral ratios for the 73- and 228-m ranges.

## EFFECTS OF DEPTH ON MUELLER-MURPHY SOURCE POTENTIAL

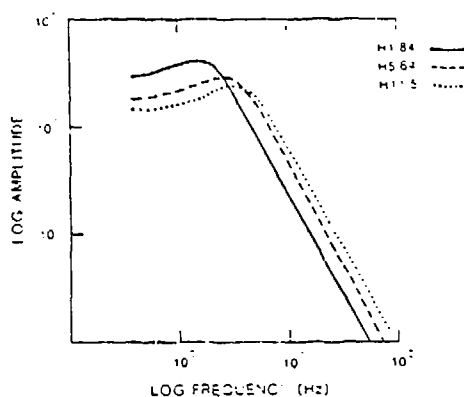


Fig. 11. Predicted effects of depth on the far-field source potential of [Mueller and Murphy, 1971]. Theoretical source spectra are shown for the 1.8-, 5.6-, and 11.5-m source depths.

where  $E$  is energy in ergs and  $R$  is range in centimeters. For cylindrical waves the total energy becomes

$$E = 2\pi R n F \quad (6)$$

where  $n$  is depth of cylindrical wave front and is derived for Rayleigh waves in the appendix.

The total spherical (P) and cylindrical (SV-Rayleigh) energy as determined from the observational data is plotted in Figure 17. The decay of energy with range is called the apparent attenuation. The linear slope of the log energy plot is the decay constant,  $\alpha$ , in (2) and represents the combination of all remaining mechanisms of spatial attenuation. The energy values represent a variety of frequencies. Since these measurements were utilized in the attenuation determinations, the decay coefficient  $\alpha$  is estimated in the 6- to 40-Hz band for the P wave and the 4- to 12-Hz band for the SV-Rayleigh wave. Based upon this analysis technique, it is difficult to constrain any frequency dependence in  $\alpha$ . Table 2 lists the least squares values of the energy decay rates and their correlation coefficients. Interpreting the spatial attenuation in terms of  $Q$ , one must assume a frequency dependence. Values in the literature for regional data range from  $f^{1/6}$  to  $f^{1/4}$  [Priestley and Chavez, 1987; Butler et al., 1987]. For simplicity,  $Q$  is assumed linear in frequency:

$$A = A_0 \exp(-\alpha r) = A_0 \exp(-\omega r/2cQ) \quad (7)$$

$$Q = \omega/2c\alpha \quad (8)$$

The  $Q$  values calculated from the P and SV-Rayleigh attenuation rates are given in Table 3. For the radial component,  $Q$  ranged from 5 (8 Hz) to 25 (40 Hz) for P and 10 (4 Hz) to 30 (12 Hz) for SV-Rayleigh. For the vertical component,  $Q$  ranged from 15 (8 Hz) to 95 (4 Hz) for P and 18 (4 Hz) to 54 (12 Hz) for SV-Rayleigh. These

differences in radial and vertical decay rates may be partially attributed to the different propagation path effects that were synthetically modeled earlier.

### Energy as a Function of Depth

The  $\alpha$  values are used to correct for the final range dependence in the energy calculations. The range-corrected P and SV-Rayleigh energies are plotted as a function of source depth in Figure 18. The range corrections are particularly effective for the radial component where the energies calculated at each range for a given depth differ at most by a factor of 3. The vertical P wave energies still contain some scatter for the different ranges, with energies differing by nearly a factor of 10 at a given depth. Some improvement in these estimates may be obtained by allowing  $\alpha$  in the decay estimates to become frequency dependent.

Normalizing the P and SV-Rayleigh energies to the sum total of P plus SV-Rayleigh energy, it can be seen from Figure 19 that the shift in energy distribution from the shallowest to the deepest source is a shift from SV-Rayleigh to P energy. The average recording of the shallowest event contains 40% P wave and 60% SV-Rayleigh energy. The average recording of the 3.9- and 11.5-m events contained 72% and 83% P wave energy, respectively. The percentage P wave energy increases rapidly from 1.8- to 3.9-m source depth, and more slowly to the final depth of 11.5 m.

The increase in P wave energy from 40% to 83% of the total seismic energy confirms that the fully contained source is a more efficient generator of P wave energy than the near-surface source. The absolute energy increases from an average of  $8 \times 10^{12}$  ergs for the shallowest event to an average of  $22 \times 10^{12}$  ergs for the fully contained event. Since all events were of the same size, with a yield of  $10^{15}$  ergs [Meyer, 1981], the increase in total seismic energy

## MUELLER-MURPHY SOURCE RATIO

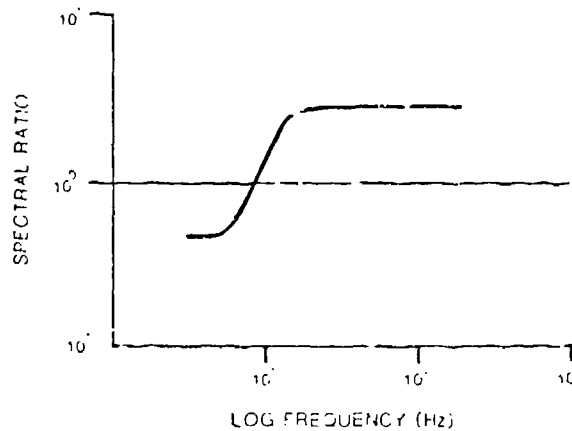


Fig. 12. Spectral ratio of the deepest to shallowest Mueller-Murphy sources.

## GRADIENT VELOCITY STRUCTURE

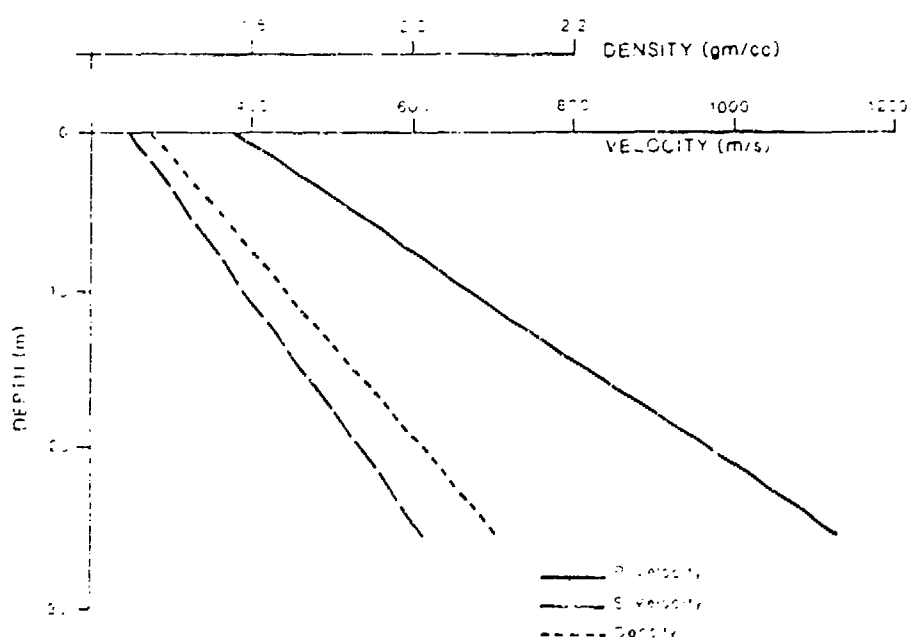


Fig. 13. Gradient velocity structure. Compressional and shear velocity and density increase steadily through 28 m (replicated by 13 layers). The P and S wave Q's are taken to be 10 and 40 times greater than the model.

corresponding to an increase in source coupling efficiency from 0.7% to 1.1% for the near-surface source to between 1.1% and 1.4% for the fully contained event (Fig. 14a). For nuclear explosions in aluminum, (Bentley, 1965) obtained similar coupling efficiencies between 0.1% and 0.15%, while other materials such as salt, buff and salt gave efficiencies of 2-3%. (Makinson, 1970) determined coupling efficiencies of 0.1% for the containing shot cavities in buff while the contained explosion, Bentley, et al. (1965), gave a

coupling efficiency of 6.1%. In this study a tenfold to fourteenfold increase in coupling from the cratering to the fully contained explosion was determined.

### Conclusion

Input effects fall under two broad categories: source depth effects and propagation depth effects. The separation of the source and propagation depth effects has been completed with

## GRADIENT SYNTHETICS

### EARTH



### VERTICAL



Fig. 14. Vertical seismograms for the gradient models. (a) Earth gradient model; (b) vertical gradient model. The vertical axis is amplitude and the horizontal axis is time.

## GRADIENT SPECTRAL RATIOS

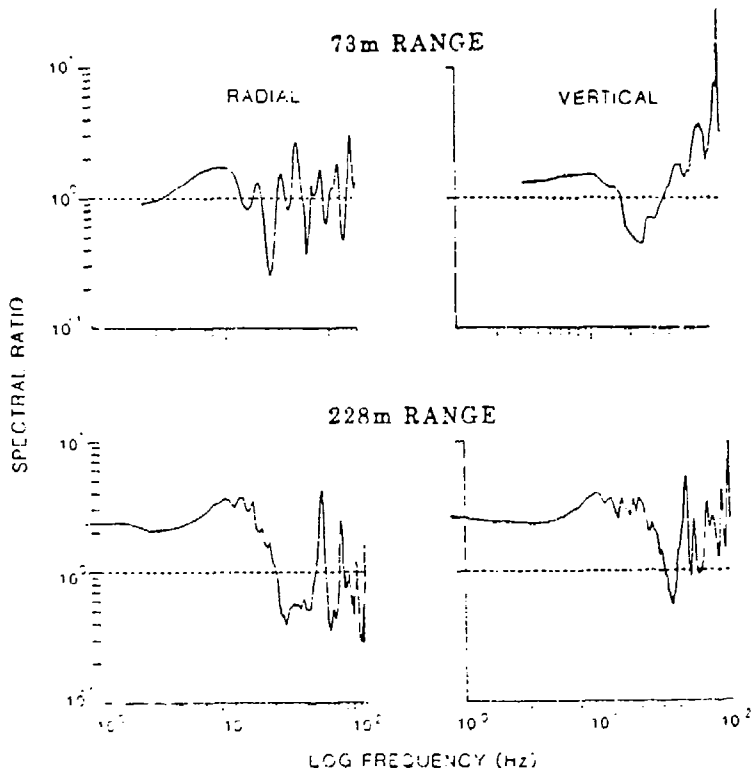


Fig. 1. Spectral ratios of gradient spectra with source effects included.

the help of theoretical source and propagation models. The data set to which this analysis was applied is unique for two reasons: the small scale of the experiment, configuration and the control of source depth and recording ranges.

Observations at several distances allowed the wave field to be quantified in terms of its spatial characteristics, namely the dominance of P and SV-Rayleigh motion, the amplitude decay of the two arrivals, and their spatial attenuation

rates. The source depths spanned the range from partially to fully contained, corresponding to source symmetries which vary from cylindrical to spherical. The dominance of P and surface wave motions is therefore important to this investigation because the relationship between the spherical P and the cylindrical SV-Rayleigh arrivals is in part a measure of the changing symmetry of the source with increasing overburden. The P and SV-Rayleigh arrivals were

## WINDOWED VELOCITY SPECTRA

H1.84m, R228m

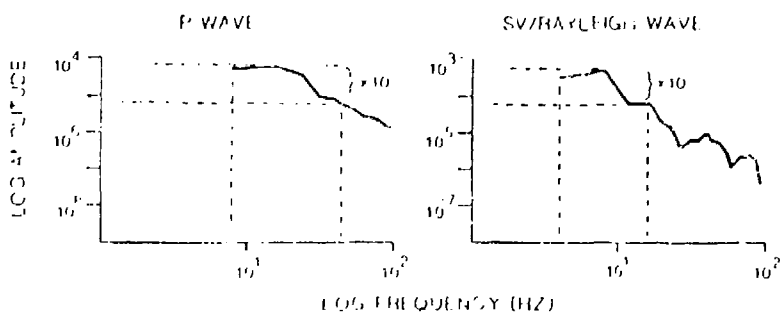


Fig. 2. P and SV-Rayleigh amplitude spectra. P wave amplitude falls off by a factor of 10 from 5 to 40 Hz. SV-Rayleigh amplitudes fall off by a factor of 10 from 4 to 12 Hz.

## ENERGY vs RANGE

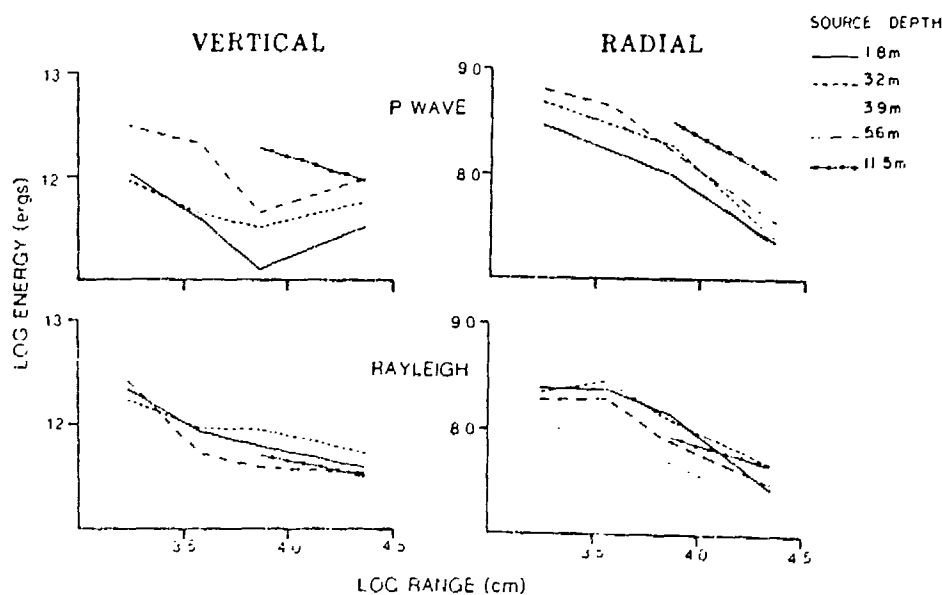


Fig. 17. Decay of P and SV-Rayleigh energy with range for the radial and vertical components.

shown to consist of individual frequency bands, 4-10 Hz for the SV-Rayleigh wave and 10-40 Hz for the P wave. Together, these arrivals comprise the bandwidth of the data. Thus the P and SV-Rayleigh arrivals were also used as a measure of the relative coupling of high to low frequencies as a function of source depth.

The observed depth effects included a twofold to fivefold increase in P wave amplitude and a

1.5-fold decrease in the SV-Rayleigh amplitude over the range of source depths, and a shift to higher frequencies with increasing depth.

The increase in P amplitude relative to SV-Rayleigh amplitude with depth was modeled as a theoretical propagation effect. The gradient velocity model accounted for observed increases in P amplitudes but was unable to match the slow decay of surface wave amplitude with increasing source depth.

The Mueller-Murphy source model predicts a decrease in long period spectral level with increased source depth while exhibiting an increase in corner frequency and high-frequency content. The propagation path effects give a decrease in corner frequency with increasing

TABLE 2. Apparent Spatial Attenuation, Least Squares Energy Decay Rates and Linear Correlation Coefficients (LCC,  $\times 10^{-3}$ )

Depth, m	Radial	LCC	Vertical	LCC
<u>P Energy</u>				
1.80	-5.0	0.90		
3.16	-6.1	0.93	-1.2	0.31
3.96	-5.9	0.98	-2.0	0.48
5.66	-5.8	0.91	-1.2	0.34
Average	-5.7		-1.5*	
<u>Rayleigh Energy</u>				
1.80	-4.7	0.99	-2.7	0.82
3.16	-3.5	0.95	-1.9	0.97
3.96	-3.7	0.96	-1.8	0.74
5.66	-3.8	0.96	-2.6	0.63
Average	-3.9		-2.3	

\*Decay rates are slow for the vertical P wave and correlation coefficients are poor, largely because P wave energy at the 75-m range is anomalously low.

TABLE 3. Q Values for P and SV-Rayleigh Waves

	Frequency Q ( $\times 10^3$ cps)	
Radial P wave,	0-5	40-25
a = $5.7 \times 10^{-3}$ ergs/cm, c = 920 m/s		
Radial SV-Rayleigh wave,	10-4	30-10
a = $3.9 \times 10^{-3}$ c = 320 m/s		
Vertical P wave,	10-8	90-40
a = $1.5 \times 10^{-3}$ c = 920 m/s		
Vertical SV-Rayleigh wave,	10-4	30-10
a = $1.3 \times 10^{-3}$ c = 320 m/s		

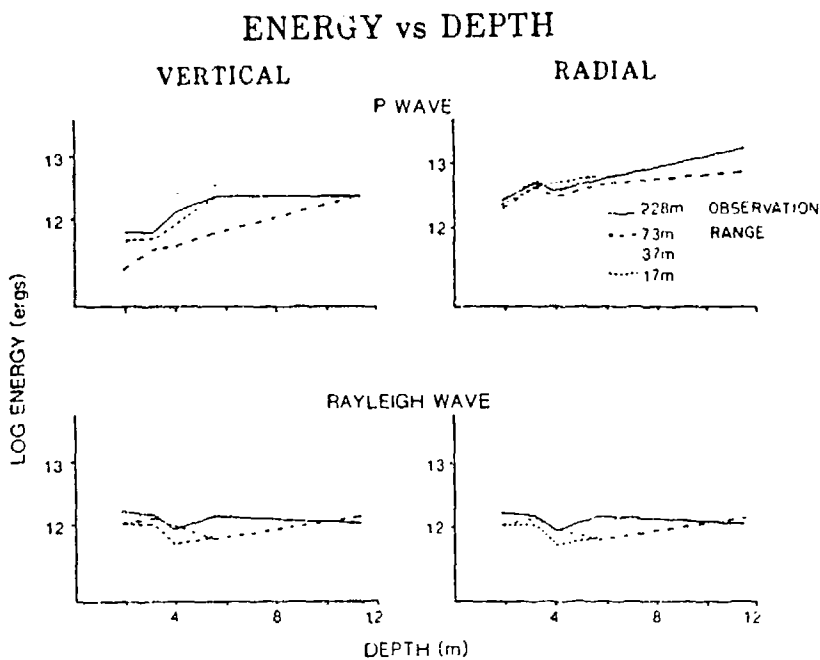


Fig. 18. P and SV-Rayleigh energy as a function of source depth for the radial and vertical components.

source depth. The combined source and propagation effects thus gave no increase in high frequency energy unlike the observational data. The increase of the 10- to 40-Hz P wave energy from 40% to 80% of the total seismic energy quantifies the observed shift to higher frequencies and identifies the shift as one from surface wave energy to P wave energy as source depth increases. Based upon the modeling, this

increase in high-frequency energy is attributed to the difference between the shallow partially contained cylindrical source and the deeper fully contained spherical contained source. These conclusions could only be made after accounting for propagation effects at the test site. The source coupling efficiency increased from 0.7-1.0% for the near-surface explosion to 1.5-2.9% for the fully contained.

This investigation has quantified the depth dependence of P and SV-Rayleigh arrivals from small explosions at near-source distances. Such depth effects might be observable at regional distances, but a set of controlled experiments to quantify these effects is not available. Regional data used to study depth effects usually include a variety of source types (explosions, earthquakes, quarry blasts). In addition, local structural variations may mask the source effects [Suteau-Henson et al., 1987]. The apparent sensitivity of  $R_g$  to source depth may be the regional equivalent of the SV-Rayleigh observa-

#### P and RAYLEIGH PERCENT OF TOTAL ENERGY vs DEPTH

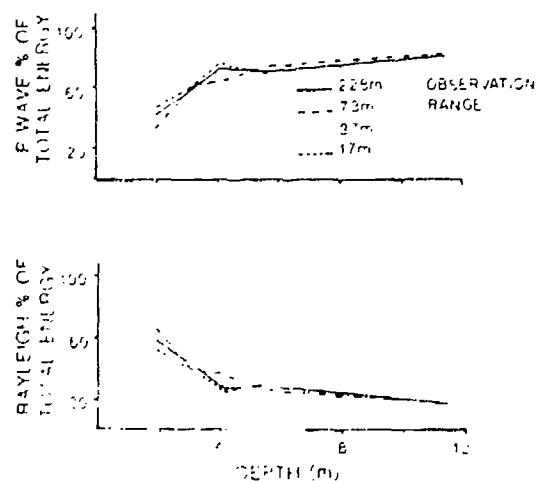


Fig. 19. Percentage P and SV-Rayleigh energy of the total seismic energy.

TABLE 4. Total Seismic Energy  $\times 10^{13}$

Depth, m	Range, m			
	17	37	73	228
1.0	1.53	0.79	0.57	0.55
3.2	1.20	1.10	0.91	1.05
10.0	0.93	0.94	0.72	0.87
37.0	1.70	1.30	0.85	1.11
228.0	-	-	-	-

Total, Total energy is  $1.5 \times 10^{13}$  ergs.

tions made in this study [Kafka, 1987]. As this small-scale study illustrates, such conclusions cannot be made quantitatively until both the source and propagation depth effects are carefully isolated.

#### Appendix

Rayleigh amplitude  $A_r$  is assumed to be a decaying function of depth,  $Z$ :

$$A_r = A \exp(-iksz)$$

where  $s = (c^2/b^2 - 1)^{0.5}$ ,  $k$  is the wave number,  $2\pi/\lambda$ , and  $A$  is a constant. Wavelength  $\lambda = cT$ , where  $c$  is phase velocity and  $T$  is period.

The Rayleigh wave front is approximated by a cylinder of height  $h$ . For a particular observation of SV-Rayleigh amplitude,  $A$ ,

$$\int_0^h A_r dz = Ah$$

where  $h$  is some depth given by

$$\begin{aligned} \int_0^h A_r dz &= \int_0^h A \exp(-iksz) dz \\ &= A/iks \exp(-iksz) \Big|_0^h \\ &= -A/iks \end{aligned}$$

Acknowledgments. The data for this study were made available by the Air Force Weapons Laboratory Civil Engineering Division. The work was supported under grant AFOSR-84-0016. Thanks to E. Herrin, J. Ferguson, R. Phillips, R. Reinke, and T. Sereno for reviews of the work.

#### References

- Butler, R., C. S. McCreery, L. N. Frazer, and D. A. Walker, High frequency seismic attenuation of oceanic P and S waves in the western Pacific, *J. Geophys. Res.*, 92, 1383-1396, 1987.  
 Dobrin, M. B., R. F. Simon and P. L. Lawrence, Rayleigh waves from small explosions, *Eos. Trans. AGU*, 32, 822-832, 1951.  
 Eisner, H. K., and H. Kanamori, Depth estimates of large earthquakes on the island of Hawaii since 1948, *J. Geophys. Res.*, 91, 2063-2076, 1986.

Flynn, E. C., Effects of source depth on near source seismograms, M.S. thesis, S. Methodist Univ., Dallas, Tex., 1986.

Kafka, A. L., Rg waves as a depth discriminant for earthquakes and explosions in New England, paper presented at the 9th Annual DARPA/AFGL Seismic Research Symposium, Air Force Geophys. Lab, Nantucket, MA, June 15-18, 1987.

Langston, C. A., Moments, corner frequencies, and the free surface, *J. Geophys. Res.*, 83, 3422-3426, 1978.

Meyer, R., Explosives, 2nd ed., Verlag Chemie, Weinheim, Federal Republic of Germany, 1981.

Mueller, R. A., and J. R. Murphy, Seismic characteristics of underground nuclear detonations, *Bull. Seismol. Soc. Am.*, 61, 1675-1692, 1971.

Perret, W. R., Seismic source energies of underground nuclear explosions, *Bull. Seismol. Soc. Am.*, 62, 763-774, 1972.

Perret, W. R., Seismic source energies of four explosions in a salt dome, *J. Geophys. Res.*, 78, 7717-7726, 1973.

Priestley, K. F., and D. E. Chazez, Apparent Q of Pg and Lg in the great basin, paper presented at the 9th Annual DARPA/AFGL Seismic Research Symposium, Air Force Cambridge Res. Lab, Nantucket, MA, June 15-18, 1987.

Stump, B. W., and R. E. Reinke, Spall-like waveforms observed in high-explosive testing in alluvium, AFWL-TR-82-15, Air Force Weapons Laboratory, Kirtland Air Force Base, N.M., 1982.

Suteau-Henson, A., T. Sereno, and T. Bacne, Spectral characteristics and attenuation of regional phases recorded at Norcess, paper presented at the 9th Annual DARPA/AFGL Seismic Research Symposium. Air Force Geophys. Lab., Nantucket, MA, June 15-18, 1987.

Wu, F. T., Part I, Lower limit of the total energy of earthquakes and partitioning of energy among seismic waves; Part II, Reflected waves and crustal structures, Ph.D. thesis, Calif. Inst. of Technol., Pasadena, 1966.

---

E. C. Flynn and B. W. Stump, Department of Geological Sciences, Southern Methodist University, Dallas, TX 75275.

(Received January 26, 1987;  
 revised September 10, 1987;  
 accepted September 22, 1987.)

# Bulletin of the Seismological Society of America

Vol. 78

June 1988

No. 3

## STOCHASTIC GEOLOGIC EFFECTS ON NEAR-FIELD GROUND MOTIONS IN ALLUVIUM

BY ROBERT E. REINKE AND BRIAN W. STUMP

### ABSTRACT

Analysis of accelerograms recorded at the 20 m range from a buried 5-lb detonation in alluvium revealed wide (as large as 20 dB in the amplitude modulus of the Fourier transform) variations in response for frequencies above 35 Hz. Additional experiments were performed which ruled out source asymmetry or instrumental irregularity as the cause of these variations. The observations suggest that scattering by geologic inhomogeneity is responsible for the frequency-dependent spatial variability in ground motion. A thorough understanding of the physical processes responsible for this variability requires that a quantitative relationship be established between the subsurface material property information and the observed ground motion characteristics. An attempt was made to do this using available standard penetration test data from the test bed where the initial experiment was detonated. Autocorrelations of the blow count data from the standard penetration test were computed and compared with theoretical exponential and Gaussian distributions. The exponential distribution with a scale length between 2.0 and 3.0 m best matches the data. Assuming the Born approximation, a scale length of 2.0 to 3.0 m implies that significant scattering should occur above 10 Hz. The recorded ground motions are, however, coherent out to about 35 Hz, suggesting a scale length on the order of 0.5 to 1.0 m, which is beyond the resolution of the standard penetration test technique. This scale length is, however, not unreasonable in light of the general geologic characteristics of the test area.

### INTRODUCTION

Several recent studies have found a surprising lack of coherence between ground motion waveforms recorded at stations separated by only a few tens of meters. McLaughlin *et al.* (1983) discuss the station-to-station waveform coherence for near-field explosion accelerograms recorded on a nine-station array at Pahute Mesa, Nevada Test Site. For this array, at a range of 6 km from a 5.6  $M_L$  underground explosion with an interstation spacing of 100 m, strong incoherent signals were found above 5 Hz on all components. This incoherence was attributed to scattering. Vernon *et al.* (1985) discuss earthquake seismogram coherence for a nine-station array with an interstation spacing of 50 m. This temporary array was located near the Pinon Flat observatory in California. Several events with magnitudes between 3.0 and 4.2 and hypocentral distances ranging from 10 to 50 km were analyzed. For this data set,  $P$  waves were found to be coherent up to the 25 to 30 Hz region, with  $S$  waves up to about 15 Hz. This variability in ground motion over such short distances raises questions about the appropriateness of using single-station point measurements of the ground motion

field for the inversion of source functions as well as the use of the peak ground acceleration statistic based on single-point measurements.

Smith *et al.* (1982) analyzed the near-field motions from the 1979 Imperial Valley earthquake. This data set was obtained from a closely spaced array of five stations. This study confirmed that incoherence of higher frequency ground motions could, because of averaging effects, reduce the high-frequency input to buildings with foundations of large areal extent. Analysis of this particular data set suggested that base-averaging reduction factors of 10 to 30 per cent would have occurred for foundations 50 m in diameter for frequencies above 20 Hz. No significant reduction would have occurred for frequencies below 5 Hz.

This frequency-dependent spatial variability in ground motion has also been observed on some small-scale, high-explosive tests conducted in dry alluvium. An array of six triaxial accelerometers spaced at six azimuths at the 20 m range from a buried 5-lb detonation yielded waveforms which were incoherent above 30 to 35 Hz. In an effort to determine whether these variations were induced by instrumentation, source asymmetry, or scattering due to geologic variability, a series of small-scale, high-explosive experiments were performed. This paper describes the results of these experiments and the physical interpretation of the data.

#### THE INITIAL EXPERIMENT—THE ART 2 TEST

The Array Test Series (ARTS) was a series of single and multiple 5-lb explosive tests conducted in dry alluvium. The ARTS was formulated, designed, and implemented to investigate the quantitative effects of finite explosive sources upon observed motion fields. The single-burst tests in the series were intended to thoroughly characterize the single-burst ground motion environment (Stump and Reinke, 1987). One of these tests, ART 2 (Table 1), was intended to determine the degree of azimuthal variation in ground motion levels resulting from a single-charge event. The experimental layout for this test is shown in Figure 1. Six triaxial servoaccelerometers were placed at the 20 m range at six different azimuths. These accelerometers were recorded by three-channel digital event recorders at a rate of 200 samplers/sec, with a 5-pole low-pass Butterworth filter at 70 Hz. The original accelerograms, along with low-pass (30 Hz corner) and high-pass (40 Hz corner) filtered versions, are shown in Figures 2 and 3. Fourier acceleration spectra for the waveforms are shown in Figure 4. Examination of the acceleration traces and the spectra in these figures reveals considerable similarity in the various waveforms below 30 Hz, while large azimuthal amplitude variations are observed for frequencies above 30 to 35 Hz. The accelerograms show that the high-frequency energy arrives after the initial coherent low-frequency response with a great variability in wave shape as well as amplitude. The vertical and radial spectral shapes (Figure 4) are similar between 5 and 35 Hz, while variations up to 15 to 20 dB occur above 35 Hz.

#### EXPERIMENTAL DESIGN

Three possible sources for the observed azimuthal variations in waveforms have been identified: (1) nonuniformity in instrumentation response; (2) asymmetry in the explosive source; and (3) geologic inhomogeneity. In order to experimentally investigate the first possibility—instrumental irregularity—the ART 19 test (Table 1), also called the *huddle* test, was performed. In this test, all 7 three-component accelerometers were placed in a closely spaced group at the 20

TABLE 1

## DESCRIPTION OF EXPERIMENTS

Experiment	Description
ART 2	Single 5-lb charge buried at 1 m. Recording array showed 6 triaxial accelerometers at different azimuths at the 20 m range.
ART 19	"Huddle test." Single 5-lb charge buried at 1 m recorded by 6 triaxial accelerometers in a closely spaced group at the 20 m range.
ART II	The "pit shots." Series of five 5-lb buried charges all fired at the same ground zero and recorded by 6 triaxial accelerometers spaced at equal azimuths at the 20 m range. The initial charge was detonated <i>in situ</i> ; subsequent charges were fired in a sand-filled pit.
ART III-2	Single 5-lb buried charge recorded by 6 accelerometers at the 10 m range and 6 accelerometers at the 30 m range. Accelerometers were spaced at equal azimuths.

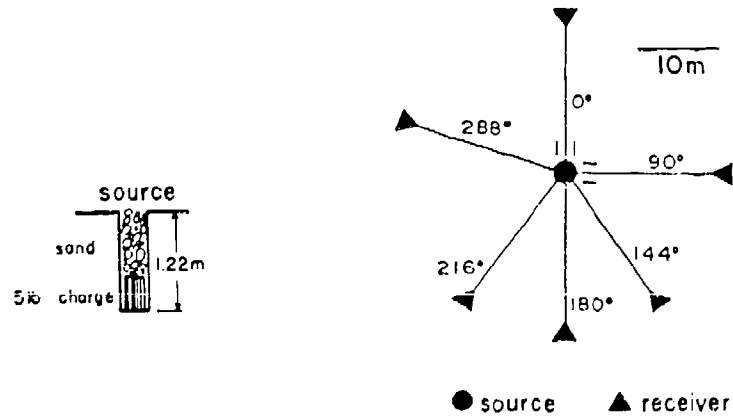


FIG. 1. Experimental layout for the ART 2 test event

m range (Figure 5) from a 5-lb charge detonated at a depth of 1 m. Individual vertical and radial spectra from this test are compared in Figure 6. The resulting spectral scatter, as observed in these figures, is at most 3 to 4 dB over the band from 5 to 70 Hz, much less than that observed for the azimuthal data. In fact, the higher frequency scatter (40 to 70 Hz region) shown in these figures may not reflect true instrumental irregularity, since, as seen by examination of Figures 5 and 6, the accelerometers which are physically closest in the field do possess the greatest degree of similarity in spectral shape.

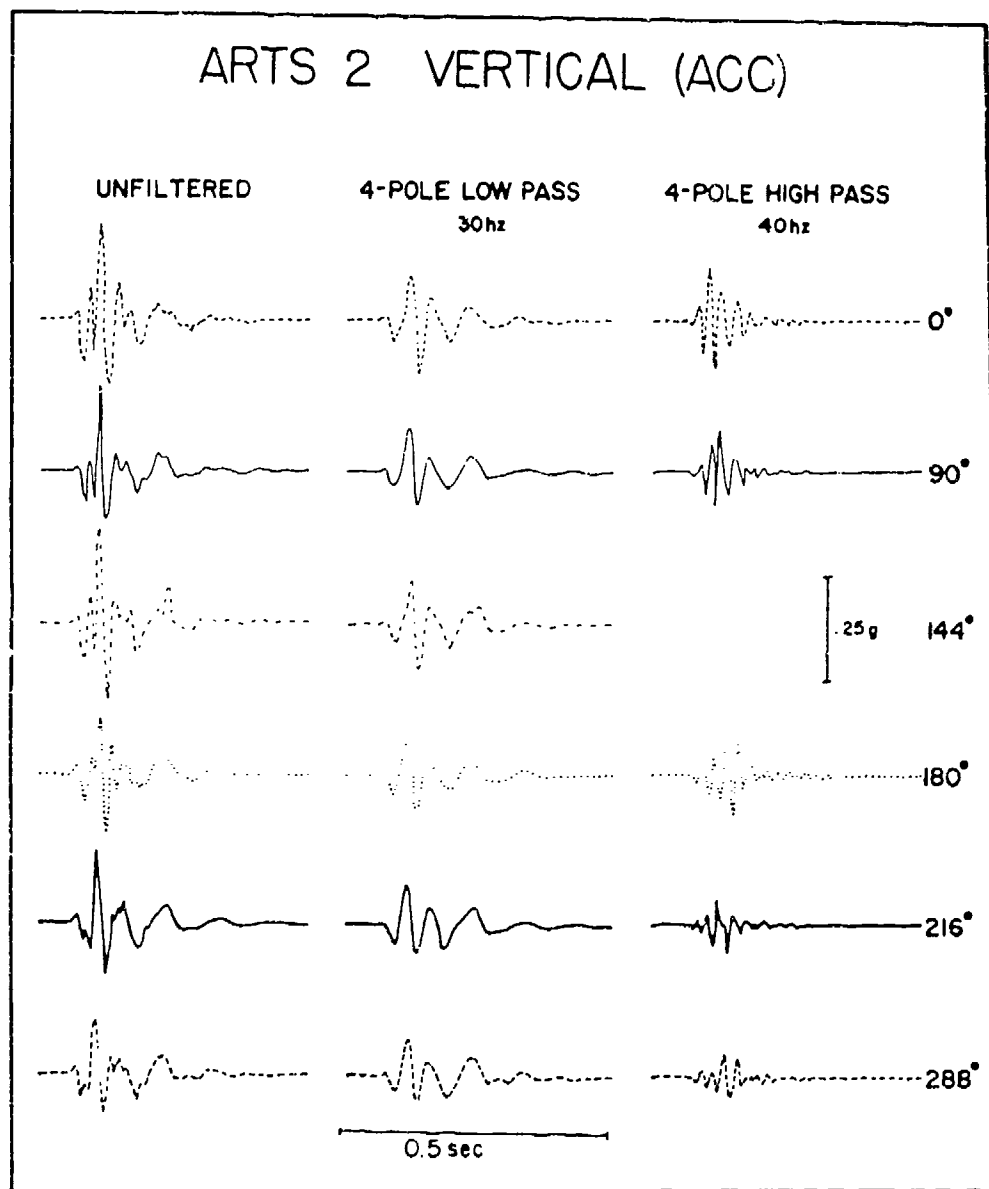


FIG. 2. Filtered vertical acceleration records from ART 2. Record length is 0.5 sec.

An additional set of experiments, the ART II series (Table 1), was designed to determine whether azimuthal irregularities in ground motion result primarily from propagation path variations and scattering by geologic inhomogeneity or explosive source asymmetry. The test bed layout for the ART II tests is shown in Figure 7. Ground motions were recorded by triaxial servoaccelerometers and three-channel digital event recorders at six equally spaced azimuths at a range of 20 m. The ART II series of tests consisted of four separate 5-lb detonations—all fired at the same test bed with the accelerometers remaining in the same position from shot to shot. The initial detonation was fired at a depth of 1 m *in situ*. The resulting crater was then excavated and a new 5-lb charge emplaced in the resulting pit with uniform sand rained around the charge. This process

was repeated a total of four times. Thus, the ART II series of tests consisted of five shots, one *in situ* and four pit shots—all using the same test bed and an identical recording array.

The goal of the ART II tests was to determine whether source asymmetry or geologic factors were the dominant cause of the observed scatter. By repeating the experiment five times at the same location, five sets of triaxial accelerograms and spectra were obtained for each azimuth. If the observed data scatter were produced by geologic inhomogeneity, then one would expect very similar acceleration waveforms, as well as amplitude spectra, to be observed from shot to shot.

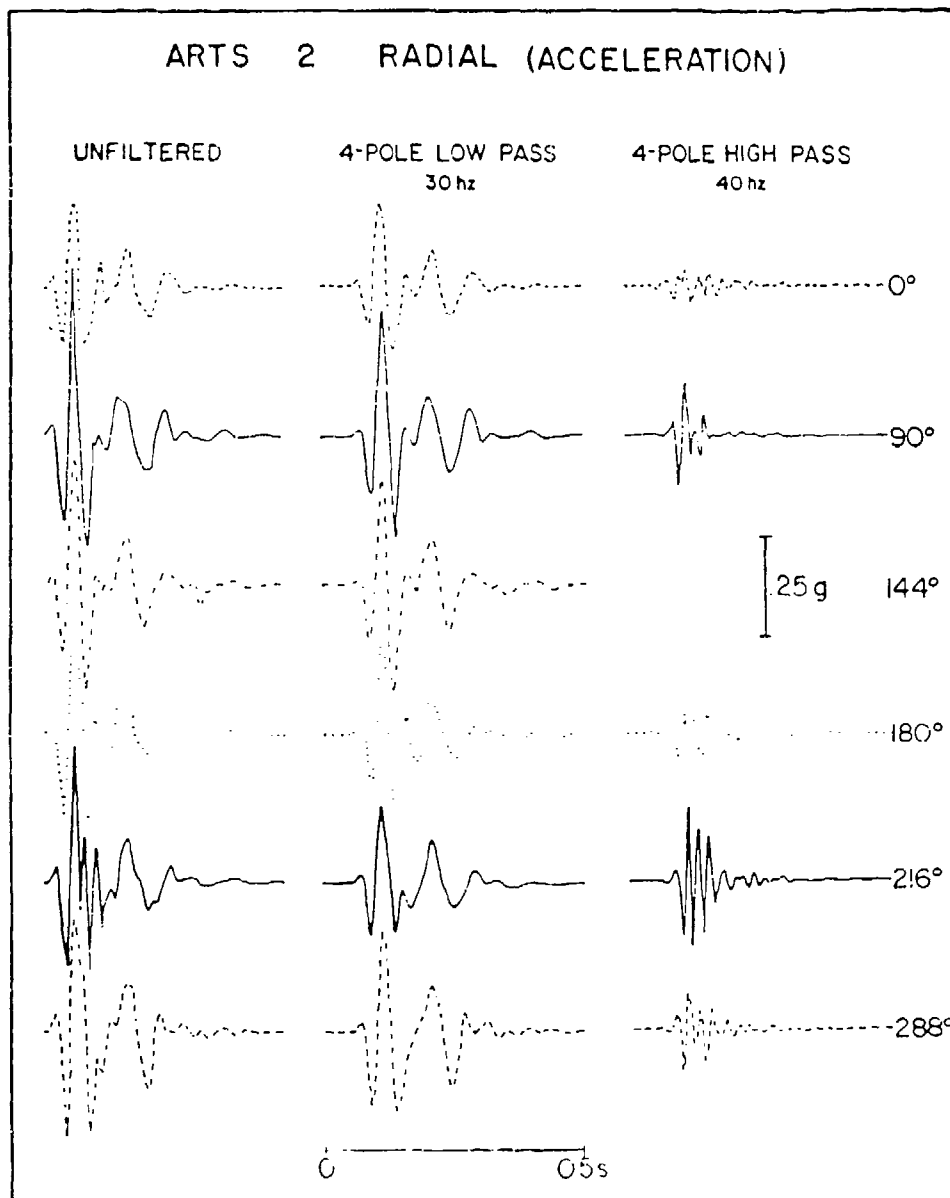


FIG. 3. Filtered radial acceleration records from ART 2. Record length is 0.5 sec.

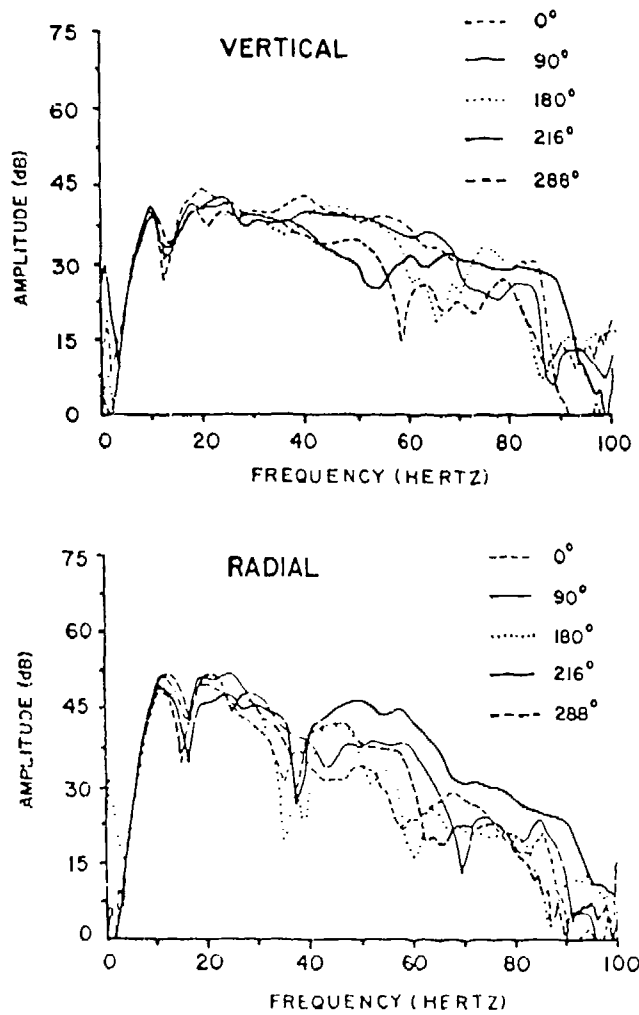


FIG. 4. Vertical and radial Fourier acceleration spectra for ART 2.

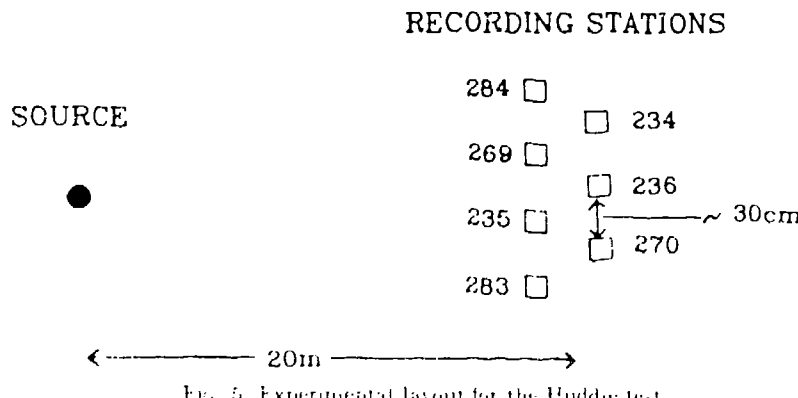


FIG. 5. Experimental layout for the Huddle test.

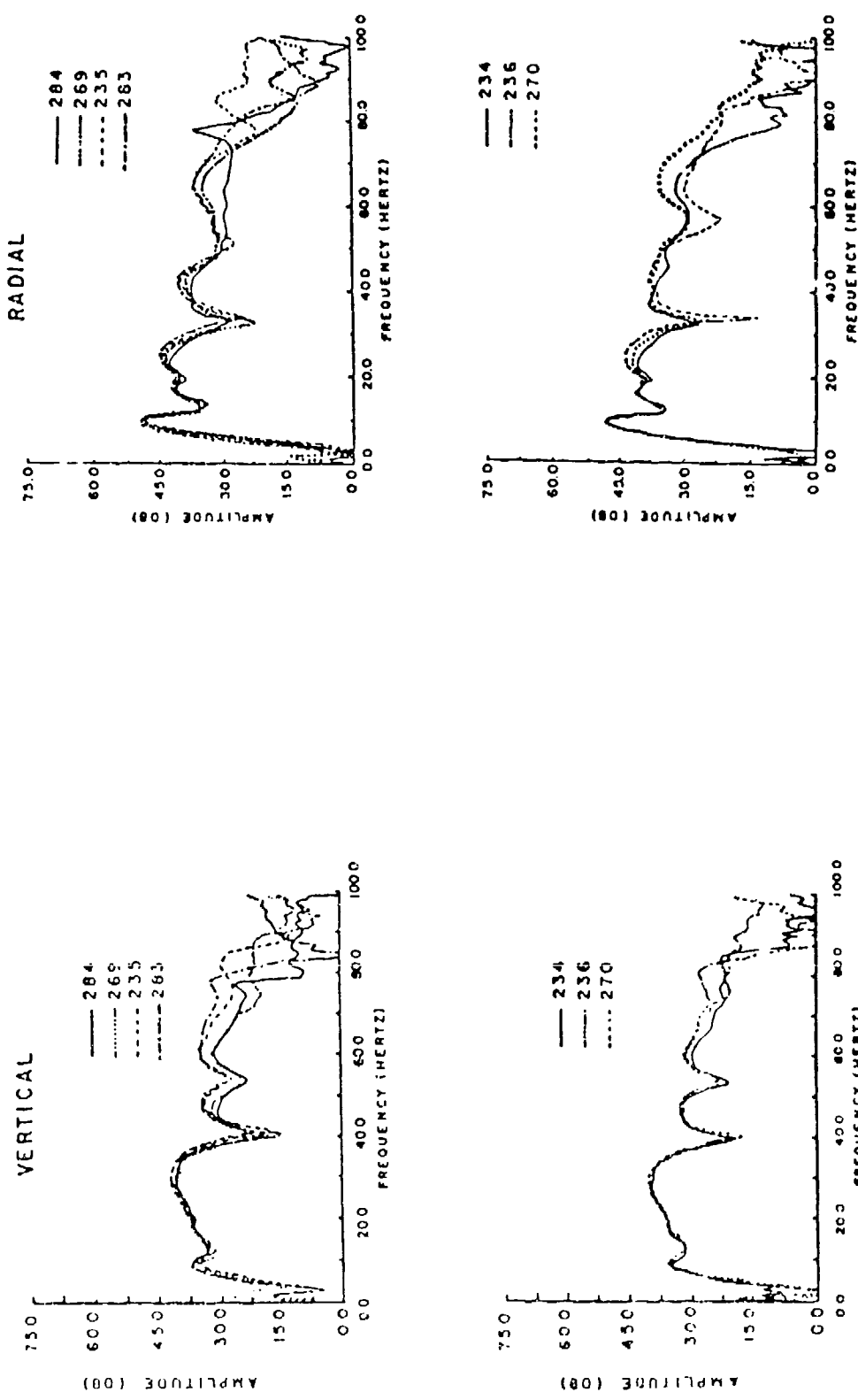


FIG. 6. Vertical and radial Fourier acceleration spectra from the Huddle test.

▲ 302

▲ 300

▲ 299

▲ 301

▲ 284

▲ 269

● source

▲ receiver

FIG. 7. Test-bed layout for the ART II tests.

at the same recording station. The detonation of a 5-lb charge is, of course, not strictly a repeatable phenomenon, since the initial *in situ* detonation destroys a portion of the test bed by formation of the crater. Excavation of the severely disturbed material comprising the crater and subsequent emplacement of the charge within the pit was intended to make the experiment as repeatable as possible. The transition from the *in situ* test to the pit sequence was the most severe. The *in situ* shot produced a crater roughly 2.2 m in diameter. The crater was excavated, producing a pit about 3 m in diameter and 1.3 m deep. The dimensions of both crater and pit increased slightly with each shot. The final pit was about 3.5 m in diameter and the final crater about the same diameter.

While the ART 2 and the ART Phase II (the pit shots) experiments investigated azimuthal ground motion variations at the 20 m range, the ART III-1 experiment (Table 1) was designed to investigate the influence of range upon the observed azimuthal variations. If scattering by geologic inhomogeneity is the dominant factor producing the azimuthal variation, then one might expect the degree of variation to increase with range of the receiver array. The ART III-1 test consisted of a 5-lb cylindrical charge detonated *in situ* at a depth of 1 m. The ground motions were recorded at a total of 12 locations using triaxial servoaccelerometers and three-channel digital event recorders. Six recording stations were placed at equal azimuths at the 10 m range, and the remaining six were placed at equal azimuths at the 30 m range.

#### STOCHASTIC DETERMINISTIC CLASSIFICATION TOOLS AND DATA ANALYSIS

One approach to quantify the observed variation in the data sets is to compute the coherency between station pairs in a manner analogous to that employed by

McLaughlin *et al.* (1983). The coherency is defined by

$$\gamma_{xy}(\omega) = \frac{|\dot{\phi}_{xy}(\omega)|}{(\dot{\phi}_{xx}(\omega) \cdot \dot{\phi}_{yy}(\omega))^{1/2}}$$

where  $\dot{\phi}_{xy}(\omega)$  is the cross-power spectrum.  $\dot{\phi}_{xx}(\omega)$ ,  $\dot{\phi}_{yy}(\omega)$  are the power spectra of the two time series, and  $\omega$  is the circular frequency. As is well known, smoothing must be applied to the spectra prior to estimation of the coherency in order to minimize variances at each frequency. For the coherency estimates computed here, a 4-point lag window was applied to the spectra prior to estimation of the coherency factors.

Coherencies were computed between the 0° data and each of the other recording stations. The time windows used were 128 samples or 0.64 sec in length. This length window encompasses all of the wave train. At this relatively short range, it is effectively impossible to separate the various components of the waveform.

The computed coherencies for the station pairs are shown in Figure 8. The coherence factors for the vertical and radial components are higher than might be intuitively expected after examination of the spectral plots in Figure 4. However, as Smith *et al.* (1982) point out, the coherency will be unity when the signals at two stations are related by any linear transfer function, so the coherence function is not a direct estimator of the variation of amplitude across an array.

Based upon the results of the coherency analysis, an alternate approach for analysis of the data was taken. The set of amplitude spectra of the azimuthal observations was treated as a statistical ensemble. An example of this technique applied to the ART 2 data is shown in Figure 9. The mean and variance of the spectral ensemble were calculated as shown assuming a log-normal distribution. These figures illustrate  $\mu$  (the mean) and  $\mu \pm \sigma$  (the mean  $\pm$  1 s.d.) for the vertical, radial, and transverse data from ART 2. The vertical and radial data show small standard deviations between 5 and 30 Hz. Beyond 35 Hz, the width of the deviation band increases until at 40 Hz the expected scatter in the Fourier modulus is 8 dB or greater. The transverse motions, on the other hand, show at least 8 dB scatter throughout the entire frequency band; although the overall mean amplitude is reduced about 10 dB from the radial and vertical amplitude levels.

The lack of coherence below 5 Hz on all components has several possible sources. This effect was first thought to be due to signal-induced tilts in the accelerometers. Integration of the acceleration traces and subsequent attempts to correct the resulting velocity and displacement records did not significantly change the estimates. It is likely that aliasing and/or noise is the cause of this low-frequency incoherence. The amplitude level in this region is very low relative to the higher frequencies. Even a small amount of aliased energy would significantly affect the apparent coherence in this region which is well below the corner frequency of the 5-Hz source. At higher frequencies, the aliased energy level is insignificant relative to the amplitude of the direct source energy.

Another measure of the data scatter in the frequency domain is the coefficient of variation (CV) (Bethea *et al.*, 1985). The CV is the ratio of the standard deviation to the mean ( $CV = \frac{\sigma}{\mu}$ ). CVs for the ART 2 spectra are given in Figure 10. For ART 2, the CV on the radial and vertical components increases with frequency (CV = 0.5 from 5 to 30 Hz), the transverse component CV remains

## COHERENCE WITH 0° DATA

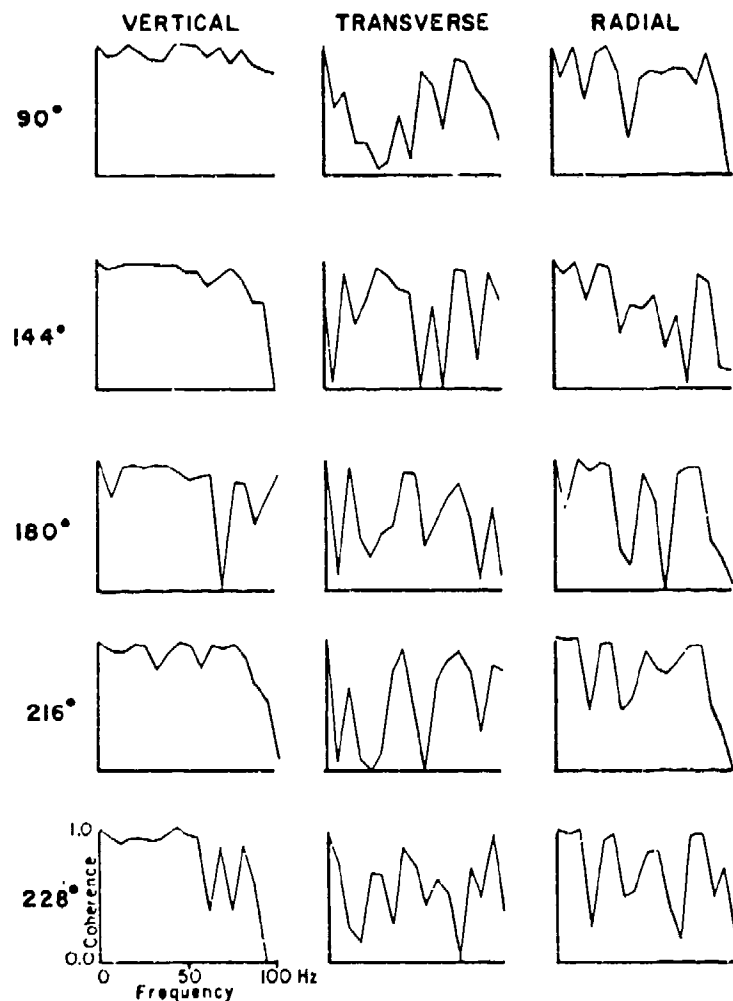


FIG. 8. Computed coherencies for ART 2.

approximately constant at a relatively high level ( $>0.5$ ) across all frequencies, suggesting that the transverse component is uncorrelated at all frequencies. By way of contrast, Figure 11 shows the very low values of the CV between 5 and 60 Hz for the radial and vertical components of the Huddle (ART 19) test. The advantage of the CV as an estimator of the data scatter across the array is that all stations in the array may be used in the single estimate as opposed to only a pair of stations in the coherence estimate.

Amplitude spectra of the vertical acceleration waveforms recorded at the 0° azimuth for all five of the ART II pit shots are compared in Figure 12. The sets of spectra recorded at the other azimuths and the other components are similar in character to the 0° vertical test. The four pit shot spectra are quite similar in shape and amplitude, while the *in situ* shot spectrum exhibits a shape which is

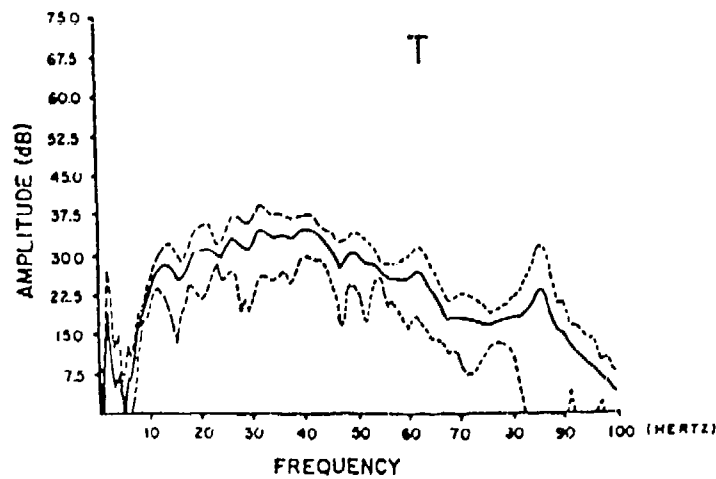
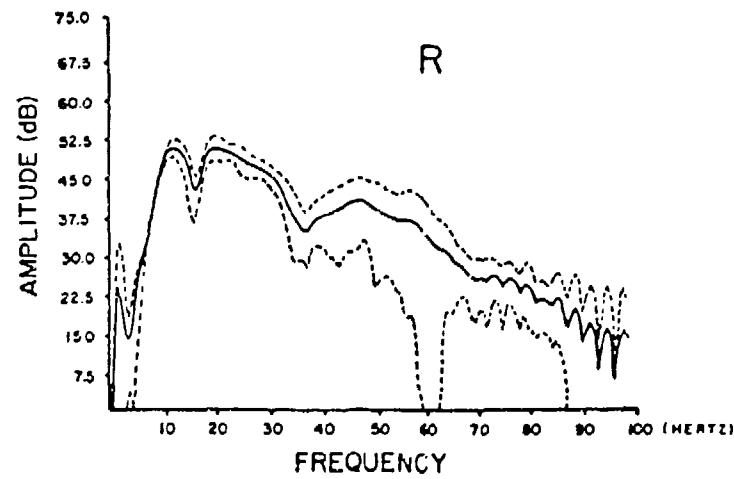
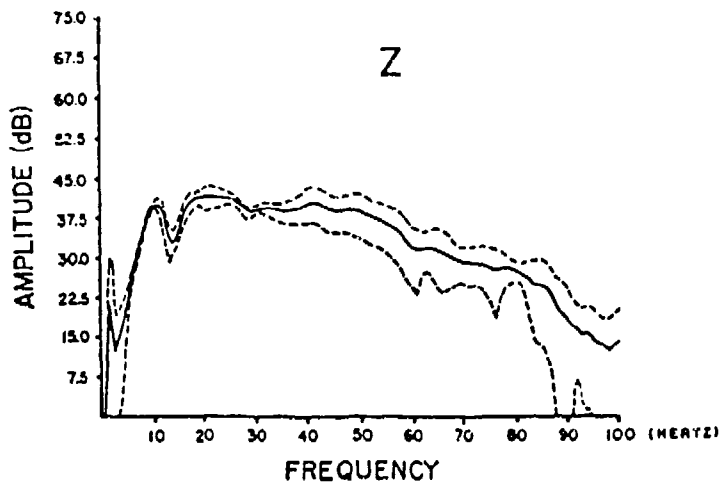


FIG. 9. The mean ( $\mu$ ) (solid line) and the mean  $\pm$  1 s.d. ( $\mu \pm \sigma$ ) (dotted lines).

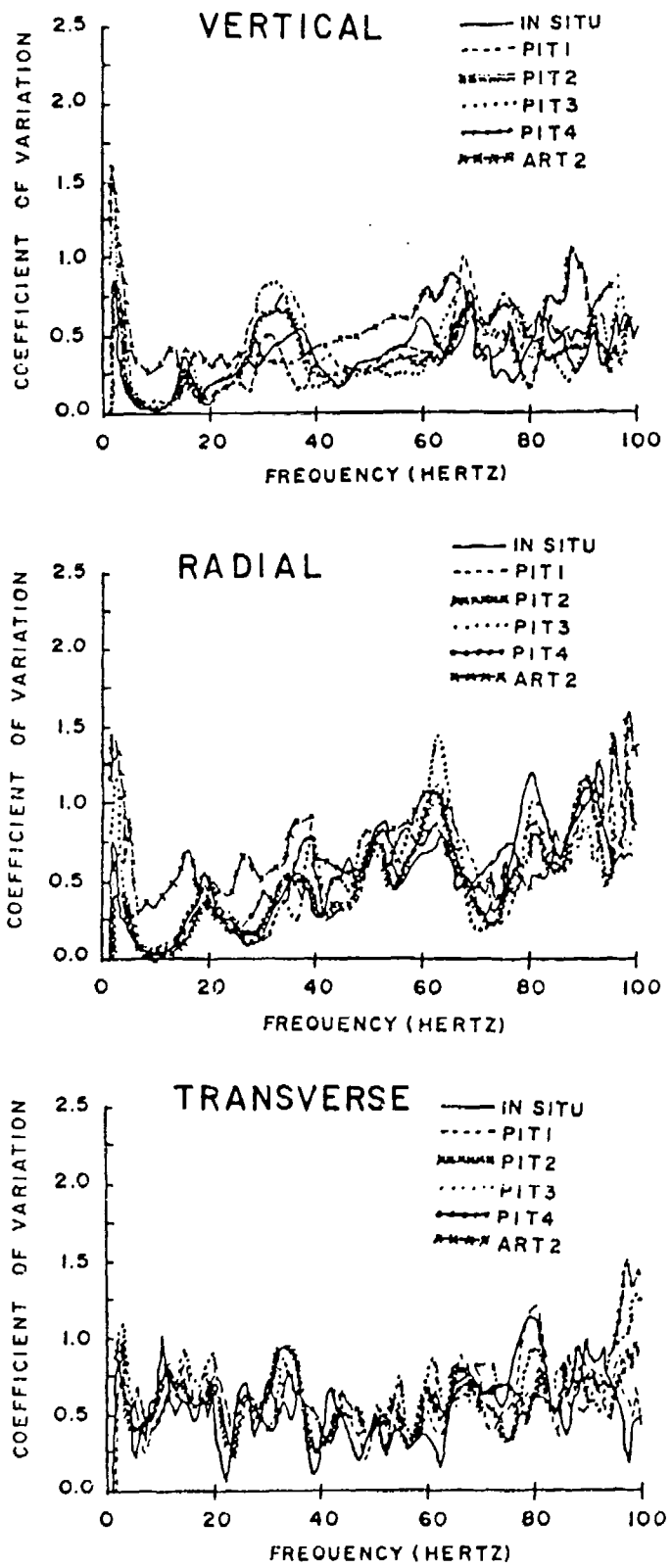


FIG. 10. Spectral CV curves for the ART II pit shots compared with ART 2.

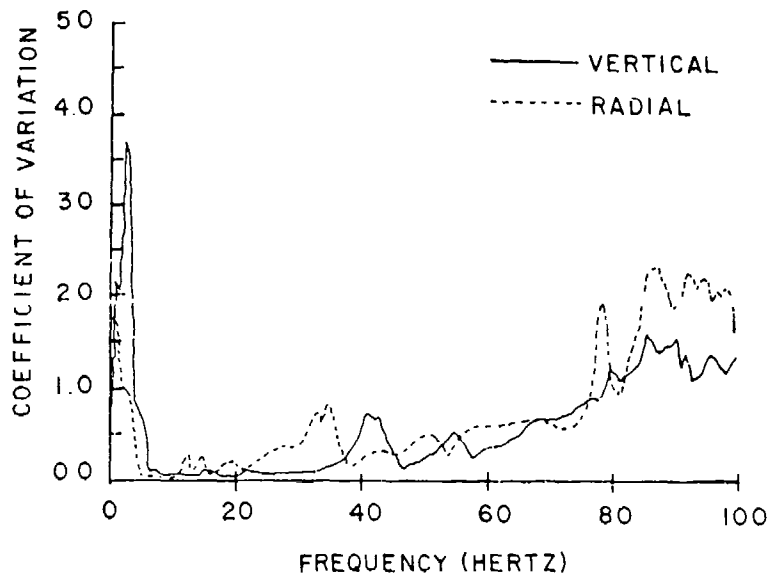


FIG. 11. Spectral CV curves for the vertical and radial components of the Huddle test.

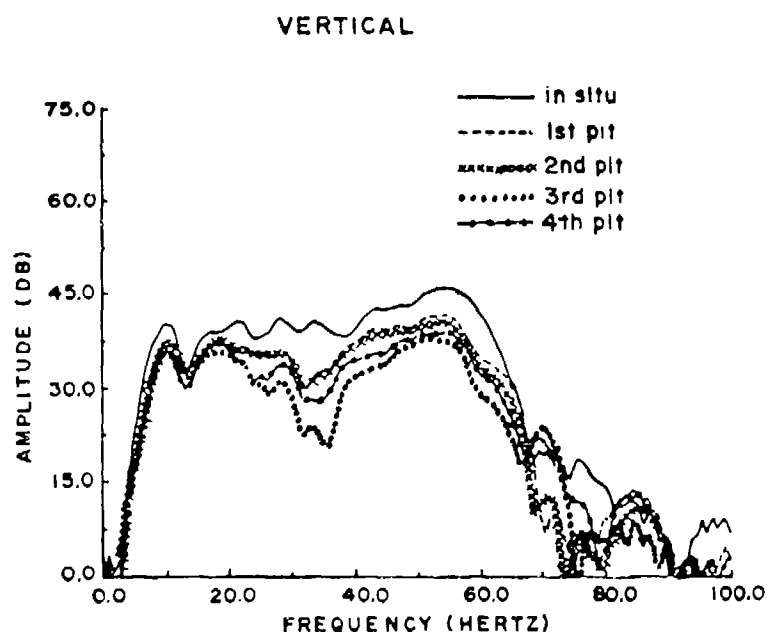


FIG. 12. Comparison of vertical acceleration spectra for the five shots of the ART II series.

similar to that of the pit shot spectra, but higher in amplitude for almost all frequencies. Two of the pit shots are almost identical in the frequency domain; pit shots 3 and 4 also group closely together over most of the frequency band. The greatest change in amplitude from shot to shot occurs in the 30 to 35 Hz region. This area of the spectrum is fairly flat for the *in situ* shot; however, a spectral hole develops for the pit shots which deepens with each successive pit shot. Even though the shape of the source spectrum may change from shot to

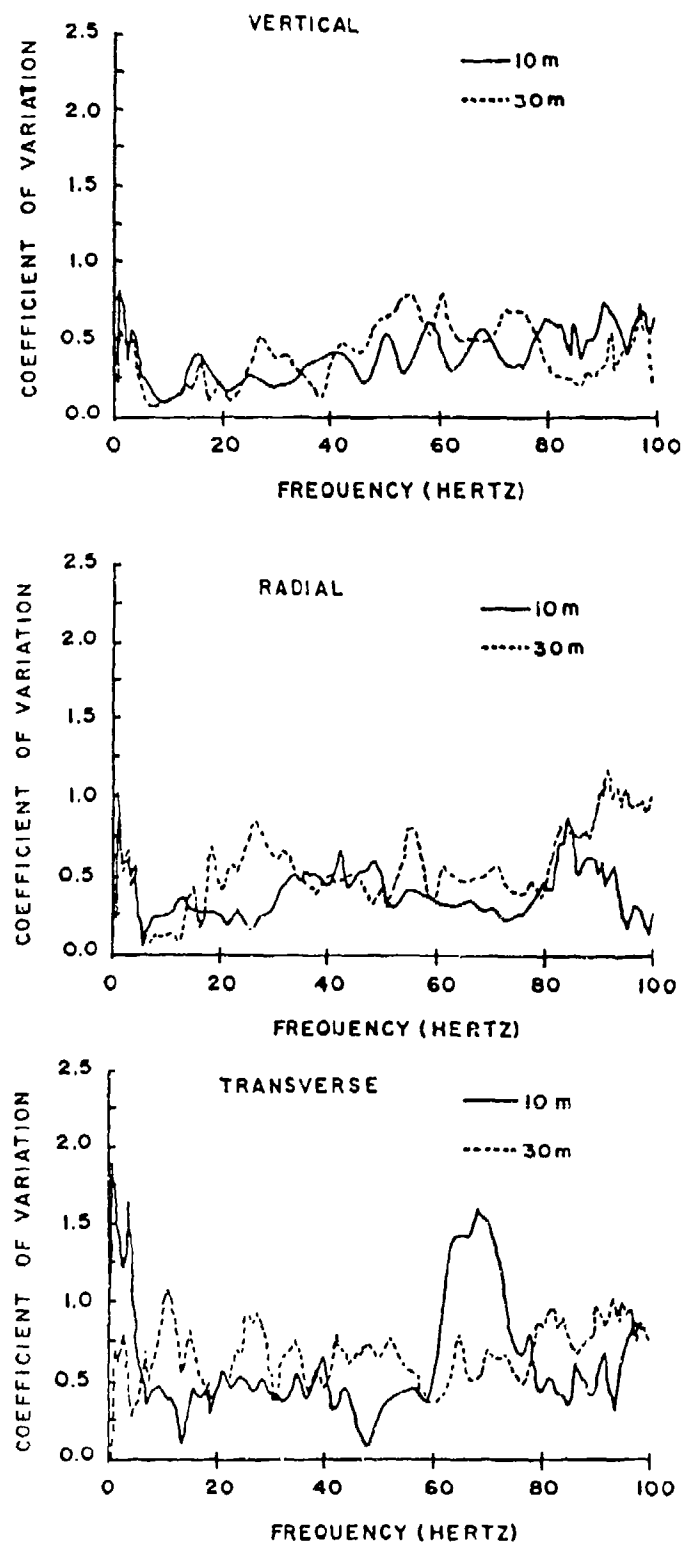


FIG. 13 Comparison of 10 and 30 m CV curves for ART III-2.

shot, which is to be expected since introduction of the backfilled cavity results in more energy lost in cratering, greater attenuation and a larger cavity, the CV should change very little if the source remains cylindrically symmetric for all shots. Figure 10 shows the azimuthal CV plotted as a function of frequency for the vertical, radial, and transverse components, respectively, for all five shots. The normalized standard deviation curves are very similar for all five shots out to the system antialias filter at 70 Hz. The CV curves from ART 2, which was conducted near the pit shot site but on a different test bed, are also plotted in this figure. The change in the CV curves between the two sites is much larger than the variation from shot to shot for the pit shot sequence. The relatively small scatter in the CV curves for the five events of the pit shot sequence (the *in situ* shot plus the four pit shots) suggests that source asymmetry plays an unimportant role in the development of the azimuthal variation in ground motion response.

The ART III-2 (Table 1) shot was designed to determine the degree to which azimuthal variation increases with range from the source. In this test, ground motions were recorded by circular arrays at both the 10 and 30 m ranges. CV plots for the vertical, radial, and transverse spectra for both the 10 and 30 m ranges are given in Figure 13. These results support the contention that the CV increases with range.

#### RELATION OF OBSERVED AZIMUTHAL VARIABILITY TO TEST SITE GEOLOGY

The tests discussed in this paper were conducted at the same test site in the Rio Grande Valley south of Albuquerque, New Mexico. The subsurface geology consists of dry alluvium down to the water table at a depth of approximately 75 m. The site lies in a small shallow basin which in earlier times contained a playa. In general, the site is underlain by unconsolidated eolian sands, alluvium, and lacustrine deposits 15 to 30 m thick. Beneath this material are the tertiary Santa Fe and Galisteo formations, 180 to 300 m thick (Bedsun, 1983). A typical near-surface P-wave velocity section is shown in Figure 14 (Stump and Reinke, 1982).

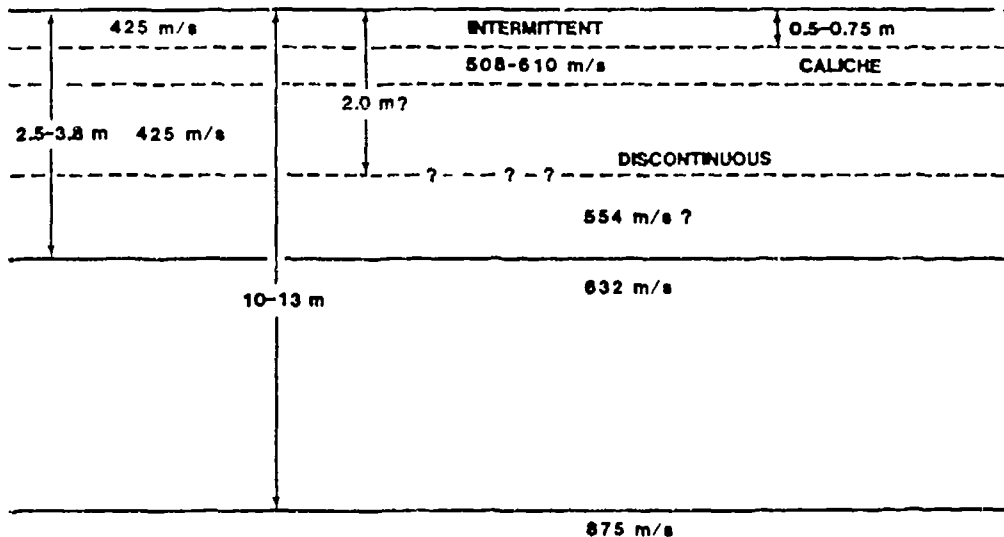


FIG. 14. Generalized geologic cross-section of McCormick Ranch.

Near-surface deposits are fairly variable with intermittent caliche beds present. Trenching at other test sites in the area has revealed discontinuous subsurface caliche beds typically on the order of 0.5 to 1.0 m in thickness (Stump and Reinke, 1982). In an effort to quantify the nature of the subsurface variability at the ART 2 test site, 18 boreholes were drilled within the confines of the test bed (as shown in Figure 15). Each borehole was drilled to depth of 6.1 m. Standard penetration tests were performed in each hole. The standard penetration test involves determining the number of hammer blows required to drive a sampling tube a unit distance. This blow count is related to the *in situ* density and compressive strength of the subsurface material (Terzaghi and Peck, 1967). Figure 16 displays the blow counts per meter for each borehole down to the 6 m depth. Figure 15 contains isopach maps showing the lateral distribution of the areas of similar blow counts as a function of depth.

A thorough understanding of the physical processes responsible for the observed azimuthal variability in the ART 2 test requires that a quantitative relationship be established between the subsurface material property information and the observed ground motion characteristics. Aki and Richards (1980) present such a relationship. Following Chernov (1960), they characterize the statistical nature of geologic media by the autocorrelation of the velocity fluctuation.

#### PENETRATION TEST - ARTS

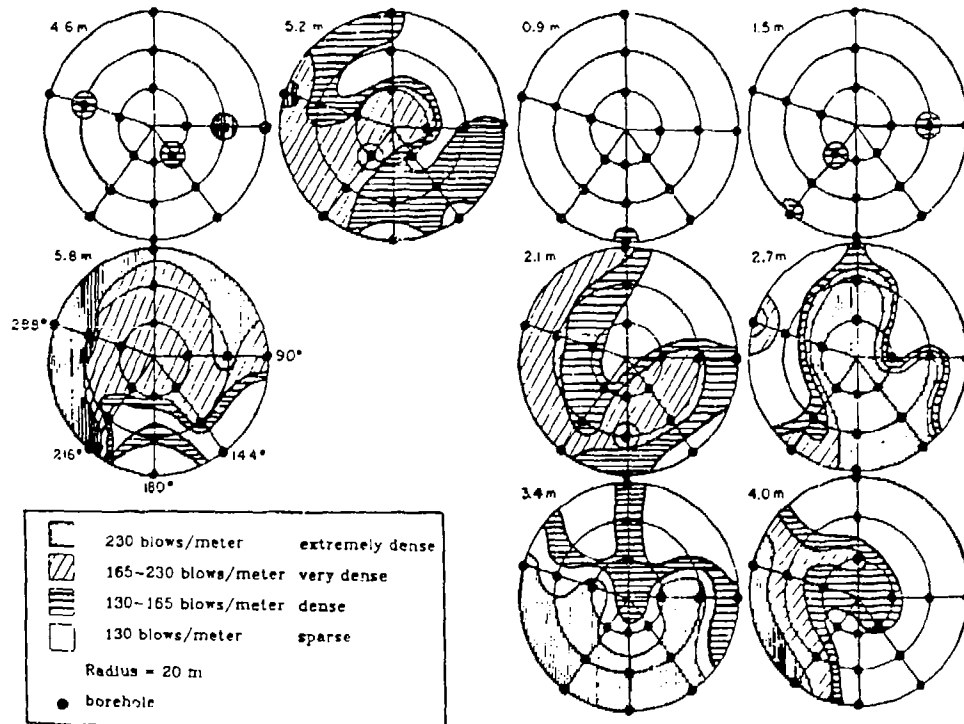


FIG. 15. Layout of boreholes within the ART 2 test bed and isopach map of blow counts

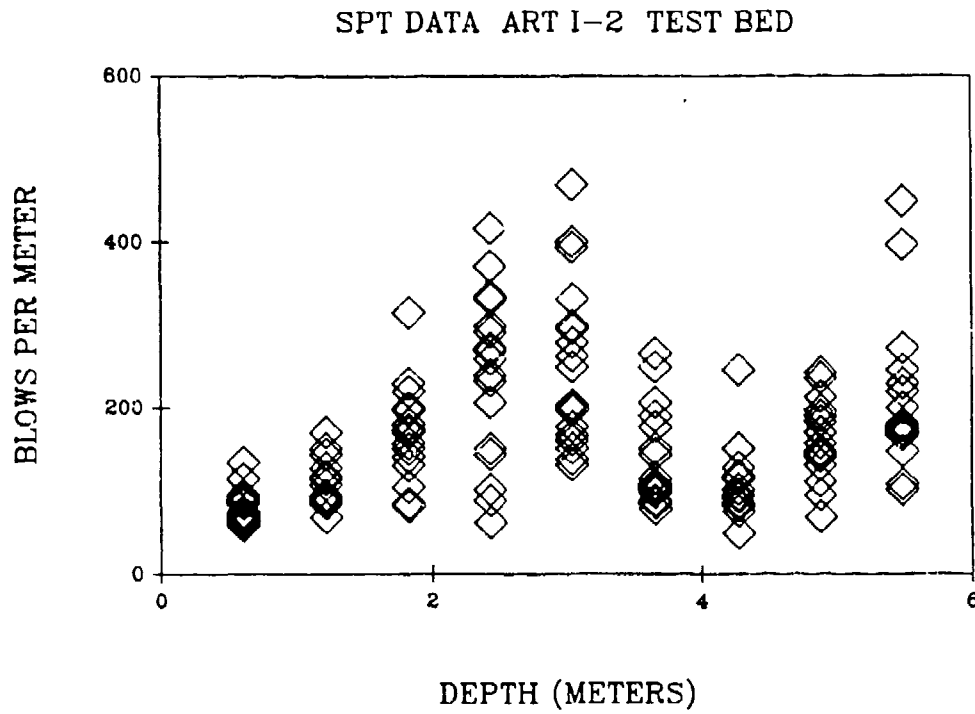


FIG. 16. Plots of blow counts versus depth (data points from all 18 boreholes are included.)

For  $\mu = -\delta C/C_0$ , where  $C_0$  = velocity, the normalized autocorrelation function is defined by

$$N(r) = \langle \mu(r') \cdot \mu(r' + r) \rangle / \langle \mu^2 \rangle$$

where  $r$  denotes position.

Two statistical distributions are considered

1. the exponential distribution:  $N(r) = e^{-r/a}$
2. the Gaussian distribution:  $N(r) = e^{-r^2/a^2}$ .

The quantity  $a$  is the measure of scale length of the medium inhomogeneity called the correlation distance.

Once a medium is described statistically in terms of  $N(r)$ , then the Born scattering approximation may be used to determine the strength of the scattering as a function of frequency for the medium. The Born approximation assumes that the primary waves are unchanged by propagation through a scattering medium so that energy conservation is violated. Only single scattering is considered. Following Aki and Richards (1980), the ratio of scattered energy to total energy is given as follows

$$\delta I/I = 8\langle \mu^2 \rangle \cdot k^4 \cdot a^3 \cdot L \quad \text{for } ka < 1, \text{ and}$$

$$\delta I/I = 2\langle \mu^2 \rangle \cdot k^2 \cdot a \cdot L \quad \text{for } ka > 1$$

where  $\delta I/I$  is the ratio of scattered energy to the total energy carried by the wave,  $\langle \mu^2 \rangle$  is the average of the square of the velocity perturbation,  $k$  is the wavenumber,  $a$  is the scale length or correlation distance of the medium, and  $L$  is the length of the travel path.

Making the assumption that there is a linear correlation between the blow count value at a particular point and the  $P$ -wave velocity at the same point, we shall attempt to relate the observed azimuthal variability in the ART 2 data with the blow count data using the scattering theory discussed previously. The mean was computed for the set of blow count data for all of the holes. This yields a mean value of 50 blows/0.30 m. This value was treated as  $C_0$  in the scattering equations. The autocorrelation function was then computed of the following ratio:  $(BC_i - \bar{BC})\bar{BC}$ , where  $BC_i$  is the individual blow count value, and  $\bar{BC}$  is the mean value of all blow counts. The autocorrelation functions were computed separately for each hole.

Values of the autocorrelation functions of the blow count data for all of the holes are plotted in Figure 17. Also plotted in Figure 17 are several theoretical autocorrelation functions for different values of the correlation length  $a$ , for both the Gaussian and exponential distributions. Based on examination of these plots, the theoretical distribution function which best fits the data is apparently an exponential function with a scale length between 2.0 and 3.0 m. This scale length applies, of course, only to the vertical distribution of inhomogeneities. The horizontal inhomogeneity scale length could well be different in character. The horizontal spacing of the boreholes ( $\approx 6.7$  m) is much too wide to allow any sort of reasonable estimate of the horizontal scale length. (This spacing yields a Nyquist wavelength of 13.4 m.)

Using the Born equations, the ratio of scattered energy to total energy ( $\delta I/I$ ) was computed for the ART 2 test bed using several values of the inhomogeneity scale length as shown in the plots in Figure 18. The  $ka \ll 1$  case is appropriate for most of the frequency-scale length combinations under consideration here. The  $ka \gg 1$  case is appropriate for scale lengths greater than 2 m in the higher frequency region ( $> 20$  Hz). Both curves indicate that, for scale lengths of 2.0 to 3.0 m, significant ( $\delta I/I > 0.10$ ) scattering begins near 10 Hz. Significant scattering in the ART 2 test data occurs above 30 to 35 Hz (Figure 4). There are several possibilities for this apparent poor correlation: (1) the Born approximation is valid only for small values of scattered energy; (2) the autocorrelation function which was derived pertains only to the vertical distribution of inhomogeneity and thus the scale length which is appropriate for the overall propagation medium could be considerably different from 2.0 to 3.0 m; (3) a finer spatial sampling of the near surface blow count values might well yield a smaller scale length; and (4) the assumed correlation between blow count data and  $P$ -wave velocity may be incorrect.

To determine the effect of varying the scale length upon the theoretical scattered energy,  $\delta I/I$  as a function of frequency was computed for correlation lengths of 1.0, 0.5, and 0.25 m (Figure 18). For these scale lengths, the frequency at which scattering becomes significant is in the 25 to 30 Hz region. This result, particularly the 0.5 curve, correlates much better with the observed threshold of amplitude fluctuation in the ART 2 test. A correlation scale length in the neighborhood of 0.5 to 1.0 m is also not unreasonable in light of the results of the "Huddle" test (ART 19) in which all of the instrumentation was placed in a group approximately 1 m in width (Figure 5). Examination of the spectra from this test

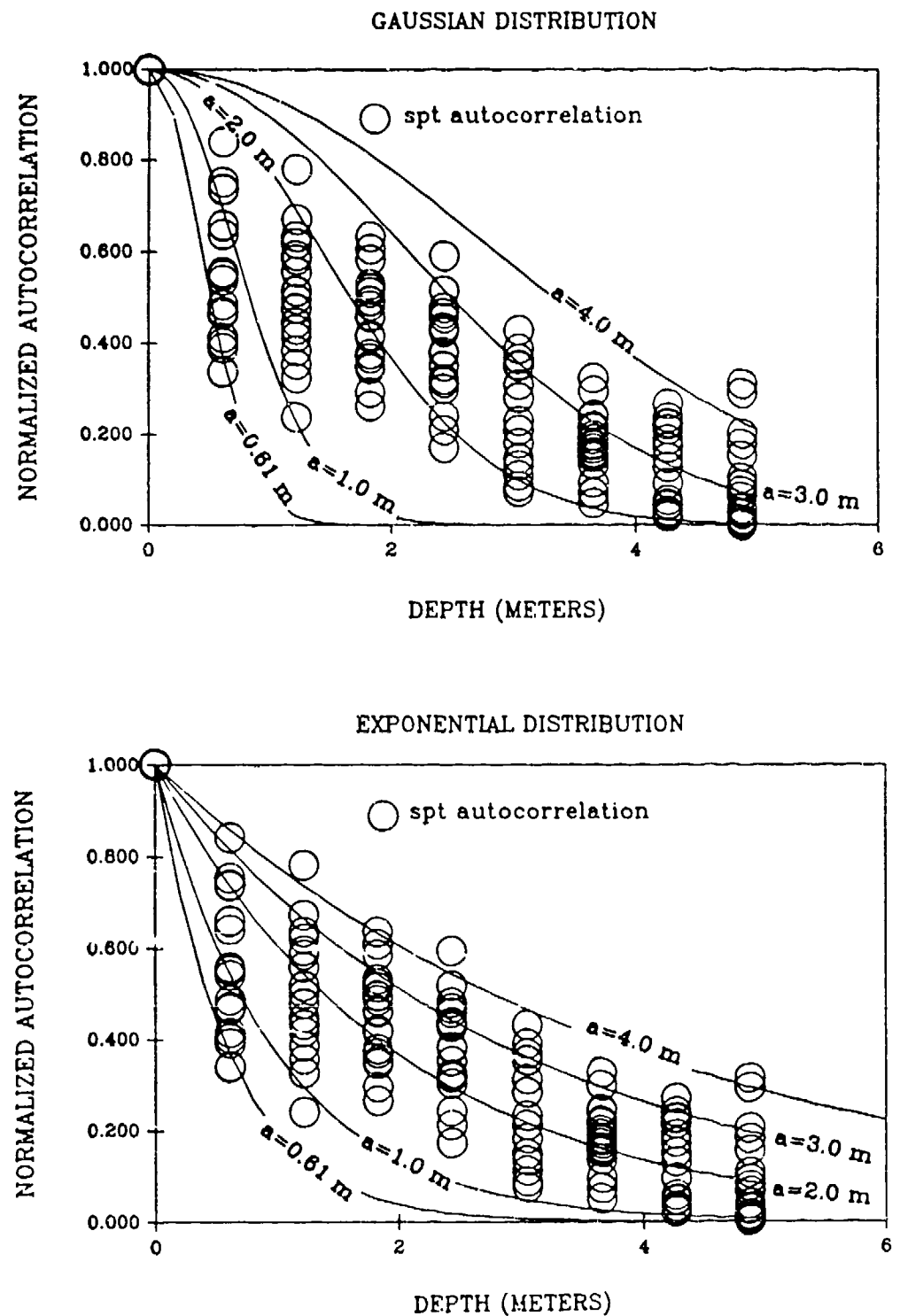


FIG. 17. Experimental autocorrelation function compared with Gaussian and exponential autocorrelation functions. The lines on the plot are the theoretical autocorrelation functions. The experimental autocorrelation functions from all holes are represented by data points. spt = standard penetration test.

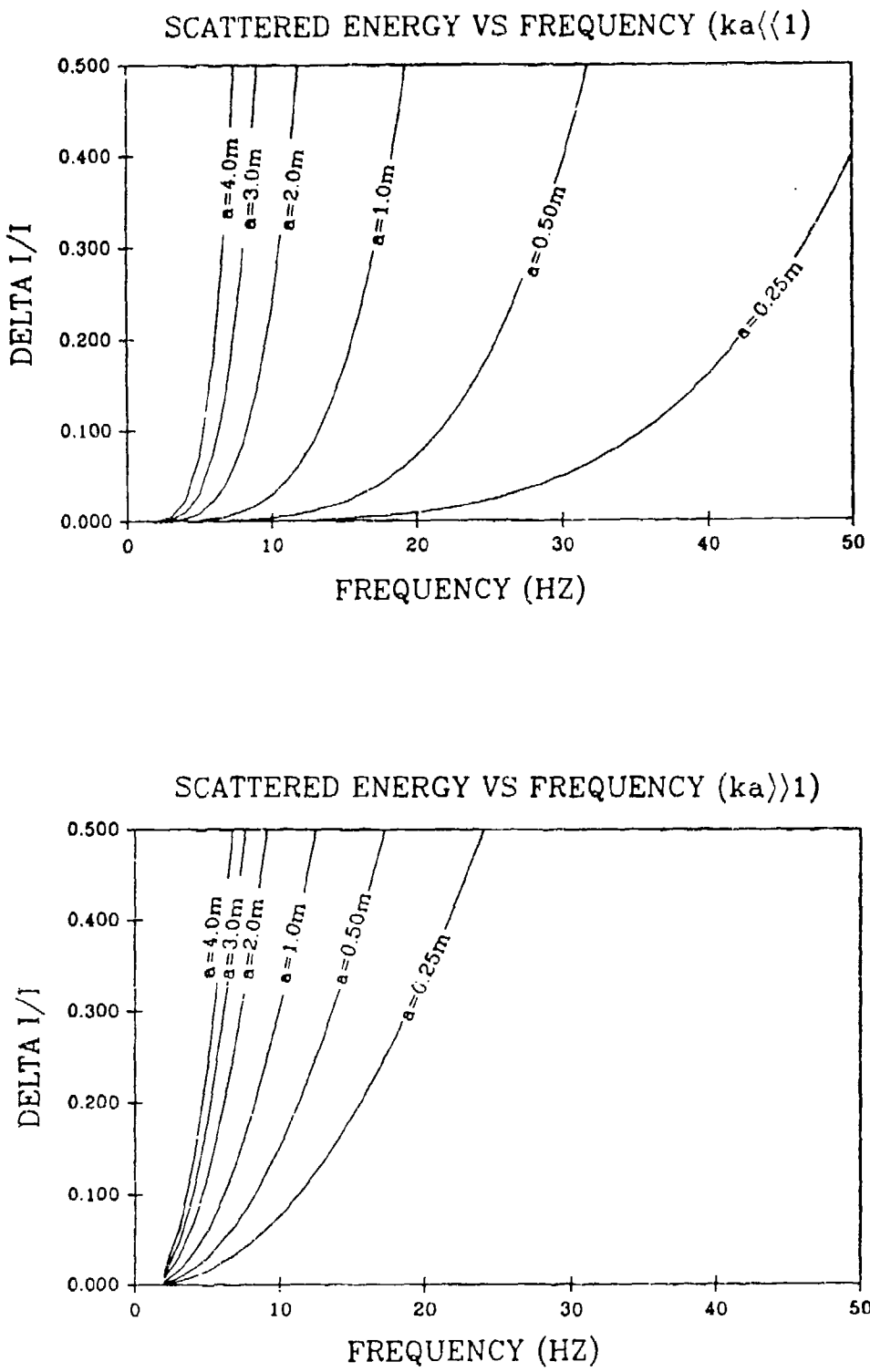


FIG. 18 Plot of scattered energy as a function of frequency for different scale lengths.

in Figure 6 reveals that the spectra of the endmost instruments separated by a distance of approximately 1 m begin to diverge, whereas the spectra from instruments spaced more closely correlate very well. Shallow trenching in the general test site area suggests that a typical caliche bed thickness is on the order of 0.5 to 1.0 m, although a typical lateral extent may be slightly greater (Stump and Reinke, 1982).

This simple forward model indicates that the azimuthal variability in the ART 2 data can be explained with a scattering model based upon the Born approximation. The implication is that the particular standard penetration test array did not properly characterize the appropriate scale length due to inadequate horizontal or vertical spatial sampling, since blow count values were obtained by counting the number of blows required to drive the sampling tube a distance of 0.6 m. This sample interval yields a Nyquist wavelength of 1.2 m.

#### DISCUSSION AND CONCLUSIONS

The results of the ART experiments have shown, at least for this particular alluvial test site, that the predominant cause of azimuthal variation in ground motion response is inhomogeneity in near-surface geologic material rather than very near-source asymmetry. Considering that this particular site in general is thought to have a fairly uniform near-surface geologic composition, the degree of azimuthal variation observed from these small tests is fairly remarkable. Experiments of this type should be performed at several sites to further constrain the relationship between the spectral CV and the variation in the geologic structure. Such surveys will aid greatly in the interpretation and understanding of ground motion data from small-scale field tests. It is clear that, for a small-scale test performed at the ART 2 site, deterministic interpretations of the data cannot be made above the 30 to 35 Hz region. CV surveys could also place limitations upon the interpretation of near-source, regional, and teleseismic measurements of earthquakes and explosions made at a single point. These surveys may be useful in explaining the lack of coherence between individual station pairs in small seismic arrays, such as the Pinon Flat array (Vernon *et al.*, 1985).

In this study, an initial attempt was made at relating the available subsurface information at the ART 2 site with the observed waveform variation in the test. This attempt was not very successful, probably due to insufficient spatial resolution of the subsurface sampling performed. Forward modeling argues that the scale lengths which are present in the ART 2 test bed are perhaps on the order of 0.5 to 1.0 m rather than 2.0 to 3.0 m, as determined from the autocorrelation of the standard penetration test blow count data. Use of other sampling techniques, such as the seismic cone penetrometer test (in which the force necessary to drive a rod into the ground is measured and a geophone in the rod tip is used to perform a velocity survey), could enable much finer spatial resolution to be obtained both horizontally and vertically, allowing a greatly improved characterization of the random properties of the medium.

#### ACKNOWLEDGMENTS

Funding for these experiments was provided by the Air Force Weapons Laboratory Independent Research Program under Projects ILIR8207 and ILIR8414. Additional support was provided by The Air Force Office of Scientific Research through Grant AFOSR-84-0016 to Southern Methodist University.

## REFERENCES

- Aki, K. and P. Richards (1980). *Quantitative Seismology: Theory and Methods*, W. H. Freeman and Company, San Francisco, California, 2 volumes, 932 pp.
- Bedsun, D. (1983). Summary of geotechnical testing and material models for subsurface soil conditions at McCormick Ranch, Kirtland AFB, New Mexico, Letter Report, NMERI 7.11-TA7-20.
- Bethea, R., B. Duran, and T. Boullian (1985). *Statistical Methods for Engineers and Scientists*, Marcel Dekker, Inc., New York, 698 pp.
- Chernov, L. (1966). *Wave Propagation in a Random Medium*, McGraw-Hill, New York, 168 pp.
- McLaughlin, K., L. Johnson, and T. McEvilly (1983). Two-dimensional array measurements of near-source ground accelerations, *Bull. Seism. Soc. Am.* **73**, 349-376.
- Smith, S. W., J. Ehrenberg, and E. Hernandez (1982). Analysis of the El Centro differential array for the 1979 Imperial Valley Earthquake, *Bull. Seism. Soc. Am.* **72**, 237-258.
- Stump, B. and R. Reinke (1982). Spall-like waveforms observed in high explosive testing in alluvium, AFWL TR-82-15, Air Force Weapons Laboratory, Kirtland Air Force Base, New Mexico, 122 pp.
- Stump, B. and R. Reinke (1982). Spall-like waveforms observed in high explosive testing in alluvium, AFWL TR-82-15, Air Force Weapons Laboratory, Kirtland Air Force Base, New Mexico, 122 pp.
- Stump, B. and R. Reinke (1987). Experimental confirmation of superposition from small-scale explosions, *Bull. Seism. Soc. Am.* **78**, 1059-1073.
- Terzaghi, K. and R. Peck (1967). *Soil Mechanics in Engineering Practice*, John Wiley and Sons, New York, 729 pp.
- Vernon, F., J. Fletcher, L. Haar, T. Bolswick, E. Sembera, and J. Brune (1985). Spatial coherence of body waves from local earthquakes recorded on a small aperture array (abstract), *EOS, Trans. Am. Geophys. Union* **66**, 954.

AIR FORCE WEAPONS LABORATORY NTESG  
KIRTLAND AIR FORCE BASE, NEW MEXICO 87117-  
6008 (R.E.R.)

SOUTHERN METHODIST UNIVERSITY  
DEPARTMENT OF GEOLOGICAL SCIENCES  
DALLAS, TEXAS 75275 (B.W.S.)

Manuscript received 4 February 1987

## EXPERIMENTAL CONFIRMATION OF SUPERPOSITION FROM SMALL-SCALE EXPLOSIONS

BY BRIAN W. STUMP AND ROBERT E. REINKE

### ABSTRACT

An *in situ* experimental program in alluvium is implemented and analyzed to test linear superposition. After separating stochastic and deterministic propagation path effects, direct superposition is experimentally validated at 20 m for two 5-lb charges spaced as close as 2 m in alluvium. The charges are separated by the scaled range of  $147 \text{ m}/\text{kt}^{1/3}$  and observed at the scaled range of  $1470 \text{ m}/\text{kt}^{1/3}$ . Finite-spatial source effects are observed and simulated in the plane passing through two charges separated by 2 to 10 m. The deterministic single-burst waveforms are used to model the multiple-burst data. The effects observed and simulated include direct superposition below the corner frequency, shift to lower corner frequency with increasing charge separation, and spectral scalloping. For charges closely spaced (up to 4 m, observed at 20 and 24 m), the primary effect on the waveform is replicated by a constant delay time between two identical waveforms. For charges spaced by 10 m (observed at 20 and 30 m), the effects of propagation path differences must be included. These effects result in smoothed spectra.

### INTRODUCTION

The effect of finite sources on radiated wave fields has received considerable attention from the earthquake source community. Such work has increased the understanding of source phenomenology while improving the ability to estimate ground motions from broad classes of earthquake sources. Finite-explosive array effects have received far less attention within the seismological literature.

The primary focus of this study is the investigation of finite-spatial source effects from chemical explosions. In particular, the interaction of deterministic and stochastic wave propagations with the source characterization problem will be discussed. Evidence supporting linear superposition will be shown. The assumption of linear superposition leads to a predictive capability.

Spatial arrays of chemical explosions are used in a number of different fields. The mining industry uses arrays of explosives in both open-pit and subsurface excavation. The spatial distribution of charges and timing of their detonation are used to control the extent of material excavated, the size of the rubble, and the far-field ground motion levels (Bergman *et al.*, 1974; Hagan and Just, 1974; Winzer, 1978). The majority of work in this area has dealt with laboratory and field data, resulting in the development of practical relationships for explosive array design (Winzer and Ritter, 1980; Winzer *et al.*, 1981; Anderson *et al.*, 1982). Little theoretical work or numerical modeling of these effects has been completed. This type of investigation has not been necessary, since the properly scaled experiments in the materials of interest can be conducted.

The second area where arrays of explosives are employed is in the simulation of ground motions from earthquakes (Bleisweis, 1973; Higgins *et al.*, 1978). Although data from natural events are available, the recurrence interval of great earthquakes has retarded the development of adequate natural data sets. Where site-specific data are required and the historical data base is absent, explosive

simulation of earthquake environments may help refine loads on engineering structures.

Since the onset of the above ground test ban treaty, the utilization of high explosive arrays in simulating ground motion environments from nuclear explosions has been the only way to exercise engineering structures (Cooper, 1970). These studies have focused upon regions where the stress-strain relations are apparently nonlinear. The spatial and temporal dimensions of the source are adjusted to produce motion environments with prescribed amplitudes and pulse widths.

In each of the three previous applications of explosive arrays, the focus has been upon the near-source wave field. The radiated energy from these explosive arrays in the far-field is of interest to the community responsible for discriminating earthquakes from explosions. In the advent of a comprehensive test ban treaty, one would have to be able to discriminate between a mining blast which might be as large as several hundred thousand pounds of explosives and a low-yield nuclear explosion. Quantification of the effects of arrays of chemical explosions may aid in this discrimination. Preliminary work in this area has been completed by Greenhalgh (1980). A complete understanding of the problem relies upon relating the near-source models and data to the far-field environment.

The investigation of superposition from *in situ* experiments is of interest as it relates to the intermediate stress level response of the media. The distance at which the transition from linear to nonlinear response occurs has been questioned by a number of investigators (Trulio, 1978; Larson, 1982; Minster and Day, 1986). Larson (1982) reports that linear superposition holds in the plane of symmetry from two small charges in salt in the laboratory (range of  $168 \text{ m} \cdot \text{kt}^{1/3}$ ).

The approach to finite-explosive arrays reported here relies on a characterization of the single-burst ground motion. The specific quantification used is from Reinke and Stump (1987), referred to as Paper I. In that work, the single burst is experimentally quantified, with consideration given to source symmetry, propagation path, and scattering. The wave field is experimentally divided into a deterministic and stochastic component, with the deterministic component utilized in predictions. Practically, the single-burst quantification is completed in both the time and frequency domains, yielding mean and variance estimates.

The single-burst source quantification is used to test for linear superposition with multiple-burst experimental data. This model is used to explore finite-spatial source effects in the observational data base.

#### EXPERIMENTAL DESIGN AND IMPLEMENTATION

The experiments are summarized in Figure 1. The 5-lb charges were placed in 1.22 m holes with a diameter of 0.15 m. Charges were placed at the bottom of the hole. The holes were then backfilled with sand.

Force-balance accelerometers were used as sensors. The three components (housed in a single case) were oriented in the radial (positive away), transverse (positive clockwise), and vertical (positive up) directions with respect to the source. The case was buried in the alluvium so that its top was flush with the free surface. Paper I reports the good coherence between 1 and 70 Hz observed when all instruments were placed side-by-side in a Huddle test. The accelerometer outputs were passed through a 12-bit analog to digital converter in the field and recorded on cassette tape with a sample rate of 200 samples/sec. A five-pole antialias filter was placed at 70 Hz.

## EXPERIMENTAL LAYOUT

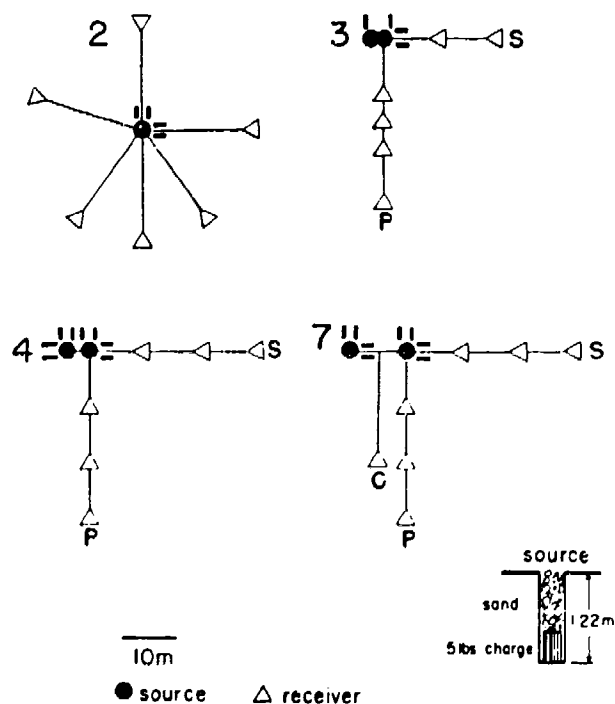


FIG. 1. Gauge layout for ARTS 2, 3, 4, and 7. The solid lines indicate crater diameters. (In ARTS 3, the two craters overlapped, leaving only a single, elongated crater.) Charge placement is illustrated in the lower left-hand corner.

The test site was chosen for its apparent homogeneity and consisted of dry alluvium. Further discussion of its properties are given in Paper I.

As reported in Paper I, a number of single-burst experiments were conducted to characterize the source and media with offsets between 10 and 30 m. The finite-source data focused upon the two explosion cases, since this data can be used to constrain the basic characteristics of source interaction. As Figure 1 illustrates, charge separation was varied between 2 and 10 m at 2 m increments. The proximity of the charges to the free surface (1.22 m) resulted in significant venting to the free surface at detonation and the formation of craters. Ground motion from the airblast arrival was not perceptible in the data due to the 1.22 m source burial depth. Crater diameters are given as the solid lines bounding the charge locations in Figure 1 and were typically near 2 m. ARTS 3 produced a single, elongated crater since the lateral charge separation was only 2 m.

Gauge arrays for the two explosion tests can be separated into two categories. The first set of gauges (primary or center) were placed at right angles to the plane passing through the charges. These gauge lines intersected either the midpoint between the two charges (center) or one of the charges (primary) and were emplaced to check direct superposition. The second set of gauges (secondary) were placed in the plane of the charges, and thus the effects of source finiteness were

maximized by the travel path and time differences between the two sources (Figure 1).

#### SUMMARY OF SINGLE-BURST CHARACTERIZATION

In order to check linear superposition and quantify the effects of spatial finiteness, the single explosion source and wave propagation to a variety of distances must be quantified. ARTS 2 in Figure 1 is one such test designed to quantify the single source and propagation. A complete discussion of the single source is given in Paper I. The time-domain records from ARTS 2 are given in Figure 2. When the records are low-pass filtered at 30 Hz, they appear identical to one another. The high-pass filtered records show significant variation above 40 Hz. A variety of tests were conducted and reported in Paper I to quantify the cause of these high-frequency amplitude variations. Strong evidence supported scattering within the geological media as the cause of this variation.

This realization led to the calculation of mean and variance estimates for the waveforms from a single explosion. Figure 3 is the mean  $\pm$  1 s.d. spectra for the 20 m range from the single burst. Figure 4 is a similar representation, but in the time domain.

#### ARTS 2 VERTICAL (ACC)

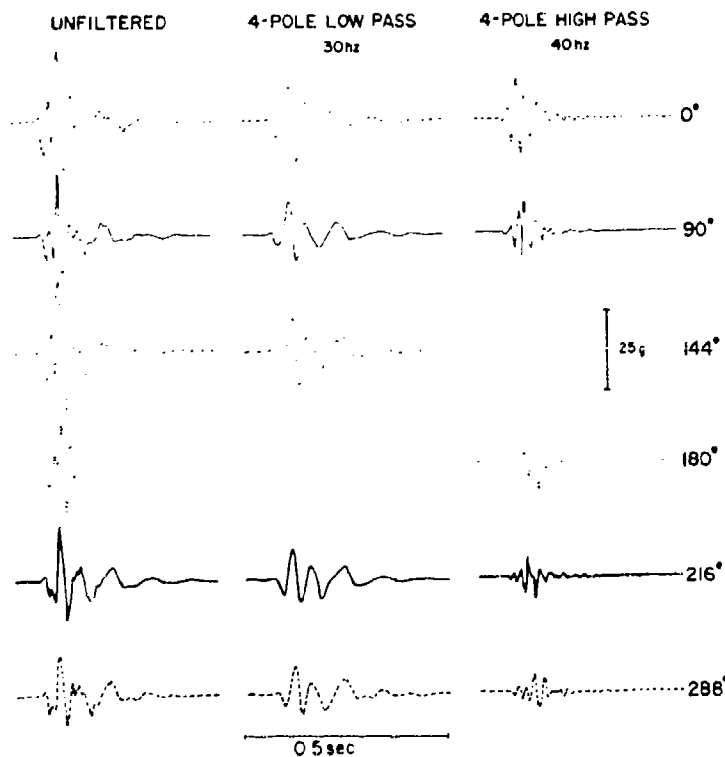


FIG. 2. The vertical acceleration records from ARTS 2. All gauges are at 20 m, and azimuths range from 0° to 288°. Unfiltered, low-pass filtered (30 Hz), and high-pass filtered (40 Hz) accelerograms are given.

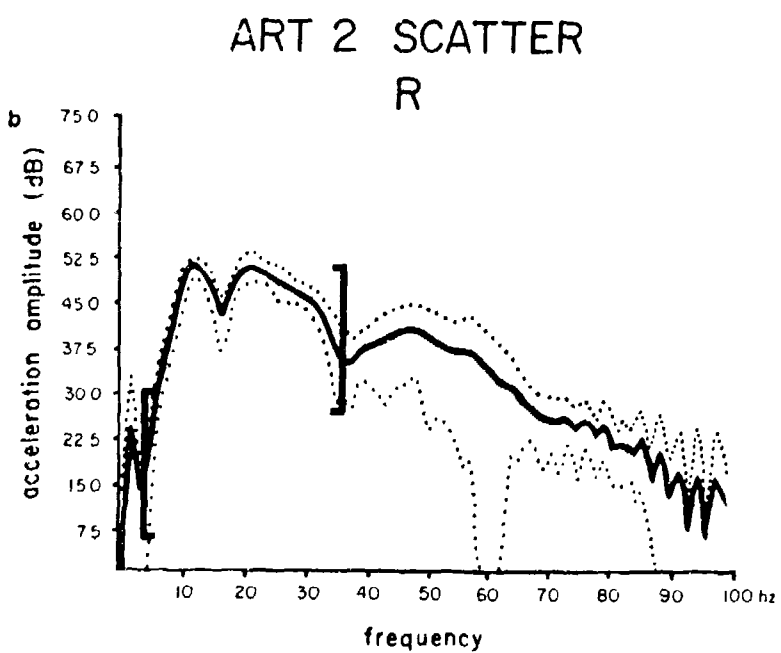
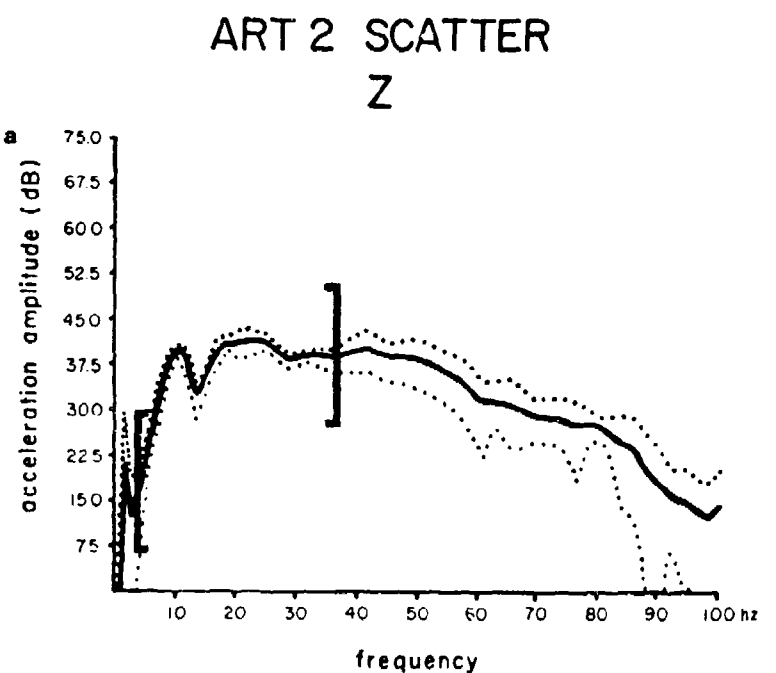


Fig. 3. The mean (dark line) and mean  $\pm 1$  s.d. (dotted line) spectral estimate from the 20 m records of ARTS 2. The vertical (a), radial (b), and transverse (c) acceleration spectra are given.

## ART 2 SCATTER

T

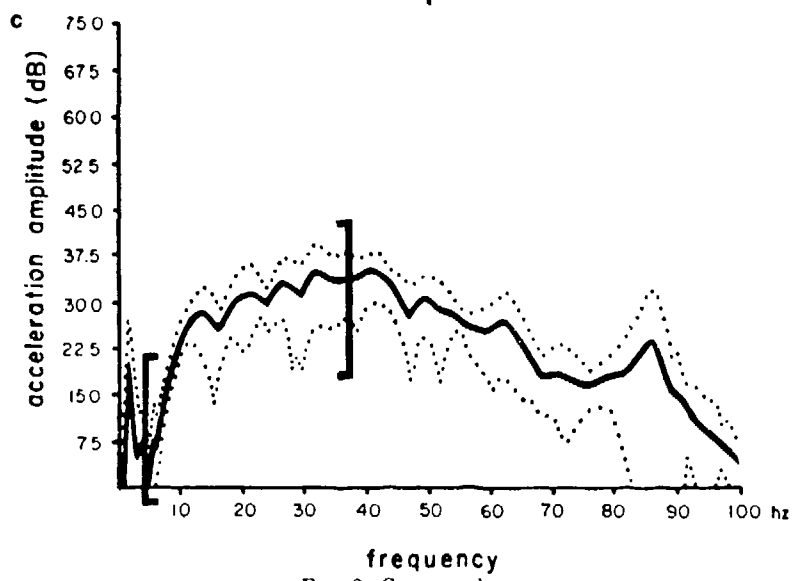
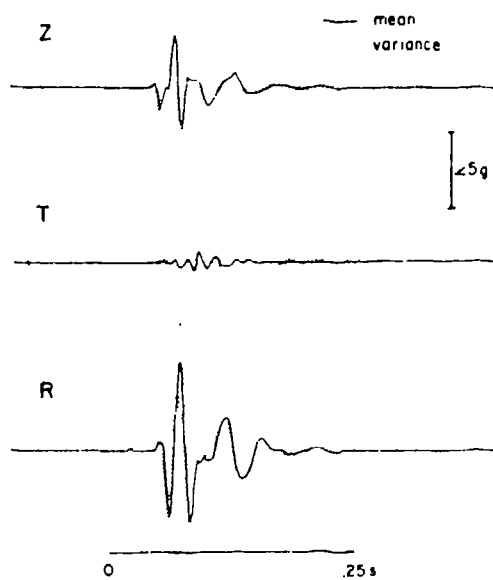


FIG. 3. Continued.

## ARTS 2

FIG. 4 The mean (solid line) and mean  $\pm$  1 s.d. (dotted line) time-domain estimates for ARTS 2.

The ensemble estimates for the spectra show small variances between 3 and 35 Hz for the 20 m range. Beyond this "coherent frequency," the scatter with azimuth in the data becomes large as exemplified in the bandpass seismograms of Figure 2. The 20 m data exhibit 8 dB scatter at 40 Hz.

As reported in Paper I, a series of tests were conducted to separate the effects of gauges, gauge placement, source asymmetry, and propagation path on the high-frequency data. The variation in the data was attributed to the geological media. Therefore, the deterministic part of the wave field is defined as the azimuthally symmetric data below 35 Hz.

#### SUPERPOSITION

The single-burst ensemble spectral estimates are used to check the applicability of linear superposition by direct comparison to the multiple-burst data from ARTS 3 and 7 (Figure 1). The first quantification of these effects considers the case where each source is equidistant from the charge; thus, time delays between the two sources are nonexistent. The primary and center gauge lines are used to check for superposition. Comparisons between the ensemble estimates and the data will be reported only for the 20 m range. Similar conclusions follow from the analysis of data at the 30 m range.

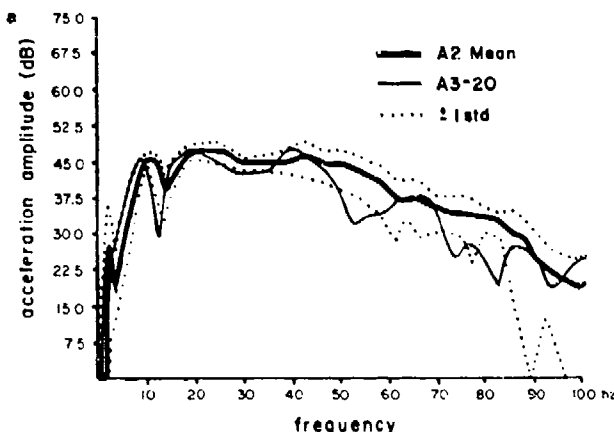
Based upon the 3 to 35 Hz coherent bandwidth from the 20 m ensemble estimates, this frequency band is chosen to check superposition. For completeness, all frequencies between 1 and 100 Hz are displayed in the plots. The criterion chosen to test for superposition is that the multiple-burst data fall within  $\pm 1$  s.d. of the ensemble estimate of the multiple-burst environment. Since the stochastic component of the wave field leads to large variances beyond 35 Hz, the criterion is not robust beyond this frequency. Within the coherent bandwidth, the  $\pm 1$  s.d. bounds are 3 to 4 dB for the Z component and 4 to 5 dB for the R component. The variability in the geological structure limits checks on superposition to within these bounds when *in situ* measurements are made.

The 20 m ensemble estimate of the superposed spectra with variances is compared to the primary and center gauges for ARTS 3 and 7 in Figure 5. The vertical observational data compare well with the superposed spectra between 3 to 35 Hz. Comparison of the predicted spectra with the observations from ARTS 4 (Figure 1) led to similar conclusions. Each test bed was displaced approximately 30 m from the previous test so that between ARTS 2 (used to make single-source ensemble estimates) and ARTS 7, the test bed was displaced by 150 m. Subtle changes in the geology over these scale lengths may explain the systematic changes in the multiple-burst spectra.

The conclusion to be drawn from this analysis is that, within the variance of the multiple-source estimate, superposition holds for 5-lb charges 20 m from the receiver over the frequency band of 3 to 35 Hz. This includes two charges spaced as close as 2 m where individual craters overlap. Larson (1982) reports superposition in laboratory salt validated for two charges separated by  $168 \text{ m}/\text{kt}^{1/3}$  from the observer. In these *in situ* results, superposition is validated within the data scatter (3 to 35 Hz) for two charges separated by  $147 \text{ m}/\text{kt}^{1/3}$  at an observation range of  $1470 \text{ m}/\text{kt}^{1/3}$ .

These results can be compared qualitatively with the reduced displacement potential predicted from the Mueller-Murphy (1971) scaling relation. Figure 6 gives the reduced displacement potential for 5- and 10-lb explosions, respectively.

## VERTICAL 3-20



## VERTICAL 7-20

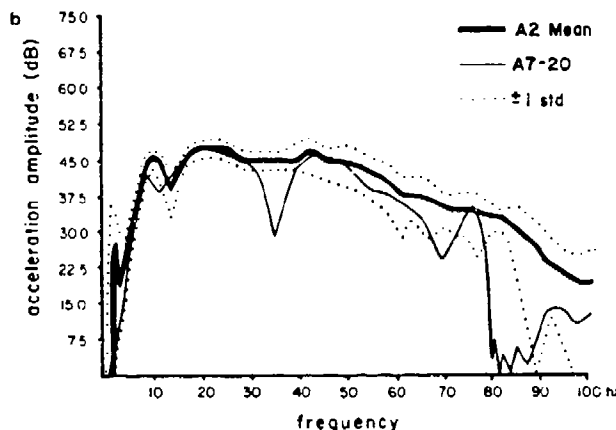


FIG. 5. (a) Predicted and observed acceleration spectra for ARTS 3, with 5-lb charges separated by 2 m. (b) Predicted and observed acceleration spectra for ARTS 7, with 5-lb charges separated by 10 m.

The source corner frequency is between 6 and 9 Hz, remarkably close to what one would estimate from the acceleration spectra (Figures 3 and 4). The model predicts that below the corner that a single charge of 10 lb will nearly match twice the 5-lb result. Above the corner frequency, the single 10-lb charge will not reach twice the 5-lb result. The critical region in the data for testing superposition falls between 10 and 35 Hz at the 20 m range. The exact location of this band is subject to some error, since the Mueller-Murphy (1971) scaling relations were developed for nuclear sources of much greater yields. The critical point is that the principle region of interest for checking superposition is beyond the source corner. The experimental results in Figure 5 support strict superposition well beyond the source corner.

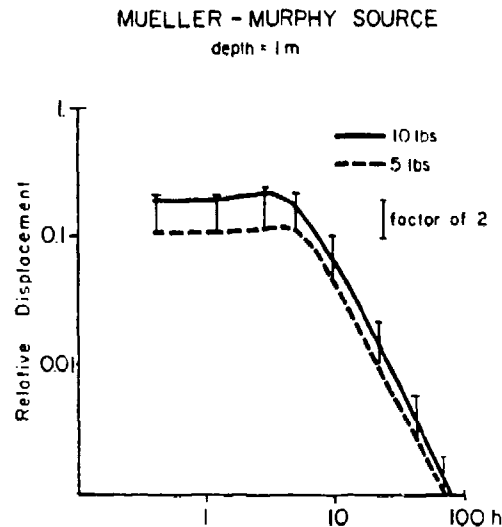


FIG. 6. The displacement spectra from a Mueller-Murphy source model for 5 and 10 lb of explosives.

#### RESOLUTION OF SPATIAL FINITENESS

In an attempt to characterize the finite-spatial effects of the multi-burst environment, synthetics are compared to data recorded in the plane of the linear array of sources (Figure 1, secondary lines). The predictions are made using mean seismograms constructed from data such as that generated in the ARTS 2 experiment (Figure 4).

These mean seismograms are computed by time aligning the direct  $P$  wave from each observation and then computing a mean. The 20 m seismogram from the ARTS 2 experiment along with its  $\pm 1$  s.d. bound is given in Figure 4. The mean radial and vertical accelerograms show little scatter, while the transverse component has standard deviations comparable to the mean. This observation is in agreement with the coherent nature of the radial and vertical motions between 3 and 35 Hz, and the large scatter for all frequencies of the transverse motion. Since the deterministic component of the wave field is of primary interest in the superposition study, the transverse motion will not be considered.

When two sources are displaced from a receiver at different distances, the following effects occur: (1) a change in arrival time of the radiated energy for one source relative to the other; and (2) a change in the waveform shape, since one contribution has traveled a greater distance than the other. If the receiver to charge separation is large relative to the spacing of the two charges, one may neglect the change in wave shape for the two charges. This case is investigated first by superposing the mean seismograms from Figure 4, with an appropriate delay time for charge separation. The delay time becomes

$$T_D = X_{12}/v$$

where  $X_{12}$  is the difference in length of the two propagation paths, and  $v$  is the velocity of the media. The material at the test site has typical near-surface velocities ranging from 244 to 366 m/sec. These values, coupled with charge sep-

aration of 2 to 10 m, led to consideration of time delays of 5 to 40 msec. The time-domain results of this delay and sum procedure are given in Figure 7. Qualitative analysis of these results show constructive interference for the direct-arriving body waves for short delay times (5 msec), with destructive interference leading to complex waveforms for delays between 15 and 30 msec. For delay times greater than 30 msec, one can observe the individual body waves from the two sources. The surface waves (which arrive at 200 msec) show a gradual decay in amplitude over all delay times. The 40 msec delay yields a peak amplitude which is 60 per cent of the 5 msec delay. When the delay times between the two sources are small compared to the single-burst pulse width, constructive interference occurs while complex waveforms with reduced amplitudes are predicted for delay times comparable to the pulse width from the single source. Amplitude changes as a function of delay time for these synthetics are summarized in Figure 8.

The frequency-domain representation of the superposed waveforms more explicitly exhibits the constructive-destructive interference. The superposed acceleration spectra are compared against the single-burst mean observation in Figure 9. As quantified by Pilant and Knopoff (1964), spectral modulation is given by

$$\cos(\omega T_D/2)$$

where  $\omega$  is the angular frequency of interest.

Four qualitative observations of the multi-burst spectra are made: (1) the low-

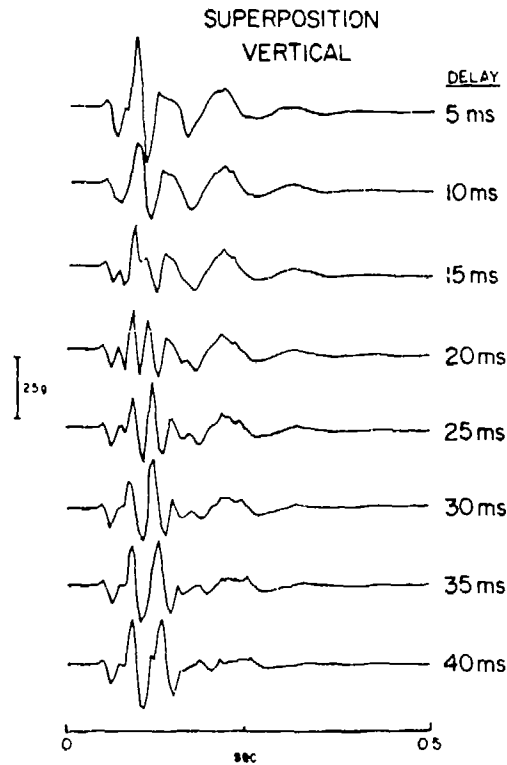


FIG. 7. Vertical accelerations from two explosions using the time-domain mean seismogram from ARTS 2 and summing with an identical record delayed in time between 5 and 40 msec.

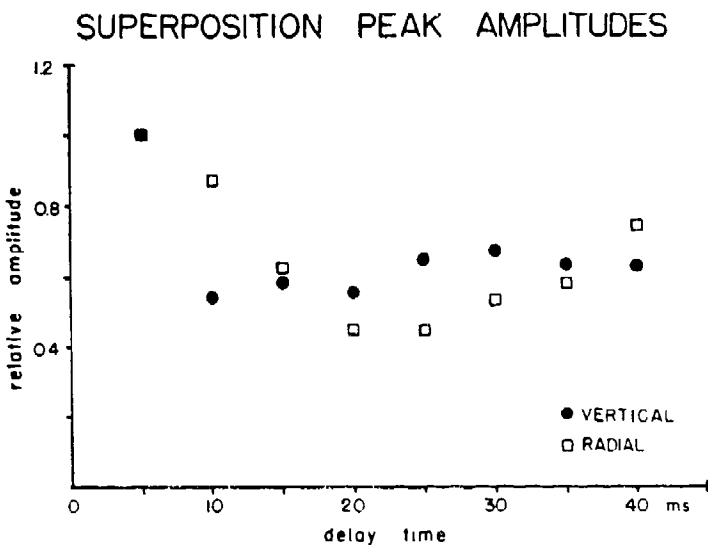


FIG. 8 Peak acceleration amplitudes of the superposed seismograms given in Figure 7 plotted against delay time between the two sources. All amplitudes are relative to peak amplitude for the simulation with a 5 msec delay.

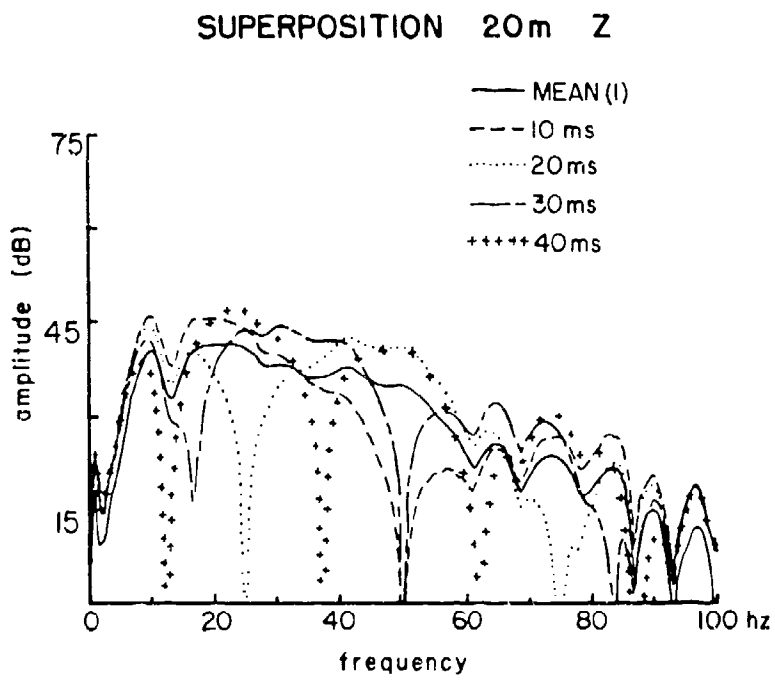


FIG. 9 The spectral estimates of the superposed accelerations given in Figure 7.

frequency level of all spectra are identical, reflecting constructive superposition; (2) the point that the spectra diverge from the long-period level occurs at lower frequencies with increasing time delays; (3) large spectral holes are observed as predicted with the frequency-domain spacing decreasing with increasing time delay between sources; and (4) return to constructive interference occurs between holes.

These results assume no change in Green's functions or propagation path effects as the charge separation increases. The validity of this assumption can be checked against the multi-burst observational data (Figure 1). The secondary gauge lines in the plane of the charge array yield the necessary data.

The secondary gauge data for ARTS 4 and prediction utilizing the 20 m mean data (15 msec delay) is given in Figure 10. The prediction closely replicates the observational data, including the large spectral hole at 32 Hz. Although the observation and the superposition diverge above 35 Hz (the coherent bandwidth), the variation is small. Since the variation discussed in Paper I was attributed to intermittent caliche lenses, one might hypothesize that these lenses were not as prevalent near the ARTS 4 site. The 15 msec delay time represents a propagation velocity of 266 m/sec between the two closely spaced charges. This velocity is near the surface wave velocity, suggesting the surface wave contribution is dominant. Over these close ranges, Green's functions change slowly, and the primary effect on the superposed waveforms is a time delay.

For event 7, the 20 m secondary observation is 20 and 30 m from the two charges. The change in propagation path effects for the 20 and 30 m ranges were dramatic enough that successful prediction required the use of mean seismograms from single bursts observed at 20 and 30 m, respectively. The 30 m mean seismogram was calculated in the same manner as that for the 20 m given in Figure 4. Figure 11 displays the prediction and observation for event 7. The spectral nulls are more closely spaced than in the ARTS 4 data, representative of the 25 msec arrival time difference. Due to the change in propagation path between the two sources, the spectral nulls are not as pronounced as those observed when two identical waveforms are superposed.

#### EVENT 4 VERTICAL

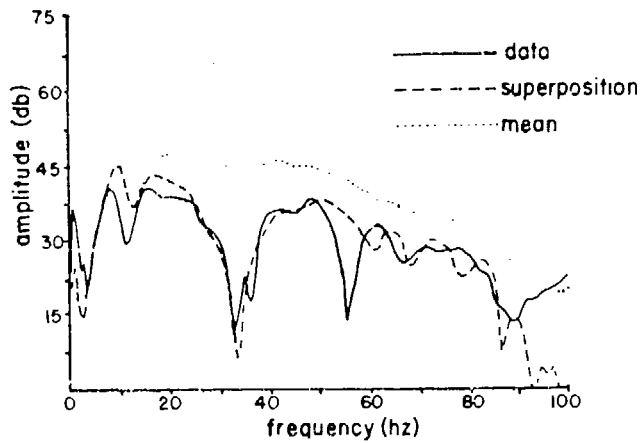


FIG. 10. The predicted superposition spectra for two charges at 20 and 24 m (ARTS 4—secondary) compared to the data and superposition with no delay time (mean).

## EVENT 7 VERTICAL

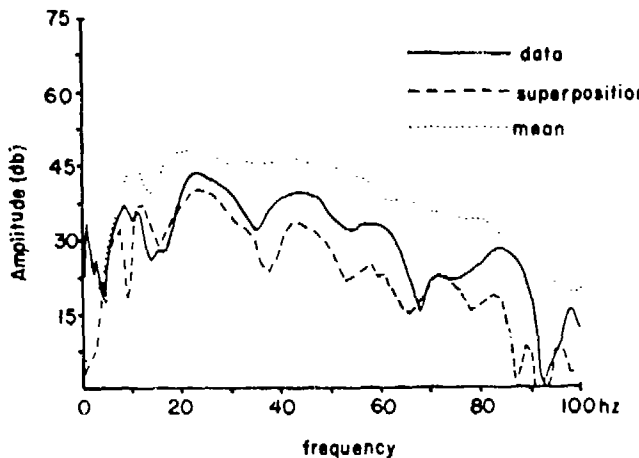


FIG. 11. The predicted superposition spectra for two charges at 20 and 30 m (ARTS 7—secondary) compared to data and superposition with no delay time or propagation differences (mean).

There are three propagation effects which lead to the necessity of including mean seismograms from each of the two sources in ARTS 7: (1) a change in  $t_s - t_p$  time; (2) geometrical spreading effects; and (3) attenuation. A simple analysis of these effects can explain the success of the ARTS 4 superposition using the 20 m mean seismograms and the failure of ARTS 7 utilizing only the 20 m waveforms. Taking the near-surface velocities as  $V_p = 366$  m/sec,  $V_s = 244$  m/sec (Stump and Reinke, 1982) the  $t_s - t_p$  time differences are 0.005 sec for ARTS 4 and 0.014 sec for ARTS 7. The 0.005 sec change is one sample interval in the observational data and corresponds to a 31° phase shift at 17 Hz and a 63° phase shift at 35 Hz. For ARTS 7, the phase shift is 86° at 17 Hz and 176° at 35 Hz. The phase shifts for ARTS 7 are dramatic enough to jeopardize the single waveform superposition procedure. At higher frequencies, the ARTS 4 results should also deteriorate.

Geometrical spreading will lead to amplitude differences from the two sources which are not accounted for in the single seismogram superposition. Experimental determination of geometrical decay rates for this test site give  $r^{-1.6}$  for the body waves and  $r^{-0.5}$  for the surface waves (Stump, 1983). For ARTS 4, with charges at 20 and 24 m, the ratio of body wave amplitudes from the two ranges is predicted to be 0.75, while the ratio for the surface wave amplitudes is 0.93. Similar calculations for ARTS 7 give the body wave ratio as 0.54 and the surface-wave ratio as 0.82. These calculations indicate that, at least for the body waves, the single range superposition procedure for ARTS 7 is inadequate.

Finally, the effect of attenuation ( $Q$ ) must be quantified. The range of  $Q$  values for the dry alluvium environment can be bounded between 10 and 40 (Flynn, 1986). The simple exponential  $Q$  model  $e^{-2\pi f t Q}$ , where  $f$  is the frequency and  $t$  is the shear arrival time, was developed to quantify these effects for the 3 to 35 Hz band. The 24 to 20 m ratios show only moderate  $Q$  effects even at the highest frequencies and smallest  $Q$ . The 30 to 20 m ratios give a value of 0.63 for  $Q = 10$  and  $f = 35$  Hz. Although  $Q$  effects are less dramatic than the phase shifts

and geometrical spreading terms, they may become significant for ARTS 7, if the  $Q$  value of 10 is taken.

### CONCLUSIONS

The series of small-scale explosive experiments tested the applicability of linear superposition in the near-field. The study has shown that one must separate stochastic and deterministic propagation path effects from the single-burst wave field prior to testing for superposition. Once this process has been completed (Paper I), then superposition is verified as the two burst wave fields fall within  $\pm 1$  s.d. of the ensemble estimate (3 to 35 Hz). Thus, superposition is supported for two, 5-lb charges spaced as close as 2 m ( $147 \text{ m} \cdot \text{kt}^{1/3}$ ). Comparison with the Mueller-Murphy source function for 5 and 10 lb shows that superposition must be checked above the corner frequency.

Finite-spatial source effects are experimentally quantified by recording data in the plane of the two charges. These finite effects in the near-field include: (1) a rise in long-period spectral values that match direct superposition; (2) lowering of corner frequency with increased source separation; and (3) spectral scalloping at high frequencies. Comparison of superposed ensemble spectra (time delayed) show that, when travel-time differences between the two sources are the primary effects in the observed wavefield, then the observed data are replicated, which include large interference holes in the spectra. As propagation path differences between the two charges result in waveform changes, the superposition procedure can be applied using separate ensemble estimates for each range. The resulting waveforms again match the observations. Interference holes that were so prevalent when only source delay time was present (ARTS 4) are not as well defined when wave shape changes due to propagation are present in the superposition (ARTS 7). These propagation effects were quantified with the change in  $t_s - t_p$  from the two charges leading to large phase shifts for ARTS 7. Differences in geometrical spreading and  $Q$  for the two charges in ARTS 7 were important, although not as strong.

Utilizing the principles of superposition as applied to the deterministic portion of the wave field, a procedure has been developed which can be used to predict waveforms from arrays of explosives. This procedure assumes that the single-burst environment has been characterized and may require the environment to be quantified at a number of ranges when arrival time differences, geometrical spreading differences, and attenuation differences are important. The effect of arrival time and attenuation differences increases with frequency.

### ACKNOWLEDGMENTS

This project was supported by the Air Force Office of Scientific Research through Grant AFOSR-84-0016 to Southern Methodist University. Funding for the experiments was provided by the Air Force Weapons Laboratory Independent Research Program under Projects ILIR8207 and ILIRb414.

### REFERENCES

- Bergman, O. R., F. C. Wu, and J. W. Edl (1974). Model rock blasting measures effects of delays and hole pattern on rock fragmentation. *Eng. Mining J.* **175**, 124-127.
- Bleisweiss, S. R. (1973). Simulation of strong motion earthquake effects on structures using explosive blasts. *Nuclear Eng. Design* **25**, 126-149.
- Cooper, H. F. (1970). On the simulation of ground motions produced by nuclear explosions. AFWL-WLC-TN-70-001, Air Force Weapons Laboratory, Kirtland Air Force Base, New Mexico.

- Flynn, E. C. (1986). Effects of source depth on near source seismograms, *M.S. Thesis*, Southern Methodist University, Dallas, Texas.
- Greenhalgh, S. A. (1980). Effect of delay shooting on the nature of P-wave seismograms, *Bull. Seism. Soc. Am.* **70**, 2037-2050.
- Hagan, T. N. and G. D. Just (1974). Rock breakage by explosives: theory, practice, and optimization. *Proc. Third Int. Soc. Rock Mech.* **2**, 1349-1358.
- Higgins, C. J., R. L. Johnson, and G. E. Triandafyllidis (1978). The simulation of earthquake-like ground motions with high explosives, Report CE-45 (78) NSF-507-1, Department of Civil Engineering, University of New Mexico, Albuquerque, New Mexico.
- Larson, D. B. (1982). Inelastic wave propagation in sodium chloride, *Bull. Seism. Soc. Am.* **72**, 2107-2130.
- Minster, J. B. and S. M. Day (1986). Decay of wave fields near an explosive source due to high-strain nonlinear attenuation, *J. Geophys. Res.* **91**, 2113-2122.
- Mueller, R. A. and J. R. Murphy (1971). Seismic characteristics of underground nuclear detonations. Part I. seismic scaling law of underground nuclear detonations, *Bull. Seism. Soc. Am.* **61**, 1675-1692.
- Pilant, W. L. and L. Knopoff (1964). Observations of multiple seismic events, *Bull. Seism. Soc. Am.* **54**, 19-39.
- Reinke, R. E. and B. W. Stump (1987). Stochastic geologic effects on near-field ground motions in alluvium, *Bull. Seism. Soc. Am.* **78**, 1037-1058.
- Stump, B. W. (1983). Source characterization of bermed surface bursts, *Bull. Seism. Soc. Am.* **73**, 979-1003.
- Stump, B. W. and R. E. Reinke (1982). Spall-like waveforms observed in high-explosive testing in alluvium, AFWL-TR-82-15, Air Force Weapons Laboratory, Kirtland Air Force Base, New Mexico.
- Trulio, J. G. (1978). Simple scaling and nuclear monitoring, Applied Theory, Inc., Report ATR-77-45-2, Los Angeles, California.
- Winzer, S. R. (1978). The firing times of ms delay blasting caps and their effect on blasting performance, Report to the National Science Foundation, Contract DAR-77-05171, Martin Marietta Laboratories, Baltimore, Maryland.
- Winzer, S. R. and A. Ritter (1980). The role of stress waves and discontinuities in rock fragmentation: a study of fragmentation in large limestone blocks, Proc. 21st U.S. Symposium on Rock Mechanics, University of Missouri, Rolla, Missouri, 362-370.
- Winzer, S. R., D. A. Anderson, and A. P. Ritter (1981). Application of fragmentation research to blast design: relationships between blast design for optimum fragmentation and frequency of resultant ground vibration, Proc. 22nd U.S. Symposium on Rock Mechanics, Massachusetts Institute of Technology, Cambridge, Massachusetts 237-241.

SOUTHERN METHODIST UNIVERSITY  
DEPARTMENT OF GEOLOGICAL SCIENCES  
DALLAS, TEXAS 75275 (B.W.S.)

AIR FORCE WEAPONS LABORATORY NTESG  
KIRTLAND AIR FORCE BASE, NEW MEXICO 87117-  
6008 (R.E.R.)

Manuscript received 9 March 1987

END

FILMED

8-89

DTIC